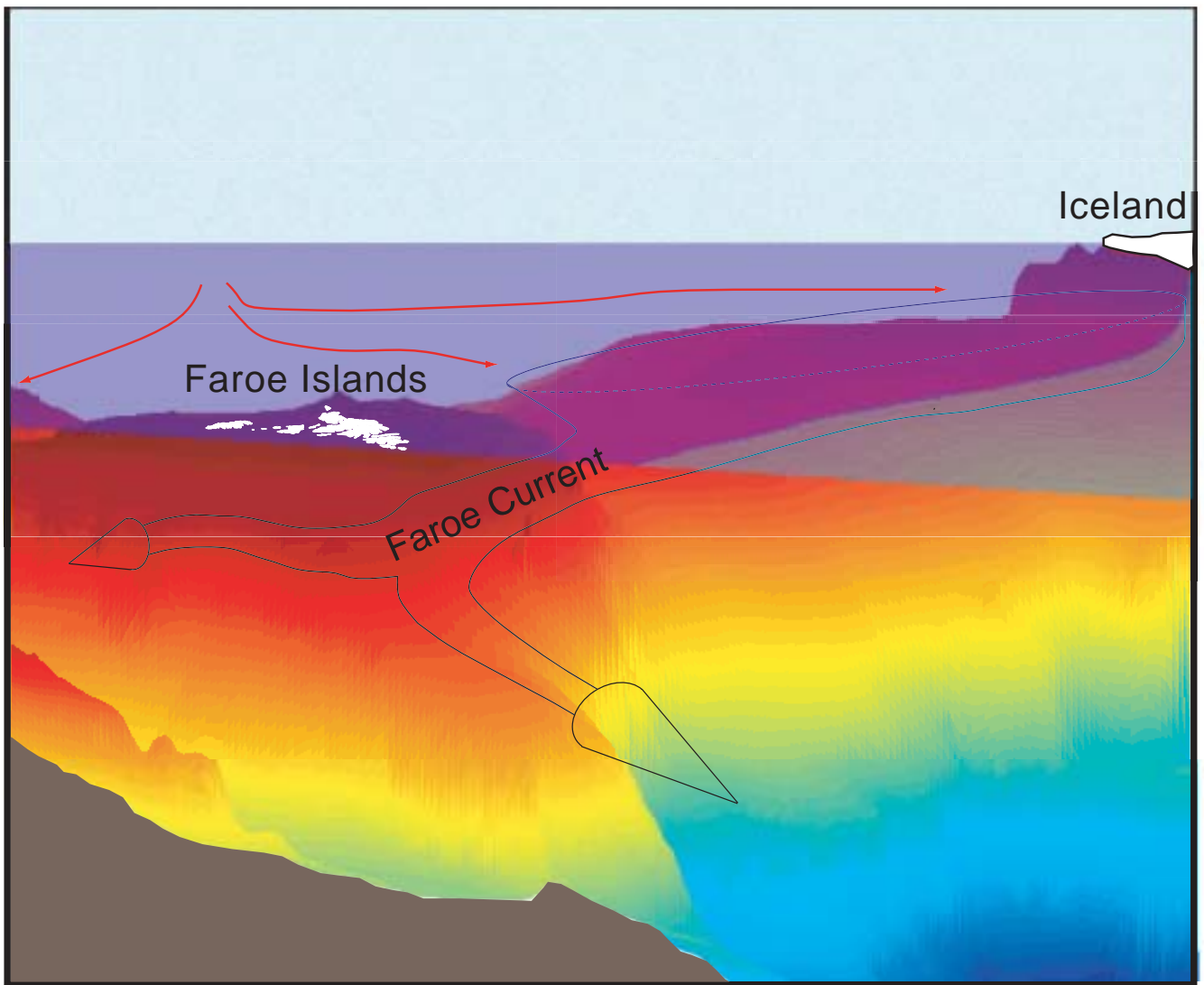


The Faroe Current



by
Hjálmar Hátún

Dr. Scient. Thesis
Tórshavn, February 2004

ISSN 1502-5519

ISBN 82-8116-001-2

REPORTS IN METEOROLOGY AND OCEANOGRAPHY,

UNIVERSITY OF BERGEN.

Report No. 1-2004.

II

PREFACE

This work constitutes a thesis for the degree of Doctor Scientarum in physical oceanography at the Geophysical Institute, University of Bergen, Norway. The work has been carried out at the Faroese Fisheries Laboratory, Faroe Islands, with some shorter stays in Bergen.

The Atlantic inflow from the North Atlantic Ocean to the Nordic Seas is the main theme discussed, and observational material and a mathematical ocean model have been used to study some aspects of this inflow. A synthesis is given first followed by a collection of five papers, whereof four have been through a peer review. I have chosen to include some unpublished results since these give a more complete analysis of the theme discussed. Relatively much space in the synthesis is given to these unpublished results as there is no paper to support the findings. The synthesis contains a number of figures in order to make this first part readable on its own.

ACKNOWLEDGEMENTS

I first want to thank my supervisor, Dr. Bogi Hansen, for his untiring assistance throughout this work and his readiness for discussions. His critical and thorough reviews of my drafts have been a good guide for improvements and an assurance when handing my work for further review. Having had Professor Peter Haugan as my remote supervisor at the Geophysical Institute in Bergen has also given me the confidence that all my University-related issues were in the best hands.

I value my collaboration with Dr. Annebritt Sandøe and Professor Helge Drange at NERSC. It has been inspiring, rewarding and fun, and I hope that this co-work will continue into the future. My mentor, friend and former supervisor at NTNU, Professor Thomas McClimans, also deserves the greatest thanks for introducing me to Oceanography and for being an inexhaustible source of inspiration. I also wish to express my gratitude to friends and colleges from near and abroad for discussions, social company and for supplying me with literature and data when needed. This work is a part of the *West Nordic Program for Ocean Climate Research* (WNPOCR) project, which is financed by the Nordic Council of Ministers.

And finally, thank you Birita for your support and patience.

Tórshavn, February 2004

Hjálmar Hátún

EXECUTIVE SUMMARY

The Atlantic inflow is of key importance for the marine ecology in the Nordic Seas and for the climate in the countries surrounding these waters. This thesis focuses on the large inflow branch between Iceland and the Faroe Islands, but the inflow between the Faroes and Scotland is also discussed.

Comprehensive hydrographic and current data, obtained along a north-south standard section crossing the Faroe Current to the north of the Faroes, have been analyzed. The principal patterns of hydrographic and current variation along this section were identified. These represent a pulsation in the near core current velocities, lateral fluctuations of the current core and vertical movements of the main pycnocline, which constitutes the sub-surface signature of the Iceland-Faroe Front in the region. A connection was found between the current mode representing the lateral fluctuations and the hydrographical pattern linked to the vertical movement of the pycnocline. Daily information on the temperature and the salinity fields was obtained from the current field via this relation.

Combining the current data and the additional hydrographic information, a relatively accurate volume transport estimate of the Atlantic inflow could be obtained. The mean transport for the period July 1997 to June 2001 was estimated to be 3.5 ± 0.5 Sv ($1 \text{ Sv} = 10^6 \text{ m}^3\text{s}^{-1}$). The eastward (downstream) current velocities are largest in March-April, but the spatial coverage of Atlantic water is also smallest during this period, resulting in an Atlantic water transport with only a weak seasonal signal. Most transport variation was seen at time-scales between a half and two months, but a secondary peak in the spectrum was found at five to seven days. A reversal of the flow with transport towards the west was not observed, illustrating the persistency of the Faroe Current. The transport was not found to be correlated to wind, wind stress, or sea surface air pressure.

The potential of using sea level gradients for transport estimation has been examined. This approach was not found to be viable unless other monitoring as e.g. seabed pressure, inverted echo sounders or similar is conducted concurrently. The possibility of using the Nansen Center version of the Miami Isopycnal Coordinate Ocean Model (MICOM) for transport estimation was likewise studied. Some of the observed transport variability is correctly simulated, but the model is not yet at the stage where it can replace the current observations. The relatively expensive current profilers are thus the only option for reliable transport estimation at present.

Regular fluctuations with periods between four and seven days are identified in the Atlantic inflow. Similar oscillations were also observed throughout the water column under the Faroe Current and as deep as 1700 m. These oscillations are explained as southward propagating Topographic Rossby waves impinging onto the Faroe Slope. A simple two-layer analytical model explains the salient features of the current intensification and the vertical pycnocline deflection as the wave propagates onto the slope. The waves may influence the bifurcation of the Faroe Current at the northeastern corner of the Faroe Plateau.

This bifurcation is decisive for how much of the Atlantic water, enters the slope current west of Norway and how much continues in the outer branch of the Norwegian Atlantic Current. It may also influence, how much ends as the recirculated Faroe Current in the Norwegian Sea and how much continues all the way to the Arctic regions. Significant correlations were found between current measurements to the north and to the east of the Faroe Shelf. Altimeter data, combined with hydrographic data in the FSC, are used to estimate the seasonality of the Faroe Current transport southwards into the FSC. No seasonality was seen in the Southern Faroe Current prior to 1995, but during the subsequent years a clear seasonal cycle with a maximum in February-April and an amplitude of ~ 0.6 Sv was found. More data is needed in order to understand the fate of the Faroe Current in the Nordic Seas.

The analyzed current time series are short in a climatic context and the MICOM model was invoked to get a longer time perspective. A 53 years hind-cast simulation with the regional model version was conducted to explore the nature of the pole-ward flowing Atlantic water in the Iceland-Scotland region. It was found that the simulated seasonal and long-term temperature variations in the Continental Shelf Current closely resemble observations from the North Atlantic Ocean, the Faroe Shetland Channel, and from the Norwegian Sea. The simulated temperature on the Faroe Plateau was compared to a long-term time-series of daily coastal temperature. In addition to correctly simulated seasonal and long-term temperature variations, a realistic seasonal modulation with a varying amplitude and phase was also found. The potential for using the simulations as a support when interpreting long-term hydrographic records and as a guide for future monitoring, has been examined.

Table of Contents

PREFACE	III
ACKNOWLEDGEMENTS	III
EXECUTIVE SUMMARY.....	V
1. INTRODUCTION	1
2. GENERAL DESCRIPTION	2
2.1 Historical Perspective	2
2.2 Fluxes	2
2.3 Forcing	3
2.4 The Atlantic Water Flow to and Through the Iceland-Faroe Gap.	3
2.5 The Iceland-Faroe Front.....	3
2.6 The Faroe Current.....	5
3. MATERIAL	6
3.1 Observations in Section N	6
3.2 Model Description.....	7
4. RESULTS	7
4.1 Current and Hydrographic Variability (Section N)	7
4.2 Transports	8
4.3 Shorter Time-Scale Variations (Section N).....	11
4.4 Bifurcation of the Faroe Current.....	12
4.5 Observed and Simulated Hydrography	14
5. CONCLUDING REMARKS	16
5.1 Summary.....	16
5.2 Future Perspectives.....	16
APPENDIX A.....	17
Data material	17
APPENDIX B.....	18
Modeled/Observed Hydrography in the Faroe Current	18
APPENDIX C.....	18
Bifurcation of the Faroe Current.....	18
REFERENCES	19
Paper I	Hátún, H., Hansen, B., and Haugan, P. M. (2003), Using an “inverse dynamic method” to determine temperature and salinity fields from ADCP measurements, <i>Journal of Atmospheric and Oceanic Technology</i> , 21, 527-533.
Paper II	Hansen, B., Østerhus, S., Hátún, H., Kristiansen, R., and Larsen, K. M. H. (2003), The Iceland-Faroe inflow of Atlantic water to the Nordic Seas, <i>Progress in Oceanography</i> , 59, 443-474.
Paper III	Hátún, H. and McClimans, T. A. (2003), Monitoring the Faroe Current using altimetry and coastal sea-level data, <i>Continental Shelf Research</i> , 23, 859-868.
Paper IV	Hátún, H., Variability in the Iceland-Faroe Front and in the Faroe Current due to incident Topographic Rossby waves, <i>Manuscript</i> .
Paper V	Hátún, H., Sandø, A., Drange, H., and Bentsen, M. (2004), Seasonal to decadal temperature variations in the Faroe-Shetland inflow waters, <i>The climate of the Nordic Seas</i> , AGU Monograph, In Press.

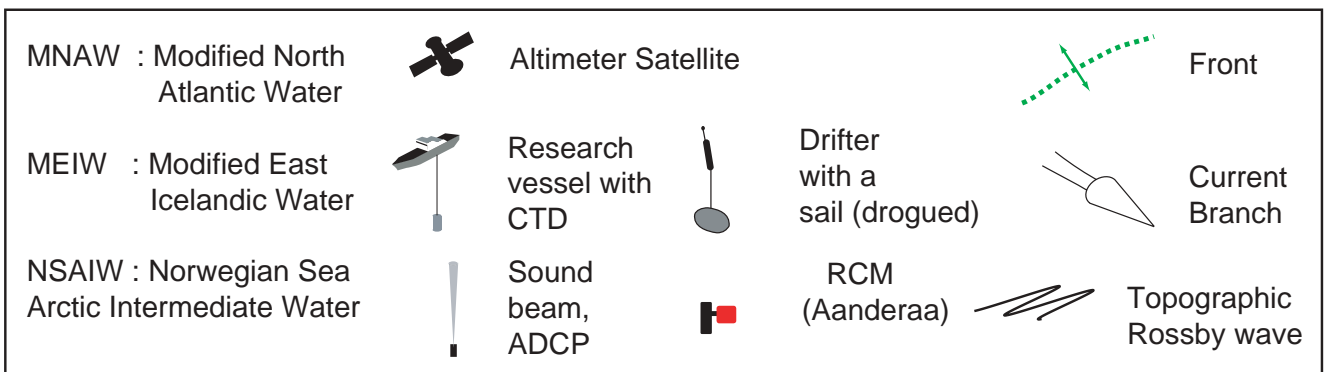
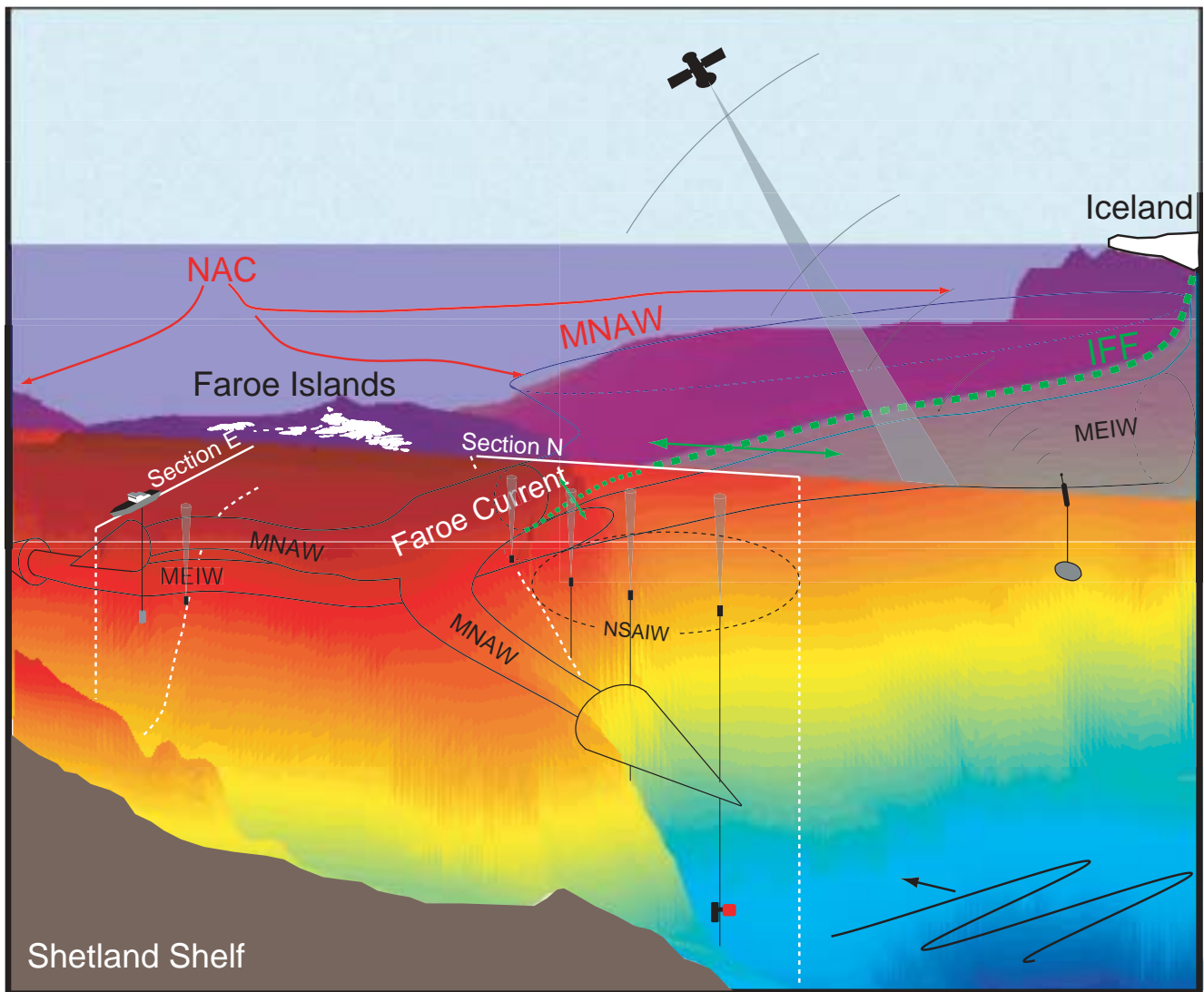


Figure 1 The main observations utilized and some salient features concerning the Faroe Current

1. INTRODUCTION

The relatively mild climate in Northern Europe and in the countries adjacent to the eastern shores of the Nordic Seas is partly ascribed to the pole-ward Atlantic inflow over the Greenland-Scotland Ridge [Seager et al., 2002]. After having released large amounts of heat to the region [Simonsen and Haugan, 1996], these Atlantic water masses sink due to their cooling and their relatively high salinity, and the denser and deeper equator-ward flowing overflows are formed [Aagaard et al., 1985]. The overflows draw more water from the south and this process is named the Thermohaline Circulation (THC). The overflows constitute much of the North Atlantic Deep Water (NADW), which is one of the key variables to Earth's response to climate change [Dickson and Brown, 1994]. The North Atlantic wind stress curl will also force Atlantic water towards the Greenland-Scotland Ridge [Orvik and Skagseth, 2003]. In addition to this, vertical mixing processes, primarily due to winds and tides, will supply potential energy needed for the ocean general circulation [Wunsch and Ferrari, 2004]. All the mentioned processes will contribute in driving the Meridional Overturning Circulation (MOC) popularly referred to as the "Great Conveyor Belt" [Broecker, 1991]. But there is still some dispute about the relative importance of the respective processes.

The globally averaged temperature has increased by about 0.6°C during the last century [IPCC, 2001], and the IPCC (International Panel on Climate Change) projects further global warming of approx. 1.4-5.8°C by the year 2100. Most climate scientists agree that the increasing levels of greenhouse gases, like carbon dioxide (CO₂), play a significant role in the global temperature rise [IPCC, 2001]. As the climate becomes warmer, the amount of fresh water in the Arctic increases due to the melting of sea ice and glaciers.

The hydrological cycle is expected in addition to intensify causing more rainfall in the northern regions. The surface water masses become fresher and lighter, and their tendency to sink decreases [Aagaard and Carmack, 1989]. As a consequence, the conveyor can lose motive force, resulting in a decrease in the heat transport to the Arctic regions.

Observations of the equator-ward overflows between the Faroe Islands and Scotland indicate a gradual decrease in volume transport of at least 20% during the last 50 years [Hansen et al., 2001]. Being a link in the same conveyor, the relatively warm Atlantic inflow is thus thought to have weakened during this period as well, although data are too scarce to support this.

The scenario of *rapid climate change* as opposed to *gradual climate change* has received much attention during the last years. Large research programs like the RAPID at the Natural Environment Research Council of UK have recently been established. The main objective of these studies is to improve our understanding of the MOC and the THC.

The region north of the Greenland-Scotland Ridge may be profoundly affected by a reduced Atlantic inflow and, e.g. the sea surface air temperature around Svalbard has been predicted to drop as much as 21 °C in case of a complete turn-off [Seager et al., 2002]. The heat, salt and nutrients carried northward in the Atlantic inflow are also highly important for the marine ecology in the Arctic Mediterranean [Beaugrand and Reid, 2003].

The Iceland-Faroe Gap and the Faroe-Scotland Gap are the main gateways for the Atlantic water flowing northward across the Greenland-Scotland Ridge [Hansen and Østerhus, 2000]. The Iceland-Faroe Gap feeds the eastward flowing Faroe Current to the north of the Faroe Islands, and this current branch prevents the Iceland-Faroe Front from reaching the Faroes. A weakening of this current may allow the front, which forms a boundary between the Atlantic and the cold Arctic water masses, to reach the islands with local, but critical consequences.

In contrast, the highest sea surface temperatures at the Faroese coast on record were actually measured last year (2003) (pers. communication with Bogi Hansen). An illustrative consequence of the warmer conditions is that many Scottish ski resorts are put up for sale this year [Seenan, G., The Guardian 14 Feb. 2004].

This may seem contradictory since many premonitions predict a critical cooling around the British Isles. Heating from the global warming presently occurring and cooling from a possibly weakening Atlantic inflow constitute two competing processes in the northern north Europe. It is uncertain which one will dominate in the future, yet predictions of changes in the near future seems, nonetheless certain.

Since the inflows and possible changes constitute the key components of the climate system, it is of paramount importance that they be monitored. In the North Atlantic the poleward flows generally occur over a vast area and reliable quantification of the transports is impractical. However, the Atlantic water masses converge at the gateways situated in the north and south of the Faroes making this area a natural monitoring site of the inflows. The objective of this thesis is:

- 1) To describe the Faroe Current and analyze its current and temperature variations both in time and space. To utilize observations across this current to generate accurate time-series of the volume transport of Atlantic water.

- 2) To describe the bifurcation of the Faroe Current at the northeastern corner of the Faroe Plateau. To estimate from this the fraction of the Faroe Current that continues directly towards Norway and the fraction that turns into the Faroe-Shetland Channel.

- 3) To validate a General Circulation Model (GCM) against modern current measurements and historical hydrographic observations in the Atlantic inflow over the Iceland-Scotland Ridge. This task is a part of the *West Nordic Program for Ocean Climate Research*.

A general description of aspects related to the Atlantic inflow, focusing on the Iceland-Faroe Gap, is given in Section 2. Observational material from a standard section north of the Faroe Islands and a basic description of the Miami Isopycnal Coordinate Ocean Model (MICOM) ocean model is presented in Section 3. In section 4 the results of Paper I-V are combined and summarized with an emphasis on describing the current and hydrographical variability in the Faroe Current (4.1), transport calculations (4.2.1–4.2.4), variability due to topographic Rossby waves (4.3), the bifurcation of the Faroe Current (4.4), and observed and simulated long-term temperature variations in the Faroe-Scotland area (4.5). Some future perspectives are given in Section 5, followed by appendices with supplementary information.

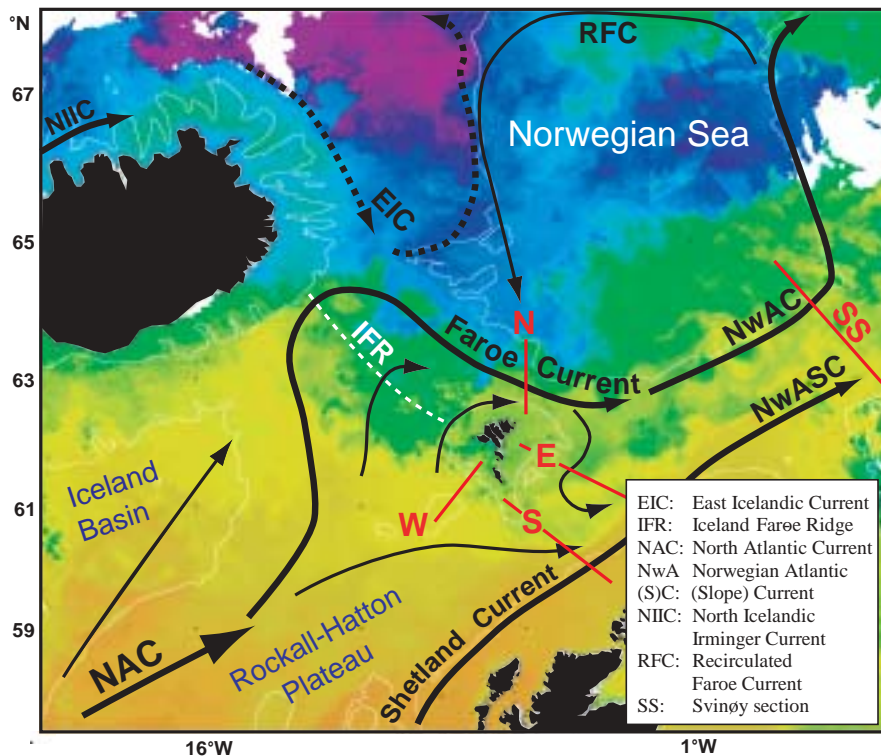


Figure 2 The main inflow branches over the Iceland-Scotland Ridge. Solid lines represent Atlantic water and the dotted curves indicate Arctic water. The Nordic WOCE measurement sections are shown with red lines. The background colors show a satellite image of sea surface temperature (December). The image is a 7-day composite of once/day high-resolution AVHRR images with 1.1 km spatial resolution. It was kindly made available by Dr. Peter Miller, Plymouth Marine Laboratory.

2. GENERAL DESCRIPTION

2.1 Historical Perspective

Regular surveys along the present day Nolso-Flugga Faroe-Shetland section commenced at the beginning of the 20th century as a part of the International cooperative research, which ultimately led to the formation of the International Council for the Exploration of the Sea (ICES) [Helland-Hansen and Nansen, 1909]. The intention was to monitor both water mass characteristics and transports, as it already then was known that the Iceland-Scotland Ridge was the main entryway for the significant transports of heat, salt and nutrients from the Atlantic towards the Arctic.

In 1955, regular hydrographic surveys were initiated along the Svinøy section north of the ridge [Mork and Blindheim, 2000], and from 1975 to present a standard section in the Rockall Trough south of the ridge [Holliday et al., 2000] has been regularly visited. The dynamical theory to calculate fluxes from hydrography [Helland-Hansen, 1903] was the only technique available during the first half century [Tait, 1957] of measurements, but when direct current measurements became available in the 1960s, it was soon realized that the geostrophic calculations were inadequate due to strong bottom guided barotropic flows in the ridge area [Hansen and Østerhus, 2000]. Transport estimation based on direct current measurements necessitates an adequate spatial coverage of the flows, which is difficult to maintain due to loss of instruments, primarily caused by intensive fisheries. The first reported yearlong transport series based on direct measurements was by Gould et al., [1985] in the Faroe-Shetland Channel.

In addition to the dynamical method and direct current mea-

surements, other approaches to transport calculations have been tried, for example: mass budgets [Worthington, 1970], inverse methods [Van Aken, 1988], altimetry and hydrography [Pistek and Johnson, 1992], altimetry and model, [Samuel and Johannessen, 1994], coastal sea level and bottom pressure [McClimans et al., 1999], coastal sea level and altimetry [Hátún and McClimans, 2003], and recently with ocean general circulation models (OGCMs) [Nilsen et al., 2003], [Hátún, 2004].

As concluded by Worthington and Volkman [1965], the greater part of the volume of North Atlantic Deep Water (NADW) is contributed by the Norwegian Sea outflows, and in his pioneering work, Worthington [1970] calls attention to the connection between the Atlantic inflow and the denser overflows. Since it has been realized that the NADW is of key importance to the global climate [Dickson and Brown, 1994], the exchanges between the North Atlantic and the Nordic Seas have got much increased international interest.

2.2 Fluxes

The three inflow paths across the Greenland-Scotland Ridge are: 1) the North Iceland Irminger Current west of Iceland, 2) the flow over the Iceland-Faroe Ridge, which ultimately continues as the Faroe Current and 3) the Shetland Current through the Faroe Shetland Channel (Fig. 2). The first mentioned branch carries about 1 Sv ($\text{Sv} = 10^6 \text{ m}^3 \text{ s}^{-1}$) [Kristmannsson, 2001] and is thus inferior to the other two. The Faroe Shetland Channel branch, which historically has been seen as the dominant of the two latter branches, is the most studied, and many of the methods mentioned above have been applied for flux calculations. Estimates ranging from 1.9 Sv to 9.0 Sv and typically with maximum transports in winter have been reported. [Jacobsen, 1943], [Herman, 1949], [Tait, 1957], [Timofeyev,

1963], [Mosby, 1970], [Worthington, 1970], [Dooley and Meincke, 1981], [Gould et al., 1985], [Van Aken, 1988], [Pistek and Johnson, 1992], [Samuel and Johannessen, 1994] and [Turrell et al., 1999]. The most complete estimate available is, however, presented in Turrell et al. [2003], giving an average transport of 3.2 Sv, a weak seasonal amplitude of 0.2 Sv and maximum in winter.

North of the Faroes, Hermann [1949] found a transport of 4.5 Sv through one section using the classical dynamical method, but only a part of this represented Atlantic water that had recently crossed the Iceland-Faroe gap. Tait [1957] reported transport of Atlantic water of considerably smaller magnitudes through several sections, while Sukhovey [as cited by Rosso, 1972] estimated a transport of almost 10 Sv between Iceland and the Faroes. These numbers were all based on the dynamic method, whereas Hansen et al. [1986], using a dense net of short-term current observations, derived an estimate of 2.9 Sv for the Atlantic water flow in the Faroe Current crossing a section along the 6°W line. It was only until remote measuring, using near-bed-mounted acoustic profiling current meters, became possible at the start of the 1990s that long-term direct measurements of transports became reliable and a practical monitoring tool. The Nordic WOCE (World Ocean Circulation Experiment) project, commencing in 1994, made it possible to deploy rows of semi-permanent acoustic Doppler current profilers (ADCPs) along the already existing standard hydrographic sections radiating out from the Faroes (Fig. 2). In addition to the current meters, the CTD (Conductivity, Temperature and Depth) surveys along these lines were intensified. This material put together constitutes the first both spatially and temporally comprehensive *in situ* dataset on the Iceland-Scotland Ridge. Based on two years of this data material, Hansen and Østerhus [2000] estimated the volume transport of Atlantic water north of the Faroes to be 3.3 Sv with a maximum in February-March. The present work includes the most recent and accurate transport estimate, which is 3.5 ± 0.5 Sv with a hardly significant seasonal variation [Hansen et al., 2003] (paper II). The most updated estimate from the Faroe-Shetland Channel [Turrell et al., 2003] (see above) is also mainly based on the Nordic WOCE dataset. A comparison between the two estimates indicates that the Faroe Current might actually be the stronger of the two main inflow branches.

2.3 Forcing

There is some dispute about the driving mechanisms for the exchanges across the Greenland-Scotland Ridge. The primary candidates are; 1) pressure gradients established over the ridge by thermohaline processes in the Arctic Mediterranean and 2) the wind stress over the North Atlantic.

Thermohaline forcing involves estuarine circulation from substantial river discharge and ice melting during summer, and deep and bottom water formation in the central as well as in

marginal seas. The deeper waters fill up the Nordic Seas basins and being denser than the waters in the North Atlantic, they spill over the Greenland-Scotland Ridge. Basically through internal adjustment (continuity), this overflow of dense water contributes to the inflow of the lighter Atlantic water masses into the Nordic Seas.

A cyclonic wind stress over the North Atlantic Ocean will force a northward Sverdrup transport in the North Atlantic. This will induce a sea level gradient over the Greenland-Scotland Ridge, which again will force Atlantic water to cross the ridge pole-wards.

Recent studies that support the former mechanism are; [Hansen and Østerhus, 2000], [Jakobsen et al., 2002], [Turrell et al., 2003] and studies that support the latter are; [Mork and Blindheim, 2000], [Orvik et al., 2001] and [Orvik and Skagseth, 2003].

2.4 The Atlantic Water Flow to and Through the Iceland-Faroe Gap.

The North Atlantic Current passes through a gap connecting the Mid-Atlantic Ridge and Reykjanes Ridge (Charlie Gibbs Fracture Zone) and farther east it splits into two major northeastward flowing branches; through the Iceland Basin and the Rockall Trough [Orvik and Niiler, 2002]. The flow through the Iceland Basin is guided by the Rockall-Hatton Plateau, but the flow pattern in the Rockall-Hatton Plateau region is still not well established [Otto and Van Aken, 1996], [Van Aken and Becker, 1996]. When approaching the banks west of the Faroes, the North Atlantic Current splits up into two branches, one branch that flows into the Faroe-Shetland Channel and the other heading towards the Iceland-Faroe Ridge [Hansen and Østerhus, 2000].

The presence of Atlantic water over the Iceland-Faroe Ridge has been known for a long time [Nielsen, 1904], and the main circulation pattern on the ridge was described already a few years later by Helland-Hansen and Nansen [1909]. The first description of the on-ridge circulation supported by long-term current meter moorings was presented by Meincke [1983]. The resulting near-surface and bottom layer current maps have been verified by others [Perkins et al., 1998], [Hansen et al., 1999a] and show a general clockwise circulation, largely consistent with Helland-Hansen and Nansen's [1909] picture. Despite this knowledge, it is still unclear where the principal inflow of Atlantic water across the ridge takes place. Hansen and Østerhus [2000] discuss a topographically guided 'fast track' near the Faroe Shelf as shown by drifter data, but in a study including 999 drifters, the fastest near-surface drifters crossed the ridge close to Iceland, indicating a major pathway of Atlantic water in that area [Orvik and Niiler, 2002]. Another study based on drifters [Jakobsen et al., 2002] indicates a broad, almost zonal flow across the entire length of the ridge. This issue is the subject of ongoing research.

Table 1 Typical properties of the main water masses in Section N

Acronym	Name	Temperature range	Salinity range
MNAW	Modified North Atlantic Water	7.0 → 8.5°C	35.10 → 35.30
MEIW	Modified East Icelandic Water	1.0 → 3.0°C	34.70 → 34.90
NSAIW	Norwegian Sea Arctic Intermediate Water	-0.5 → +0.5°C	34.87 → 34.90
NNAW	Norwegian North Atlantic Water	3°C	35.00

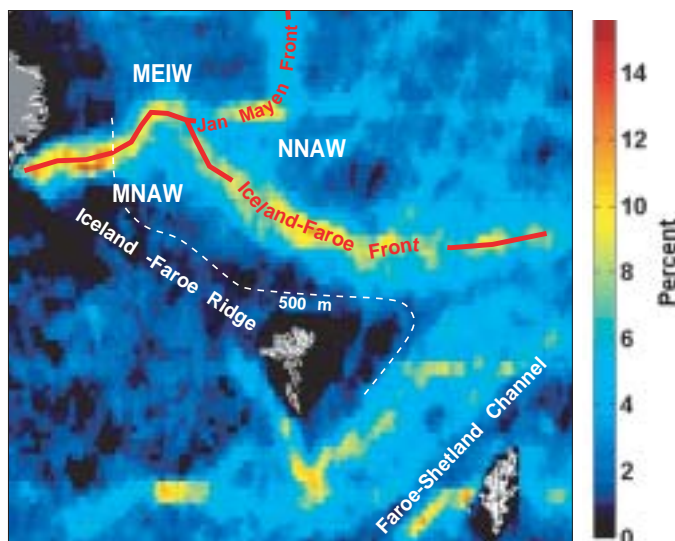


Figure 3 Long-term (1985-1996) frequency of occurrence of SST front in spring (April-June) in the Iceland-Shetland region, based on 9-km resolution AVHRR SST images from the NOAA satellites sampled twice daily. These have been processed with the Cayula-Cornillon algorithms for cloud screening and front detection. The color scale shows the percentage of the total cloud-free time that a given 9 km x 9 km pixel contained a front. This picture was kindly provided by Igor Belkin (see Belkin et al., 2003 for further information).

2.5 The Iceland-Faroe Front

Having crossed the Iceland-Faroe Ridge, the Atlantic water meets colder and less saline waters in the Iceland-Faroe Front. The average position of the front presented in Fig. 3 is consistent with the depiction presented in Hansen and Østerhus [2000], which is based on a compilation of many studies, [Tokmakian, 1994], [Read and Pollard, 1992] and many others. The front originates near the Icelandic shore where abrupt cross-frontal temperature and salinity changes are observed [Stefánsson, 1972]. Along the first stretch from Iceland and eastwards, the front constitutes a boundary zone between the relatively warm Modified North Atlantic Water (MNAW) and the colder Modified East Icelandic Water (MEIW), carried by the East Icelandic Current (EIC) [Hansen and Østerhus, 2000]. Further east a Y-junction between the Iceland-Faroe Front and the Jan-Mayen Front is normally encountered [Smart, 1984], [Read and Pollard, 1992] (Fig. 3), and the front continues eastwards as a border line between MNAW and the Norwegian North Atlantic Water (NNAW), which partly consist of water from the Recirculated Faroe Current [Hansen and Østerhus, 2000]. Typical TS-characteristics of these water-masses are shown in Table 1.

As the front progresses eastwards, it becomes more diffuse so that to the north of the Faroes, cross-frontal gradients may be considerably smaller than originally encountered at the Icelandic shore [Hallock, 1985]. When the front has reached the sharp eastern corner of the Faroe Plateau, it loses bottom contact, and at this stage its near-surface expression is hardly detectable by infrared radiometry (Fig. 3). But this is partly due to the fairly persistent mixed layer in the uppermost 25-50 m, which tends to confuse the temperature signature of the front [Hopkins et al., 1992]. The front has been defined by the 35.0 isohaline [Hansen and Meincke, 1979] and this signature is

seen as a subsurface front continuing through the Svinøy section [Mork and Blindheim, 2000; Orvik et al., 2001] and further northwards along the Vøring plateau [Poulain et al., 1996], [Nilsen, 2003].

At its Iceland-shore origin the frontal slope is relatively steep (~ 0.015) [Read and Pollard, 1992]. The ‘foot’ of the front seems constrained by the Iceland-Faroe Ridge crest [Tait, 1967] and as the surface expression, defined by the 35.0 isohaline, drifts away from the topography when going east [Hansen and Meincke, 1979], the slope of the front decreases by more than a factor of 5 when arriving at the northeast of the Faroes [Read and Pollard, 1992]. At the junction between the ridge and the Faroe Plateau, the bottom expression of the front continues eastwards on the northern Faroe slope, at about crest depth, somewhat shallower than 500 m [Meincke, 1978] (Fig. 3). The near bottom front configuration at the northeastern Faroe Plateau region is still not well understood.

The described front as shown in Fig. 3 is an average interpretation. There is a clear seasonal variation associated with the front with larger northward extensions of the front during the summer period, while it outcrops nearer the Faroe Shelf during the winter [Hansen et al., 2000], (Fig. 4). The instantaneous frontal position is complicated, as it is distorted by meanders and eddies of 30-50 km scale as first notified by Hansen and Meincke [1979]. Since then large efforts have been put into understanding this variability using a wide range of *in situ* observations, remotely sensed large-scale maps and theoretical studies [Hansen and Østerhus, 2000]. The frontal variability implies a cross-frontal exchange of heat and salt [Willebrand and Meincke, 1980], [Hallock, 1985] which has to be evaluated in budget considerations. As a second implication, the frontal variability provides a mechanism to intermittently increase, the overflows of arctic and subarctic waters over the Iceland-Faroe Ridge [Hansen and Meincke, 1979]. The third implication concerns the waters on the Faroe Shelf. Analyzing a long term series of daily sea surface temperatures from the Faroe coast, Hansen and Meincke [1984] found characteristically cold anomalies of less than one week’s duration, with the most prominent occurrence during winter. This feature is explained as intrusions of cold and relatively fresh water from north of the Iceland-Faroe Front. These intrusions will have obvious biological consequences, as they will advect subarctic plankton and nutrients onto the Faroe Plateau [Hansen and Meincke, 1979], [Gaard and Hansen, 2000], [Gaard and Nattestad, 2002]. Sub-inertial oscillations (periods from 3 to 5 days) in the area are reported by Meincke and Kvinge [1978]. Based on a one-year current record at near-bottom depth close to the front in the northwest of the Faroes, Willebrand and Meincke [1980] find a winter-doubling of horizontal kinetic energy for the 3 to 10 day period. Hansen and Meincke [1979] hypothesize that the eddies could be derived from baroclinic-barotropic instabilities, i.e. wave perturbations growing unstable when traveling within a sheared flow over a sloping bottom. From the year-long current series Willebrand and Meincke [1980] conclude that baroclinic instability is the major source of the fluctuations, while the influence of wind is estimated to be an order of magnitude less influential. Despite the large effort given to understanding low-frequency fluctuations since then, the knowledge about the generating mechanisms is still rather inconclusive.

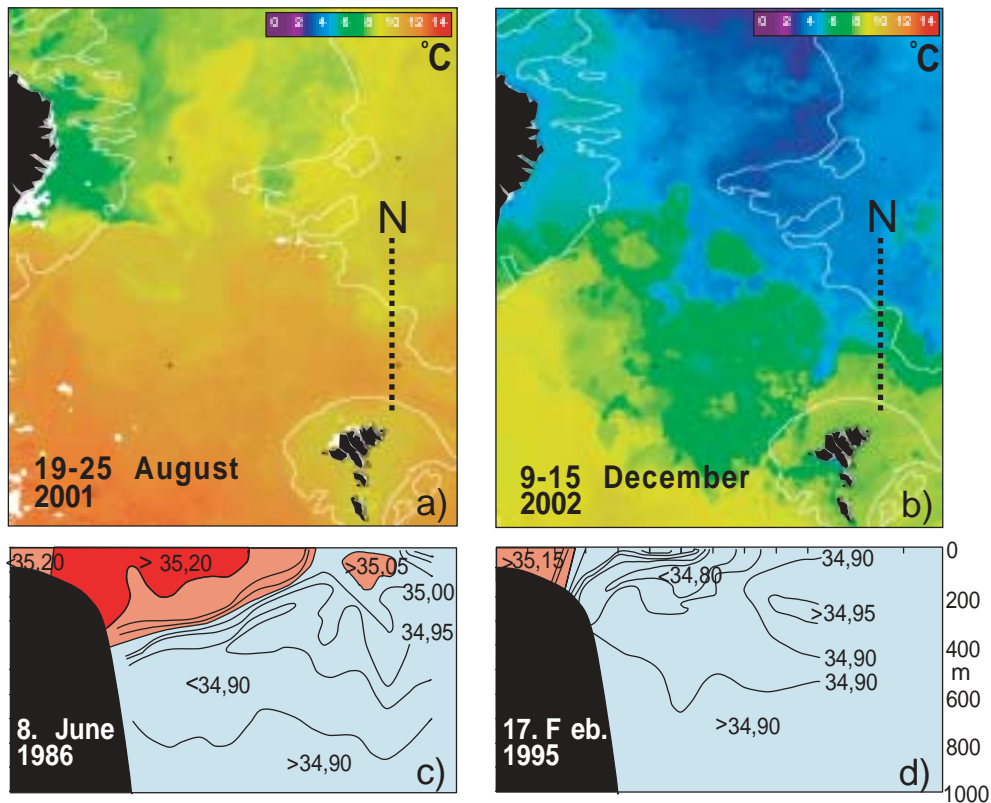


Figure 4 Seasonal variability in the Iceland-Faroe Front. a) and b) show AVHRR SST images for summer and winter, respectively, and c) and d) show extreme in-depth deflections of the front as observed along standard section N (dotted lines). (The lower panel figures should not be interpreted as the typical seasonal variation). The satellite images were kindly made available by Dr. Peter Miller, Plymouth Marine Laboratory.

2.6 The Faroe Current

The Iceland-Faroe Front constitutes a northern and underlying boundary to the Atlantic water that crosses the Iceland-Faroe Ridge northward. The Atlantic water masses are thus forced to flow eastwards towards the Faroe Shelf in layers shallower than the crest depths of the ridge (<500m). The topography becomes steeper as approaching the Faroe Shelf and the flow is converted into a more persistent and concentrated flow termed the *Faroe Current* [Hansen and Meincke, 1984]. North of the relatively steep Faroe Shelf, the flow attains a wedge-like shape bounded to the north by the Arctic and Sub-arctic water masses and to the south by the shelf and the coastal current [Hansen and Østerhus, 2000]. In this area (around 6°W) a measurements section, densely populated by semi-permanent ADCPs and regularly visited by CTD cruises, crosses the current (Section 3). As the Atlantic water progresses farther eastwards, it approaches the eastern corner of the Faroe Plateau and as it passes east of about 4°W the Faroe Current either has to continue eastwards without the bottom contact, which has steered it, or turn the corner and proceed into the Faroe-Shetland Channel. Apparently, it does both, as indicated already by Helland-Hansen and Nansen [1909]. The branch that turns south will be referred to as the *Southern Faroe Current* and the branch continuing directly northeast will be termed the *Frontal Faroe Current*. The former maintains to some extent the wedge-shape, while the latter is not well understood. The Frontal Faroe Current continues as the Norwegian Atlantic Current (NwAC) typically referred to as the western branch observed in the Svinøy section.

On the surface this bifurcation has been clearly demonstrated

by drifters [Poulain et al., 1996], [Orvik and Niiler, 2002], [Jakobsen et al., 2002], while it has been studied by strategic CTD cruises in the deeper layers [Hermann, 1953], [Meincke, 1978], [Hansen et al., 1998]. The common finding in these studies is a low-salinity tongue protruding southwards into the Faroe-Shetland Channel. The water brought southwards into the channel is generally a mixture where Atlantic water is dominating the near-surface layers, and increasing amounts of low-salinity water are observed at deeper levels [Meincke, 1978]. The low-salinity core clearly derives from north of the Iceland-Faroe Front and the term Modified East Icelandic Water (MEIW) is used here to represent it [Hansen et al., 2000; Read and Pollard, 1992]. Seven current meters moored during the period June-July 1987 and in the region where the Faroe Current splits confirm the bifurcation thesis [Hansen and Østerhus, 2000]. These series are, however, short and the variability is large, so little is known about the persistence and temporal character of this bifurcation. The surface circulation picture of an anticyclonic flow around the Faroe Shelf, proposed by Dooley and Meincke [1981], is opposed by Van Aken and Eisma [1987] and Van Aken [1988] who instead suggest a total retroflexion of the MNAW in the Faroe-Shetland Channel back to the Norwegian Sea (Fig. 2). This latter is supported in the drifter studies mentioned above.

The retroflected Southern Faroe Current joins the Shetland Current and these continue together, partly after a round-trip in the Norwegian trench, becoming the eastern branch in the Svinøy section, also called the Norwegian Atlantic Slope Current (NwASC), [Orvik and Niiler, 2002].

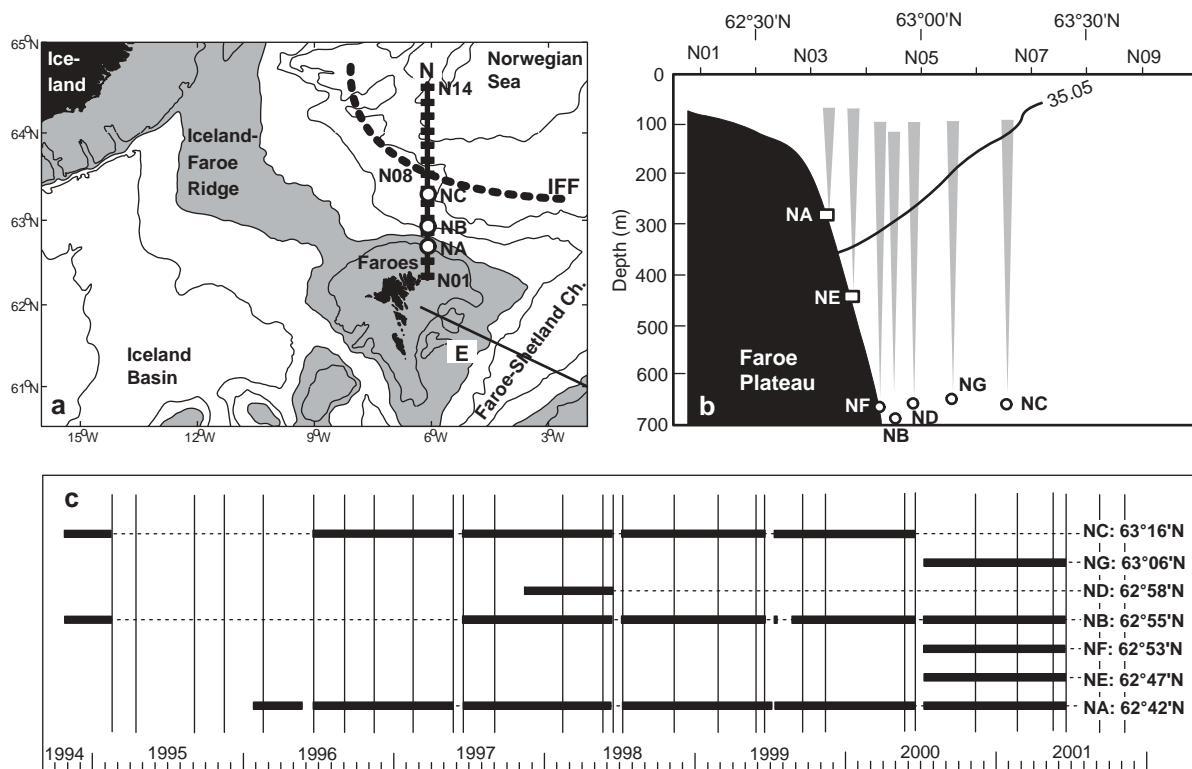


Figure 5 The main data set reported in this study is collected along section N, indicated on the map a) and illustrated in b). On a) CTD standard stations are indicated by black rectangles, labeled N01 to N14. Circles labeled NA, NB and NC indicate three of the ADCP mooring sites. Shaded areas are shallower than 500 m. The dotted curve indicates the general location of the Iceland-Faroe Front (IFF), (see Fig. 3). On b) the innermost CTD standard stations on section N are indicated as well as all the ADCP mooring sites. Gray cones indicate approximate ADCP ranges. An average 35.05 isohaline shows the typical boundary of Atlantic water on the section. In c) periods with successful ADCP observations at the various sites (thick horizontal bars) are shown together with CTD cruises along standard section N (thin vertical lines) from October 1994 to the summer of 2001.

3. MATERIAL

3.1 Observations in Section N

The standard section N, extending from 62°20'N 6°05'W to 64°30'N 6°05'W, crosses the Faroe Current where the bathymetry is steep and the current is relatively confined. Both hydrographic and current measurements were acquired along this section (Fig. 5).

3.1.1 CTD observations

The hydrographic data were acquired during a number of cruises along standard section N in the period 1987-2001. The standard section has 14 standard stations, labeled N01 to N14, with 10 nautical miles equidistant spacing between stations. Hydrographic transects since 1990 to present are used in this work. More thorough information on these data can be found in Hansen et al. [1999b].

3.1.2 ADCP observations

In the period October 1994 to June 2001, current measurements were obtained through a number of deployments at 7 different mooring sites, labeled NA, NB, ... NG, along the standard section (Fig. 5b). Up to summer 2000, the three Nordic WOCE standard mooring sites were at NA, NB and NC. Using these three moorings to analyze the average cross sectional current profile [Hátún, 2000], the Faroe Current was found to

be narrower and more confined to the shelf than previously assumed. From July 2000 to June 2001, the mooring at site NC was therefore moved to site NG and two additional moorings (NE and NF) were deployed between NA and NB (Figs. 5b and 5c).

All the deployments have used upward-looking RDI ADCPs to profile the water column (Fig. 5b) and they are moored at 600-700 m depths, or placed on the sea bed where it is shallower than this (NA and NE). These instruments provide the current velocity for each 25 m (NA has a bin length of 10 m) up through the water column and data are logged each 20th minute. (See Larsen et al. [1999] and Hansen et al. [2003] for more information).

3.1.3 Averaged flow character

The averaged flow in the Faroe Current is persistent and directed somewhat south of east (Fig. 6a). The current component perpendicular to the measurement section represents the main downstream character and most focus is henceforth given to this zonal component.

The time averaged cross-sectional structure of the Faroe Current has a core over the ~600 m isobath with the highest velocities (~25 cm/s) near the surface and no residual motion around 500 m depths (Fig. 6b). Residual currents increase in line with depth from 500 m and deeper, but the observations are unsuitable to describe this characteristic fully since the instruments are moored at around 600 m depths. The current

is generally baroclinic although there is a barotropic component near the shelf.

The deep boundary between the MNAW and the MEIW and the contact between the MNAW and the NNAW in shallower waters to the north, constitutes the Iceland-Faroe Front (Fig. 7). In the averaged picture it meets the shelf at 400-500 m and outcrops near by standard station N09, but Figs 4c and 4d show that large deviations from this average occur. The flow above the front is identified as the Faroe Current and its wedge-like shape, reflecting its baroclinic character, is apparent.

3.2 Model Description

The model system adopted in this study consists of the global Nansen Center version of MICOM [Bentsen et al., 2004; Furevik et al., 2002; Nilsen et al., 2003], and a regional version of the same model system covering the Atlantic Ocean between 30°N-78°N. The global version of the model used in this study has a horizontal resolution of about 40 km over most of the North Atlantic Ocean. The grid configuration of the regional model is identical to the global model but with doubled horizontal resolution, e.g. with about 20 km grid spacing in the region of the Iceland-Scotland Ridge.

In the vertical, both model versions have 26 layers of which the uppermost mixed layer has temporal and spatial varying density, and the 25 layers below have constant density. Daily mean NCAR/NCEP re-analyses [Kistler et al., 2001] fresh water, heat and momentum fluxes are used to force the system by applying the scheme of Bentsen and Drange [2000]. In the regional model, the mixed layer temperature and salinity fields are relaxed towards the monthly mean climatological values of Levitus et al. [1994] and Levitus and Boyer [1994], respectively, with a relaxation time-scale of 30 days for a 50 m deep mixed layer, decreasing linearly with mixed layer thickness exceeding 50 m. All integrations are performed by Annebritt Sandøe at NERSC (Nansen Environmental and Remote Sensing Center).

4. RESULTS

4.1 Current and Hydrographic Variability (Section N)

The current velocities near the core of the Faroe Current (see Fig. 6b) showed a consistent seasonal variation with an amplitude of about a fourth of the average velocity and with a maximum in March-April. The seasonality of the entire velocity field, however, only represented about one tenth of the total velocity variance (paper I). Inter-annual variations are seen, but these have not been given much attention because of the relatively short duration of the time-series discussed.

The spatio-temporal variability in the Faroe Current is complex and the so-called Empirical Orthogonal Function (EOF) analysis is used to describe this (paper I).

More than 40% of the total (eastward) current velocity variance can be described by the strength, or the pulsation, of the current core itself. This pattern (Fig. 8a) is clearly related to the transport and has thus been termed the *Transport mode* (paper I). A second clear and physical current velocity mode, (the *Fluctuation mode*), (Fig. 8b) which accounts for about one quarter of the total current variance, is related to move-

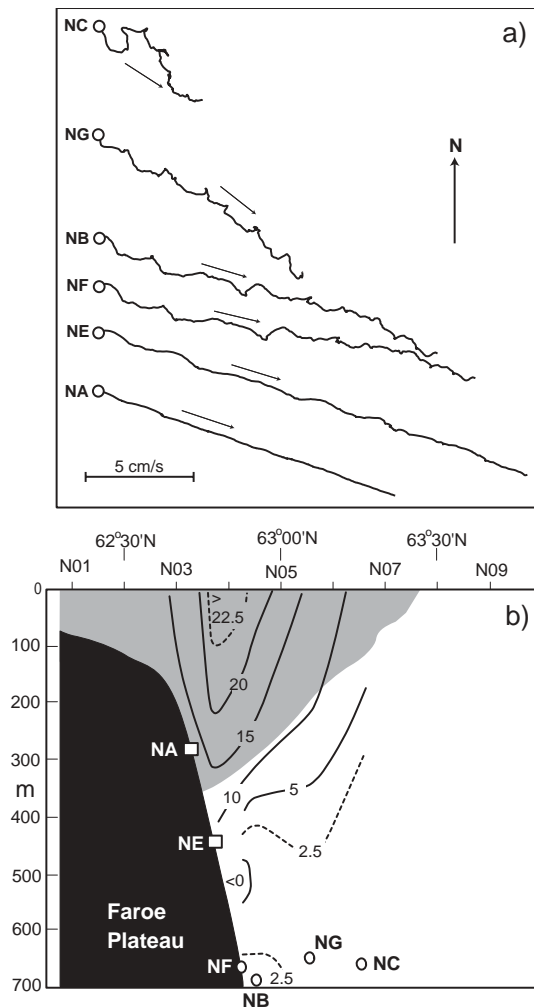


Figure 6 Averaged current field. In a) progressive vector diagrams for 343 days from daily averaged current at about 225 m depths for all sites. At NC, a deployment from summer 1999 to summer 2000 is shown. For the other sites, the deployment was from summer 2000 to summer 2001. As all the tracers have the same duration, they indicate residual flow velocity and the velocity scale is shown. In b) the distribution of eastward velocity (in $\text{cm} \times \text{s}^{-1}$) on section N based on extrapolated ADCP measurements at sites NA, NE, NF, NB and NG, using averages for the 2000-2001 period, and at site NC, using averages for the 1997-2000 period. The shaded area is on average more saline than 35.05, representing Atlantic water.

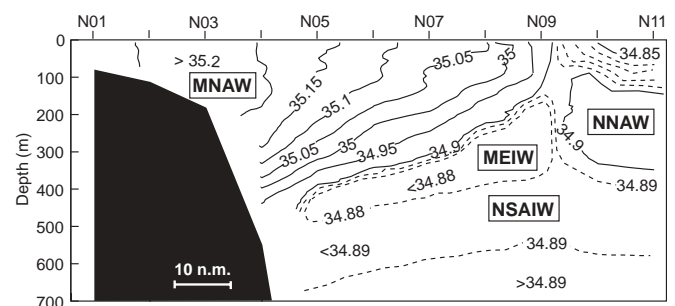


Figure 7 Average salinity distribution. Contouring interval for salinity is 0.05, except for salinities below 34.90, where broken lines indicate isohalines with contouring interval of 0.01. The main water masses are indicated.

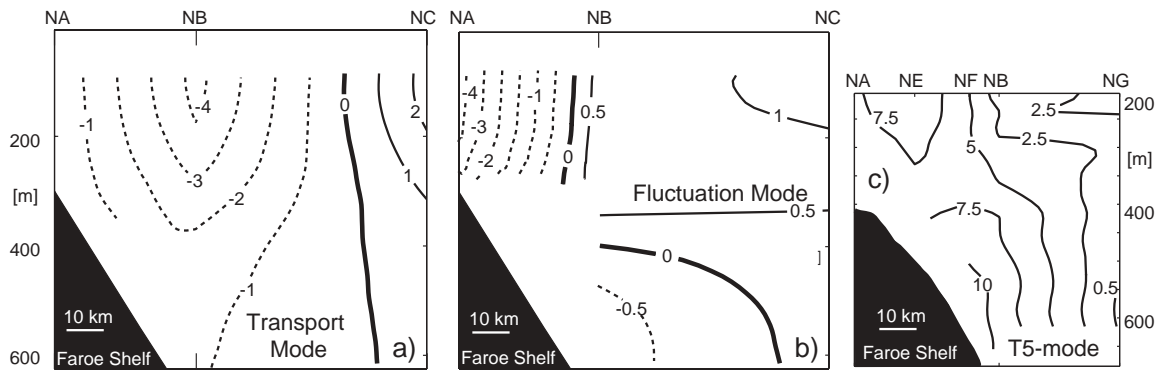


Figure 8 Modes (EOF-modes) of characteristic of current variability. The *Transport mode* (a), *Pycnocline mode* (b) and the *T5-mode*. Solid and dashed contours show positive and negative values, respectively. The modes in (a) and (b) are derived from the 1997-2000 data set (see the mooring sites along the upper axis) while the mode in (c) is derived from the 2000-2001 dataset (Fig. 5). Units are not physical.

ment of the pycnocline (front), as will be discussed in Section 4.2.1. These modes describe motions with periods between two weeks and two months, but periods of four to seven days are also noticeable. A third EOF-mode, called the *T5-mode*, segregates the motions responsible for these shorter periods (Paper IV). This mode (Fig. 8c) resembles the fluctuation mode somewhat, showing a dipole with most variation near the shelf, but is under the pycnocline and over the shelf break in 0-250 m depths.

The principal components associated with the *Transport mode* and the *Fluctuation mode* are related to the total volume transport variability and variability of the width of the Faroe Current, respectively. These have been regressed against the NCAR/NCEP sea surface air pressure and wind stress field (Appendix A) over the North Atlantic and the Nordic Seas. No correlation is found between the atmosphere and the volume transport, whereas a weak correlation is found between southward winds east and northeast of Iceland and the width of the Faroe Current, i.e. strong southerlies near Iceland might induce a broad Faroe Current.

The seasonal temperature amplitude is largest in the surface, but a secondary maximum is found along the permanent pycnocline from 450 m depths at the shelf and shoaling towards the north (see Fig. 7). The salinity seasonality is also clearest along the pycnocline, and both the temperature and the salinity culminate around August-October. This verifies that the front ascends during winter-spring and descends during summer-autumn, as shown in Figs. 4c and 4d.

It is found that 34% of the temperature variance is explained by the seasonal variations while 24% of the salinity variance is seasonal (paper I).

After removing the linear trend and the seasonality in the CTD fields and applying EOF-analysis, it is found that the leading temperature and salinity modes describe variability along the permanent pycnocline, and these modes acquire therefore the collective term, the *Pycnocline mode* (Fig. 9). This mode explains 49% and 36% of the non-seasonal residual temperature and salinity fields, respectively (paper I). Little can be said about shorter timescale hydrographic variability using CTD observations only, since these are just sampled 3-5 times each year. Such variations are, however, discussed using other approaches (see section 4.2.1).

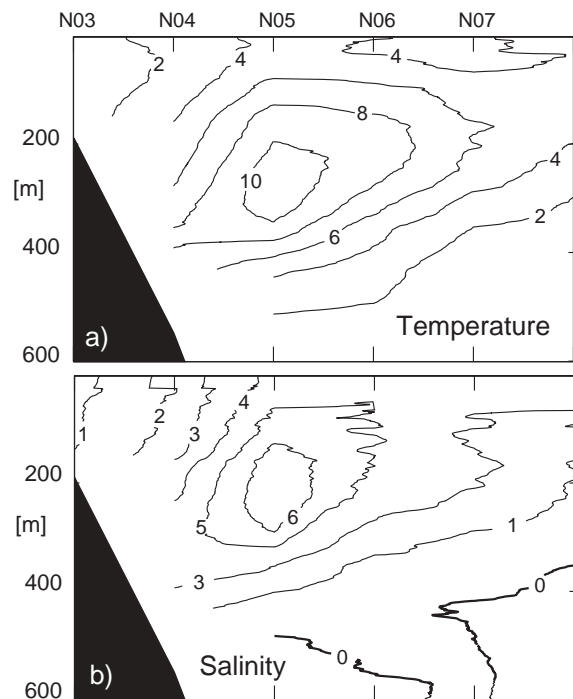


Figure 9 The *Pycnocline mode* for (a) temperature and (b) salinity. The standard CTD stations are showed along the upper axis. Units are not physical.

4.2 Transports

The total volume transport through section N is found by integrating the eastward current component over the section. This transport includes a contribution from all four water types present in the section (Fig. 7), whereof only the MNAW has recently crossed the Iceland-Faroe Ridge. The actual transport carried by the Faroe Current is the transport of MNAW and this will be called the Atlantic water transport. The only way to extract the Atlantic component from the total transport is with information on the *in situ* hydrography and the source water characteristics.

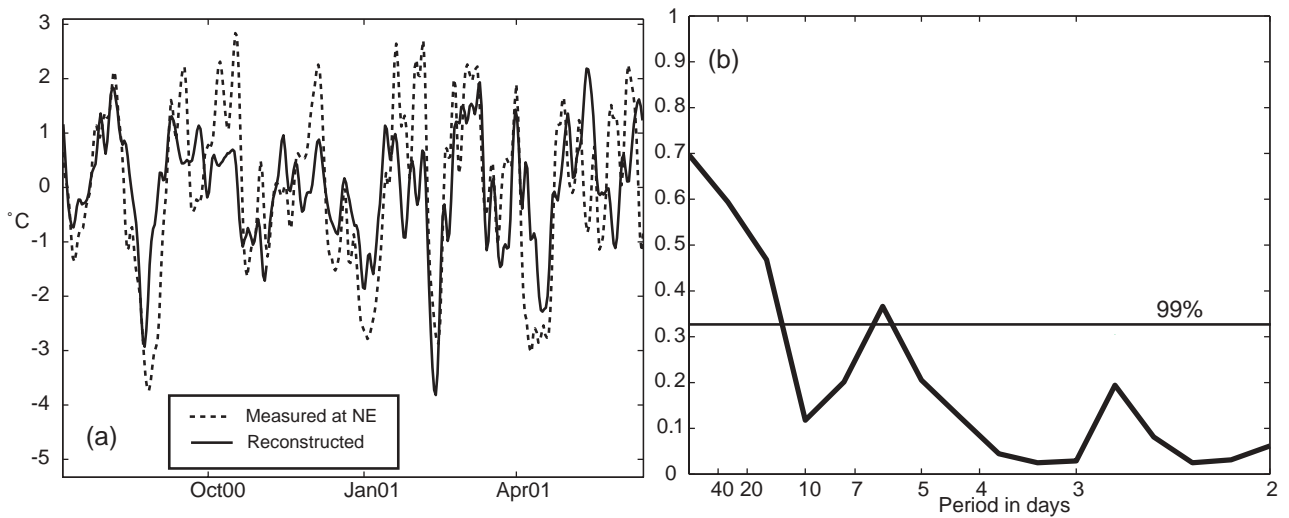


Figure 10 A comparison between the measured temperature at mooring site NE summer 2000 to summer 2001 and the reconstructed temperature at the approximate same location: (a) the three-day low-passed time-series and (b) the coherence squared between these and the significance line on a 99% level is shown.

A daily temperature/salinity (TS) field is thus needed in order to calculate the Atlantic transport with the same temporal resolution (daily) as the total volume transport. This information is not available in the CTD transects occupied three to five times a year, but the information from the current field itself has been used to partly circumvent this problem.

4.2.1 Temperature and salinity from the current field

The average TS-field, possible linear trends and the seasonal variations at each point in the section are obtained from the CTD observations. The additional shorter time-scale TS-variations are found from the ADCP current fields by inverting the classical dynamic method of determining current from temperature and salinity observations (paper I), [Hátún et al., 2003].

It is found that the temporal development (principal component) of the *Pycnocline mode* (Fig. 9) is closely related to the time variations of the current *Fluctuation mode* (Fig. 8b). These are linked through geostrophy. Temporal information from the *Fluctuation mode* and spatial information from the *Pycnocline mode* is then used to calculate non-seasonal residual fields of temperature and salinity with a daily resolution. By collecting the average fields, the linear trends, the seasonal variations and the shorter time variations, reconstructed fields are ob-

tained, which account for 60% (T) and 44% (S) of the total variance in the measured fields.

A continuous (daily) temperature series is acquired from one of the ADCP instruments near the foot of the pycnocline (deployment NE on the bottom at 490 m depth) (see Fig. 6b), and an independent check between this observed bottom temperature and the reconstructed temperature near this position is performed, showing a close relation (Fig. 10). Much of the explained hydrographic variability is clearly related to vertical motion on the pycnocline with periods between two weeks and two months and a weaker signal with periods between five and seven days (Fig. 10b).

4.2.2 Atlantic water transport

Only NSAIW and MEIW will get into contact with the Atlantic source water, and therefore the *in situ* water characteristics in the Faroe Current arises through a mixing between these water masses. The NSAIW has fairly well defined characteristics ($T = 0.5$ °C, $S = 34.9$), but the other two source water characteristics are somewhat more uncertain (see Table 1). With daily information on the *in situ* hydrography (from the above), assuming realistic characteristics for the source waters MNAW and MEIW and by using a simple 3-point mixing model [Hermann, 1967], the fraction β_{yz} of Atlantic water at any sec-

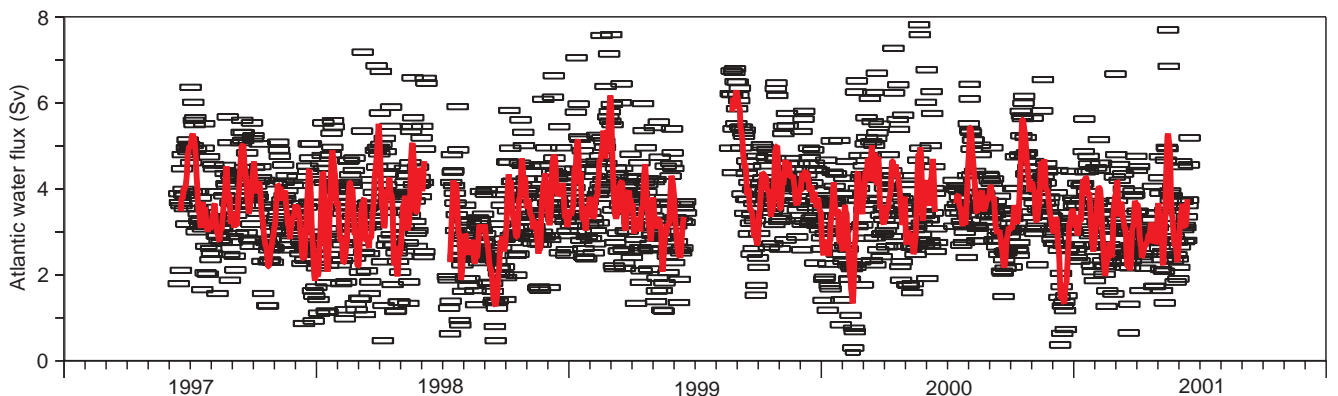


Figure 11 Volume flux of Atlantic water through section N from June 1997 to June 2001. Rectangles indicate daily values. Continuous lines indicate 7-day running average values.

tional point (y, z) is estimated. Including this fraction when integrating the eastward current over the section gives an average Atlantic water transport of 3.5 ± 0.5 Sv. The estimated error-sources are discussed in paper II, [Hansen et al., 2003].

The total transport shows a consistent seasonal variation with a maximum in March-April, but the Atlantic water transport does not show any clear seasonal variation (Fig.11). The sectional fraction (area) of Atlantic water is smallest during March-April when currents are strongest and these opposite phases appear to neutralize each other to a large extent. The interannual Atlantic transport variation is less than 16% during the four years discussed, and any conclusion on a long-term trend would be premature for such a short series.

The most energetic transport variability is found at periods of 15 days or longer, but a peak in the spectrum appears for periods around a week (paper II).

A noteworthy feature is that none of the 1348 daily transport estimates are negative, implying a westward flow towards the Atlantic. The Iceland-Faroe Atlantic inflow is, thus, a highly stable flow (Fig. 11).

4.2.3 Calculating transports from sea-level measurements

Comprehensive direct current measurements give accurate estimates of volume transports, but such observations are expensive to maintain. Directly observed transport time series are still short in a climatic context, and alternative, less expensive, methods with the possibility for longer time series would therefore be helpful.

The integrated surface current profile in the Faroe Current will give a sea-level rise across the current due to geostrophy, with a slightly more elevated water level relative to the geoid on the right hand side when looking downstream.

If a linear relation exists between the transport and the integrated surface currents, then it should be possible to estimate these fluxes simply by measuring the sea-level difference across the current. This was the objective of the MAIA (Monitoring the Atlantic inflow towards the Arctic) project [the MAIA team, 2003] and the work in paper III was a pilot study in the Faroe Current associated to this project [Hátún and McClimans, 2003].

The potential for using surface slopes as a proxy for transports in the Faroe Current was examined using coastal sea-level observations from the Faroes, altimetry satellite data (Appendix A) from the Norwegian Sea north of the Faroe Current and transport estimates from the direct current measurements. Coastal sea-level time series are inexpensive and extensive, and altimetry data are freely available and extend back to 1992. The sea-level difference across the Faroe Current, found as the coastal sea-level adjusted for atmospheric pressure minus the adjusted altimetry, was compared to the Atlantic water- and the total transport. The correlations are significant (Fig. 12), and based on these correlations, linear algorithms are suggested between the surface slope and the flows. These correlations are, however, probably too small ($r = 0.56$) to justify the use of sea-level in transport calculations. Baroclinic and barotropic current components will give different contributions to sea-level elevations, and to overcome this difficulty the MAIA paradigm assumed a constant ratio between these components in the Norwegian Atlantic Current (NwAC)[McClimans et al., 1999]. In addition to this, it was assumed that the deep water is at rest. The Faroe Current is

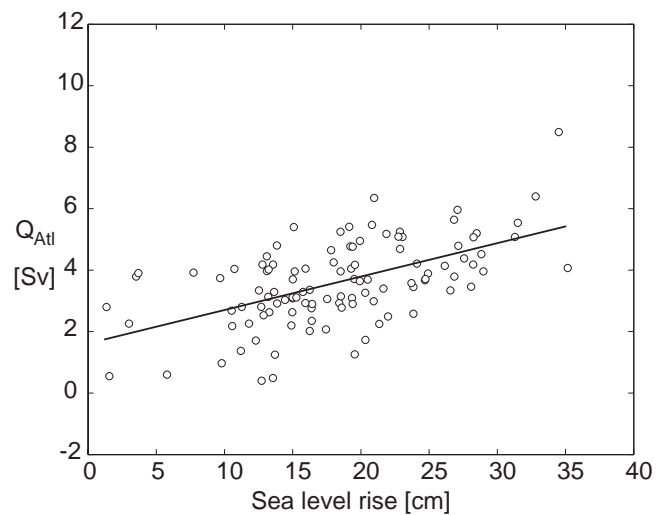


Figure 12 Correlation between the sea level rise across the Faroe Current and the daily Atlantic inflow transport. Linear regression lines are fitted to data measured from June 1997 to June 2000.

mainly baroclinic, but the baroclinicity is variable because of the highly variable interface (pycnocline) between the Atlantic water and the Arctic water masses. Furthermore, the motion in the sub-interface water masses is indeed non-zero (Section 4.3). Neither of the two assumptions made in the NwAC are thus valid in the Faroe Current, and this might partly explain the unsatisfactory correlations.

Attempts have been made to overcome this problem by deploying inverted echo sounders (IES) and bottom pressure sensors [the MAIA team, 2003]. This might mitigate the problem, but if such additional measurements are required for obtaining reasonably accurate transports with this method, then the economical advantages and the advantages by obtaining longer transport series, compared to the direct current measurements, will be lost.

4.2.4 Model (MICOM)

a) Global version

Simulated transports (volume, heat and salt) through all the passages in the Arctic Mediterranean, using the global model version, have been compared to the literature with generally consistent results [Hátún, 2004]. The simulated transports are calculated by summing the transport in all 26 layers, respectively, giving a total in-, out- and net transport through each passage. The denser Arctic water masses flowing equator-wards in deeper layers (*overflow*) are found in the lower isopycnal model layers, while the pole-ward flowing Atlantic water masses are found in the upper isopycnal layers. Summing all layers to find transports means that a temporary equator-ward flow in the upper layers will count as *overflow* and vice versa. It is therefore somewhat unclear how these values should be compared to the observations. The simulated net inflow over the Iceland-Faroe Ridge found as an average over the period 1996-2001 is 2.0 Sv. This value should be compared to the transport of Atlantic water (3.5 Sv) minus the overflow over the Iceland-Faroe Ridge, which is not well documented. An overflow of 1.0 Sv seems a reasonable estimate [Hansen and Østerhus, 2000], and this gives an observed average value of 2.5 Sv.

a) Regional version (unpublished results)

The data from the regional model were provided layer-wise by NERSC, and a more physical comparison can therefore be conducted. The upper 15 layers in the model represent the relatively light Atlantic water, and a sum of the transport over the Iceland-Faroe Ridge in these 15 layers should thus represent the Atlantic inflow. The simulated average transport over the period 1996-2001 gave 2.2 Sv, and this should be compared to the observed 3.5 Sv.

A direct section-to-section comparison is not meaningful using the global model version since the resolution is too coarse (40 km), but this becomes feasible with the regional model version, which has a grid-size that is comparable to the distance between standard CTD stations (~20 km) along section N. The simulated and observed current fields along section N are compared showing too weak modeled current velocities (simulated current core velocities of 14 cm/s compared to the observed 25 cm/s), and this is reflected in a too weak simulated total transport. But the simulated total transport anomalies (variations) show the same seasonal amplitude and phase as the observations, and these pick up some of the observed shorter time-scale variability as well (Fig. 13).

4.3 Shorter Time-Scale Variations (Section N)

The *Transport mode* and the *Fluctuation mode* of current variations in the Faroe Current have most energy for periods longer than 15 days, but a distinctive spectral peak was found around five to seven days.

Periods between five and seven days are thus seen on the interface (paper I), (Fig. 10) and the Atlantic transport (paper II) did also reveal a peak around a week. Only daily data were used in these former studies, so in order to elucidate the relatively rapid motions better, hourly current series are analyzed (paper IV). Wavelet analysis [Torrence and Compo, 1998] reveals that these motions are of intermittent nature, and applying EOF-analysis to a 100 days period when these fluctuations were energetic, revealed a mode (Fig. 14a) similar to the *Transport mode*. Therefore this new mode is probably also related to the transport variability in the Faroe Current. A clear period around five days was seen in the appurtenant principal component (Fig. 14b), and these fluctuations were in phase with current oscillations below the Atlantic layer. The signal is very distinct in the deeper layers north of the Faroe Current where it consists of zonal current oscillations across the weak east-west topography of the Iceland-Faroe Ridge. Coherence analysis between the moorings along section N reveals that the oscillations propagate southwards with a velocity of 0.2 m/s, and if they are interpreted as waves, the wavelength will be around 80 km. The topographical gradient, the period and the wavelength fulfill the dispersion relation for barotropic Topographic Rossby (T-R) waves. The group velocity, and thereby the energy of T-R waves with wavelengths on this order of magnitude, travel with shallower topography on their right. It is therefore hypothesized that the five to seven day's variability in the Faroe Current is due to southward propagating T-R waves guided by the Jan Mayen Ridge and the Iceland-Faroe Ridge and finally impinging onto the Faroe Shelf.

The influence of the waves on the interface and currents in the Faroe Current has been studied using a simple two-layer

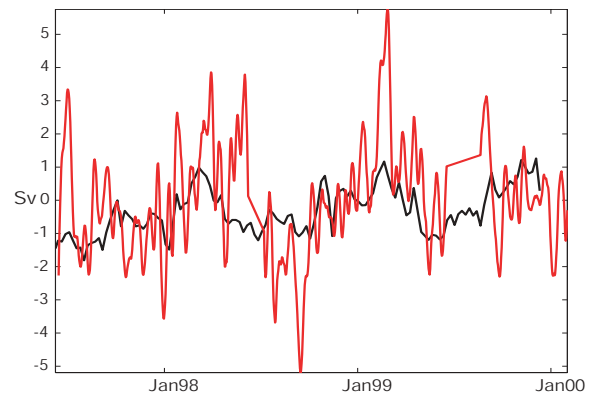


Figure 13 Simulated (black) and observed (red) total volume transport anomalies through section N between 62° 42' N and 63° 16' N and from surface to 600 m depth. The simulated values are logged once a week and the observations are low-passed with a one-week long running average filter.

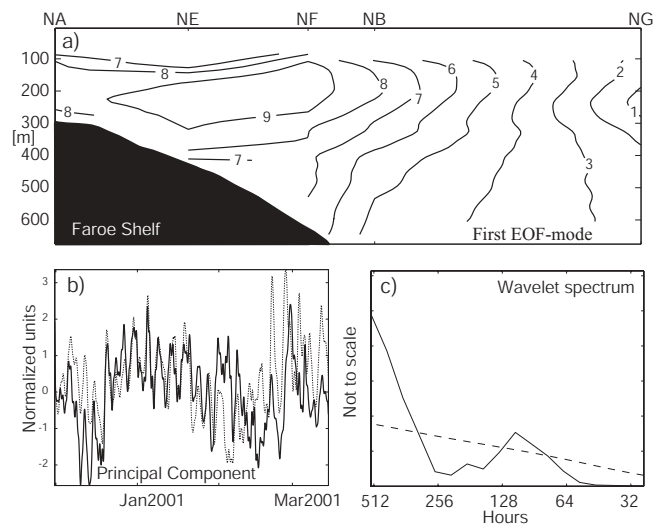


Figure 14 Fluctuations in the Faroe Current from December 2000 to March 2001. (a) The pattern (EOF-mode) representing most of the variance (35% of total), (b) the temporal development of this pattern (principal component) and (c) a spectrum showing the dominating periods present. Tides have been removed prior to the analysis.

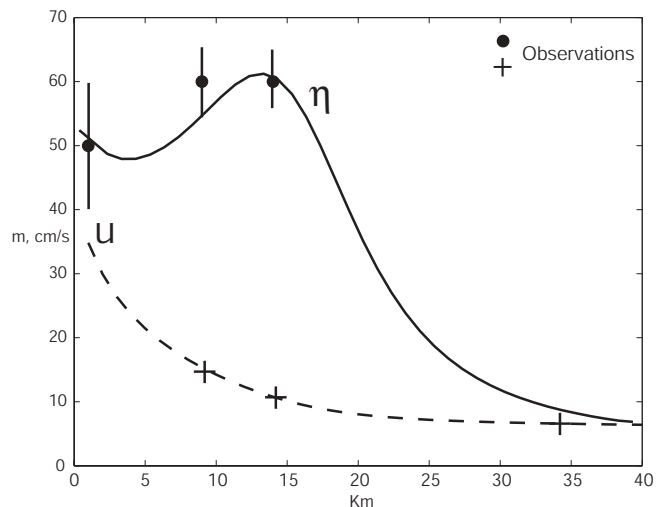


Figure 15 Observed and modeled along-isobath current velocities (u) in the lower layer (broken line) and amplitude of interface deflection (η) (full line) due to incoming waves. These are plotted against the northward distance from mooring NE.

model. Despite its simplicity, the model seems to explain the observed lower-layer current amplitudes, the interface deflections (Fig. 15) and the phase relations between these. The larger broadband variability in the upper layer makes it somewhat more difficult to validate the modeled dynamics here, but the model predicts large velocities in the Atlantic layer. The observed eastward current pulses, which in the upper layer propagate towards the shelf, are described qualitatively correct in the model.

The presence of the waves and the short-term variability is clearly seasonal, with most energy during the period January - March and least energy in the period August - November. The flow pattern in the Faroe Current completely changes character after December-January from the dominance of slow and regular variations with periods around one to two months to the dominance of more rapid and vigorous zonal and meridional motions. It is hypothesized that this meso-scale variability might influence the bifurcation of the Faroe Current.

4.4 Bifurcation of the Faroe Current

4.4.1 Unpublished results on the bifurcation

The Faroe Current bifurcates somewhere around the north-eastern corner of the Faroe Plateau with one branch continuing directly towards the northeast and the other branch flowing into the Faroe Shetland Channel as the Southern Faroe Current (Fig. 16). Assessment of the dynamics of this bifurcation is difficult since no regular *in situ* data exist from this region. Occasional surveys of this area indicate that the flows are complicated and non-stationary [Hansen and Østerhus, 2000], [pers. comm. with K. A. Orvik]. In spite of this, some preliminary and unpublished results will be presented.

The surface flow pattern has qualitatively been studied using drifters (Appendices A and C1). One out of four drifters initially flowing near the core of the Faroe Current when crossing section N followed the southerly route into the Faroe Shetland Channel. All drifters in the Faroe Shetland Channel did eventually turn eastward again, and 67% of these ended up in the NwASC (see Fig. 2). Some drifters did also flow directly to the NwASC branch without making a U-turn in the Faroe Shetland Channel, and a total of 32% of the drifters, once situated near the core of the Faroe Current, did ultimately end in the NwASC branch. An expected intermittent flow pattern is seen near the northeastern corner of the Faroe Plateau with just a statistical chance for the flows to either continue east or to turn south. An interesting observation is that the drifters in the Southern Faroe Current will typically lose track of the Faroe Plateau at the protrusion of the 500 m isobath near ADCP mooring EB (Fig. 16).

These drifters are in the wind driven Ekman layer (drogued at 15 m depth) and might therefore deviate significantly from the deeper currents. Another deficiency with this qualitative drifter analysis is that the temperature series associated with the drifters were not available. It is therefore not possible to affirm whether or not a drifter was embodied in Atlantic water when passing section N.

A persistent connection is found between direct current observations over the 300-800 m depth contours north of the Faroes (moorings NA and NB) and observations at 780 m depths on the southeastern edge of the Faroe Plateau (moor-

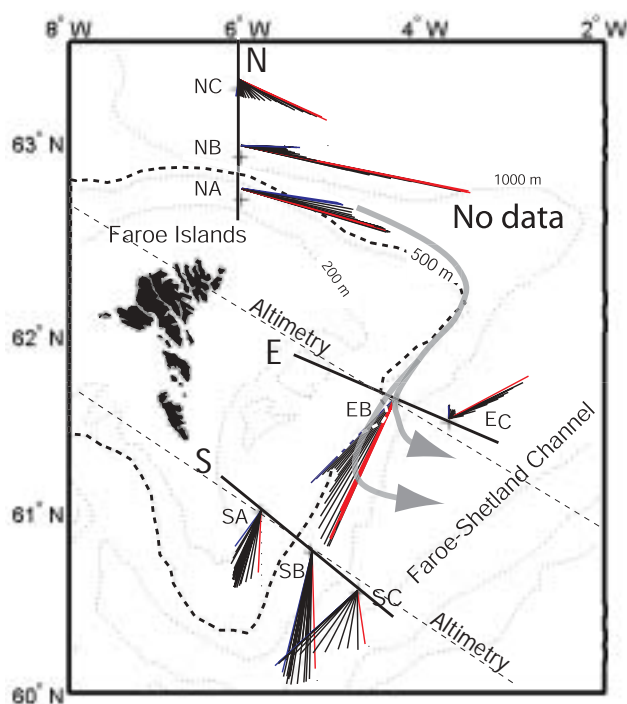


Figure 16 The Southern Faroe Current. Standard CTD sections N, E and S are shown and the average current observed by ADCP instruments moored along these sections from summer 1999 to summer 2000 are indicated by the sticks. Each stick represents the average current velocity and direction for a 25 m depth interval. The red sticks are nearest to the surface. Two altimetry tracks nearly coinciding with sections E and S are shown with broken curves. The 500 m depth contour is emphasized.

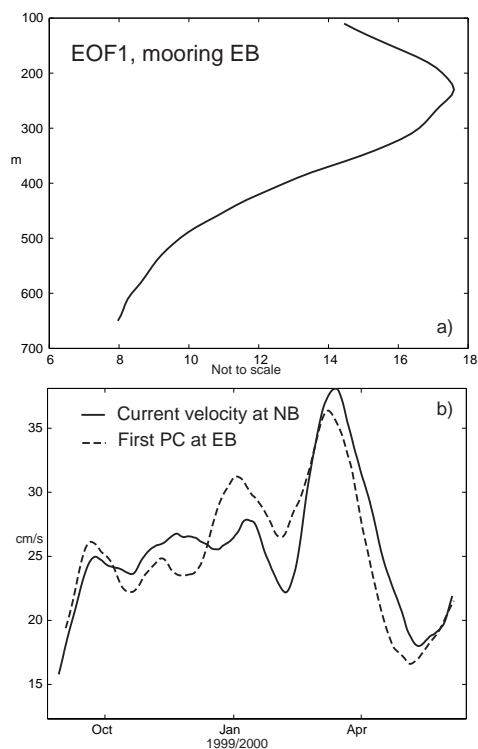


Figure 17 Connection between mooring NB (section N) and mooring EB (section E), (see Fig. 16). (a) The first EOF-mode at mooring EB, explaining 70% of the total downstream current variance throughout the water column. (b) The principal component (PC) associated to the mode in (a) and the eastward current velocity at NB (200 m). A 25-day running average filter has been applied to the series.

ing EB, appendices A and C2), (Fig. 16). Individual near-core current velocity series from section N and the volume transports through this section were significantly correlated to the downstream current velocity at mooring EB and to the principal component associated to the dominant mode of the downstream current variability (Fig. 17). This connection is clearest during the winter-spring period. No correlation is found between the currents at EB and the current further south on the same depth contour (mooring SB). The current over shallower water along section S (mooring SA) is, however, weakly related to the observations further north. This latter could be related to the circulating coastal current on the plateau.

The results above indicate that a portion of the Faroe Current steadily flows through section E as the Southern Faroe Current, and that much of this latter branch is probably admixed with the pole-ward flowing Shetland Current before reaching section S. While comprehensive current data are available along section S [Turrell et al., 2003], only the yearlong series from mooring EB is available along section E.

Samuel et al. [1994] tried to combine GEOSAT altimeter observations of sea surface height with a numerical model in order to calculate transports through the Faroe Shetland Channel. The TOPEX/Poseidon satellites give more accurate data than the GEOSAT, and one of the repeated tracks coincides with section E (Fig. 16). This section is perpendicular to the Southern Faroe Current and is thus ideal for studying the transports carried in this branch. Following Han and Tang [2001], seasonal variations in currents and transports are calculated from altimeter and density using the sea surface as the level of known motion (Appendix C3). Figure 18 shows that there is a clear seasonal variation in the baroclinic velocity field through standard section E and in the sea surface slope across the Southern Faroe Current at this location. The seasonal variations in the sea surface slope became much more apparent after 1996 (Fig. 19), and the seasonal transport amplitude for the period 1996-2002 is found to be ~ 0.6 Sv with a maximum in February-April and minimum in August-October. This estimate is in general agreement with the observed current at mooring EB from July 1999 to June 2000 (Appendix C3 and Fig. 17). The seasonal transport amplitude through section S has previously been estimated to 0.2 Sv [Turrell et al., 2003], and this smaller seasonal amplitude supports the suggestion that much of the Southern Faroe Current joins the Shetland Current between section E and section S.

4.4.2 Discussion of the bifurcation of the Faroe Current

Many works reporting wind driving and seasonality in the Atlantic inflow are based on observations from the Svinøy section (Fig. 2) [Blindheim, 1993; Mork and Blindheim, 2000; Orvik et al., 2001]. The observations from the Svinøy section show that in summer there exist two cores of water with salinity above 32.25 at about 100 m depth, but in the spring and the winter the core furthest offshore (NwAC) is less distinct. The mean summer volume transports were 3.7 Sv for the NwAC, and the minimum in spring showed a mean of 2.5 Sv, giving a seasonal amplitude of 0.6 Sv in this outer branch [Mork and Blindheim, 2000] based on the classical dynamical method.

There is an opposite phase between the geostrophic volume transports in the NwASC and in the NwAC, and the leading hydrographic EOF-mode clearly reveals this dual structure along the Svinøy section with opposite signs in the outer and

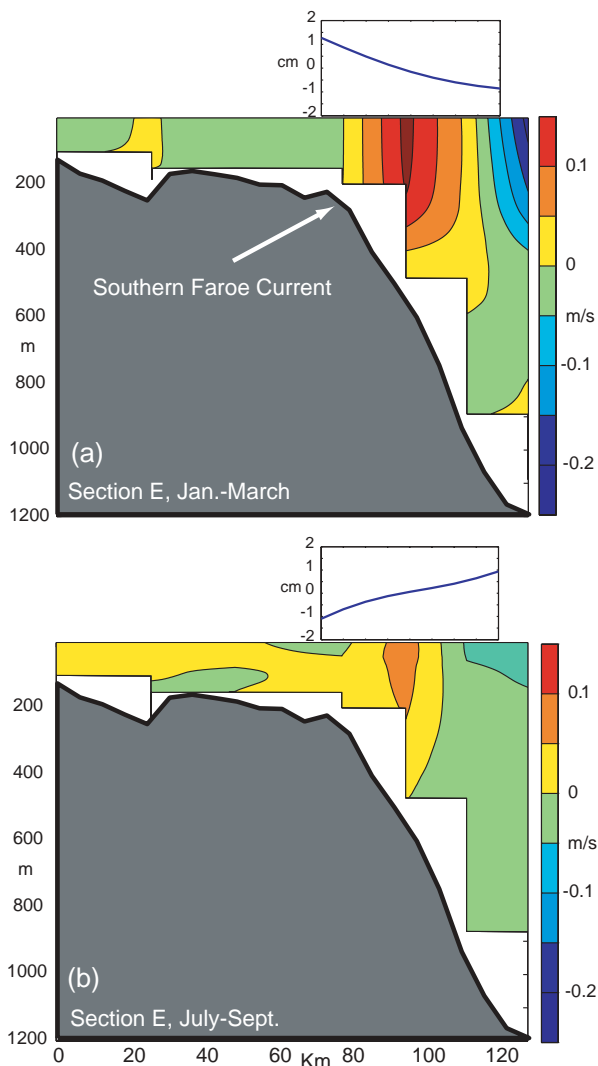


Figure 18 Seasonal variations in the baroclinic velocity field and in the sea surface slope along standard section E. The January-March velocity field (a) is an average of eight CTD transects from the nineties and the July-September field (b) and average of nine such transects. The sea surface slopes are averages of 87 individual altimeter tracks.

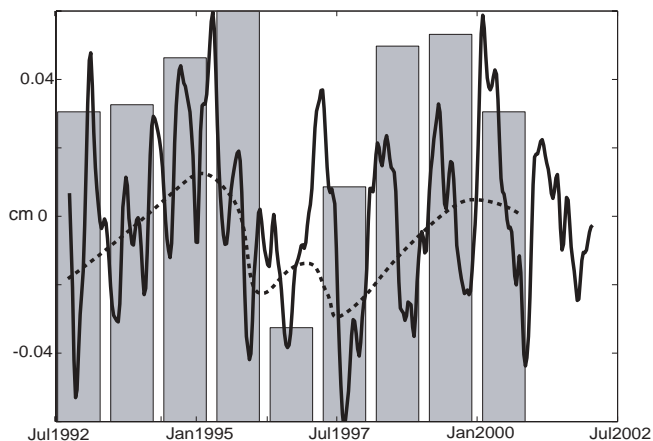


Figure 19 Sea surface height difference (anomalies) across the Southern Faroe Current in the Faroe-Shetland Channel as measured by an altimetry track near section E. The broken curve indicates the interannual sea level difference and the bars show the annual mean rotation of the wind stress (not to scale) over the Nordic Seas (65-80°N, 20°W-20°E), derived from the NCEP/NCAR re-analysis data set [Jakobsen et al., 2002].

in the inner branch [Mork and Blindheim, 2000].

Contrary to the NwAC, the NwASC has been thoroughly monitored by current meters since April 1995 [Orvik et al., 2001]. A winter maximum is reported for the inflow during the period 1996-1999, but no systematic seasonal signal was found from April 1995 to August 1996 [Orvik and Mork, 1996], [Orvik et al., 2001]. A strong connection is found between the NAO index and the NwASC for the period from April 1996 to February 1999. Based on this, they conclude that the Atlantic inflow is related to the westerlies in the North Atlantic through a large northward Sverdrup transport. A striking feature appears to be that a high-inflow event coincides with a high NAO-index typically from January to March-April [Orvik et al., 2001], and these series are not so clearly linked to a regular sinusoidal seasonal variation.

To summarize, we have nearly non-seasonal inflows in the Shetland Current [Turrell et al., 2003] and in the Faroe Current [Hansen et al., 2003], but the Southern Faroe Current has a very clear seasonal signal after 1995 (Fig. 19), with a maximum in February-April and an amplitude of ~ 0.6 Sv. A one-year long current series (summer 1999 to summer 2000) in this branch of the Faroe Current verifies this seasonality with a strong current peak (25-30 cm/s) during March. This current velocity is on the same order of magnitude as the core-current north of the Faroes, indicating that a large fraction of the Faroe Current may turn into the Faroe Shetland Channel during spring. This connection was also verified by current observations from north and east of the Faroes (section 4.4.1).

The southwestward flowing Southern Faroe Current seems to follow both the decadal scale and the seasonal variations of the wind stress curl over the Nordic Seas, which again is closely related to the NAO. Both series show a characteristic 5-year cycle, a maximum in February-April and a clear regime change in 1995-1996 (Fig. 19).

The anti-phase between the NwAC and NwASC, the weaker NwAC during spring, the seasonal transport amplitude of ~ 0.6 Sv in this branch, the commencing of a seasonal transport signal in the NwASC after 1995, the pulses of inflow from January to March-April through the NwASC [Orvik et al., 2001] and the flow characteristics around the Faroes all support the same conclusion. A part of the seasonality and the NAO-linked transport variability observed along the Svinøy section most probably derives from seasonality and NAO-dependence in the bifurcation of the Faroe Current.

The simulated (MICOM) temperatures at 250 m depth horizontally integrated along the Svinøy section and along the Faroe Shetland Channel section are regressed against the NCEP/NCEP sea surface air pressure field over the North Atlantic and the Nordic Seas (unpublished). A NAO-like pressure pattern is strongly linked to the temperature at the Svinøy section, while the temperature in the Faroe Shetland Channel is un-correlated with the sea surface pressure (Fig. 20). This indicates that temperature anomalies observed along the Svinøy section in the Norwegian Sea are not necessarily transported northward from the Atlantic Ocean over the Greenland-Scotland Ridge, but could merely be caused by a narrowing of the Norwegian Atlantic Current [Blindheim et al., 2000]. Studying drifters, Jakobsen et al., [2002] show that the internal basin scale cyclonic gyres in the Nordic Seas are modulated by the large-scale rotation of the wind, but that this is not found to affect exchanges between the North Atlantic and the Nordic

Seas. The rotation of the wind stress over the Nordic Seas exhibits a very pronounced seasonal cycle with most energy from December to March and very little energy from May to August, but this seasonality is not reflected in the drifters over Greenland-Scotland Ridge.

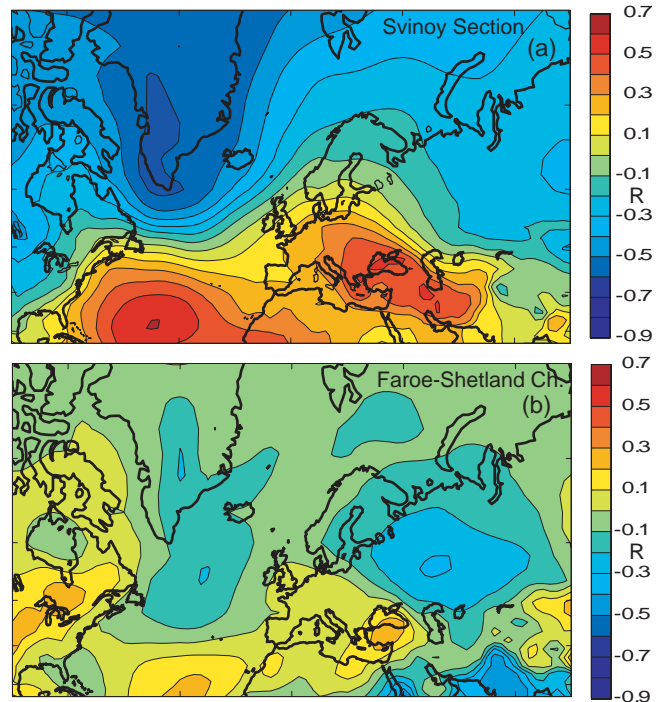


Figure 20 Regression maps between sea surface pressure, derived from the NCEP/NCAR re-analysis data set, and modeled temperature at (a) the Svinøy section and (b) the Faroe-Shetland Channel. The modeled series are calculated as horizontal averages along the standard sections at 250 m depths. The color code represents the correlation coefficient between the simulated temperature series and sea surface pressure series at all presented locations.

4.5 Observed and Simulated Hydrography

The regional version of the Micom model has a grid resolution comparable to typical distances between standard hydrography stations, and section-to-section comparisons are therefore possible.

Special attention is paid to the Atlantic inflow, but there is no standard way of comparing simulated and observed data sections. A discussion of this issue regarding the Faroe Current is presented in Appendix B. Simulated and observed time series of: a) sectional temperature/salinity (TS) maxima and b) spatial averages over a selected window typically representing Atlantic water have been compared.

The best method is found to be b) since this method includes a large fraction of the Atlantic inflow while both air-sea interactions, mixing and advective influences are included. The observed temperature and salinity changes in the Faroe Current during the period 1991-2002 are realistically simulated (Figs. 21c and 21d), (unpublished), but this period is relatively short in a climatic context.

The simulated decadal scale temperature variations in the Continental Shelf Current, Shetland Current and in the NwASC closely resemble observations. This is verified by a compari-

son between the model and a 26-year-long temperature series from the Rockall Trough, a more than 53-year-long series from the Faroe-Shetland Channel (Fig. 22) and a 26-year-long series from the Svinøy section (paper V), [Hátún et al., 2004]. A unique daily time series representing the temperature on the Faroe Plateau (Mykines) from 1914 to 1969 is used to validate the model. It is found that long-term temperature variations, the seasonal cycle, and amplitude and phase changes in the seasonal cycle are correctly simulated. One main complication associated with the use of temporally scarce hydrographical records is the problem of aliasing due to changes in the sea-

sonal cycle and due to other shorter time variability. Assuming that the simulated seasonality in the Atlantic inflow is correct, as is supported by the Mykines series, the potential for using simulations to complement the observed time series in periods with sparse sampling is examined. Advice is given to treat the observation-based cold anomaly in the late 1960s with caution and to survey the hydrographical section in the Faroe Shetland Channel four times a year or more if decadal scale temperature variations are of interest. The regional, finer resolution model is superior to its global equivalent when it comes to predicting the hydrography on the Iceland-Faroe Ridge.

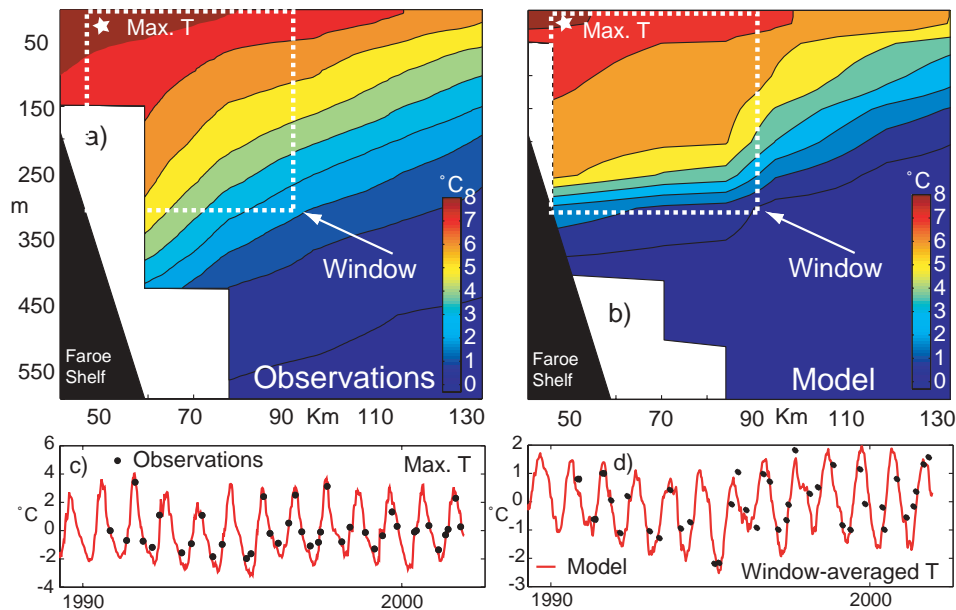


Figure 21 A model-data comparison along standard section N. (a) Averaged observed temperature, (b) averaged simulated temperature, (c) time series of maximum temperature and (d) time series of window-averaged temperature. Approximate positions of the windows are drawn in (a) and (b) and the typical location of the maximum temperature is shown with a star.

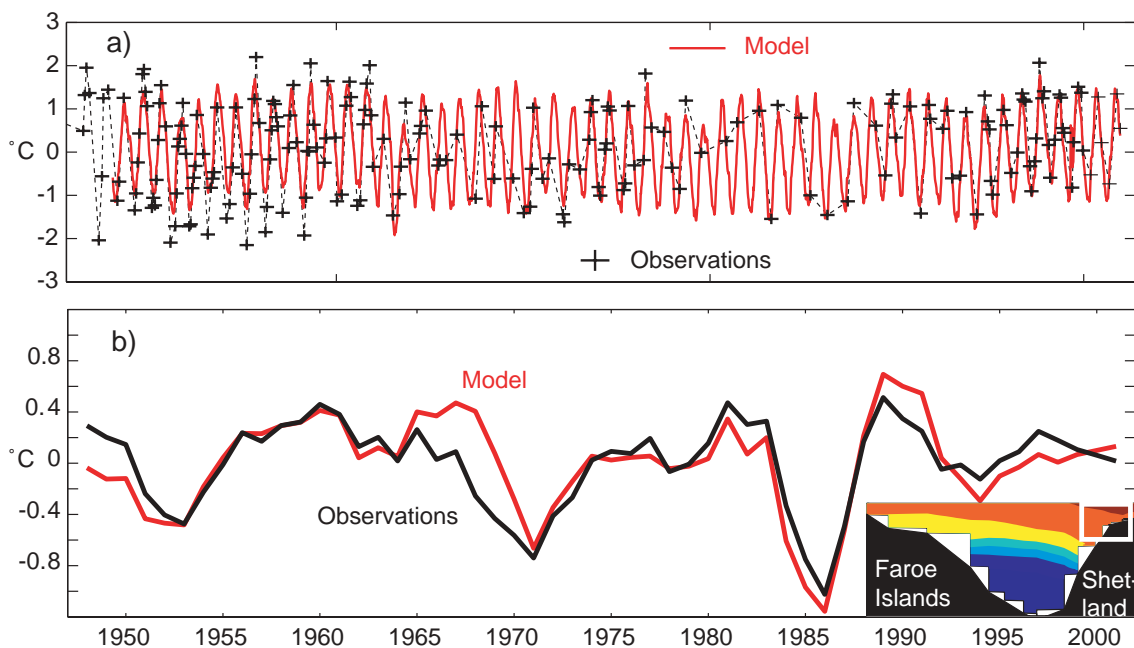


Figure 22 Temperature anomalies in the Faroe-Shetland Channel. Observed and simulated time series from section S and within the white rectangle in the inset are presented. a) The observations (plusses) and the weekly resolved simulated time series. b) Three-year running averages.

5. CONCLUDING REMARKS

5.1 Summary

1. Two main modes of the eastward (downstream) variability are identified: a) The *Transport mode* explaining about 40% of the total current variance and b) the *Fluctuation mode* explaining about 25% of the total current variance. The former mode is related to the total volume transport in the Faroe Current, and the latter mode is related to lateral (north-south) movement of the current (Paper I and Section 4.1).

2. The seasonal cycle explains 34% of the temperature variance and 24% of the salinity variance in the Faroe Current. Much of the seasonality is related to the position of the main pycnocline, which is the sub-surface signature of the Iceland-Faroe Current (Paper I and Section 4.1).

3. The main hydrographical EOF-mode, called the *Pycnocline mode*, explains 49% and 24% of the non-seasonal temperature and salinity variance, respectively. This mode is related to vertical movement of the main pycnocline (Paper I and Section 4.1).

4. A good correlation is found between the temporal variability of the hydrographic *Pycnocline mode* and the current *Fluctuation mode*. This relation is used to construct temperature and salinity fields from the current field. The obtained temperature and salinity fields have a daily temporal resolution, as opposed to the 3-5 observed fields per year, and they account for 60% (T) and 44% (S) of the total variance in the measured fields (paper I and Section 4.2.1).

5. This daily hydrographic information is used together with the current data to calculate a volume transport of Atlantic water of 3.5 ± 0.5 Sv in the Faroe Current (paper II and Section 4.2.2).

6. The current velocities in Faroe Current are strongest in spring (March-April) (paper II and Section 4.1), but the seasonality in the Atlantic water transport is weak since the spatial extent of Atlantic water and current velocities are in opposite phase. The flow is very persistent showing no reversals, with volume transports towards the west (paper II and Section 4.2.2).

7. We have not been able to find any significant correlations between volume transport and winds, wind stresses, or the sea surface air pressure. The width may be related to north-south winds east of Iceland (Section 4.1).

8. The prospect of estimating fluxes from sea level data has been tested, using coastal sea level data from the Faroes, altimeter data from the Norwegian Sea and transport estimates from the current profilers. The geostrophic signal is clear, but the correlations are too weak ($r \sim 0.56$) for using sea level gradient as a proxy for fluxes in the Faroe Current (Paper III and Section 4.2.3).

9. Volume transport estimates from the MICOM ocean model have been compared to the current observations. The seasonal and some of the shorter time-scale variability are realistically simulated, although the absolute simulated values are somewhat too low (Section 4.2.4).

10. The clear and regular 5-7 days variability in the current velocities, and in the deflection of the main pycnocline across the Faroe Current are identified as southward propa-

gating Topographic Rossby waves, impinging on the Faroe slope (paper IV and Section 4.3).

11. A simple two-layer analytical model of the wave-incidence onto the slope explains the observed near-shelf current intensification and the amplitudes of the pycnocline deflection. The southward propagation velocity of the interfacial waves, and the phase relation between the interface movements and the current velocities are realistically simulated (paper IV and Section 4.3).

12. A significant correlation is found between current observations to the north and to the south-east of the Faroe Shelf. This indicates a persistent branching of the Faroe Current at the northeastern corner of the Faroe Plateau, with one branch (the Southern Faroe Current) flowing into the Faroe-Shetland Channel (Section 4.4).

13. The seasonality in the Faroe-Shetland Channel branch throughout the nineties has been studied using altimeter data from an exact repeat track which traverses the Southern Faroe Current at a nearly right angle, and using CTD data from a standard section coinciding with the altimetry track. No seasonality is evident prior to 1995, but a clear seasonal signal emerges after 1995. This shows maximum current velocities in February-April, and a seasonal amplitude in transport of ~ 0.6 Sv (Section 4.4).

14. The bifurcation of the Faroe Current seems to be related to the wind stress curl over the Nordic Seas (Section 4.4).

15. A regional version of the MICOM model is found to explain both seasonal and long-term temperature variations in the Continental Shelf Current and on the Faroe Plateau. In addition the modulation of the seasonal cycle with varying amplitudes and phases, is also simulated realistically (paper V and Section 4.5).

16. The potential for using simulations to complement the observed time series in periods with sparse sampling is examined. Advice is given to treat the observation-based cold anomaly in the late 1960s with caution, and to survey the hydrographical section in the Faroe-Shetland Channel four times a year or more if decadal scale temperature variations are of interest (paper V and Section 4.5).

5.2 Future Perspectives

5.2.1 Atlantic water over the Iceland-Faroe Ridge

One major uncertainty in estimating the Atlantic transport through section N stems from a lack of knowledge on the distribution of Atlantic water crossing the Iceland-Faroe Ridge. RAFOS floats [Rossby et al., 1986] will soon be launched south of the ridge and this will hopefully give some statistics on where they cross the ridge. This experiment could be imitated using the MICOM model.

5.2.2 High-resolution measurements along section N

Current meters (Aanderaa or similar) should be deployed along-isobath on the section N region in order to analyze the spatial structure of incoming Topographic Rossby waves. Cost effective temperature and salinity sensors should be placed on the bottom along section N to monitor the movement of the interface.

5.2.3 Measure and understand the bifurcation of the Faroe Current

One or two long-term ADCPs should be deployed in the northeastern region of the Faroe Plateau where the Faroe Current is believed to bifurcate. This could be supplemented with high-resolution hydrography cruises (e.g. SeaSoar or similar) or bottom mounted profilers (e.g. Yo-Yo's or similar).

5.2.4 Simulate the continuation of the Faroe Current into the Norwegian Sea

The fate of the Faroe Current in the Nordic Seas should be further examined using observations and the MICOM model. The extent to which this kind of models can describe migration patterns and other characteristics of herring and/or capelin in the Nordic Seas should be studied.

5.2.5 Place an ADCP instrument under m/s *Norrøna*

The prospect of attaching a downward looking ADCP under the passenger ferry m/s *Norrøna*, which crosses the Iceland-Faroe Gap and the Faroe-Shetland-Norway Gaps regularly, should be examined. According to experience from the Gulf Stream [Rossby and Zhang, 2001] this could be a viable supplement to the bottom mounted ADCPs in the Faroe-Shetland Channel and to the problem presented in 5.2.1.

Ancillary Data

A1 Altimetry

The altimeter data, measured by the TOPEX/Poseidon (T/P) and ERS-1 satellites are corrected for tides and the inverse barometer effect (Refer to Pathfinder (2001) for details). The altimetry observations used are all from exact repeat missions. This means that the satellites after some time (the repeat period) follow the exact same path (track) over the surface of the earth. The rms-error in the T/P-data is about 2 cm while it is somewhat higher for the ERS-1 data. Each track has an exact repeat period of almost ten days (9.92 days), giving us instantaneous data values with this sampling period.

A2 Drifters

Data from seventy WOCE/TOGA type drifters, which have crossed standard section N, were kindly provided by Philip Jakobsen (see Jakobsen et al. 2002 and Poulain et al. 1996 for further information). The basic data set is available at <http://www.noaa.aoml.gov>. The drifters are drogued at 15 m depth and the time series of positions were low-pass filtered to eliminate semi-diurnal tidal and inertial period waves.

A3 Section E

A part of the Nolso-Flugga section [Turrell et al., 1993] on the Faroese side of the Faroe Shetland Channel has since 1994 been regularly surveyed with CTDs by a Faroese research vessel [Hansen and Østerhus, 2000]. Some transects are available before 1994 as well. An ADCP (EB) was moored at 787 m depth along section E from 5 July 1999 to 17 June 2000 [Larsen et al., 2000] and data from this profiler have been utilized.

A4 Atmospheric fields

The atmospheric fields (wind speed, wind stress, sea level temperature and sea level pressure) are provided in the NCEP/NCAR re-analysis project at <http://www.cdc.noaa.gov> [Kistler et al., 2001]. The re-analyses are produced by passing all available historical atmospheric observations from the re-analysis period through a data assimilation and analysis system analogous to the systems used for weather prediction.

Modeled/Observed Hydrography in the Faroe Current

The modeled fields are interpolated from the isopycnal coordinates onto standard Levitus depths ($z = 0, 10, 20, 30, 40, 50, 75, 100, 125, 150, 200, 250, 300, 400, \dots$ m) in order to ease a comparison with the Cartesian coordinate observed data.

Time averaged simulated TS-fields along section N resemble the observed fields with the exception of a sharper thermo-, halocline and a shallower thermo-, halocline close to the shelf (Figs. 21a and 21b).

The simulated hydrography is, on average, too fresh by about 0.05-0.1 psu and too cold by 0.44°C, but only anomalies (variability) will henceforth be discussed. The maximum temperature/salinity (TS) values in each individual section are collected into a time series (Fig. 21c). The resulting simulated and observed time series are compared, giving correlation coefficients of $r = 0.98$ and $r = 0.72$ for temperature and salinity, respectively. The temperature maximum is consistently found near the shelf in the near-surface layers (Fig. 21). This measure is thus probably much influenced by the atmosphere, and the large correlation can largely be ascribed to a correctly modeled seasonal cycle.

Horizontally integrated TS time-series from model and observations have been compared. Practically perfect temperature correlations are found in the surface, while maximum salinity correlations of $r = 0.72$ are found at 125 m depth. Both parameters show significant correlations down to 250 m depths from where correlations sharply diminish. This is where the average simulated thermo-, halocline is located (Fig. 21b), and it indicates that the modeled hydrography in the Atlantic inflow is realistic. The simulated hydrography has too little variability near the thermo-, halocline showing that the interface is too rigid as is reflected by the too sharp thermocline in Fig. 21b compared to Fig. 21a.

A spatial average over the typical extent of Atlantic water in section N (Figs. 21a and 21b) will be a better measure for the hydrography in the inflow than the maximum temperature is. This latter measure will include the effects of mixing with adjacent water masses, air-sea interactions and the advection of water from the Atlantic Ocean.

*Bifurcation of the Faroe Current**C1 Drifters*

The pathways of 70 drifters (Appendix A), which have crossed section N (62° 20' N to 64° 00' N), have been studied.

The 500 m isobath around the Faroe Shelf forms a boundary line that most of the drifters in the Southern Faroe Current follow. None of the drifter did, however, cross this isobath shoreward. All drifters in the Southern Faroe Current did sooner or later turn northeast towards the Norwegian Shelf.

Assuming that a northeastward flowing drifter situated south of the latitude 62° 30' N when crossing the Greenwich meridian will continue in the NwASC (see Fig. 2), and that a drifter situated north of this latitude will continue in the NwAC, the following is found by a simple count:

- a) Of all the 70 drifters crossing section N, 54 (77%) continued in the NwAC and 16 (23%) continued in the NwAC.
- b) Of all the 28 drifters crossing section N near the core of the Faroe Current (south of 63° N), 19 (68%) continued in the NwAC branch and 9 (32%) continued in the NwASC.
- c) One out of four drifters crossing section N followed the Southern Faroe Current (reached south of 62° N in the Faroe Shetland Channel), while 39% of the near-core drifters in the Faroe Current turned south.

67% of the Southern Faroe Current drifters continued in the NwASC after making a U-turn in the Faroe Shetland Channel and the remaining 33% followed the NwAC.

C2 ADCPs

Three ADCPs along section N, two along section E (Faroe Shetland Channel) and three along section S (Faroe Shetland Channel) were concurrently in operation during the period from summer 1999 to summer 2000 (Fig. 16). The current velocities at NA and NB (section N) are found to correlate significantly with the downstream current velocity at mooring EB (section E). The first EOF-mode, explaining 70% of the downstream current variance at mooring EB is shown in Fig. 17a. The best correlation is found between the current velocities at mooring NB (200 m depth), which is close to the Faroe Current core (Fig. 6b), and the principal component associated to the first current mode at mooring EB. After low-pass filtering these series with a *running average* filter of 25-days length, the correlation coefficient between them is $r = 0.87$ (Fig. 17b). This correlation is highly significant although the filter decreases the degrees of freedom. The transport through section N is also significantly correlated to the downstream currents at 250 to 300 m depth at mooring EB. A portion of the correlation is related to a common seasonal cycle with maximum currents in March, but wavelet analysis indicates that north-south connections are also seen on shorter time scale motions (5 to 10 days) (paper IV). The coherences are also significant (on a 95 % level) for periods exceeding 20 days, and no phase lag was seen on these time scales. This indicates that intermediate-depth flows crossing section N over the 300-800 m isobaths are consistently guided by the topography into the Faroe Shetland Channel.

Weaker, but significant, correlations are also found between moorings NA, EB and SA. The bottom depths at the different moorings are NA and SA (~300m), NB (715m) and EB (787m), and the observation as depths between 200m (sections N and S) and 300m (section E) showed the clearest connections. No other combination of the ADCP records showed significant connections.

C3 Transports from altimetry and hydrography

Many studies have reported volume transport estimates based on the dynamic method by assuming zero velocities at some level. The deeper layers in the Faroe Shetland Channel are indeed not motionless [Hansen and Østerhus, 2000], and one would have to add the barotropic term $u(-H) \times H$, where H is the bottom depth and u is the current velocity, to the baroclinic estimates in order to obtain the total transport.

To avoid this uncertainty, following [Han and Tang, 2001], we use the sea surface as the level of known motion, as inferred from altimeter data, and density data from CTD transects to calculate transport variability through section E (Fig. 16). The total transport is found as the barotropic transport relative to the surface current velocity, $u(0)$, minus a component (Q_{BC}) related to the baroclinicity of the current. The barotropic transport relative to the surface, is given as:

$$Q_{BT} = H_{avg} \int_{y_1}^{y_2} u dy = H_{avg} \frac{g}{f} \cdot \Delta\eta$$

where H_{avg} is an average depth in the sectional window, g is the acceleration of gravity, f is the Coriolis parameter and $\Delta\eta$ is the sea surface height difference across the current.

An altimeter path (track 85), with an along-track ground resolution of 5.9 km, coincides with section E (see Fig 16), and 1-s altimeter data along this track from September 1992 to January 2002 have been used to obtain $\Delta\eta$. With the exact repeat period of 9.92 days this gives 332 such lines of data during the study period. The data are smoothed along the satellite track and in time using Gaussian filters with e -folding scales of 25 km and one month to remove the short wavelength variability and random noise [Han and Tang, 2001]. With this analysis, standard errors are typically ~0.01 m, but the errors will increase with shallower water.

By subtracting the sea height over the ~1000 m isobath from the sea height over the ~300 m isobath, which are isobaths straddling the Southern Faroe Current (see Fig. 18), gives a time series of $\Delta\eta$ with 332 data points. This series clearly shows seasonality after 1996 and an apparent half-year period prior to this (Fig. 19). Fitting a cosine to this series in a least square manner gives a seasonal excursion of 4 cm based on the full series, and 6 cm based on the post 1996 period, respectively. With an average upper layer depth of 500 m (H_{avg}) this gives a seasonal barotropic transport variation of 0.8-1.2 Sv (amplitudes) with a maximum in March-April and a minimum September-October.

Table 2. Number of transects and baroclinic transport anomaly (relative to surface) apportioned into four sub-periods

	Jan-Mar	April-June	July-Sept.	Oct.-Dec.	Total
Transects	8	5	9	7	29
Q_{BC} , (Sv)	0.36	0.10	-0.63	0.32	-

The baroclinic transport anomaly relative to the sea surface level of known motion (Q_{BC}) has to be subtracted from the above. A total of 29 CTD transects from section E (see Appendix A) are used in this study, and Table 2 shows when in the year these data have been sampled. The geostrophic current field relative to the surface is calculated for each transect using the *thermal wind* relation. These velocities are then integrated over the before mentioned window to obtain the baroclinic transport (Table 2). Fitting a cosine to the transport gives a maximum in February-March and a minimum in August-September, and seasonal amplitude of ~ 0.6 Sv. These extremes occur about a month before the extremes in the barotropic component, but assuming that they actually coincide, gives a seasonal variation in the total transport (BT-BC) of 0.2-0.6 Sv with a maximum in February-April and a minimum in August-October. The upper limit represents the period after 1996.

This can be compared to the ADCP observations from July 1999 to June 2000 at mooring EB. Averaging the current component normal to section E over the upper 400 m (assuming constant velocities over the shallowest 150 m because of the profilers limited range) gives an estimate of the transport variability in the Southern Faroe Current. With just one instrument available, it is not possible to quantify the transport. Assuming, however, that the time average of the velocity series observed at mooring EB (~250 m depth) corresponds to the average transport of 1.3 Sv, reported in the literature [Hansen and Østerhus, 2000], and assuming that the velocity series is proportional to the transport, an estimate of the seasonal variation is possible. A seasonal variation of 0.7 Sv with a maximum in March is found for this particular year.

REFERENCES

- Aagaard, K. and Carmack, E. C. (1989), The role of sea ice and other fresh water in the Arctic circulation, *Journal of Geophysical Research*, 94, 14485-14498.
- Aagaard, K., Swift, J. H., and Carmack, E. C. (1985), Thermohaline Circulation in the Arctic Mediterranean Sea, *Journal of Geophysical Research*, 90, 4833-4846.
- Baugrand, G. and Reid, P. C. (2003), Long-term changes in phytoplankton, zooplankton, and salmon linked to climate, *Glob.Change Biol.*, 9, 801-817.
- Bentsen, M. and Drange, H. (2000), Parameterizing surface fluxes in ocean models using the NCEP/NCAR reanalysis data, RegClim, Regional Climate Development Under Global Warming, General Technical Report, 4, 149-157, Norwegian Institute for Air Research, Kjeller, Norway.
- Bentsen, M., Drange, H., Furevik, T., and Zhou, T. (2004), Simulated variability of the Atlantic meridional overturning circulation, *Clim.Dynam.*, *In Press.*
- Blindheim, J. (1993), Seasonal variations in the Atlantic inflow to the Nordic Seas, *ICES CM 1999/C:39*, 13 pp.
- Blindheim, J., Borovkov, V., Hansen, B., Malmberg, S. Aa., Turrell, W. R., and Østerhus, S. (2000), Upper layer cooling and freshening in the Norwegian Sea in relation to atmosphere forcing, *Deep Sea Research*, 47, 655-680.
- Broecker, W. S (1991), The Great Conveyor Belt, *Oceanography*, 4, 79-89.
- Dickson, R. R. and Brown, J. (1994), The production of North Atlantic Deep Water: Sources, rates, and pathways, *Journal of Geophysical Research*, 99, 12319-12341.
- Dooley, H. D. and Meincke, J. (1981), Circulation and water masses

- in the Faroese Channels during Overflow 73', *Deutsche Hydrographische Zeitschrift*, 34, 41-55.
- Furevik, T., Bentsen, M., Drange, H., Johannessen, J. A., and Korabely, A. (2002), Temporal and spatial variability of the sea surface salinity in the Nordic Seas, *Journal of Geophysical Research*, 107, 53-79.
- Gaard, E. and Hansen, B. (2000), Variations in the advection of *Calanus finmarchicus* onto the Faroe Shelf, *ICES Journal of Marine Science*, 57, 1612-1618.
- Gaard, E. and Nattestad, K. (2002), Feeding, reproduction and seasonal development of *Calanus finmarchicus* in relation to water masses and phytoplankton in the southern Norwegian Sea, *ICES CM 1999/N:8*, 16 pp.
- Gould, J., Loymes, J., and Backhaus, J. (1985), Seasonality in slope current transports N.W. of Shetland, *ICES CM 1985/C:7*, 7 pp.
- Hallock, Z. C. (1985), Variability of frontal structure in the Southern Norwegian Sea, *Journal of Physical Oceanography*, 15, 1245-1254.
- Han, G. and Tang, C. I. (2001), Interannual variations of volume transport in the western Labrador Sea based on TOPEX/Poseidon and WOCE data, *Journal of Physical Oceanography*, 31, 199-211.
- Hansen, B., Jónsson, S., Turrell, W. R., and Østerhus, S. (2000), Seasonal variations in the Atlantic water inflow to the Nordic Seas, *CM 2000/L:03*, 1-15.
- Hansen, B., Larsen, K. M. H., Østerhus, S., Turrell, W. R., and Jónsson, S. (1999a), The Atlantic Water inflow to the Nordic Seas, *International WOCE Newsletter* 35, 35 pp.
- Hansen, B., Malmberg, S. Aa., Sælen, O. H., and Østerhus, S. (1986), Measurement of flow north of the Faroe Islands June 1986, *ICES CM 1986/C:12*, 14 pp.
- Hansen, B. and Meincke, J. (1979), Eddies and meanders in the Iceland-Faroe Ridge area, *Deep Sea Research*, 26A, 1067-1082.
- Hansen, B. and Meincke, J. (1984), Long-term coastal sea surface temperature observations at the Faroe Islands, *Rapports et Procès-Verbaux des Réunion du Conseil International pour l'Exploration de la Mer*, 185, 162-169.
- Hansen, B. and Østerhus, S. (2000), North Atlantic-Nordic Seas Exchanges, *Progress in Oceanography*, 45, 109-208.
- Hansen, B., Østerhus, S., Hátún, H., Kristiansen, R., and Larsen, K. M. H. (2003), The Iceland-Faroe inflow of Atlantic water to the Nordic Seas, *Progress in Oceanography*, 54, 443-474.
- Hansen, B., Østerhus, S., Kristiansen, R., and Larsen, K. M. H. (1999b), The Iceland-Faroe inflow of Atlantic water to the Nordic Seas, *ICES CM 1999/L:21*, 14 pp.
- Hansen, B., Sælen, O. H., and Østerhus, S. (1998), The passage of Atlantic water east of the Faroes, *ICES Cooperative Research Report*, 225, 112-123.
- Hansen, B., Turrell, W. R., and Østerhus, S. (2001), Decreasing overflow from the Nordic seas into the Atlantic Ocean through the Faroe Bank channel since 1950, *Nature*, 411, 927-930.
- Hátún, H. (2000), On the accuracy of computing slope current transports from current meter arrays, Master of Science thesis, 97 pp., The Norwegian University of Science and Technology - NTNU, Trondheim, Norway.
- Hátún, H. (2004), The heat budget in the Arctic Mediterranean, Technical Report No.: 04-01, 1-21, Faroese Fisheries Laboratory, Tórshavn, Faroe Islands.
- Hátún, H., Hansen, B., and Haugan, P. M. (2003), Using an "inverse dynamic method" to determine temperature and salinity fields from ADCP measurements, *Journal of Atmospheric and Oceanic Technology*, 21, 527-533.
- Hátún, H. and McClimans, T. A. (2003), Monitoring the Faroe Current using altimetry and coastal sea-level data, *Continental Shelf Research*, 23, 859-868.
- Hátún, H., Sandø, A., Drange, H., and Bentsen, M. (2004), Seasonal to decadal temperature variations in the Faroe-Shetland inflow waters, *The climate of the Nordic Seas, AGU Monograph*, In Press.
- Helland-Hansen, B. (1903), Faroe-Shetland Channel and the northern part of the North Sea in the year 1902., *Northern Area First Report 1902-1903, North Sea Fisheries Investigation Committee, Fisheries Board for Scotland*.
- Helland-Hansen, B. and Nansen, F. (1909), The Norwegian Sea, *Fiskeridirektoratets Skrifter Serie Havundersøkelser*, 2, 1-390.
- Herman, F. (1949), Hydrographic conditions in the South-Western Part of the Norwegian Sea, *Annales Biologiques du Conseil International pour l'Exploration de la Mer*, 5, 19-21.
- Hermann, F. (1953), Hydrographic conditions in the southern of the Norwegian Sea, 1952, *Annales Biologiques du Conseil International pour l'Exploration de la Mer*, IX, 22-25.
- Hermann, F. (1967), The T-S diagram analysis of the water masses over the Iceland-Faroe Ridge and in the Faroe Bank Channel (Overflow 60'), *Rapports et Procès-Verbaux des Réunion du Conseil International pour l'Exploration de la Mer*, 157, 139-149.
- Holliday, N. P., Pollard, R. T., Read, J. F., and Leach, H. (2000), Water mass properties and fluxes in the Rockall Trough, 1975-1998, *Deep Sea Research*, 47, 1303-1332.
- Hopkins, T. S., Povero, P., Pistek, P., and Warn-Varnas, A. (1992), Upper layer environmental parameters from CTD data GIN '87 cruises., *SACLANTEN Memoirs, SM-260, 1*, 1-214.
- IPCC (2001), *Climate Change 2001: The Scientific Basis*, 881 pp., Cambridge University Press, United Kingdom and New York, NY, USA.
- Jacobsen, J. P. (1943), The Atlantic Current through the Faroe-Shetland Channel and its influence on the hydrographical conditions in the northern part of the North Sea, the Norwegian Sea and the Barents Sea, *Rapports et Procès-Verbaux des Réunion du Conseil International pour l'Exploration de la Mer*, 112, 5-47.
- Jakobsen, P. K., Ribergaard, M. H., Quadfasel, D., and Schmith, T. (2002), The near surface circulation in the Northern North Atlantic as inferred from Lagrangian drifters: variability from mesoscale to interannual, *Journal of Geophysical Research*, submitted.
- Kistler, R., Collins, W., Saha, S., White, G., Wollen, J., Kalnay, E., Chelliah, M., Ebisuzaki, W., Kanamitsu, M., Kousky, V., Van den Dool, H. Jenne R., and Fiorini, M. (2001), The NCEP-NCAR 50-Year Reanalysis, *Monthly Means, CD-ROM and Documentation Bulletin of the American Meteorological Society*, 82, 247-268.
- Kristmannsson, S. (2001), Flow of Atlantic Water into the Northern Icelandic Shelf Area, 1985-1989, *ICES Cooperative Research Report* 225, 135. pp.
- Larsen, K. M. H., Hansen, B., and Kristiansen, R. (1999), Nordic WOCE ADCP Deployments 1994-1997, Technical Report No.: 99-05, 1-53, The Faroese Fisheries Laboratory, Tórshavn, Faroe Islands.
- Larsen, K. M. H., Hansen, B., and Kristiansen, R. (2000), Faroese GEM ADCP Deployments 1999-2000, Technical Report No.: 00-02, The Faroese Fisheries Laboratory, Tórshavn, Faroe Islands.
- Levitus, S. and Boyer, T. P. (1994), World Ocean Atlas 1994 Volume 4: Temperature. NOAA Atlas NESDIS 4.
- Levitus, S., Burgett, R., and Boyer, T. P. (1994), World Ocean Atlas 1994 Volume 3: Salinity. NOAA Atlas NESDIS 3.
- McClimans, T. A., Johannessen, B. O., and Jenserud, T. (1999), Monitoring a shelf edge current using a bottom pressure or coastal sea-level data, *Continental Shelf Research*, 19, 1265-1283.
- Meincke, J. (1978), On the distribution of low salinity intermediate waters around the Faroes, *Deutsche Hydrographische Zeitschrift*, 31, 50-63.
- Meincke, J. (1983), *The modern current regime across the Greenland-Scotland Ridge*, Proc. NATO Adv. Res. Inst., Padua Univ., 11-15 May, 1981, Plenum Press, New York.
- Meincke, J. and Kvinge, T. (1978), On the atmospheric forcing of overflow events, *ICES CM 1978/C:9*, 12 pp.

- Mork, K. A. and Blindheim, J. (2000), Variations in the Atlantic inflow to the Nordic Seas, 1955-1996, *Deep Sea Research*, 47, 1035-1057.
- Mosby, H. (1970), Atlantic water in the Norwegian Sea, *Geophysica Norvegica*, 28, 1-60.
- Nielsen, J. N. (1904), Hydrography of the waters by the Faroe Islands and Iceland during cruises of the Danish research steamer 'Thor' in the summer 1903, *Meddelser fra Kommissionen for Havundersøgelser. Serie Hydrografi*, 1 (4), 1-42.
- Nilsen, J. E., Gao, Y., Drange, H., Furevik, T., and Bentsen, M. (2003), Simulated North Atlantic-Nordic Seas water mass exchanges in an isopycnic coordinate OGCM, *Geophysical Research Letters*, 30(10), 1536, doi:10.1029/2002GL016597.
- Nilsen, J. E. Ø. (2003), Aspects of the Atlantic Flow through the Norwegian Sea, Dr. Scient thesis, 43 pp., Geophysical Institute, University of Bergen, Bergen, Norway.
- Orvik, K. A. and Mork, K. A. (1996), Atlantic water transport from long term current measurements in the Svinøy section, *ICES CM 1996/O:8*, 9 pp.
- Orvik, K. A. and Niiler, P. P. (2002), Major pathways of Atlantic water in the northern North Atlantic and Nordic Seas toward the Arctic, *Geophysical Research Letters*, 29(19), 1896, doi:10.1029/2002GL015002.
- Orvik, K. A. and Skagseth, O. (2003), The impact of the wind stress curl in the North Atlantic on the Atlantic inflow to the Norwegian Sea toward the Arctic, *Geophysical Research Letters*, 30(17), 1884, doi:10.1029/2003GL017932.
- Orvik, K. A., Skagseth, O., and Mork, M. (2001), Atlantic inflow to the Nordic Sea: Current structure and volume fluxes from moored current meters, VM-ADCP and Sea Soar-CTD observations, 1995-1999, *Deep Sea Research*, 48, 937-957.
- Otto, L. and Van Aken, H. M. (1996), Surface circulation in the north-east Atlantic as observed with drifters, *Deep Sea Research*, 43, 467-499.
- Perkins, H., Hopkins, T. S., Malmberg, S. Aa., Poulain, P. M., and Warn-Varnas, A. (1998), Oceanographic conditions east of Iceland, *Journal of Geophysical Research*, 103, 21531-21542.
- Pistek, P. and Johnson, D. R. (1992), Transport of the Norwegian Atlantic current as determined from satellite altimetry, *Geophysical Research Letters*, 19, 1379-1382.
- Poulain, P. M., Warn-Varnas, A., and Niiler, P. P. (1996), Near surface circulation of the Nordic Seas as measured by Lagrangian drifters, *Journal of Geophysical Research*, 101, 18237-18258.
- Read, J. F. and Pollard, R. T. (1992), Water masses in the region of the Iceland-Faroes Front, *Journal of Physical Oceanography*, 22, 1365-1378.
- Rosby, T., Dorson, D., and Fontaine, J. (1986), The RAFOS system, *Journal of Atmospheric and Oceanic Technology*, 3, 672-679.
- Rosby, T. and Zhang, H-M. (2001), The near-surface velocity and potential vorticity structure of the Gulf Stream, *Journal of Marine Research*, 59, 59949-59975.
- Samuel, P. and Johannessen, J. A. (1994), A study on the Inflow of Atlantic Water to the GIN Sea using GEOSAT Altimeter Data, *The Polar Oceans and Their Role in Shaping the Global Environment*, 95-108.
- Seager, R., Battist, D. S., Yin, J., Gordon, N., Naik, N., Clementsen, A. C., and Cane, A. (2002), Is the Gulf Stream responsible for Europe's mild winters?, *Q.J.R. Meteorological Society*, 128, 1-24.
- Simonsen, K. and Haugan, P. M. (1996), Heat budgets of the Arctic Mediterranean and sea surface heat flux parametrizations for the Nordic Seas, *Journal of Geophysical Research*, 101, 6553-6576.
- Smart, J. H. (1984), Spatial variability of major frontal systems in the North Atlantic-Norwegian Sea area: 1980-1981, *Journal of Physical Oceanography*, 14, 185-192.
- Stefánsson, U. (1972), Near-shore fluctuations of the frontal zone southeast of Iceland, *Rapports et Procès-Verbaux des Réunions du Conseil International pour l'Exploration de la Mer*, 162, 201-205.
- Tait, J. B. (1957), Hydrography of the Faroe-Shetland Channel 1927-1952, *Marine Research Scotland*, 2, 1-309.
- Tait, J. B. (1967), The Iceland-Faroe Ridge international (ICES) 'Overflow' expedition, May-June 1960, *Rapports et Procès-Verbaux des Réunions du Conseil International pour l'Exploration de la Mer*, 157, 1-71.
- the MAIA team (2003), Monitoring the Atlantic Inflow towards the Arctic, *Continental Shelf Research Submitted*,
- Timofeyev, V. T. (1963), Interaction of waters from the Arctic Ocean with those from the Atlantic and Pacific, *Okeanologiya*, 3, 569-578.
- Tokmakian, R. (1994), The Iceland-Faroe Front: A Synergistic Study of Hydrography and Altimetry, *Journal of Physical Oceanography*, 24, 2245-2262.
- Torrence, C. and Compo, G. P. (1998), A practical guide to wavelet analysis, *Bulletin of the American Meteorological Society*, 79, 61-78.
- Turrell, W. R., Devonshire, E., Payne, R., and Slesser, G. (1993), Analysis of the historic time-series obtained in the Faroe-Shetland Channel, *ICES CM 1993/C:29*,
- Turrell, W. R., Hansen, B., Hughes, S., and Østerhus, S. (2003), Hydrographic variability during the decade of the 1990s in the Northeast Atlantic and southern Norwegian Sea, *Marine Science Symposia*, 219, 111-120.
- Turrell, W. R., Hansen, B., Østerhus, S., Hughes, S., Ewart, K., and Hamilton, J. (1999), Direct observation of the inflow to the Nordic Seas through the Faroe Shetland Channel 1994-1997, *ICES CM 1999/L:01*,
- Van Aken, H. M. (1988), Transports of water masses through the Faroese Channels determined by an inverse method, *Deep Sea Research*, 35, 595-617.
- Van Aken, H. M. and Becker, G. (1996), Hydrography and through-flow in the north-eastern North Atlantic Ocean: the NANSEN project, *Progress in Oceanography*, 38, 297-346.
- Van Aken, H. M. and Eisma, D. (1987), The circulation between Iceland and Scotland derived from water mass analysis, *Netherlands Journal of Sea Research*, 21, 1-15.
- Willebrand, J. and Meincke, J. (1980), Statistical analysis of fluctuations in the Iceland-Scotland frontal zone, *Deep Sea Research*, 27A, 1047-1066.
- Worthington, L. V. (1970), The Norwegian Sea as a mediterranean basin, *Deep Sea Research*, 17, 77-84.
- Worthington, L. V. and Volkman, G. H. (1965), The volume transport of the Norwegian Sea overflow water in the North Atlantic, *Deep Sea Research*, 12, 667-676.
- Wunsch, C. I. and Ferrari, R. (2004), Vertical mixing, energy, and the general circulation of the oceans, *Annual Reviews of Fluid Mechanics*, 36, 281-314.

PAPER I

Using an “Inverse Dynamic Method” to Determine Temperature and Salinity Fields from ADCP Measurements

HJÁLMAR HÁTÚN AND BOGI HANSEN

Faroese Fisheries Laboratory, Tórshavn, Faroe Islands

PETER HAUGAN

Geophysical Institute, University of Bergen, Bergen, Norway

(Manuscript received 26 August 2002, in final form 25 June 2003)

ABSTRACT

In heavily fished areas, upward looking acoustic Doppler current profilers (ADCPs), moored at depth, may be the only option for long-term current measurements. Arrays of ADCP moorings that cross a current can thus be the optimal strategy for monitoring the volume flux. These instruments only measure water properties at the instrument, not through the water column, however. By itself, an ADCP array, therefore, does not give flux estimates of specific water masses unless temperature and salinity profiles can be derived from the velocity profiles. This is the opposite of the classical problem of determining currents from temperature and salinity observations, and in principle it should be possible to solve it by inverting the classical dynamic method. As for the classical method, this problem requires additional reference information. Using observations from the Faroe Current between Iceland and the Faroe Islands, it is demonstrated that this procedure can indeed be used by applying empirical orthogonal function (EOF) analysis to CTD and ADCP data from a section that crosses this current. It is found that one of the empirical velocity modes is highly correlated to the dominant temperature and salinity modes. Employing this relationship, ADCP measurements are used to reconstruct temperature and salinity fields with the same temporal resolution as the velocity field. For the Atlantic inflow of the Faroe Current, the reconstructed fields are found to explain 60% of the temperature and 44% of the observed salinity variances.

1. Introduction

This work was motivated by the wish to compute volume flux of Atlantic water through a section crossing the Atlantic water flowing between Iceland and the Faroes. This flow (the Faroe Current) is of great climatic importance and therefore continuous current measurements have been carried out on the section for several years with moored acoustic Doppler current profilers (ADCPs; Hansen et al. 2003, hereafter HOHKL). These measurements allow total volume flux to be estimated quite accurately, but to estimate how much of this derives from the Atlantic Ocean, a water-mass analysis is necessary, which requires temperature and salinity observations. On this section, a large number of CTD surveys have been carried out, but usually there were several months between each survey and the heavy fishing activity precludes mooring of sensors for continuous temperature and salinity measurement.

This discrepancy in temporal resolution of velocity and hydrographic (temperature and salinity) data could

be circumvented if there was a way to infer hydrographic parameters from velocity observations. The existence of such a relationship is implied by geostrophy, which links vertical velocity shear with horizontal changes of density and hence temperature and salinity through the thermal wind equation. The traditional “classical dynamic method” uses this relationship for the inverse problem: to derive velocity from hydrography.

As for the classical dynamic method, a straightforward use of the thermal wind equation to compute hydrography from velocity would involve integrations that introduce unknown “reference” values. Instead, we have tested the hypothesis that empirically determined spatial modes in the velocity and hydrography fields are linked through the thermal wind equations. In our study, the spatial velocity modes were determined by empirical orthogonal function (EOF) analysis (Preisendorfer 1988) of ADCP data while the hydrographic modes were determined by EOF analysis of the CTD data.

A priori, there would not seem to be any guarantee that this procedure should work, but for our data from the Faroe Current, our results show that it does work. It might therefore be worthwhile to test the method in other areas where similar datasets have been acquired.

Corresponding author address: Dr. Hjálmar Hátún, Faroese Fisheries Laboratory, 1 Noatun, FO-110 Tórshavn, Faroe Islands.
E-mail: hjalmarh@frs.fo

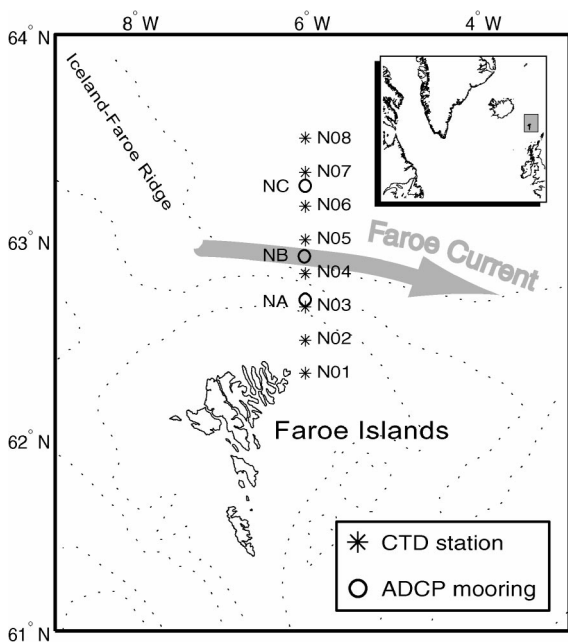


FIG. 1. An overview the standard measurement section, which intersects the Faroe Current to the north of the Faroe Islands.

The structure of the paper is summarized as follows. In section 2 the data material is surveyed. The basic theory of the EOFs is given in section 3. The hydrographical and the current EOF modes and their appurtenant time-varying principal components are shown in section 4, and the structure of the important modes is emphasized. A correlation between the current velocity field and the temperature–salinity (TS) fields is found in section 5, and it is shown how this correlation can be used to reconstruct TS data with a higher time resolution than found in the original TS fields. In section 6, the statistically obtained relationships are shown to be based on physical mechanisms including geostrophy and they are validated against further observation.

2. Material

The data material includes CTD and ADCP data obtained along a section (Fig. 1) extending northward from the Faroe Shelf. This section crosses the flow of Atlantic water that has crossed the Iceland–Faroe Ridge and flows eastward. More complete information on the observations and data treatment may be found in HOHKL.

a. CTD data

The standard hydrographic stations are shown in Fig. 1, and the data from these stations have been collected and processed by the Faroese Fisheries Laboratory (FFL). Considered are data from the six stations, N03 to N08, since these span the region where the ADCP instruments are moored. Thirty-eight complete CTD

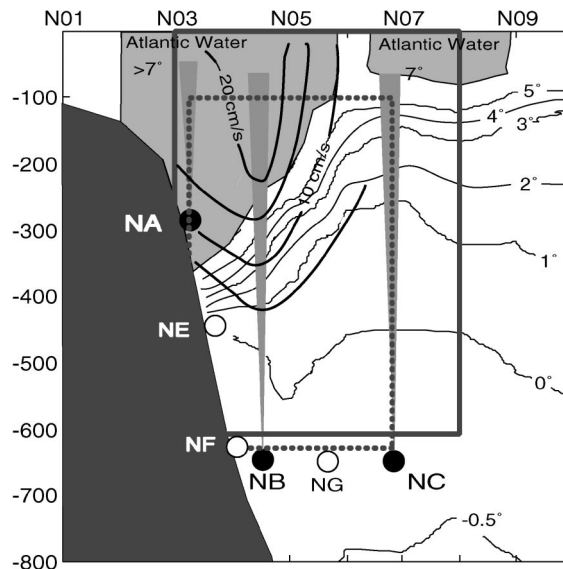


FIG. 2. A view from east to west of the measurement section. The Faroe Shelf is shown to the left, the 1997–2000 ADCP instruments are illustrated with the black circles, and the gray cones represent their acoustic beams. The 2000–01 instruments are shown with white circles. The larger rectangle is the spatial domain of the hydrographic data, and the smaller, dashed rectangle shows the 1997–2000 ADCP data domain. The bold lines illustrate the averaged profile of the jetlike Faroe Current, and the thin lines show the temperature field on 7 Nov 1999. The gray areas indicate undiluted Atlantic water (warmer than 7°C) on this particular day.

sections from 1990 to 2001 are used. The CTD stations are placed equidistantly 10 nautical miles (about 18.52 km) apart and there is a data value for each meter in the vertical. Stations N03 and N04 are in fairly shallow water and data are available down to about 175 and 495 m, respectively. The stations N05–N08 are over deeper water, but the analysis is restricted down to 600 m and this gives us 38 data matrices with temperature and salinity of dimensionality 6×600 . The larger, full line rectangle in Fig. 2 shows the region covered by these matrices.

b. ADCP data

The current velocity data set on which this paper is based, derives from an array of three ADCPs deployed across the flow from summer 1997 to summer 2000 and an array of five ADCPs from summer 2000 to summer 2001.

During the first period (1997–2000), the ADCP data were measured by one bottom mounted instrument (NA in Fig. 2) and two moored instruments, NB and NC. The EOF analysis requires complete data sections and only periods with all three instruments—NA, NB and NC—operational at the same time are included. These periods are 15 June 1997–8 June 1998, 8 July 1998–18 June 1999, and 21 August 1999–15 June 2000, where the gaps in summer come when the instruments are tak-

en ashore, serviced, and redeployed. Used are daily averaged velocities from which the tidal signal has been removed (HOHKL).

The ADCP data are given as current magnitude and direction in evenly spaced depth intervals (bins). For the bottom mounted instrument at NA the bin length is 10 m, while it is 25 m for NB and NC. The data from the latter two are interpolated to 10-m bins levelled to those at NA, using a cubic-spline interpolation. The instrument NA has a higher sound pulse frequency than those at NB and NC, and data quality in shallow water at site NA is therefore slightly better than the data at the other two sites. Data from the depth interval 0–100 m are not included because of errors. The bottom-mounted instrument NA is at almost 300-m depth, and the deepest bin at this site is from 270 to 280 m, while the deepest bins at NB and NC are from 610 to 620 m. This gives 1005 complete velocity data sections of dimensionality 3×57 and the area covered by these sections is shown with the smaller, dashed rectangle in Fig. 2.

In the summer of 2000 the deployment strategy was changed. Instead of the three moorings (NA, NB, and NC) used in the 1997–2000 period, a denser array with five moorings (NA, NE, NF, NB, and NG) was used. Due to the changed spatial resolution, the 2000–01 observations have been analysed separately from the 1997–2000 dataset, although the results from both periods can be used together.

The isobaths in the measurement region are oriented slightly south of east, and the current core, which is topographically steered, will therefore flow somewhat to the south of east, which also has been verified by a progressive vector plot of the depth-averaged velocity at site NB (Hansen and Østerhus 2000). Only the eastward velocity component u , which is perpendicular to the data section, is used in this study.

In addition to velocity profiles, the ADCP's record in situ temperature at the instrument. Of special interest is the temperature from site NE (Fig. 2), which was located in the thermocline region since it gives a continuous time series of the thermocline depth.

3. The basic assumptions and the EOFs

The data can be characterized as sections, or “maps,” of scalar variables $\psi(y, z, t)$ = (temperature, salinity, or current velocity), where y is the latitudinal coordinate, z is the depth, t is the time. Before the EOF analysis, each of the data fields is split into four components:

$$\begin{aligned} \psi(y, z, t) = & \psi_{\text{avg}}(y, z, t_0) + (t - t_0) \\ & \times [\psi_{\text{trend}}(y, z) + \psi_{\text{season}}(y, z, t) \\ & + \psi'(y, z, t)], \end{aligned} \quad (1)$$

where ψ_{avg} is an average field at time t_0 , ψ_{trend} is a coefficient matrix describing any temporal linear trend at

location (y, z) , and ψ_{season} is a sinusoidal seasonal variation, written as

$$\psi_{\text{season}}(y, z, t) = a(y, z) \left\{ \cos \left[\frac{2\pi}{365.25} t - \varphi(y, z) \right] \right\}, \quad (2)$$

where again, a is a seasonal amplitude map and φ are the phases at each spatial point. These three mentioned terms are subtracted from the data prior to the analysis and this leaves us with the term $\psi'(y, z, t)$, which will be termed the *residual field*, for convenience. The basic idea of the proposed method is to use EOF analysis to split the residual fields into modes and then to check whether any of the temperature and salinity modes can be related to any velocity mode.

An EOF analysis is designed to compress the variability in this type of time series data. The basic idea of the EOFs is that one can represent the variability in $\psi'(y, z, t)$, as a linear combination of M orthogonal eigenmodes, or “eigenmaps.” Here $\varphi_m(y, z)$, $m = 1, 2, \dots, M$, which solely depend on the spatial coordinates y and z . These spatial eigenmaps are then weighted with time dependent amplitudes $A_m(t)$, (the principal components), and in this way, one is able to split up space and time dependence in the field; M is the number of spatial points in the maps (M = number of ys times number of zs). Mathematically this can be written as follows:

$$\psi'(y, z, t) = \sum_{m=1}^M A_m(t) \varphi_m(y, z). \quad (3)$$

The advantage with this approach is that most of the variability is explained by the first few modes. Another strength of this approach is that the modes are orthogonal, which means that they are statistically independent, and one can thereby find how much variability each mode explains of the total variability in the field. The EOF modes $\varphi_m(y, z)$, and the amplitudes $A_m(t)$ are found from a singular value decomposition (SVD; Emery and Thomson 1997) of the detrended and deseasoned fields. This method splits the amplitudes furthermore into the dimensionless principal components (PCs) (normalized amplitudes) and the so-called singular values (w) that carry the physical dimensions (Preisendorfer 1988).

4. Results

a. Spatial structure of the eigenmodes

The seasonal amplitudes, a , and the phase fields, φ , as shown in (3) were first found using a least squares method. It was found that 34% of the temperature variance is explained by seasonal variations while 24% of the salinity variance is seasonal. Hereafter, when referring to variance explained by the EOFs, it will be shown as percentage of the variance in the nonseasonal residual fields, T' (66% of total) and S' (76% of total).

The three first spatial eigenmodes of each physical parameter are shown in Figs. 3 and 4. The modes are

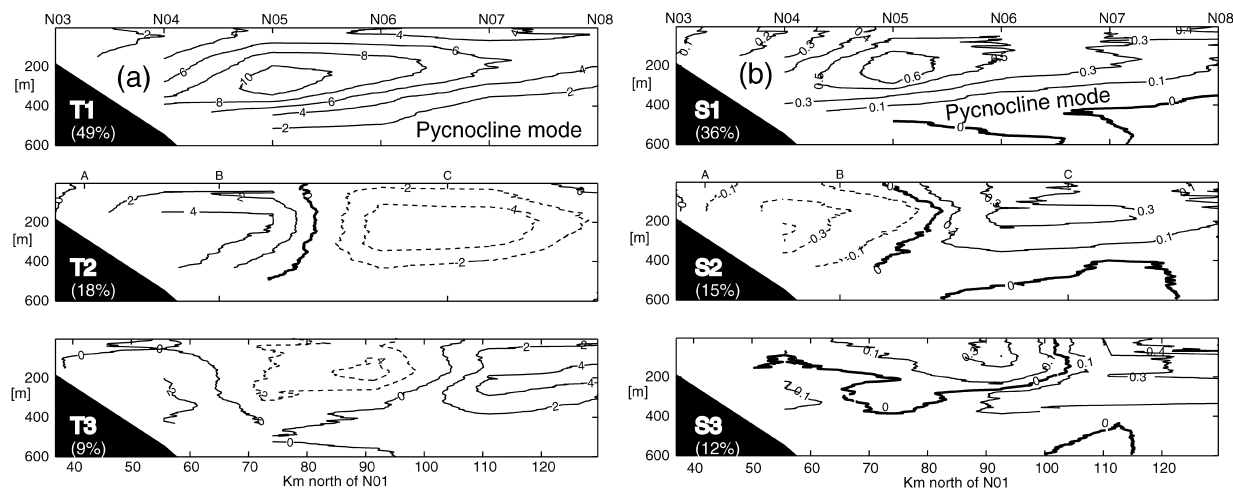


FIG. 3. The first three spatial hydrographic modes. A view from east to west is shown, with the Faroe Shelf to the left. The hydrographic station labels are seen on top, and the distance from the first station, N01 (not used in this study), goes along the bottom axis. The full lines represent positive values, and dashed lines represent negative values. The zero contour is shown as a thick line: (a) the temperature modes (T_1 , T_2 , and T_3) and (b) the salinity modes (S_1 , S_2 , and S_3). The explained variance for each mode is shown in percentages.

data matrices with the same dimensionality (number of points in the vertical and the horizontal) as the measured field. In Figs. 3a and 3b, the modes for the temperature and salinity, respectively, are shown. The modes are weighted by the singular values (and thus carry the units $^{\circ}\text{C}$ and psu), but the physical magnitudes first become apparent after multiplying by the time dependent principal components whose typical values lie between -0.25 and 0.25 . The modal structures are very similar for temperature (T_1) and salinity and the first mode in both temperature (T_1) and salinity (S_1) (hereafter referred to as the “pycnocline” mode for convenience) shows a monopole variation (only positive values). The entire re-

gion, with most variability diagonally oriented from about 400 m at the shelf toward the surface at N08, will show either positive or negative temperature anomalies, and this is linked to fluctuations up and down of the main thermocline and thereby the pycnocline. This mode explains 49% for the temperature and 36% for the salinity of the variance in the residual fields. The second mode (T_2 , S_2) has a dipolar character where (negative, positive) values between N06 and N07 are accompanied with (positive, negative) anomalies between N04 and N05 and vice versa. This second mode explains 18% of the temperature and 15% of the salinity variance. The third mode (T_3 , S_3) explains 9% in T' and 12% in S' .

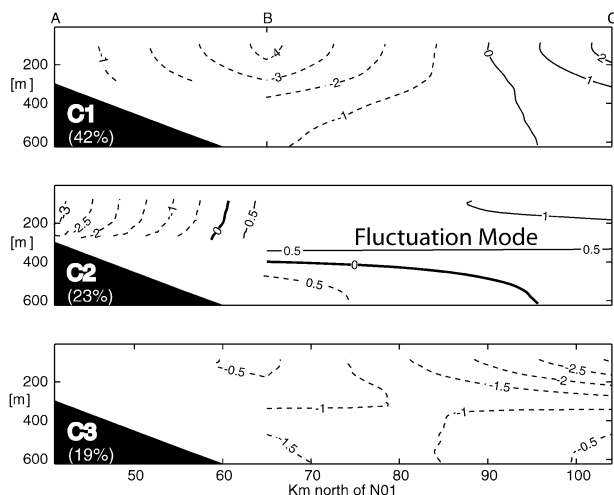


FIG. 4. The first three spatial modes (C_1 , C_2 , and C_3) of the eastward current, in a similar view as Fig. 3. The modes from the 1997–2000 analysis are shown, and the mooring site labels NA, NB, and NC are shown on top. The explained variance for each mode is shown in percentages.

The velocity modes for the first period (1997–2000) (Fig. 4) have a coarser structure than the hydrographic modes, since they are based on fewer spatial data points. The modes from the latter period 2000–01 (not shown) are similar to those found from the 1997–2000 data. The first mode (C_1) finds a strong monopole variation centred at site NB, which also is the site closest to the current core. This mode is highly correlated ($R^2 = 0.85$) to the total volume transport Q . The second mode (C_2) (hereafter referred to as the “fluctuation” mode) has a dipolar variation between the offshore and the onshore side of the mean current. The third mode (C_3) has a tripolar variation with negative values on the current flanks accompanied by a positive core in the center.

b. Temporal variations (principal components)

The principal components (amplitudes) show how much the different modes described above contribute to the total field at a certain moment of time. The first three PCs for temperature, PC_{T_1} , PC_{T_2} and PC_{T_3} , and the first three PCs for salinity, PC_{S_1} , PC_{S_2} , PC_{S_3} , are shown in Fig. 5. There are 38 data points in each PC corresponding

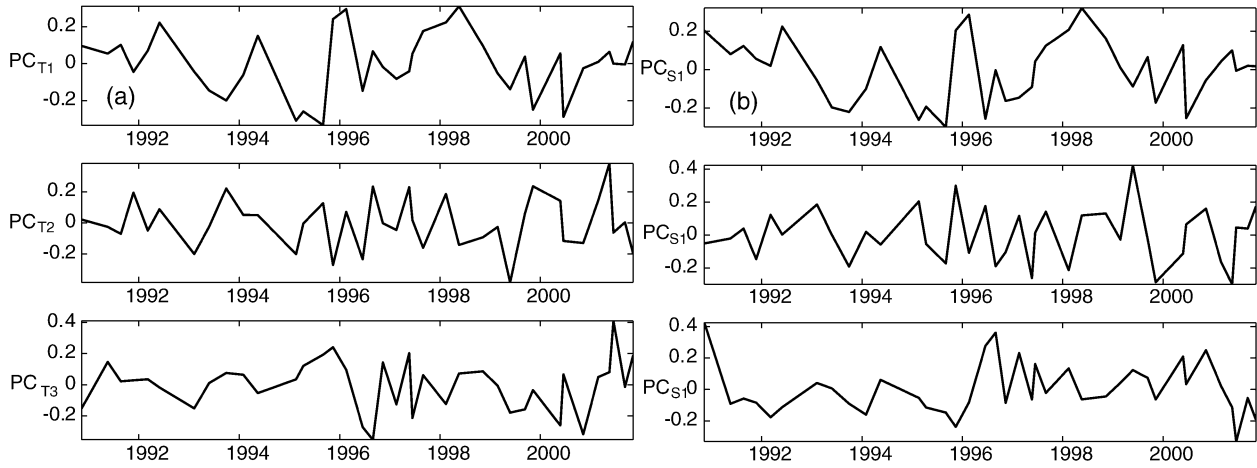


FIG. 5. The three first hydrographic amplitudes: (a) the temperature PCs (PC_{T1} , PC_{T2} , and PC_{T3}) describing the temporal development of mode $T1$, $T2$, and $T3$, and (b) the salinity PCs (PC_{S1} , PC_{S2} , and PC_{S3}) describing the temporal development of mode $S1$, $S2$, and $S3$. There are 3–5 data points per year.

to the 38 CTD cruises. It is noted in Fig. 3 that the spatial structures of the T and S modes are very similar and the temporal variations are also similar (Fig. 5; the correlation coefficient between PC_{T1} and PC_{S1} is $R^2 = 0.98$).

The principal components are normalized so that the sum of these squared equals unity. This makes their magnitudes depend on the length of the time series. The PCs from the latter 2000–01 period will be larger than the PCs from the former period, because there are fewer data points in the latter period and therefore fewer values in the sum of squares. Since the velocity modes from the two periods are similar, one can assume that the variance explained by each mode should also be comparable. This makes it possible to find a scaling factor α between the two periods so that $PC(\text{former}) = \alpha$ times $PC(\text{latter})$. This coefficient is given as

$$\alpha^2 = \frac{w_{\text{former}}^2 [\text{var}(PC_{\text{former}})]}{w_{\text{latter}}^2 [\text{var}(PC_{\text{latter}})]} \Rightarrow \alpha = \sqrt{\frac{w_{\text{former}}^2 (N_{\text{latter}})}{w_{\text{latter}}^2 (N_{\text{former}})}}, \quad (4)$$

where N is the number of data points in each period and w is the singular values. This is 1005 for the former and 343 for the latter period. The velocity principal components, PC_{C1} , PC_{C2} , and PC_{C3} from the two periods can now be presented as one (Fig. 6). The finer time resolution in the velocity data is evident in this plot.

5. Correlations between water-mass and velocity modes

The objective of this study is to find some connection between the hydrographical field and the eastward velocity field. If such a connection is found, then information from the ADCP data, which have a much better time resolution, can be used to construct a time series containing the basic variations in the hydrographical field on a weekly to monthly scale. The time dependent amplitudes have been used in a search for this connec-

tion. It would physically be more logical to compare the density and the velocity since it is these two parameters that are coupled (through the thermal wind relation). But since the aim is to obtain information on each of the hydrographical parameters (temperature and salinity) separately, a direct connection between the current field and each of these is sought.

a. Correlation between principal components

All PCs for the velocity and the hydrography corresponding to data sections that are measured less than two days apart, that is, simultaneous or almost simultaneous data sections, have been picked out.

Since the T' and S' fields have been seen to vary similarly, we may consider T' only. After comparing different combinations of the temperature PCs— PC_{T1} , PC_{T2} , and PC_{T3} —and the velocity PCs— PC_{C1} , PC_{C2} , and

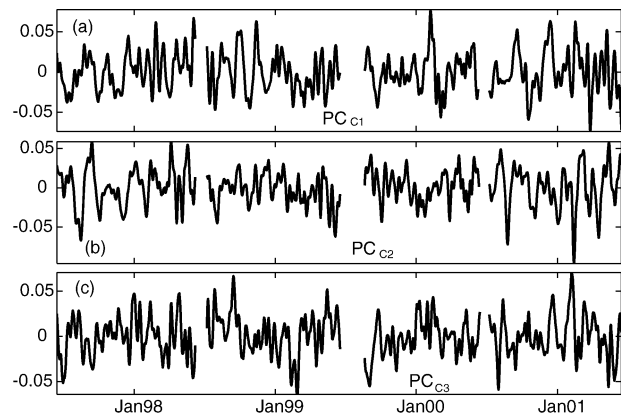


FIG. 6. The first three velocity PCs (PC_{C1} , PC_{C2} , and PC_{C3}) describing the temporal development of mode $C1$, $C2$, and $C3$. The amplitudes are 5-day low-passed for clarity. The periods in summertime when the instruments are on land are missing.

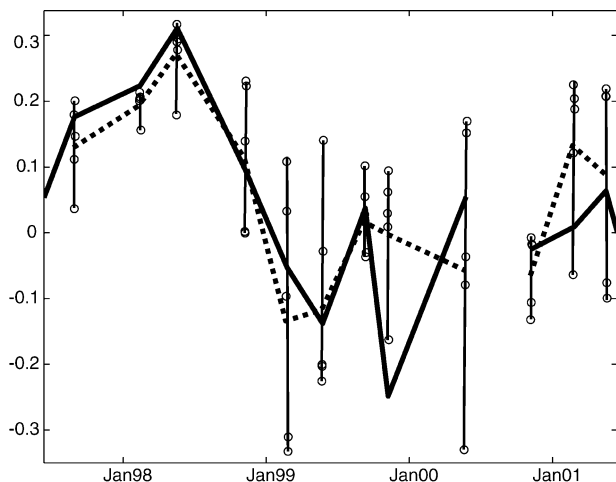


FIG. 7. A comparison of the pycnocline PC, PC_{T1} (full line), and the fluctuation mode PC, PC_{C2} (dashed line). The vertical lines illustrate the span of PC_{C2} from a 5-day period centered on the day when the CTD measurements were made. The circles show the PC_{C2} value each day, and the dashed line is found as an average over these. The values for PC_{C2} have been scaled by a factor β .

PC_{C3} —it is found that the combination PC_{T1} and PC_{C2} , that is the pycnocline mode and the fluctuation mode, shows a significant correlation ($R^2 = 0.76$ with $p < 0.01$). This correlation was found when averaging PC_{C2} values over five days centered on the day when the CTD measurement was made (Fig. 7). The CTD section takes over a day to complete and the processes which link current and hydrography will also take some time to adjust, so a best fit when averaging over some days was to be expected. No significant correlation was found for any other combination of principal components.

Assuming that the correlated modes are governed by the same physical mechanism, one can use the same argument as presented in section 4b in order to find the scaling coefficient β between PC_{T1} and PC_{C2} . The plot in Fig. 7 uses this coefficient. A simple linear regression gave a similar coefficient.

In Fig. 7 it is evident that the PCs correlate better when there is little short-term variability in the current PC. There is one point (November 1999) where the temperature PC lies outside the span of all five current PCs. There was a sudden brief drop in PC_{C2} around this time, which could have caused the discrepancy.

b. Synthesis of a hydrographic time series

The key in linking the residual fields $TS'(y, z, t)$ to the residual field $U'(y, z, t)$ now seems to be in the link between the pycnocline mode in the hydrography and the fluctuation mode in the current.

The linear relationship in Fig. 7, where velocity fluctuation PC, PC_{C2} , is a factor β times the pycnocline PCs, PC_{T1} and PC_{S1} , is assumed to be valid for all other days as well, when no hydrographic data exists. The PC_{C2} is

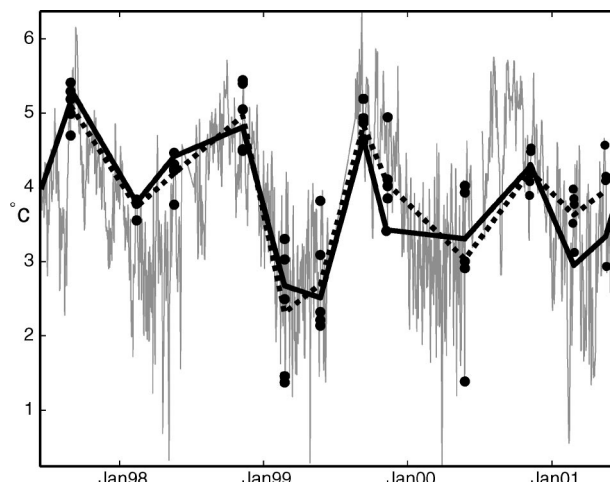


FIG. 8. A comparison of the spatially averaged measured and the reconstructed temperature fields. The full line shows measured values, and the dashed line shows 5-day averaged reconstructed values from 2 days prior to a CTD measurement, to 2 days after. The filled circles indicate these 5 days for each point, and the thin spiky line shows the daily resolution reconstructed values.

therefore used as a proxy amplitude for PC_{T1} and PC_{S1} , in order to get TS' field with a daily resolution:

$$T'(y, z, t) = \beta_T [PC_{C2}(t)] w_{T1} [T1(y, z)], \quad (5)$$

$$S'(y, z, t) = \beta_S [PC_{C2}(t)] w_{S1} [S1(y, z)], \quad (6)$$

where $T1$, $S1$ are the pycnocline modes, $w_{T1, S1}$ are the respective singular values, and $\beta_{T, S}$ are the scaling coefficients.

Putting (5) and (6) back into (1) and recollecting the other terms gives the total reconstructed fields $T_{rec}(y, z, t)$ and $S_{rec}(y, z, t)$. The reconstructed temperature, averaged spatially over the section, is shown in Fig. 8, where it is compared to the measured average temperature. The spatially averaged fields compare remarkably well, with a correlation coefficient $R^2 = 0.90$ with 12 data points, which is highly significant.

These reconstructed fields account for 60% (T) and 44% (S) of the total variance in the measured fields. This is roughly what should be expected considering the variance explained by the seasonal signal, the amount of variance explained by the pycnocline modes and the correlation between the hydrographic and the current PCs.

6. Discussion

The relationships (5) and (6) are based on a statistical analysis, and the modes found are statistical (empirical). The large correlation coefficients, cited above, indicate that they are real and so does the fact that EOF analysis applied to the individual years of velocity data show results very similar to the full 4-yr analysis. The credibility of these relationships will, however, be much strengthened if they can be explained from basic physical principles or observations.

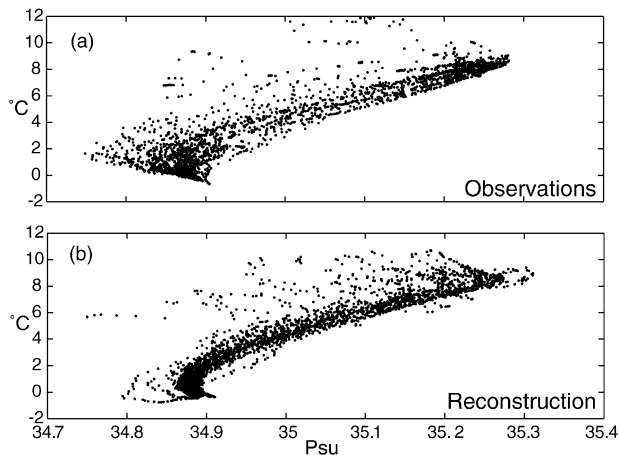


FIG. 9. Temperature–salinity diagrams for (a) 11 measured sections and (b) for the 11 concurrent reconstructed sections. There is one TS value for each vertical 10 m.

a. Temperature–salinity relationship

One such observational fact is the relationship between temperature and salinity on the section. Since there are more than two water masses involved, this is not a one-to-one relationship, but the observations still follow a consistent pattern in a TS plot (Fig. 9a). This pattern is to a large extent maintained in the reconstructed fields based on (1), (5), and (6). It has already been noted that the principal components for temperature and salt, used in (5) and (6) are highly correlated and Fig. 9b demonstrates that this relationship is fairly consistent with the observations (Fig. 9a). The main discrepancy is seen around temperature of 2°C where the observations have a large spread in salinity. This is due to variable influence of low-salinity waters from the East Icelandic Current (Hansen and Østerhus 2000) and the reconstructed fields cannot reflect this variability completely.

b. Geostrophy

The most essential question is, however, whether the relationships between the hydrographic fields and velocity, (5) and (6), have a physical explanation. As noted in the introduction, the motivation for this study was the hope that geostrophy could provide a link between hydrography and velocity. In our context, geostrophy can be expressed by the thermal wind equation

$$\frac{\partial u}{\partial z} = \frac{g}{\rho_0 f} \frac{\partial \rho}{\partial y}, \tag{7}$$

where u is eastward velocity, g is the acceleration of gravity, ρ_0 is a reference density, and ρ is the spatially dependent density.

To check on equation (7), the vertical gradient of the fluctuation mode dC_2/dz (Fig. 10a), is compared to the horizontal gradient of a density field, $d\rho/dy$ (Fig. 10b), which has been calculated from the reconstructed fields in (1), (5), and (6). The main pattern in these two figures is the same, with positive values in the deeper farther offshore regions and negative values in the shallower regions closer to the shelf. The magnitudes in these fields are also comparable with values ranging from $-4 \times 10^{-4} \text{ s}^{-1}$ to $+4 \times 10^{-4} \text{ s}^{-1}$. We therefore may conclude that the pycnocline mode is physically coupled to the velocity fluctuation mode through geostrophic balance.

Deseasoning removed 9% of the total velocity variance, and the fluctuation mode explained 23% (1997–2000 period) to 28% (2000–01 period) of the remaining variance. Thus, about one quarter of the velocity variance has been linked to hydrography through the thermal wind equation. This should not be taken to imply that most of the flow is nongeostrophic. In addition to these variations, the total flow includes the average field, which is in approximate geostrophic balance with the average density field (HOHKL) and the seasonal field. The velocity variations also include a significant bar-

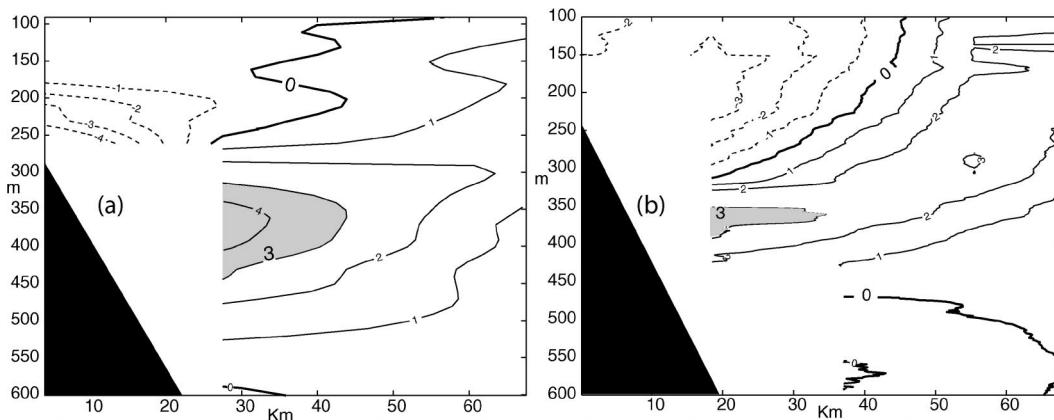


FIG. 10. The thermal wind balance: (a) the left-hand side of Eq. (7) (vertical gradient of the fluctuation mode, dC_2/dz) in units of 10^{-4} s^{-1} ; (b) the right-hand side of Eq. (7) in the same units. The dashed lines represent negative values, and the thick line is the zero line. The area exceeding $3 \times 10^{-4} \text{ s}^{-1}$ is shown in gray.

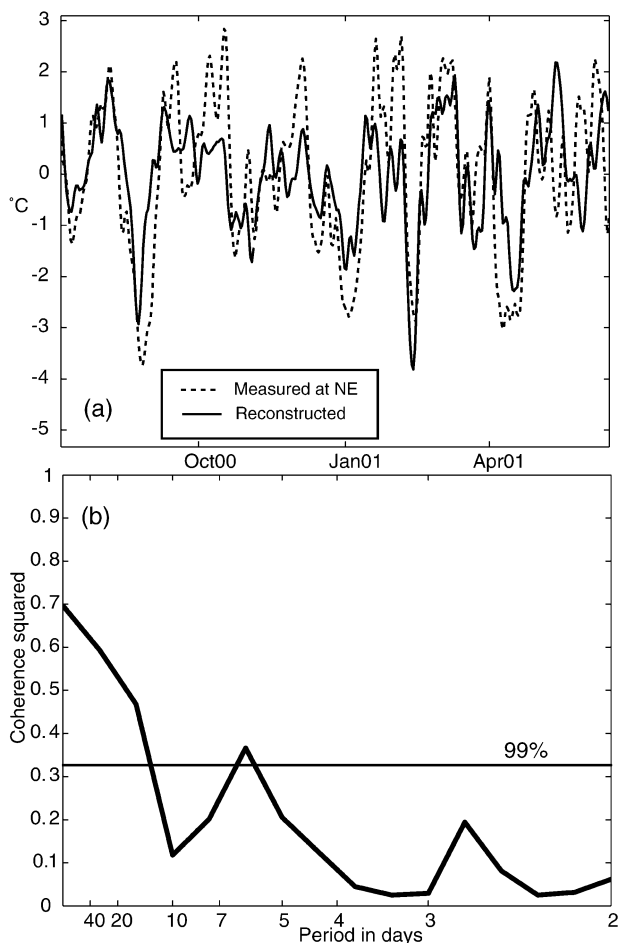


FIG. 11. A comparison between the measured temperature at NE summer 2000 to summer 2001 and the reconstructed temperature at the approximate same location: (a) the 3-day low-passed time series and (b) the coherence squared between these and the significance line on a 99% level is shown.

otropic component, which is not linked to the hydrographic fields.

c. The temperature at ADCP instrument NE as a validation

The ADCP at NE was deployed on the bottom at a depth where the pycnocline (thermocline) typically intersects the shelf (Fig. 2). This is on the intersection between the warmer upper layers and the colder lower layers. A rise in the pycnocline will therefore bring cold water over the built-in temperature sensor and vice versa for a fall in the pycnocline. Since the fields, calculated by (1), (5) and (6), very much depend on the position of the pycnocline, this temperature time series is well suited to validate the recreated hydrography. To test this, the reconstructed temperature time series at 430-m depth at N04, which should lie approximately on the same isotherm as found at NE (see Fig. 2), is compared to

the temperature measured at NE (Fig. 11a). To emphasize the short time variations, only deseasoned anomalies are shown and the figure verifies the correlation that is indicated in Fig. 8, but now with daily values instead of 3–4 data points per year. The correlation coefficient is $R^2 = 0.60$ with 343 data points, which is significant on a 99% level, and the coherence is significant on a 99% level for periods over 15 days and marginally significant for periods in the interval 5–7 days (Fig. 11b).

Thus, the fluctuation mode is clearly connected to the location of the pycnocline (thermocline) and we conclude that the very tight relationship indicated by Fig. 8 was not a statistical fluke.

7. Conclusions

An EOF analysis has been applied to ADCP and CTD data measured in the Faroe Current. The first EOF modes in the temperature ($T1$) and the salinity ($S1$), which account for 49% and 36% of the variance in the deseasoned fields, respectively, are found to correlate significantly ($R^2 = 0.76$) to the second EOF mode in the velocity ($C2$), which accounts for a quarter of the variance in the velocity field. This connection is used to reconstruct hydrographical TS fields with the same temporal data coverage as the ADCP data. The TS fields show reasonable TS diagrams. The physical link between the hydrographical modes $T1$ and $S1$, and the velocity mode is found to be through the thermal wind relation. The reconstructed TS fields account for 60% (T) and 44% (S) of the total variance in the respective fields. The high correlation between hydrographic and velocity fields found by comparing CTD and ADCP modes was verified by continuous temperature measurements from an ADCP located close to the average thermocline. This method should be tested in other places where similar data are available.

Acknowledgments. This work has been conducted within the West Nordic Ocean Climate Research Program, funded by the Nordic Council of ministers. The measuring program was supported by the Nordic WOCE project that was funded by the Nordic Environmental Research Program for 1993–97, by Nordic national research councils, and by the VEINS project (MAST IV) and the MAIA project (Framework V).

REFERENCES

- Emery, W. J., and R. E. Thomson, 1997: *Data Analysis Methods in Physical Oceanography*. Pergamon Press, 634 pp.
- Hansen, B., and S. Østerhus, 2000: North Atlantic–Nordic Sea exchanges. *Progress in Oceanography*, Vol. 45, Pergamon, 109–208.
- , —, H. Hátún, R. Kristiansen, and K. M. H. Larsen, 2003: The Iceland–Faroe inflow of Atlantic water to the Nordic Seas. *Progress in Oceanography*, in press.
- Preisendorfer, R., 1988: *Principal Component Analysis in Meteorology and Oceanography*. Elsevier Science, 425 pp.

PAPER II



The Iceland–Faroe inflow of Atlantic water to the Nordic Seas

B. Hansen ^{a,*}, S. Østerhus ^b, H. Hátún ^a, R. Kristiansen ^a, K.M.H. Larsen ^a

^a *Faroese Fisheries Laboratory, Box 3051, FO-110 Tórshavn, Faroe Islands*

^b *Bjerknes Centre for Climate Research and Geophysical Institute, Allegaten 70, N-5007 Bergen, Norway*

Received 7 April 2003; revised 24 September 2003; accepted 29 October 2003

Abstract

The flow of Atlantic water between Iceland and the Faroe Islands is one of three current branches flowing from the Atlantic Ocean into the Nordic Seas across the Greenland–Scotland Ridge. By the heat that it carries along, it keeps the subarctic regions abnormally warm and by its import of salt, it helps maintain a high salinity and hence density in the surface waters as a precondition for thermohaline ventilation. From 1997 to 2001, a number of ADCPs have been moored on a section going north from the Faroes, crossing the inflow. Combining these measurements with decade-long CTD observations from research vessel cruises along this section, we compute the fluxes of water (volume), heat, and salt. For the period June 1997–June 2001, we found the average volume flux of Atlantic water to be 3.5 ± 0.5 Sv ($1 \text{ Sv} = 10^6 \text{ m}^3 \cdot \text{s}^{-1}$). When compared to recent estimates of the other branches, this implies that the Iceland–Faroe inflow is the strongest branch in terms of volume flux, transporting 47% of the total Atlantic inflow to the Arctic Mediterranean (Nordic Seas and Arctic Ocean with shelf areas). If all of the Atlantic inflow were assumed to be cooled to 0°C , before returning to the Atlantic, the Iceland–Faroe inflow carries a heat flux of 124 ± 15 TW ($1 \text{ TW} = 10^{12} \text{ W}$), which is about the same as the heat carried by the inflow through the Faroe–Shetland Channel. The Iceland–Faroe Atlantic water volume flux was found to have a negligible seasonal variation and to be remarkably stable with no reversals, even on daily time scales. Out of a total of 1348 daily flux estimates, not one was directed westwards towards the Atlantic.

© 2003 Elsevier Ltd. All rights reserved.

Contents

1. Introduction	444
2. Data material	446
2.1. CTD observations	447
2.2. ADCP observations	447

* Corresponding author. Tel.: +298-353900; fax: +298-353901.
E-mail address: bogihan@frs.fo (B. Hansen).

3.	Hydrographic and velocity fields on section N	449
3.1.	Hydrographic fields	449
3.2.	Velocity fields	450
3.3.	Vertical velocity correlations	454
3.4.	Geostrophy	455
3.5.	Horizontal velocity correlations	458
4.	Total volume flux	458
4.1.	Total volume flux during the 2000–2001 period	458
4.2.	Total volume flux during the 1997–2000 period	461
5.	Flux of Atlantic water	463
5.1.	Generating daily fields for in situ temperature and salinity on section N	463
5.2.	Source water characteristics	465
5.3.	Average fluxes of Atlantic water, heat, and salt	467
5.4.	Flux variations	468
6.	Conclusions and outlook	471

1. Introduction

The flow of warm, saline water from the Atlantic Ocean across the Greenland–Scotland Ridge into the Nordic Seas and the Arctic Ocean (hereafter termed “*Atlantic inflow*”) is of major importance, both for the regional climate and for the global thermohaline circulation. Through its heat transport, it keeps large areas north of the Ridge much warmer, than they would otherwise have been, and free of ice. Thus, [Seager et al. \(2002\)](#) have computed a temperature increase due to oceanic heat transport by this flow which over large areas is considerably larger than the anticipated temperature increase during the 21st century due to anthropogenic effects. Significant reductions in the Atlantic inflow could therefore offset or even reverse the projected temperature increase in the areas most affected. At the same time, the Atlantic inflow completes the loop formed by thermohaline ventilation in the northern regions and the deep overflows back into the Atlantic across the Ridge. Thus, the salt, carried by the Atlantic inflow to the Nordic Seas, is a precondition for high densities in the upper layers and thus for the formation of intermediate and deep water. To the extent that thermohaline ventilation contributes to driving the Atlantic inflow, this opens the possibility for a positive feedback mechanism that will de-stabilize the thermohaline circulation ([Broecker, Peteet, & Rind, 1985](#)).

In spite of the obvious importance of the inflow, quantitative estimates of its fluxes of volume (mass), heat, and salt have been hard to obtain. Until recently, one of the most frequent sources for these numbers has remained that of [Worthington \(1970\)](#), even though he based his estimates on a few, fairly uncertain, current measurements and budgets that involved exchanges of heat and freshwater with input parameters that even today are not well known ([Simonsen & Haugan, 1996](#)). Worthington’s estimate has also been questioned by later budget studies ([McCartney & Talley, 1984](#)), and quantitative estimates of the fluxes, based on measurements, are needed to settle the uncertainties. This was a main motivation for the “Nordic WOCE” project, within which the observations reported in this paper were initiated.

The flow of Atlantic water into the Nordic Seas occurs through three main branches ([Hansen & Østerhus, 2000](#)) as shown in [Fig. 1](#). Long-term measurements indicate that the branch west of Iceland transports slightly less than 1 Sv ($10^6 \text{ m}^3 \cdot \text{s}^{-1}$) of Atlantic water ([Jónsson & Briem, 2003](#)) and therefore on the order of 10% of the total inflow. Of the other two branches, the flow through the Faroe–Shetland Channel is

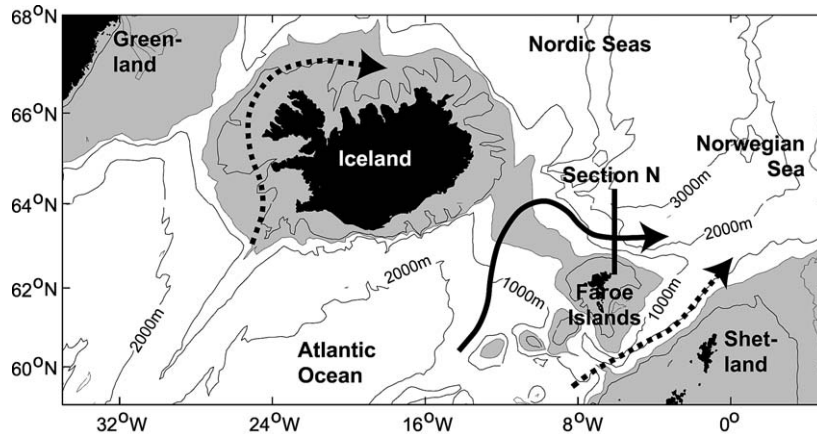


Fig. 1. The Greenland–Scotland Ridge (the shaded area on the figure indicates regions shallower than 500 m) separates the Atlantic Ocean from the Nordic Seas. Arrows indicate the three branches of Atlantic inflow to the Nordic Seas. The Faroe Current (unbroken arrow) is the branch studied in this work. The thick line termed “N” indicates the section from which most of the observations derive.

generally cited (explicitly or implicitly) as by far the dominant one, but there has been little evidence to support that view (Hansen, 1985).

The observations, initiated in the Nordic WOCE project (Østerhus, Turrell, Hansen, Lundberg, & Buch, 2001), were therefore designed to measure fluxes through both of the gaps between Iceland and Scotland (Fig. 1). In these gaps, hydrographic (temperature and salinity) observations have been carried out on standard sections for almost a century in the Faroe–Shetland Channel and for more than a decade in the Iceland–Faroes Gap. To provide flux estimates, the Nordic WOCE project established a series of quasi-permanent mooring sites to measure currents directly. The waters surrounding the Faroes are heavily fished, and experience has taught, that traditional moorings extending far up into the water column have short survival. In the planning phase of the project, it was therefore decided to rely on the newly developed Broadband acoustic Doppler current profiler (ADCP) produced by RD Instruments. After termination of the field phase of Nordic WOCE, the measurements have continued with EU support through the two projects VEINS (Variability of Exchanges in the Northern Seas) and MAIA (Monitoring the Atlantic Inflow toward the Arctic) and from the Faroese Fisheries Laboratory (FFL). Measurements are planned to continue with support from the FP5-funded project MOEN (Meridional Overturning Exchange with the Nordic Seas) that is a component of ASOF (Arctic Subarctic Ocean Flux) study.

Here, we report on the measurements in the Iceland–Faroes Gap where the Atlantic water generally is confined to a region north of the Faroes by the Iceland–Faroes Front (Fig. 2). The measurements have mainly been carried out along a standard section (section N) crossing the Atlantic inflow branch (Fig. 2). Regular CTD surveys were initiated along this section in 1987 and, in most years since then, at least four cruises have been made. The ADCP moorings have been deployed along the same section.

The combined CTD and ADCP data sets contain information on various oceanographical processes, including the considerable mesoscale activity which occurs in this area, but that will be treated elsewhere. In this work, we focus on the fluxes of water (mass, volume), heat, and salt through the section. Preliminary estimates of typical fluxes and their seasonal variations have previously been reported in the “grey literature”, based on subsets of the data and less rigorous treatment (Hansen, Larsen, Østerhus, Turrell, & Jónsson, 1999; Hansen, Østerhus, Kristiansen, & Larsen, 1999; Hansen, Jónsson, Turrell, & Østerhus, 2000). These preliminary results have also been reported in two overview papers discussing the exchanges across the Greenland–Scotland Ridge (Hansen & Østerhus, 2000; Østerhus et al., 2001). The objectives of this paper are threefold: (1) to document the measurements in a form more generally available to the

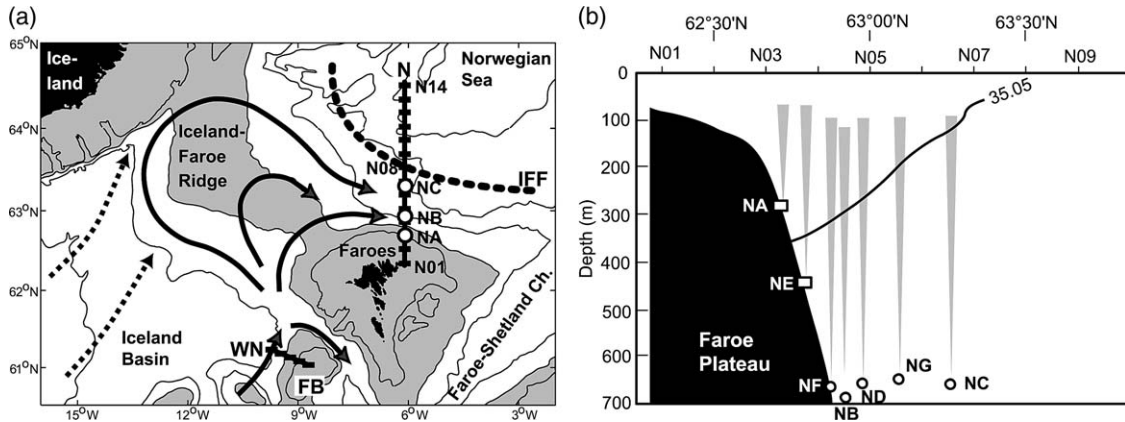


Fig. 2. Most of the observations reported in this work were collected along section N, indicated on the map (a) and shown in (b). CTD observations from five standard stations on section WN northwest from Faroe Bank (FB on a) were also used for reference. On (a), CTD standard stations are indicated by black rectangles, labeled N01–N14. Three of the ADCP mooring sites are indicated by circles labeled NA, NB, and NC. Shaded areas are shallower than 500 m. The dotted curve indicates the general location of the Iceland–Faroes Front (IFF), and arrows indicate Atlantic water pathways towards section N according to the classical view (unbroken arrows) and to alternative suggestions (broken arrows). On (b), the innermost CTD standard stations on section N are indicated as well as all the ADCP mooring sites. Rectangles indicate ADCPs in trawl-protected frames, circles indicate ADCPs in the top of moorings. Approximate ADCP ranges are indicated by gray cones. An average 35.05 isohaline (copied from Fig. 6a) indicates the typical boundary of Atlantic water on the section.

scientific community. (2) To derive flux estimates of as high an accuracy as reasonably possible and evaluate uncertainties. (3) To evaluate variations of fluxes on time scales from a few days, through the seasonal, to the interannual.

Achieving objectives (2) and (3), requires interpolation and extrapolation of data in order to cover the whole section adequately. In addition, the Atlantic water component of the flux has to be extracted. Section N covers all the Atlantic water that has passed the Iceland–Faroe Ridge, but it also includes water that does not derive directly from the Atlantic. This is water from the East Icelandic Current and other water masses. These water masses cover variable parts of the section and, to some extent, they have already been mixed with one another before passing through the section. We use temperature and salinity characteristics to identify the Atlantic component, but to evaluate the Atlantic water flux, requires the combination of hydrographic and velocity fields, which are sampled with quite different temporal and spatial resolutions. This is a non-trivial problem, and we therefore go into considerable detail with the data processing and methods for flux calculation. This forms the main part of the paper, from Sections 2 to 5 with the main results presented in Sections 5.3 and 5.4. We end the paper with a summary of the conclusions and a discussion on the role of the Iceland–Faroe Atlantic inflow in the climate system under a global change scenario.

2. Data material

Both the hydrographic data and the current measurements were acquired on the same section, standard section N (Fig. 1), extending from 62° 20' N 6° 05' W to 64° 30' N 6° 05' W (Fig. 2). The section has depths reaching more than 3000 m, but we focus on the uppermost 600 m that contain all the Atlantic water that has passed over the Iceland–Faroe Ridge.

2.1. CTD observations

The hydrographic data were acquired during a number of cruises along standard section N in the period 1987–2001. The standard section has 14 standard stations, labeled N01–N14, with 10 nautical miles equidistant spacing between stations. Lack of time or bad weather restricted the northward extension of the section on some occasions, and a few intermediate stations have been deleted in the quality assessment procedure. Here, we only include cruises with good data from at least all the innermost 10 stations, which reduces the data set to 45 cruises. Several different CTDs of type Neil Brown, EG&G, and SeaBird have been used through the period. Since 1990, salinity samples have been obtained on each station and analyzed with an Autosol salinometer for calibration. The early CTD observations were less frequently calibrated, but the slow changes in the deep water salinities allow adjustments that keep the salinity uncertainties below 0.01. In this work, we use temperature and salinity observations averaged over 10 m depth intervals in 60 layers (bins), the uppermost one centered at 5 m depth and the deepest at 595 m.

To serve as reference for the source water characteristics of Atlantic water, we also use CTD observations from five standard stations on section WN that extends northwestwards from the Faroe Bank (Fig. 2a). These observations were treated similarly as described above.

2.2. ADCP observations

In the period October 1994–June 2001, current measurements were obtained through a number of deployments at seven different mooring sites, labeled NA, NB, ... NG, along the standard section (Fig. 2b). During most of the period, instruments were deployed at the three Nordic WOCE standard mooring sites, NA, NB, and NC. From July 2000 to June 2001, the mooring at site NC was moved to site NG and two additional moorings (NE and NF) were deployed between NA and NB. At site ND, a mooring was deployed from November 1997 to June 1998. The data coverage at each of these sites is illustrated in Fig. 3, which also shows CTD cruises with full coverage of the innermost 10 stations in the same period. In the 4-year period from summer 1997 to summer 2001, there was sufficient coverage to allow volume flux estimates but, since the mooring locations changed, we split the analysis into two main periods. The first period is from summer 1997 to summer 2000 with moorings at NA, NB, and NC. The second period is from summer 2000 to summer 2001 with moorings at NA, NE, NF, NB, and NG. Table 1 summarizes details of the deployments within these two periods.

All the deployments have used upward-looking RDI ADCPs to profile the water column (Fig. 2b). At sites NA and NE, a 150 kHz RDI Broadband ADCP was placed on the bottom within a specially constructed

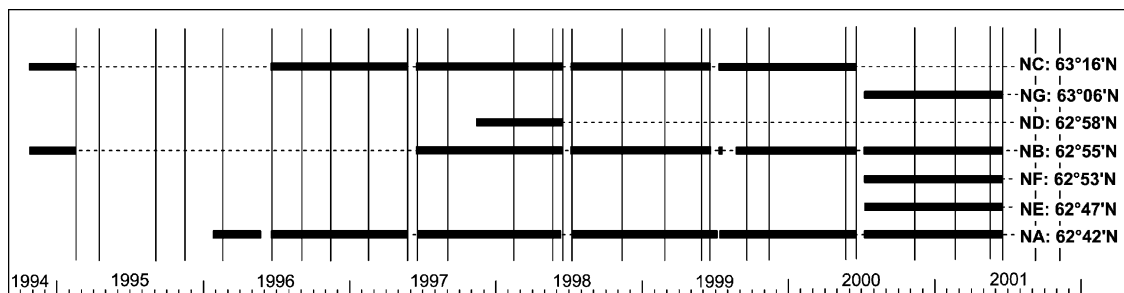


Fig. 3. Periods with successful ADCP observations at the various mooring sites (thick horizontal bars) and CTD cruises along standard section N (thin vertical lines) from October 1994 to the summer of 2001.

Table 1

Details of ADCP deployments along standard section N in the period June 1997 to June 2001. The observational period and number of days indicate whole days. The last two columns indicate the vertical extent of data for which the series of daily averaged velocities were without gaps before extrapolation and “Top” indicates the upper boundary of this range

Record	Mooring position		Depth to			Observational period yy/mm/dd–yy/mm/dd	Days	100% good	
	Latitude	Longitude	Bottom (m)	Instr (m)	Bin length (m)			Bins	Top (m)
NA9706	62° 42.315' N	6° 05.170' W	300	299	10	97/06/15–98/06/08	359	1–19	103
NA9807	62° 42.178' N	6° 05.043' W	297	296	10	98/07/08–99/07/01	360	1–18	110
NA9907	62° 41.947' N	6° 03.887' W	295	294	10	99/07/03–00/06/15	349	1–17	118
NA0007	62° 42.048' N	6° 04.456' W	297	296	10	00/07/08–01/06/15	343	1–18	110
NE0007	62° 47.490' N	6° 05.100' W	456	455	25	00/07/07–01/06/15	344	1–11	147
NF0007	62° 52.700' N	6° 05.031' W	697	689	25	00/07/08–01/06/15	343	1–19	203
NB9706	62° 54.818' N	6° 04.957' W	925	659	25	97/06/14–98/06/12	365	1–18	198
NB9807	62° 55.158' N	6° 04.844' W	961	708	25	98/07/05–99/06/18	349	1–20	197
NB9908	62° 55.133' N	6° 05.052' W	957	715	25	99/08/21–00/06/15	300	1–19	229
NB0007	62° 55.106' N	6° 05.024' W	954	712	25	00/07/08–01/06/15	343	1–19	226
ND9711	62° 57.540' N	6° 05.600' W	1276	670	25	97/11/12–98/06/12	214	1–17	234
NG0007	63° 05.955' N	6° 05.015' W	1816	643	25	00/07/08–01/06/15	343	1–19	157
NC9706	63° 16.425' N	6° 06.600' W	1731	659	25	97/06/14–98/06/12	364	1–18	198
NC9807	63° 15.944' N	6° 06.299' W	1728	655	25	98/07/06–99/06/18	348	1–18	194
NC9907	63° 15.920' N	6° 06.390' W	1740	667	25	99/07/03–00/06/15	349	1–19	181

trawl-proof protection frame (Østerhus & Hansen, 1995), with later modifications. At the other sites, 75 kHz RDI Broadband ADCPs were moored in the top of single point moorings (with the ADCP typically at depths of 600–700 m). At the deep sites, acoustic echo from the surface could be used for most of the records to infer the depth of the instrument. These observations show that drag-down of the instrument rarely exceeded 5 m and could be ignored. Sound velocity variation along the beam path was also found to be sufficiently small to be ignored.

In the early versions of the trawl-protection frame used at NA from summer 1997 to summer 1998, the steel construction affected the ADCP compass considerably. This was circumvented by two short-term calibration deployments with a traditional (Aanderaa) current meter mooring at NA while the ADCP was operating (Larsen, Hansen, Kristiansen, & Østerhus, 1999). The consistency in direction of the long-term residual flow from different deployments indicates that this procedure gave correct current direction to within a few degrees. Since summer 1998, non-magnetic aluminium frames have been used to protect the ADCPs at NA and NE. During one of the deployments at NB, one of the four ADCP sound transducers was malfunctioning. This record was therefore analyzed with only three beams, but simulations on other records at NB indicate that this has no significant effects for the averaged types of data used in this work.

The deployments at site NA were set up with a 10 m bin length (vertical averaging layer) while the other deployments had 25 m bins. Sound speed variations are sufficiently small so that the bin lengths do not need adjustment. To ensure long-term records, only one ping was used in each ensemble. This produced fairly noisy records and many observations had to be deleted during the data editing process. This process included an automatic flagging procedure, which detects outliers and large error velocities (Gordon, 1996). In addition, all observations were visually scanned in a graphical editing package, specially developed using MATLAB routines.

The resulting data sets contain a number of gaps, especially for the near-surface bins, most distant from the ADCP. In this work, high frequency variations are irrelevant and we use only daily averaged current

values, but the large number of gaps in the data makes filtering difficult. Therefore, the current velocity components were de-tided before averaging. Harmonic constants were computed from the velocity data for each bin. Using these constants, the tidal signal was “predicted” for the observational period and subtracted from the original series. The Foreman FORTRAN package (Foreman, 1978) was used for both the analysis of harmonic constants and prediction. The general consistency in harmonic constants obtained from different deployments at the same site (Larsen, Hansen, Kristiansen, & Østerhus, 2000) verifies the applicability of this procedure. For each day, the de-tided velocity series were then averaged over a period as close as possible to 24 h and 50 min. Average velocity values for a bin were accepted for all days with at least 25% good coverage.

With this procedure, daily averaged current velocity components were produced for all deployments and for the deepest bins data coverage is 100% (Table 1). In the uppermost bins, the error frequency is much larger, partly due to surface reflection of side-lobes (Gordon, 1996) and partly due to range limitation. Typically, the series do, however, have more than 75% coverage up to at least the 100 m depth level.

Detailed information on moorings and data from the ADCP deployments is available in three data reports (Hansen, Larsen, & Kristiansen, 1999; Larsen, Hansen, & Kristiansen, 2000, 2001).

3. Hydrographic and velocity fields on section N

3.1. Hydrographic fields

Average sections of temperature, salinity, and density are shown in Fig. 4. Northwards from the Faroe shelf, a warm, saline area on the section identifies the wedge of Atlantic water. Its boundary towards the colder, less saline waters reaches the bottom of the Faroe Plateau at depths of 300–500 m and slopes upwards to reach the surface in the Iceland–Faroe Front between standard stations N05 and N09.

When single cruises are considered, they often look like the average distributions in Fig. 4, although usually with sharper boundaries. Meso-scale activity may deform the distribution and more irregular sections are seen occasionally (Fig. 5). When we include only cruises in the period from July 1997 to June 2001 with complete current measurements, the irregular features are smoothed out, as illustrated by the average salinity section from this period (Fig. 6a). This section looks very similar to the long-term average (Fig. 4b), although somewhat more saline. The temperature–salinity relationship on the section is illustrated in Fig. 6b, where the main water masses as described by Read and Pollard (1992) and Hansen and Østerhus (2000) are indicated.

To study the seasonal variation, the temperature and salinity fields were linearly detrended and fitted to a sinusoidal function with amplitudes and phases that were determined by a least-square algorithm for each point on the section separately. The seasonal temperature amplitude (Fig. 7a) is largest in the surface, as could be expected, but a secondary maximum is also seen at larger depths between stations N04 and N07. It seems to follow the thermocline (Fig. 4a), becoming shallower towards the north, until it surfaces in the frontal region. In the Atlantic water, above the thermocline, maximum temperatures are consistently found around August–October. The seasonal amplitude of the salinity variation (Fig. 7b) has a similar distribution as the temperature amplitude with maxima in two regions. In the surface layer, the salinity has a maximum around April–May, but the deeper amplitude maximum, close to the thermocline, culminates around August–October, as for temperature. We conclude that the areal extent of Atlantic water on the section has a seasonal variation with a maximum in autumn.

In addition to the CTD observations, some information about water mass properties can be obtained from the temperature sensors in the ADCP instruments. Mostly, the instruments were located more or less constantly either in Atlantic (at site NA) or in cold water (most of the other sites) and have therefore not been very useful for indicating changes in water mass distribution. From summer 2000 to summer 2001,

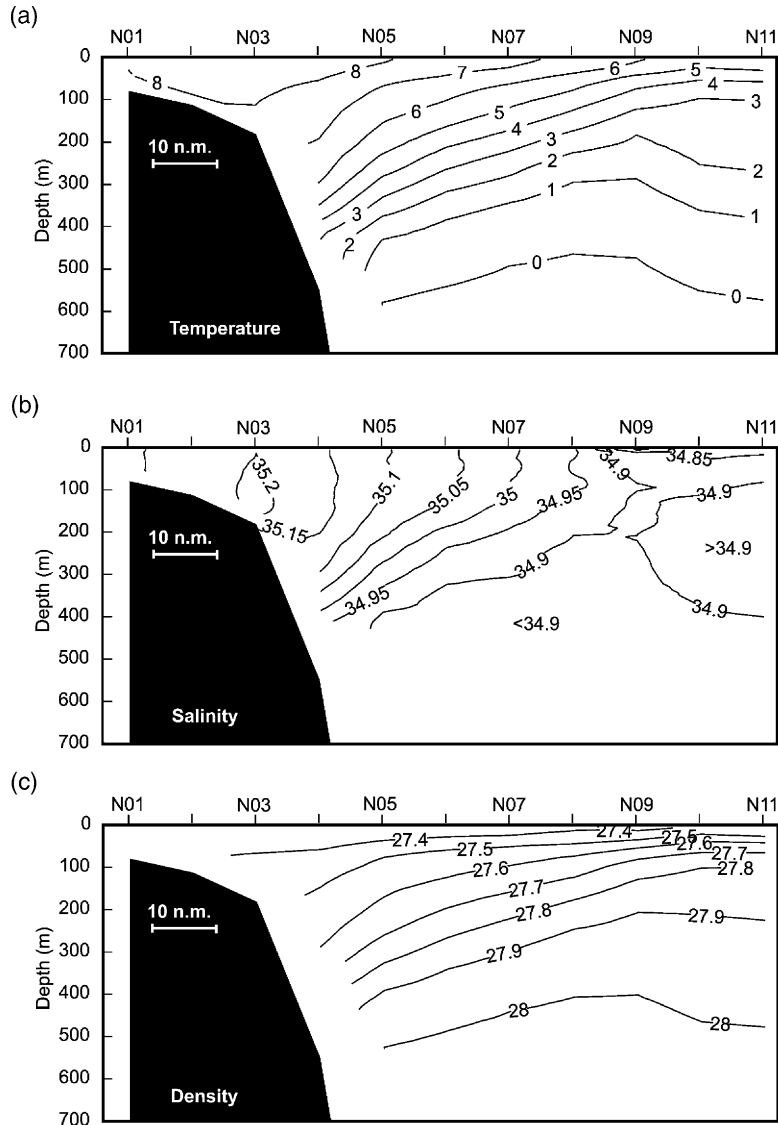


Fig. 4. Average distributions of temperature in °C (a), salinity (b), and density γ_θ in $\text{kg}\cdot\text{m}^{-3}$ (c) on the inner part of section N based on CTD observations by R/V Magnus Heinason in the period 1987–2001 (45 cruises for stations N01–N10, 44 cruises for station N11).

the ADCP at site NE was, however, located close to the typical boundary between the Atlantic and the cold waters. This is seen in Fig. 8, which shows the temperature at this site and at sites NA and NF for the same period. All these series show the temperature close to the bottom and demonstrate that the boundary moves on a wide range of time scales.

3.2. Velocity fields

The general flow through section N is illustrated by progressive vector diagrams (PVDs) in Fig. 9 with observations from one deployment at each of the sites except ND (which did not have as long a deployment

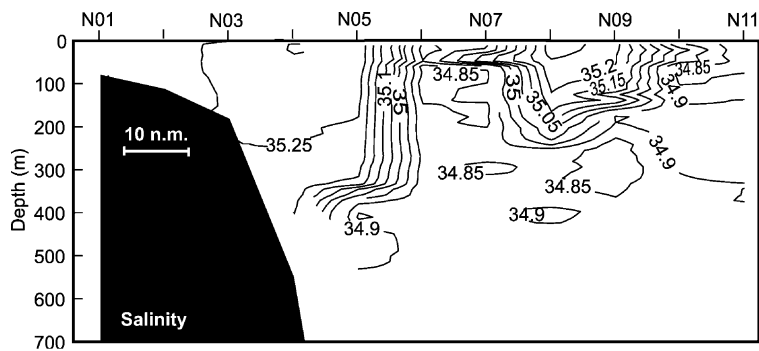


Fig. 5. Salinity distribution on standard section N, 12 June 1998.

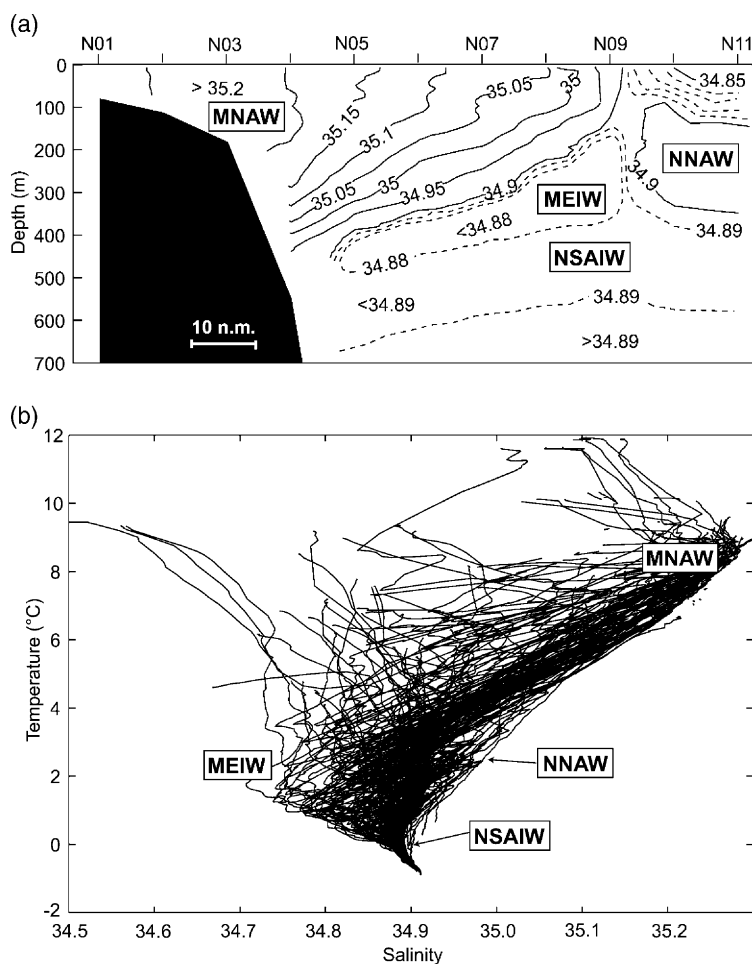


Fig. 6. Average salinity distribution (a) and TS diagram (b) for the main observational period (1997–2001). On (a), contouring interval for salinity is 0.05, except for salinities below 34.90, where broken lines indicate isohalines with contouring interval of 0.01. The main water masses are indicated.

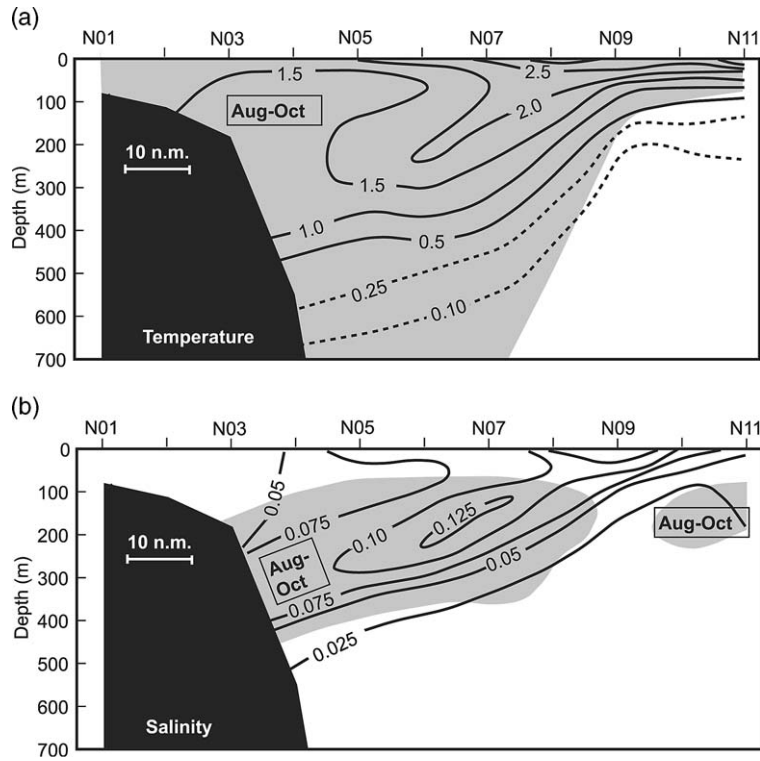


Fig. 7. Seasonal variation of temperature (a) and salinity (b) on the section. Isolines indicate magnitude of the seasonal amplitude in °C and practical salinity units, respectively. Shaded areas indicate parts of the section where maximum temperature or salinity occur in the period August–October.

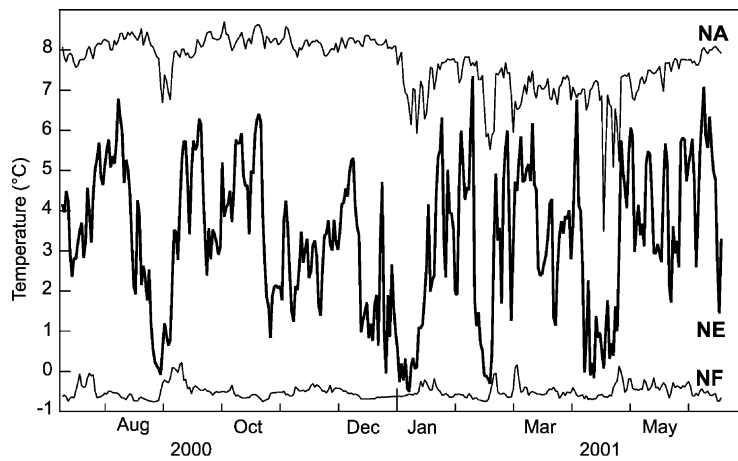


Fig. 8. Daily averaged temperature at the ADCP instruments deployed at NA, NE (thick curve), and NF from July 2000 to June 2001.

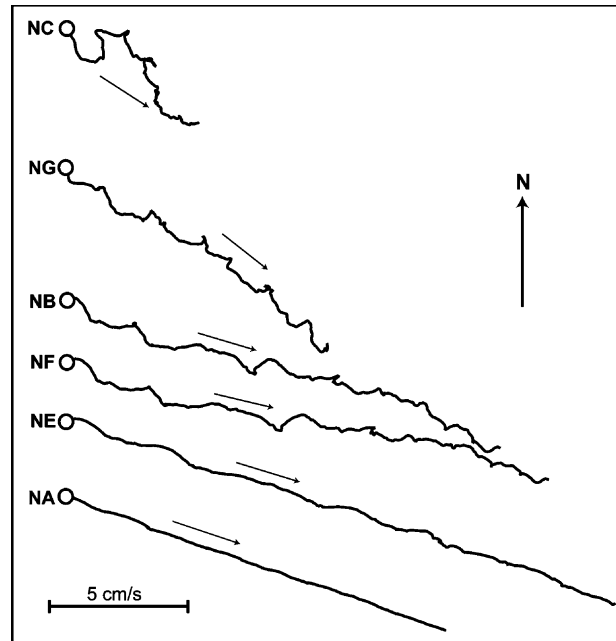


Fig. 9. PVDs for 343 days from daily averaged current at about 225 m depth for all sites with sufficient duration. At NC, a deployment from summer 1999 to summer 2000 is shown. For the other sites, the deployment was from summer 2000 to summer 2001. As all the traces have the same duration, they indicate residual flow velocity and the velocity scale is shown.

period). All the records are from about 225 m depth and they show that the water at this depth has a residual flow somewhat south of east. The PVDs are all for the same duration (343 days) and their lengths therefore indicate current speed in the scale shown.

Fig. 9 indicates that the upper layer flow is to a large extent perpendicular to the section and, since this is the component responsible for the volume flux through the section, we will henceforth focus on the eastward velocity component. The vertical variation of this component (Fig. 10) has a strongly baroclinic character at the deep sites, but usually there is also flow with an eastward component below the sill depth of the Iceland–Faroe Ridge (480 m), so there is a barotropic component, as well. To illustrate the temporal

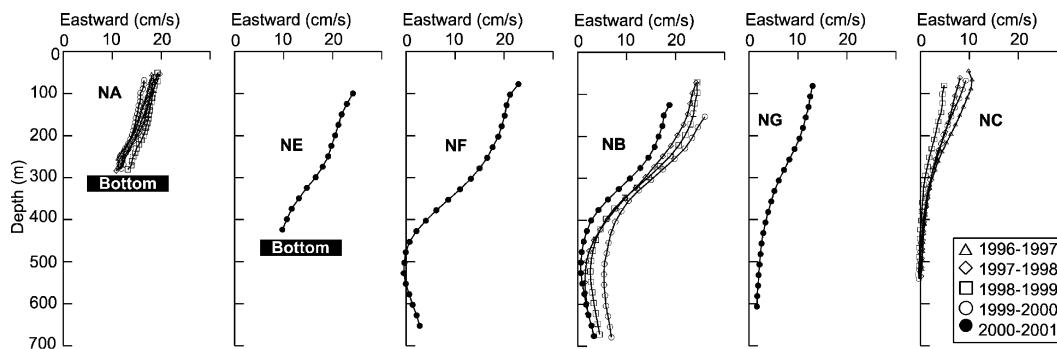


Fig. 10. Average profiles of the eastward velocities for all deployments from 1996 to 2001 with duration more than 9 months.

variability of the flow, Fig. 11 shows the eastward component for the two sites, NA and NB, from which we have continuous time series from summer 1997 to summer 2001 except for the annual servicing periods. The flow is seen to vary on several time scales, but only occasionally is it reversed and then, only for short periods.

The fact that the ADCP measurements do not cover the uppermost 50–100 m of the water column is a major drawback when computing volume fluxes. Including the top layer, requires vertical extrapolation, which we base on observed correlations and on geostrophy. These aspects are therefore discussed in some detail below.

3.3. Vertical velocity correlations

The relationship between velocities at different levels at the same site was investigated by correlating the eastward velocity component for pairs of bins for each deployment. An example is shown in Table 2. The numbers in the upper right triangle of the table show values for the coefficient $\alpha_{k,j}$ that have been determined by least-square fitting to the equation:

$$u_k(t) = \alpha_{k,j} \cdot u_j(t) \quad (1)$$

for each pair of bins (k,j), where $u_k(t)$ is the eastward velocity for bin k at time t , etc. These numbers therefore are coefficients determined by a linear regression analysis with zero offset. The numbers in the lower left triangle of Table 2, similarly, are correlation coefficients between the velocities of the two bins.

The fact that neighbouring bins in Table 2 are well correlated, is no surprise since the instruments have a certain overlap between the bins that causes a fictitious correlation of about 15% between neighbouring bins (Gordon, 1996). The correlations in Table 2 are, however, much higher than this and extend much farther than to neighbouring bins. This implies that the temporal velocity variations have a vertically uniform character and this fact can be used to increase the data coverage of the uppermost bins. For the

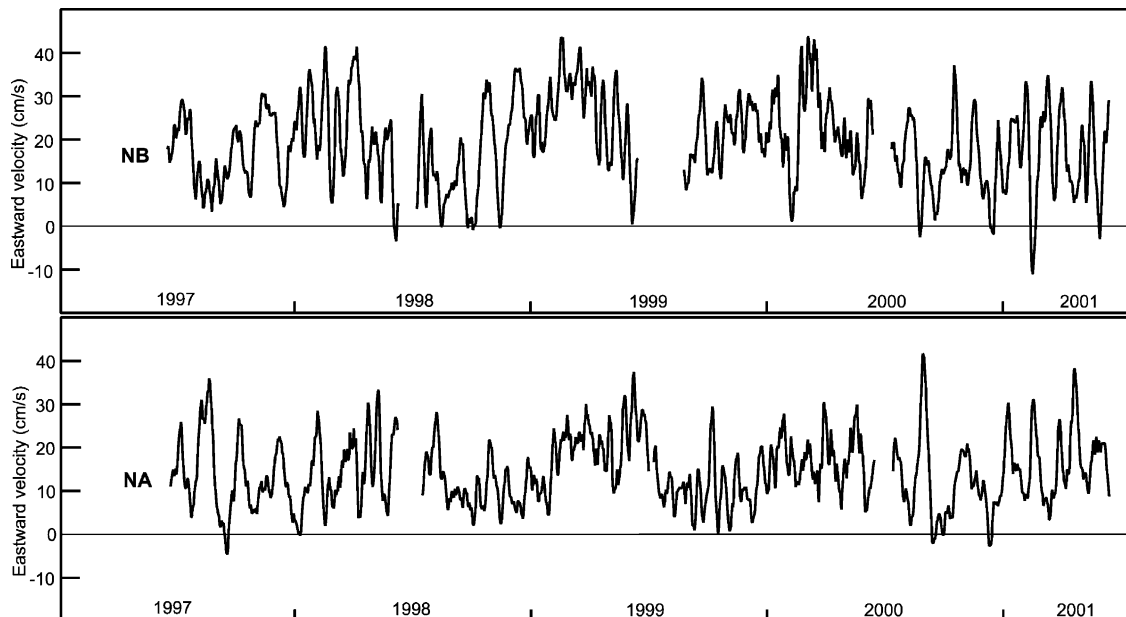


Fig. 11. Seven-day running mean of the eastward velocity component at 225 m depth from mid-June 1997 to mid-June 2001 at sites NA and NB.

Table 2

Relations between eastward velocity in different bins on the deployment at site NE from July 2000 to June 2001. Bin 1 represents the deepest layer, centered at 424 m depth while bin 15 was centered at 74 m. The lower left triangle in the table shows correlation coefficients between velocities of two different bins. The upper right triangle lists the regression coefficient in Eq. (1). From bin 1 to 11, the observations were complete with 344 days of data (Table 1). Above this level (bold types in the table), the data coverage was reduced and for bin 15, only 222 days had usable data

Bin	1	2	3	4	5	6	7	8	10	11	12	13	14	15	
1		1.07	1.10	1.15	1.24	1.33	1.41	1.47	1.51	1.54	1.57	1.61	1.65	1.70	1.77
2	0.94		1.05	1.11	1.20	1.29	1.37	1.43	1.47	1.50	1.53	1.57	1.60	1.64	1.69
3	0.86	0.97		1.07	1.17	1.26	1.34	1.39	1.43	1.47	1.50	1.53	1.57	1.59	1.64
4	0.78	0.90	0.97		1.10	1.18	1.26	1.32	1.36	1.40	1.43	1.45	1.49	1.51	1.55
5	0.71	0.85	0.93	0.98		1.09	1.16	1.22	1.26	1.30	1.33	1.35	1.38	1.41	1.45
6	0.66	0.81	0.89	0.95	0.98		1.08	1.13	1.17	1.21	1.24	1.26	1.29	1.32	1.36
7	0.62	0.77	0.85	0.91	0.96	0.99		1.06	1.10	1.13	1.16	1.19	1.21	1.24	1.28
8	0.58	0.73	0.81	0.87	0.93	0.97	0.99		1.04	1.08	1.11	1.13	1.15	1.18	1.21
9	0.54	0.70	0.78	0.84	0.89	0.95	0.98	0.99		1.04	1.07	1.09	1.11	1.14	1.16
10	0.51	0.66	0.74	0.80	0.86	0.92	0.95	0.98	0.99		1.03	1.06	1.07	1.09	1.11
11	0.48	0.64	0.72	0.77	0.83	0.89	0.93	0.96	0.98	1.00		1.02	1.04	1.05	1.07
12	0.47	0.62	0.70	0.76	0.82	0.88	0.92	0.95	0.97	0.99	1.00		1.02	1.03	1.05
13	0.46	0.60	0.68	0.74	0.80	0.86	0.90	0.94	0.96	0.98	0.99	0.99		1.01	1.03
14	0.45	0.59	0.65	0.70	0.76	0.83	0.88	0.91	0.94	0.96	0.97	0.98	0.99		1.02
15	0.45	0.57	0.62	0.66	0.72	0.79	0.85	0.89	0.92	0.94	0.95	0.96	0.97	0.99	

example in Table 2, the uppermost four bins had gaps in the time series, but using the regression coefficients in the table, the gaps can be filled with confidence as implied by the high correlation coefficients.

Using this procedure, all the deployments in the main observational period (Table 1) could be gap-filled up to depths of around 50 m for deployments at site NA and 70–100 m for the other sites. In the worst case, this involved extrapolating over seven bins. Not all the deployments had as high correlations as the example in Table 2, but the correlation coefficients were at least 0.86 for all the bin pairs used to gap-fill. In most cases, they exceeded 0.9.

After extrapolation, linear interpolation between bins was used to sub-sample the eastward velocity profile at 10 m intervals, centered at 5, 15, ..., 595 m depth, whenever there was valid data. In this way, a homogeneous velocity data set with the same vertical structure as the CTD data was produced.

3.4. Geostrophy

Even after the extrapolations, discussed in the previous paragraph, there is still a surface layer, 50–100 m deep, for which we do not have velocity time series from the ADCP observations. It would, however, seem likely that the uniform character of the velocity variations, seen below this layer (Table 2), also extends into it. Unfortunately, we do not have direct velocity measurements that can be used to verify this and to estimate coefficients like the α_{kj} in Eq. (1). The hydrographic measurements do, however, extend all the way to the surface and we have therefore used the geostrophic approximation to estimate the typical vertical velocity shear in the surface layer.

The validity of the geostrophic approximation on the section as a whole is explored in Fig. 12, which compares average geostrophic velocity profiles between station pairs to average ADCP profiles from deployments between these stations. For the long-term mooring sites (NA, NB, and NC), the ADCP profiles in the figure are averages over several years. At NE, NF, and NG, the average is over about 1 year from summer 2000 to summer 2001, while the profile from ND is based on about half a year of observations. The geostrophic profiles are, on the other hand, based on 17 single CTD cruises between summer 1997

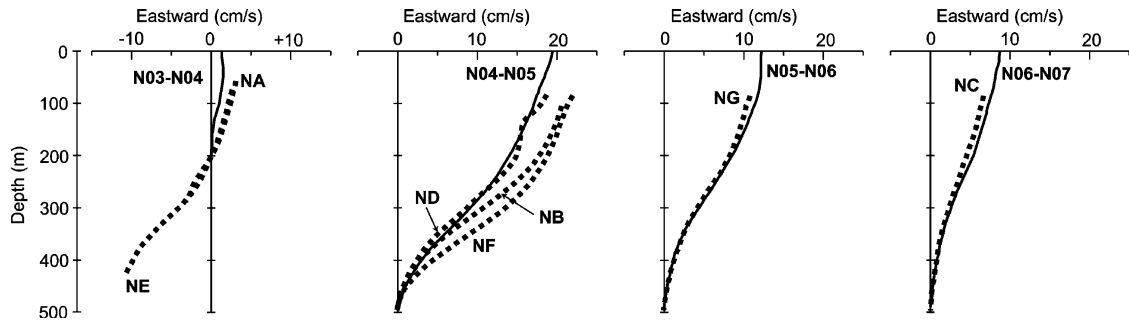


Fig. 12. Averaged eastward velocity profiles determined from geostrophy and from ADCP measurements for the uppermost 500 m. Each of the four diagrams shows the average geostrophic profile between two neighbouring standard stations (continuous curves) and average profiles for ADCPs moored between them (dashed curves). The geostrophic profiles are based on 17 cruises in the 1997–2001 period. For sites NA, NB, and NC, the ADCP profiles are the average of all records in the same period. The ADCP profiles have been offset so that they coincide with the geostrophic profiles at their deepest (reference) level.

and summer 2001. When this is taken into account, the correspondence between ADCP and geostrophic profiles is remarkably good.

The largest discrepancy in Fig. 12 is between station N04 and N05. This is where the current core is usually located and there is a large variation in the current both spatially and temporally which is demonstrated by the difference between the ADCP profiles in the diagram. The variability may explain part of the discrepancy, but hardly all, as indicated by Fig. 13. There, the eastward velocity difference between 200 and 500 m depth for station pair N04–N05 has been computed from 18 separate CTD cruises and compared to the velocity difference found by the ADCP at NB for the same days. There is a certain correspondence and the correlation coefficient is 0.45, which is marginally significant at the 95% level, but on the average, the geostrophic velocity differences were only 70% of the ADCP differences. We also

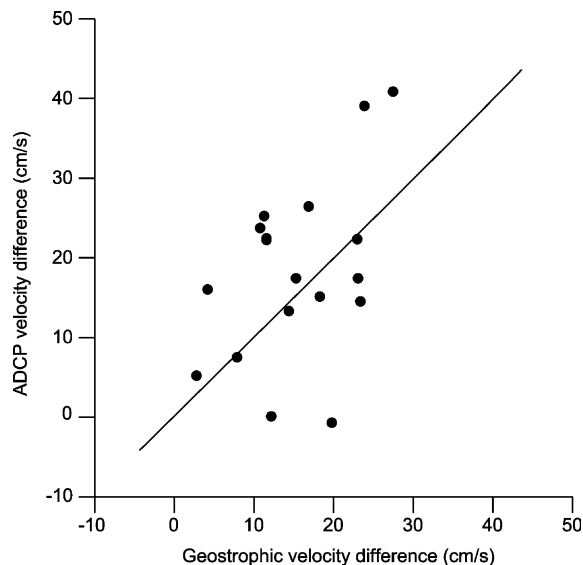


Fig. 13. Eastward velocity difference (shear) between 200 and 500 m depth measured by ADCP (daily average) at site NB compared to geostrophic shear between the same levels calculated from CTD observations at stations N04 and N05 on the same day. The line indicates equality.

tried to compare the geostrophic velocity differences to 3-day ADCP averages centered on the day of the cruise, but this reduced the correlation coefficient considerably.

In the core of the current, geostrophy thus seems to underestimate the vertical current shear somewhat, but as a whole both the sign and overall magnitude of the shear seems fairly well represented by geostrophy. This suggests the possibility of extending the ADCP measurements all the way to the surface by using geostrophy. For sites NA and NE, the geostrophic velocity profile between standard stations N03 and N04 indicates little shear and we therefore extend the ADCP measurements at these sites from the uppermost bins upwards, unchanged. The other ADCP sites have been located between standard stations N04 and N07 and there we have explored the geostrophic velocity variations by testing the two relationships:

$$u_5(t) - u_{55}(t) = \alpha \cdot (u_{105}(t) - u_{405}(t)) \quad u_{55}(t) - u_{105}(t) = \beta \cdot (u_{105}(t) - u_{405}(t)) \quad (2)$$

where $u_5(t)$ is the eastward velocity at 5 m depth, etc. Roughly, the surface layer has been divided into two sub-layers, one from 5 to 55 m depth, and the other from 55 to 105 m depth. The vertical shear within each of these sub-layers is then related to the shear from deep water (405 m depth) to the bottom of the surface layer (105 m depth). If the geostrophic approximation is valid and if the uniform character of velocity variations extends to the surface layer, then Eqs. (2) are valid and we can estimate the coefficients α and β for each station pair.

To test this, we have correlated the geostrophic velocity differences on both sides of each of the two equations in (2), using all CTD cruises with complete coverage of the inner part of the section (Table 3). For the deeper layer (55–105 m), the correlation coefficients in Table 3 are statistically highly significant, indicating a fairly tight relationship. For the upper layer (5–55 m), the correlation coefficients are smaller, but still significant ($p < 0.05$ for N06–N07 and $p < 0.01$ for the other two station pairs). The table also shows the two coefficients α and β , above, determined by linear regression. For the deeper layer, the values of β are seen to be fairly similar, about 0.09, for the three station pairs considered. For the upper layer, α is more variable, but we use the value of 0.06 that applies to the two station pairs with highest correlation coefficients.

On the assumption, that the geostrophic approximation applies throughout the water column from the surface to 400 m depth (see Appendix A), Eqs. (2) can be used to extend the ADCP data all the way to the surface using the values for α and β as determined above. With these methods, all the ADCP records in Table 1 were extrapolated to cover the total depth range from the surface down to 600 m or the bottom, if shallower. Based on this, an average eastward velocity section, mainly based on the 2000–2001 period, is shown in Fig. 14.

Table 3

Relations between the vertical geostrophic shear in the uppermost 100 m and the 100–400 m interval. The vertical velocity difference across the 5–55 m and the 55–105 m depth layers, respectively, is compared to the velocity difference across the 105–405 m depth layer for each of 45 geostrophic profiles for three standard station pairs. The row termed regression factor lists the factors α (for the 5–55 m layer) and β (for the 55–105 m layer) in Eq. (2) as determined by linear regression analysis with zero offset

Station pair	Difference 5–55 m			Difference 55–105 m		
	N04–N05	N05–N06	N06–N07	N04–N05	N05–N06	N06–N07
Correlation coefficient	0.53	0.53	0.29	0.68	0.76	0.66
Regression factor	0.06	0.06	0.04	0.09	0.09	0.10

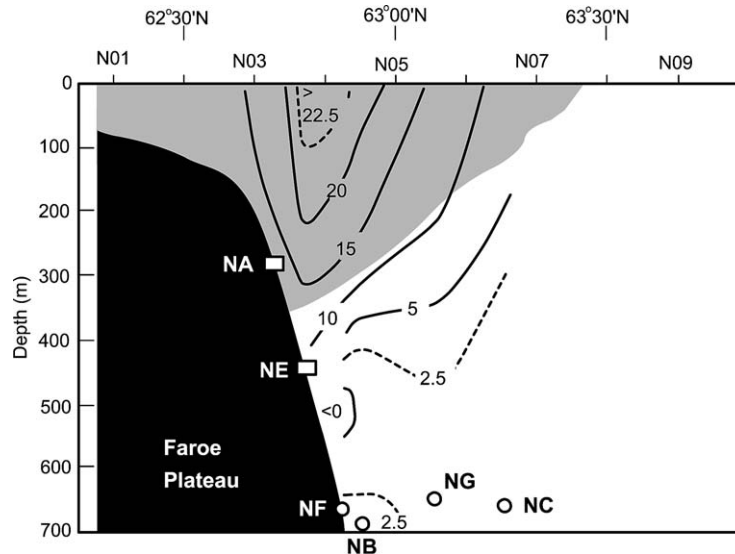


Fig. 14. The distribution of eastward velocity (in $\text{cm}\cdot\text{s}^{-1}$) on section N based on extrapolated ADCP measurements at sites NA, NE, NF, NB, and NG, using averages for the 2000–2001 period, and at site NC, using averages for the 1997–2000 period. The shaded area is on average more saline than 35.05 (Fig. 6a), representing Atlantic water.

3.5. Horizontal velocity correlations

A thorough treatment of the structure of velocity variations on the section is not within the scope of this paper (see Hátún, Hansen, & Haugan, *in press*). The ability of a current measuring array to cover the section adequately for flux estimation depends, however, on the distance between moorings in relation to the de-correlation distance. We therefore study the horizontal velocity correlations in the upper part of the section in Fig. 15. To this end, the average eastward velocity for the 0–200 m depth layer was calculated for each deployment and Fig. 15 shows coherence plots for pairs of mooring sites.

With the exception of the pair NF–NB (and possibly NE–NF also), the coherence spectra in Fig. 15 show significant coherence only for periods of a week or longer. In this part of the spectrum, two neighbouring pairs (NA–NE and NF–NB) were strongly coherent and roughly in phase (positive correlation). Strong coherence was also found between NB and NC but with a phase lag close to 180° , indicating negative correlation at long periods. A similar, although not as strong, relationship was found between NE and NG. These negative correlations could indicate that the location of the current core moves towards and away from the shelf over long periods.

4. Total volume flux

As described above, the number and distribution of ADCP mooring sites were different in the two periods. Flux determination therefore has to be considered for each period separately and, since the second period had better instrumental coverage, we discuss that first.

4.1. Total volume flux during the 2000–2001 period

With the homogenized ADCP data set, the velocity may be integrated over the section to give estimates of total volume flux. To do this, we have divided the section into vertical columns that are 10 nautical

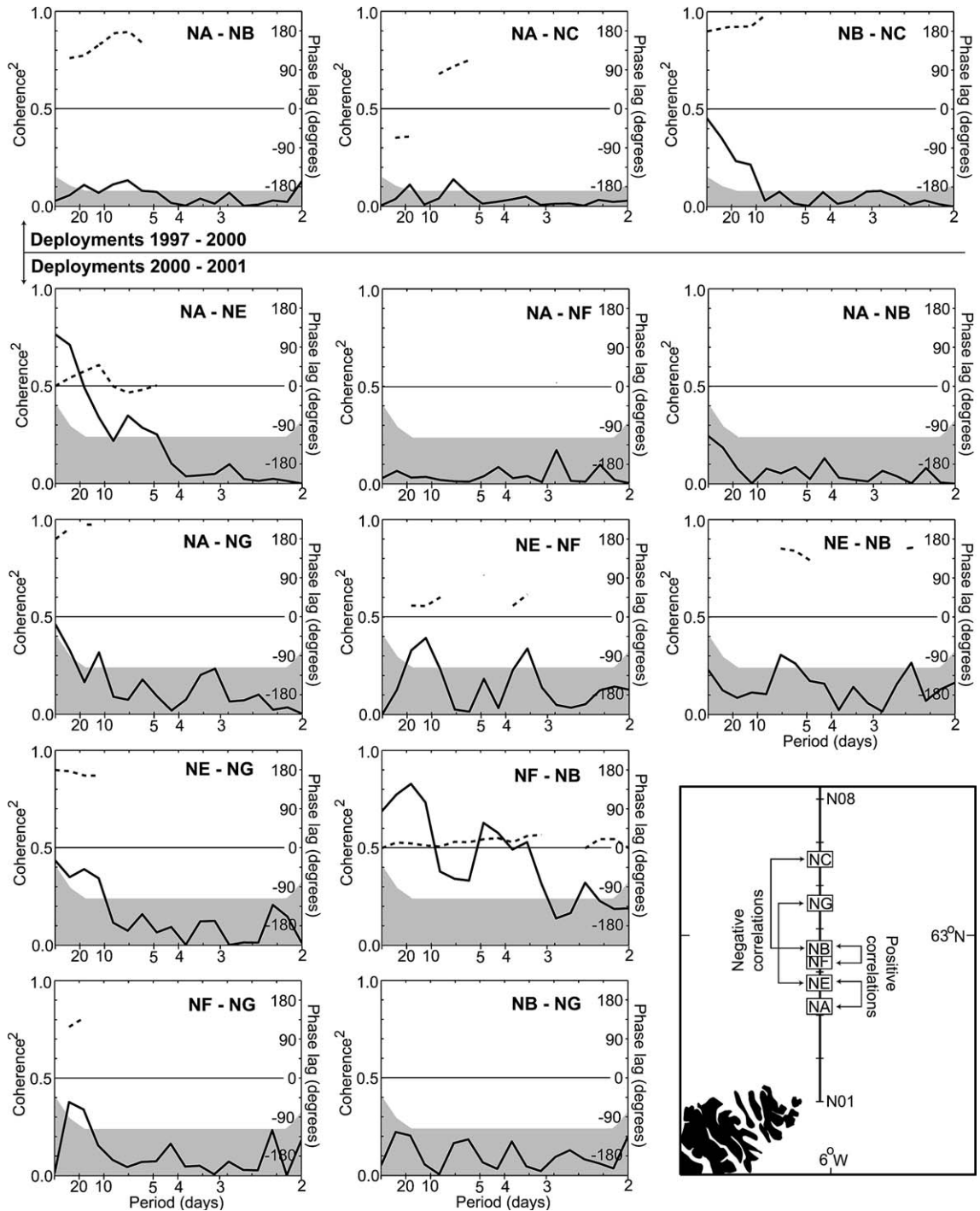


Fig. 15. Squared coherence (thick continuous curves) and phase lags (dashed curves) for pairs of eastward velocity time series (average 0–200 m) from deployments on section N. The coherence spectra were estimated using MATLAB with linear de-trending and Hanning windows with 50% overlap. In each graph, the shaded area indicates non-significance at the 99% level estimated by 10,000 Monte Carlo simulations of pairs of white noise series. Phase lag is only shown where the squared coherence was above the 99% significance level. To facilitate interpretation, the mooring sites are illustrated in the lower right-hand corner of the graph. This panel also highlights, which pairs were strongly coherent with small phaselags (positive correlation), and which were strongly coherent with phase lags close to $\pm 180^\circ$ (negative correlation), for long-period variations.

miles wide and symmetrical around the standard stations as indicated in Fig. 16. Each column is then divided into boxes of height 10 m. The boxes are labeled by an index pair (k, j) , where k varies northwards and j with depth. For each vertical column of boxes, k is given the number of the standard station in the middle of the column. In order to exclude Faroe Shelf water, the innermost column is the one centered around station N02.

With this geometry, the center of each box is at a depth where the homogenized ADCP data set has velocity values for the different sites. We therefore linearly interpolated the velocity between the mooring sites and prescribed constant values outside the mooring array, and then piece-wise averaged the resulting velocity distributions to obtain eastward velocity values $u_{k,j}(t)$ for the boxes of Fig. 16. For the area south of the moorings, we have used measurements with traditional Aanderaa current meters, which indicate typical residual velocities on the order of 6 cm s^{-1} in the vicinity of N02 (Hansen & Larsen, 1999), as indicated in Fig. 17. Similarly, we have used the average velocity profile at NC, based on the ADCP measurements in the 1997–2000 period to extend the velocity northwards from NG. As indicated in Fig. 17, we have even extended it north of site NC. This was motivated by the average geostrophic profiles between the three station pairs N06–N07, N07–N08, and N08–N09. All of these indicated a similar eastward velocity difference around $7\text{--}9 \text{ cm s}^{-1}$ between 500 m depth and the surface. Deep boxes that intersect the bottom or are close to the slope may not have any ADCP velocity on the inner side, because the inner ADCPs are at shallower sites. For these boxes, we use the same interpolation method assuming a fictitious velocity below the inner ADCPs equal to the velocity at the deepest bin (see Appendix A).

In this way, the average eastward velocity for each box can be derived from the ADCP measurements for every day in the deployment period and the total volume flux of water each day, $V_T(t)$, is then:

$$V_T(t) = \sum_k \sum_j A_{k,j} \cdot u_{k,j}(t) \quad (3)$$

where $A_{k,j}$ is the area of the box at depth number j for standard station number k , equal to $1.852 \times 10^5 \text{ m}^2$ for boxes that do not intersect the bottom and equal to zero for boxes, totally below the bottom. In Fig. 18, it is seen how the average volume flux varies as the northern limit of integration is extended out to station N08, which normally covers all the Atlantic water (Fig. 6). Most of the flux passes through the columns under standard stations N04 and N05.

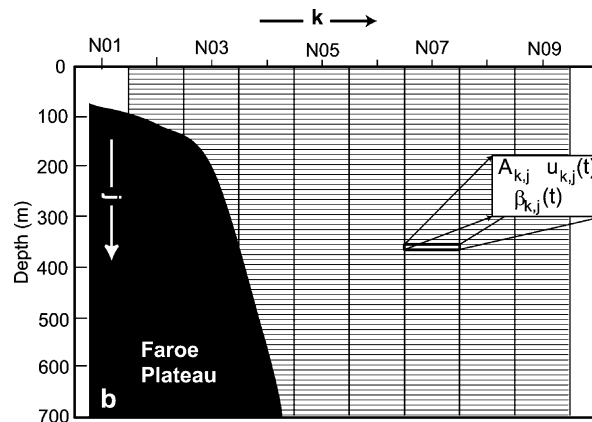


Fig. 16. Subdivision of section N into boxes for calculating fluxes. Boxes are labeled by indices k and j . One of the boxes is shown in a magnified scale indicating the parameters that must be assigned to each box: the area: $A_{k,j}$, the eastward velocity: $u_{k,j}(t)$, and the fraction of Atlantic water: $\beta_{k,j}(t)$.

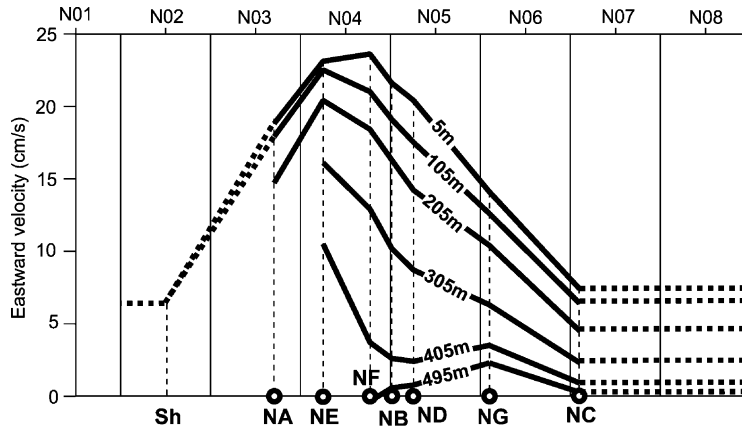


Fig. 17. The latitudinal variation of the average eastward velocity on section N for six different depths (thick continuous lines) based on averaged ADCP profiles. For sites NA, NE, NF, NB, and NG, the 2000–2001 period is used. The values for NC are based on the 1997–2000 period while the values for ND are for the deployment there, but scaled with the NB values to adjust for temporal variation. (As an example, the surface value at ND was reduced by 18%, because the surface velocity at NB was this much weaker during the ND deployment than in the 2000–2001 period.) The thick dashed lines extend the average velocity variation for flux calculations as described in the text. The continuous vertical lines, midway between standard stations, define the vertical columns that the section is divided into for flux calculations.

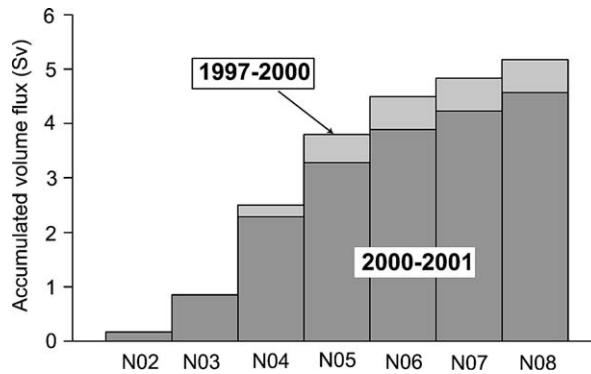


Fig. 18. Accumulated total volume flux from station N02 northwards, from the surface to 600 m depth. Columns with dark shading show the average for the 2000–2001 period while the lighter shading is for the 1997–2000 period.

4.2. Total volume flux during the 1997–2000 period

In the first measurement period, only sites NA, NB, and NC were occupied and in the preliminary estimate, reported by Hansen, Østerhus et al. (1999), the velocity between the ADCPs was assumed to vary linearly between NA and NB. The 2000–2001 measurements clearly show that this was not a good approximation (Fig. 17), but they also indicate a fairly high correlation between the velocities in the intermediate waters and at the two sites, at least for periods of a week or more (Fig. 15).

This opens the possibility that the velocities between NA and NB can be expressed by the velocities at these two sites. We have tested the models:

$$u_{NE,j}(t) = \gamma_{NE,j} u_{NA,j}(t) + \lambda_{NE,j} u_{NB,j}(t) \quad u_{NF,j}(t) = \gamma_{NF,j} u_{NA,j}(t) + \lambda_{NF,j} u_{NB,j}(t) \quad (4)$$

where $u_{NE,j}(t)$ is the eastward velocity at depth j for site NE at time t , etc. The factors γ and λ were

determined for each depth level by multiple linear regression analysis of the data from the 2000–2001 period. We have also tested models with one of the velocity series from NA or NB, only. However, both $u_{NE,j}(t)$ and $u_{NF,j}(t)$ are better described by the multiple regression models in Eqs. (4), even at depths below the ADCP at NA (300 m). When the regression coefficients are determined for all depths, j , Eqs. (4) can be used to determine interpolated velocities between NA and NB, which allows calculation of the volume flux without using data from NE and NF.

The accuracy of this method was tested by comparing volume fluxes through the inner part of the section for the 2000–2001 period, calculated in this way with the fluxes using the measurements from NE and NF (Fig. 19). For daily flux estimates, the correlation coefficient was 0.985 and with weekly averages, it increased to 0.994. The average flux over the whole period (343 days) was 1% smaller when using Eqs. (4) rather than the measured values. We also tested a multiple regression model with offsets included in Eqs. (4). The 1% discrepancy in average flux disappeared, but the correlation did not increase. Since we see no physical reason for an offset, we choose not to add more degrees of freedom to the model and used Eqs. (4) without offsets.

The high correlation coefficient and the close relationship in Fig. 19 indicate that Eqs. (4) are a good approximation and we have therefore used these relationships with the regression coefficients determined from the 2000–2001 period to calculate the flux in the 1997–2000 period when NE and NF were not occupied. In this period, NG was not occupied either, but NC was. We do not have simultaneous measurements at NB, NG, and NC and can therefore not do a multiple regression analysis as for NE and NF. We could use the 2000–2001 measurements to regress NG on NB only, but the low correlation between these two sites (Fig. 15) argues against that. Instead, we simply assume that the velocity in the 1997–2000 period varies linearly from NB to NC. As indicated in Fig. 17, this seems to be a good approximation in the average, and presumably on long time scales for the water at 300 m depth, and above. At deeper layers, this does not seem to be a good approximation, but very little Atlantic water is found there so, the flux estimate of Atlantic water will not be much affected by this.

Using this method, the volume flux of water above the 600 m level from N02 to N08 was calculated for the 1997–2000 period. As shown in Fig. 18, the average flux was found to be higher in this period than in the 2000–2001 period. Whether this difference is statistically significant is, however, doubtful, when error sources (Appendix A) and variability are considered. Averaged over the whole period, the total

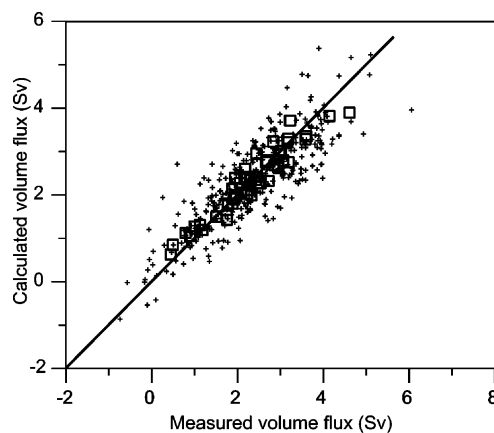


Fig. 19. The volume flux through the columns under N02, N03, and N04 during the 2000–2001 period, determined by using Eqs. (4) instead of the measured velocities at NE and NF (calculated volume flux) compared to the flux determined by using all the measured ADCP data (measured volume flux). Pluses indicate daily average flux. Open squares indicate 7-day averages. The line indicates equality.

volume flux through this part of the section was estimated to 5.0 Sv with variations, which on monthly means ranged between 1.8 and 8.7 Sv (Fig. 20).

5. Flux of Atlantic water

The total volume flux (Fig. 19), computed from Eq. (3), includes all the Atlantic water that passes through section N but, in addition, it also includes water that has not crossed the Iceland–Faroe Ridge recently (Fig. 6). Eq. (3) can, however, be modified by introducing a parameter, β , defined as the fraction of Atlantic water. If $\beta_{k,j}(t)$ is the Atlantic water fraction for the box (k, j) at time t (Fig. 16), the Atlantic water flux, $V_A(t)$, will be given by:

$$V_A(t) = \sum_k \sum_j \beta_{k,j}(t) \cdot A_{k,j} \cdot u_{k,j}(t) \quad (5)$$

With $A_{k,j}$ and $u_{k,j}(t)$ determined as previously described, calculation of Atlantic water flux is, thus, reduced to estimation of $\beta_{k,j}(t)$ for each box as a function of time. Several methods have in the past been used for this purpose in similar cases, usually based on relating in situ temperature and/or salinity characteristics to assumed source values for the water masses involved. Determination of the Atlantic water fraction, $\beta_{k,j}(t)$, therefore involves two different problems, determination of in situ water characteristics on section N, and determination of source water characteristics.

5.1. Generating daily fields for in situ temperature and salinity on section N

In order to use temperature and salinity to determine $\beta_{k,j}(t)$ in Eq. (5), we need the values of these parameters at every point of the section and for every day from June 1997 to June 2001, except for the annual ADCP servicing periods. Measured values are only available for the few days in this period when a CTD cruise took place and there is no reason to believe that interpolation between these dates would give realistic values. Including the established seasonal variation (Fig. 7) may help, but, in addition, daily temperature and salinity values on the section can, to some extent, be derived from the velocity field observed with the ADCPs. This should come as no surprise, since these fields are connected through

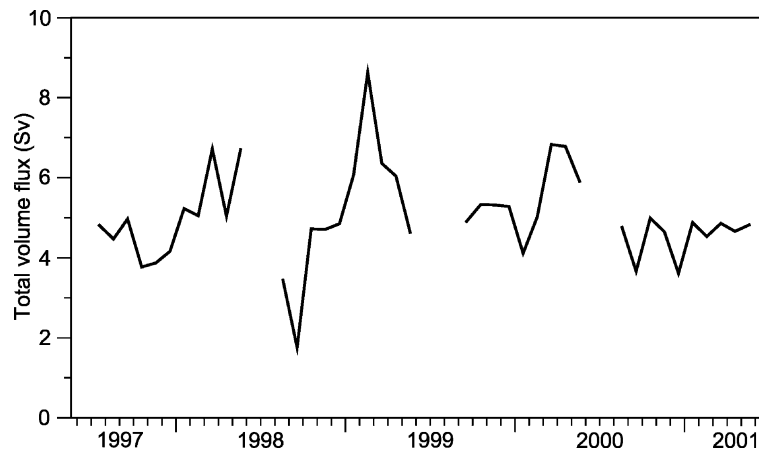


Fig. 20. Monthly averaged total volume flux through section N from 62°25' N to 63°35' N and from the surface down to 600 m. Only months with complete coverage were included.

geostrophy, and the inverse method, deriving velocity from temperature and salinity, was the backbone of classical oceanography.

As with the classical dynamical method, there are problems in deriving temperature and salinity from velocity, but Hátún et al. (in press) have shown that the problems, to a large extent, can be overcome by using empirical orthogonal function (EOF) analysis. This technique uses statistical methods on observed data to separate the spatial and the temporal variations so that, e.g. the temperature $T_{k,j}(t)$ in box (k, j) can be expressed as:

$$T_{k,j}(t) = T_{k,j}^{avg} + t \cdot T_{k,j}^r + T_{k,j}^{amp} \cdot \cos\left(\frac{2\pi}{365} \cdot t - T_{k,j}^{phase}\right) + PC-T1(t) \cdot EOF-T1_{k,j} + PC-T2(t) \cdot EOF-T2_{k,j} + \dots \quad (6)$$

Here, t is the day number since January 1, 1997, $T_{k,j}^{avg}$ and $T_{k,j}^r$ represent the average temperature field and a linear trend field, respectively. $T_{k,j}^{amp}$ and $T_{k,j}^{phase}$ represent amplitude and phase of the seasonal variation at each point (k, j) of the section and were presented in Fig. 7a. In addition to these terms, Eq. (6) includes a number of terms containing EOF modes ($EOF-T1_{k,j}$, etc.) with spatial variation, which are modulated by their associated principal components ($PC-T1(t)$, ...) that vary with time. In principle, a large number of modes are needed on the right-hand side of Eq. (6) to get exact equality, but for the temperature and salinity fields on section N, Hátún et al. (in press) found that most of the variance was explained by the first EOF modes. They furthermore found that the principal components for these modes were highly correlated to one of the principal components of the velocity field. This means that to a large extent the temperature (and salinity) field can be reconstructed from the ADCP velocity data:

$$T_{k,j}(t) = T_{k,j}^{avg} + t \cdot T_{k,j}^r + T_{k,j}^{amp} \cdot \cos\left(\frac{2\pi}{365} \cdot t - T_{k,j}^{phase}\right) + a_T \cdot PC-C(t) \cdot EOF-T1_{k,j} \quad (7)$$

where $PC-C(t)$ is the principal component for the velocity mode that is well correlated to the principal component of the dominant temperature EOF mode and a_T is a conversion factor between the current and temperature variations. Using the data presented in our study, Hátún et al. (in press) evaluated all the terms on the right-hand side of Eq. (7) and its salinity equivalent.

The “reconstructed” temperature field, based on Eq. (7), explained 60% of the total observed temperature variance on the section and the “reconstructed” salinity field explained 44% of the total salinity variance. Hátún et al. (in press) also compared the observed temperature at the bottom of site NE (Fig. 8) to the “reconstructed” temperature at this location. Site NE is not in the area where the EOF has its largest variation. Nevertheless, the correlation coefficient between the measured and the “reconstructed” series was found to be 0.75, based on de-seasoned daily values. This independent check confirms that the temperature field, reconstructed by Eq. (7), does indeed explain a substantial part of the observed temperature variations. We have therefore used Eq. (7) and its salinity equivalent to determine daily values for $\beta_{k,j}(t)$ in Eq. (5).

From Eq. (7) and its salinity equivalent, we can evaluate the temperature and salinity distribution of the water carried through the section. For each day in the 1997–2001 period, the boxes in Fig. 16 are sorted into temperature classes of width 0.5 °C and salinity classes of width 0.025. Average volume fluxes for each class are then computed from Eq. (3). The results from this are shown by the bar charts in Fig. 21. The figure also shows accumulated volume fluxes. As could be expected, Eq. (7) generates a high variability, which extends the range of both temperature and salinity variations beyond what is found in nature, but with small flux contributions and, over most of the range, we expect Fig. 21 to be relatively accurate. Both the temperature and the salinity flux distribution have maxima that are characteristic for Atlantic water (slightly above 7 °C and around 35.2). This illustrates the dominance of Atlantic water in the flux through the section, but we note also the presence of other water masses, especially by the secondary

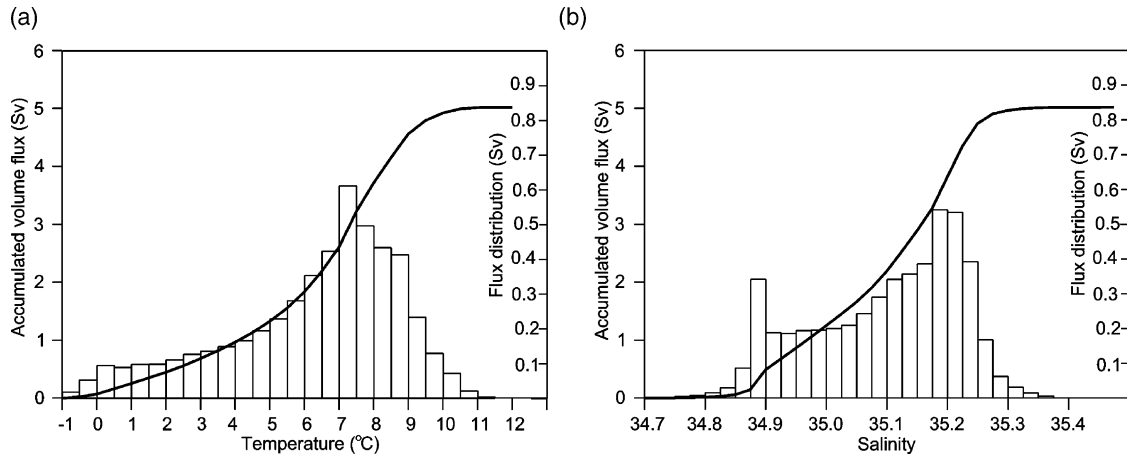


Fig. 21. Volume flux of water through section N from 62°25' N to 63°35' N and from the surface down to 600 m subdivided into temperature (a) and salinity (b) classes. In each panel, the bar chart shows the flux within each temperature or salinity class, scaled by the vertical axis on the right-hand side of the panel. The continuous curves show the accumulated flux, obtained by summing the values in the classes, scaled by the vertical axis on the left-hand side of each panel.

salinity maximum, just below 34.90, which indicates Norwegian Sea Arctic intermediate water (NSAIW) (Fig. 6b).

5.2. Source water characteristics

The in situ characteristics on section N arise through mixing between various source water masses, modified by air–sea interaction. Since we focus on fluxes across the Iceland–Faroe Ridge, the Atlantic source water is by definition the water in the upper layers (down to about 500 m) due west of the Ridge. This water is often termed modified North Atlantic water (MNAW, Fig. 6). Due to winter convection, this water mass is generally fairly homogeneous in the vertical, but it varies considerably in the horizontal. It is therefore important to consider from what areas the Atlantic water flow over the Iceland–Faroe Ridge is drawn. In the classical description (Fig. 39 in Helland-Hansen & Nansen, 1909), all the water is drawn from a branch of the North Atlantic Current located north of Faroe Bank. Section WN on Fig. 2a crosses this current and Fig. 22 shows average temperature and salinity on that section in the period 1998–2001.

Comparing the characteristics on section WN (Fig. 22) to those on section N (Figs. 4 and 6), both temperature and salinity are seen to be slightly lower on section N. Since the Atlantic water is more saline than all other water masses on section N, the Atlantic core on that section may be defined as a maximum salinity layer. The de-seasoned characteristics of this core (Fig. 23) varied considerably during the last decade, but remained fairly constant in the 1997–2001 period (Fig. 23). On the average, the Atlantic core on section N is found to be 0.02–0.04 fresher and 0.25–0.5 °C colder than the water on section WN (Fig. 22). To some extent, this may be due to air–sea interaction during the passage from section WN to section N. Hansen and Østerhus (2000) estimated annual decreases of 0.02 in salinity and 1 °C in temperature for Atlantic water in this region. They also cited observations of drifters that required more than half a year to cross the Ridge. Other drifters were, however, observed to cross much faster and it is not likely that air–sea interaction is the sole cause of the difference between section WN (Fig. 22) and the Atlantic core on section N (Fig. 23).

If it is assumed that all Atlantic water on section N must have passed through or close to section WN (continuous arrows in Fig. 2a), this difference implies that even the Atlantic core on section N has been

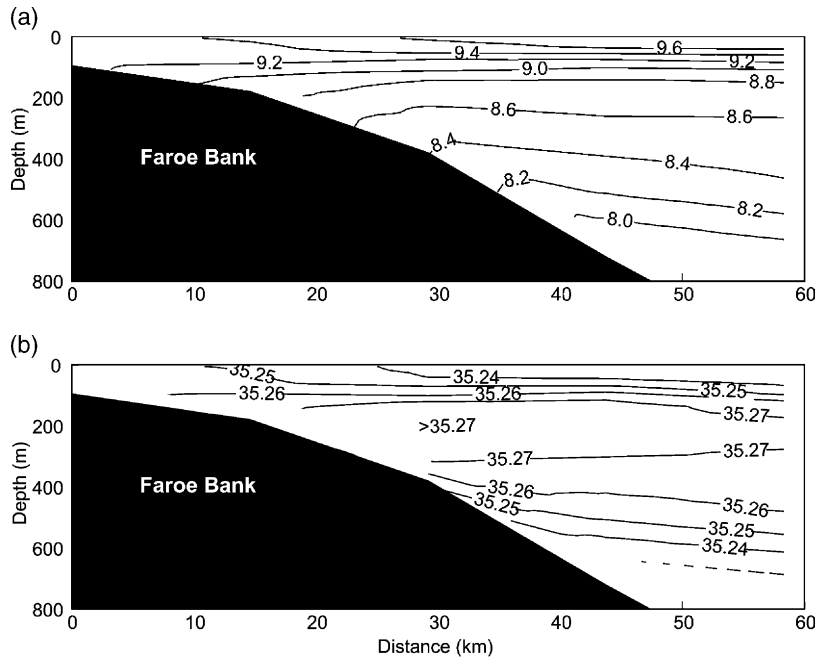


Fig. 22. Average temperature (a) and salinity (b) on section WN (Fig. 2a) based on eight CTD cruises between 1998 and 2001.

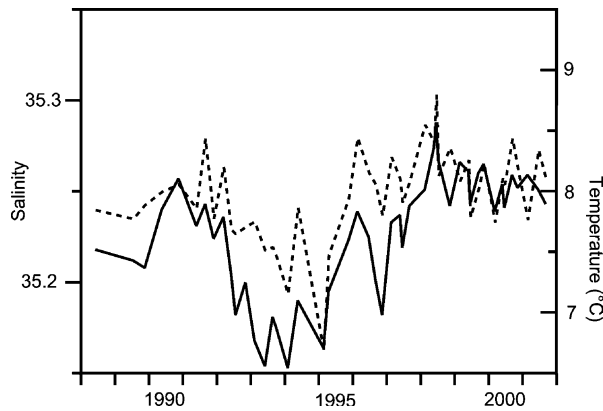


Fig. 23. Temperature (dashed line) and salinity (full line) of the core of Atlantic water on section N determined from CTD surveys. The core is defined as that level of 50 m vertical extension on the section that has the highest average salinity. The curves have been “de-seasoned” by subtracting a sinusoidal variation, determined by least-square fitting.

admixed by fresher and colder non-Atlantic waters. There is, however, evidence that some of the Atlantic water, at least, takes a different path. Based on satellite tracked drifter observations, [Valdimarsson and Malmberg \(1999\)](#) suggested an alternative path with the Atlantic water flowing closer to Iceland on its way towards the ridge (broken arrows in Fig. 2a) and [Orvik and Niiler \(2002\)](#) suggest that this is the main path. Water brought along this path would be considerably fresher and colder than on section WN.

With contribution from different branches with different characteristics, a single set of temperature and salinity values for the source characteristics of Atlantic water on section N requires a volumetric averaging

over the different contributions. At the present state of knowledge, this cannot be done in a meaningful way. The temperature and salinity values in Fig. 22 may be considered to represent maximum values, but representative source values may be considerably lower. To allow for this uncertainty, we have done several calculations with temperatures ranging between 7 and 9 °C and salinities between 35.20 and 35.27 for the source characteristics of the Atlantic water mass, which we denote as MNAW (Table 4).

In addition to the MNAW, a number of other source waters occur on section N (Fig. 6), but only NSAIW and modified East Icelandic water (MEIW) get into contact with the Atlantic source water over extended areas. The NSAIW has fairly well defined characteristics ($T = 0.5$ °C, $S = 34.9$) both in the literature (Hansen & Østerhus, 2000) and in Fig. 6. The MEIW has much more variable characteristics (Hansen & Østerhus, 2000) and, to a large extent, it seems to be formed in the region (Read & Pollard, 1992) with contribution of MNAW. As source water, we should use the other components from which MEIW is formed. These seem to enter in variable mixing ratios but all of them are considerably fresher than both the MNAW and the NSAIW. We therefore use temperatures ranging between 1 and 3 °C and salinities between 34.7 and 34.8 for the source characteristics of MEIW (Table 4).

5.3. Average fluxes of Atlantic water, heat, and salt

With information on in situ and source water characteristics, various methods can be used to determine the Atlantic water fraction $\beta_{k,j}(t)$. A common practice in the Nordic Seas is to define a reference salinity and assign the value, $\beta = 1$, to all boxes with salinity above the reference, while the value, $\beta = 0$, is assigned to the rest of the boxes. Table 4 shows average Atlantic water flux calculated with this method (mixing model: *s*-ref) and with three different choices for reference salinity. Similarly, one can define a reference temperature and Table 4 lists average fluxes with three different choices of reference temperature (mixing model: *t*-ref).

Table 4

Average volume, heat, and salt flux, as well as average temperature and salinity of Atlantic water through section N for the period June 1997 to June 2001 with different assumptions about mixing model and source water characteristics of MNAW and MEIW. To the characteristics of MNAW shown in the table was added a seasonal variation with an amplitude of 0.58 °C for temperature and 0.02 for salinity and with a maximum in September for both parameters. The unit for heat flux is TW (10^{12} W) and for salt flux, it is $\text{kT}\cdot\text{s}^{-1}$ (10^6 $\text{kg}\cdot\text{s}^{-1}$)

Mixing model	MNAW source		MEIW source		Volume flux (Sv)	Heat flux (TW)	Salt flux ($\text{kT}\cdot\text{s}^{-1}$)	Average	
	Temperature (°C)	Salinity	Temperature (°C)	Salinity				Temperature (°C)	Salinity
3-Point	8.00	35.23	2.00	34.75	3.54	124	128	8.17	35.23
3-Point	9.00	35.27	2.00	34.75	3.17	123	115	9.00	35.27
3-Point	7.00	35.20	2.00	34.75	3.81	125	138	7.67	35.20
3-Point	8.00	35.23	1.00	34.70	3.68	130	134	8.20	35.22
3-Point	8.00	35.23	3.00	34.70	3.50	123	126	8.15	35.23
3-Point	8.00	35.23	1.00	34.80	3.63	128	131	8.19	35.22
3-Point	8.00	35.23	3.00	34.80	3.37	117	122	8.11	35.23
<i>s</i> -Ref	Reference salinity=35.10				2.86	96	104	7.80	35.19
<i>s</i> -Ref	Reference salinity=35.05				3.40	111	123	7.58	35.17
<i>s</i> -Ref	Reference salinity=35.00				3.81	120	138	7.35	35.15
<i>t</i> -Ref	Reference temperature (°C)=7.00				2.57	90	92	8.13	35.19
<i>t</i> -Ref	Reference temperature (°C)=6.00				3.30	110	119	7.74	35.17
<i>t</i> -Ref	Reference temperature (°C)=5.00				3.78	121	137	7.44	35.15

Another method can be used if only three, well defined, water masses are involved and modification by air–sea interaction can be ignored. If typical temperatures and salinities of these three source water masses are known, a simple 3-point mixing model (Hermann, 1967) allows the determination of the relative content of MNAW water from the temperature and salinity at each point. The Atlantic water fraction $\beta_{k,j}(t)$ for each box on the section can then be calculated from the temperature and salinity characteristics of the box. As mentioned above, MNAW mixes mainly with MEIW and NSAIW. In Table 4, we have therefore calculated average Atlantic water flux with this mixing model and with different combinations of source water characteristics for MNAW and MEIW.

It has been noted that the in situ temperature and salinity on section N vary seasonally (Fig. 7) and this is taken into account in Eq. (7) and the equivalent salinity equation. In a similar manner, seasonal variations of source water characteristics must be considered. For MNAW, the observations of the Atlantic core on section N show a seasonal variation with an amplitude of 0.58 °C for temperature and 0.02 for salinity and with a maximum in September for both parameters. These values might seem to be too small when compared with Fig. 7, but this is because the location of the core, defined as the salinity maximum, varies during the season. This seasonal variation of MNAW source water was taken when calculating the fluxes in Table 4. For NSAIW, the source water characteristics are fairly stable without appreciable seasonal variation, while for MEIW, we have too little information to estimate seasonal variation. For these two water masses, the characteristics were therefore assumed not to vary seasonally.

In addition to volume fluxes, Table 4 also lists average fluxes of heat and salt through the section. By definition, the heat flux depends on the amount of heat lost within the system, rather than the temperature, as such. Most of the water flowing out of the Arctic Mediterranean has temperatures close to 0 °C and we therefore compute the heat flux by multiplying each term in Eq. (5) by temperature, heat capacity, and density. In contrast to temperature, the salinity differs significantly from one outflow branch to another. We therefore compute the salt flux by multiplying each term in Eq. (5) by salinity and density. To the extent that salinity represents salt concentration (within 0.5%), this results in an “absolute” salt flux. Some of the heat and salt carried through the section derives from other sources than the Atlantic and care has to be taken when only the fluxes that have come directly across the Iceland–Faroe Ridge are to be calculated. When other water masses than MNAW are present in a box ($\beta_{k,j} < 1$), in situ temperature and salinity are not equal to the values for the Atlantic water. In these cases, the assumed source characteristics of MNAW were used for temperature and salinity rather than in situ values.

The last two columns in Table 4 show average temperature and salinity for the Atlantic water flowing through the section. Average temperature was defined as the heat flux divided by the Atlantic water flux, heat capacity, and density, while average salinity was defined as the salt flux divided by the Atlantic water flux and density. These values clearly depend on the assumptions made about water mass characteristics, but with a smaller range of variation.

From the examination of error sources (Appendix A), it appears that their effects on the average Atlantic water flux are small compared to the uncertainty introduced by uncertain source water characteristics as seen in Table 4. From that table, it is clear that the somewhat arbitrary choice of a reference salinity or a reference temperature affects the result considerably. We therefore prefer the 3-point mixing model. Combining the results from the upper part of Table 4 with the error estimates discussed, we conclude that the average Atlantic water flux for the 1997–2001 period was 3.5 ± 0.5 Sv. Similarly, the heat and salt carried by the Atlantic water was found to be 124 ± 15 TW (referenced to 0 °C) and $(128 \pm 15) \times 10^6$ kg·s⁻¹, respectively. These estimates are quite similar to the preliminary estimates, based on a less thorough treatment of the ADCP measurements from 1997 to 1999 (Hansen, Østerhus et al., 1999).

5.4. Flux variations

Fluxes of water, heat, and salt will vary due to velocity variations as well as variations in the Atlantic water fraction. In order to study flux variations, the source water characteristics and mixing model have

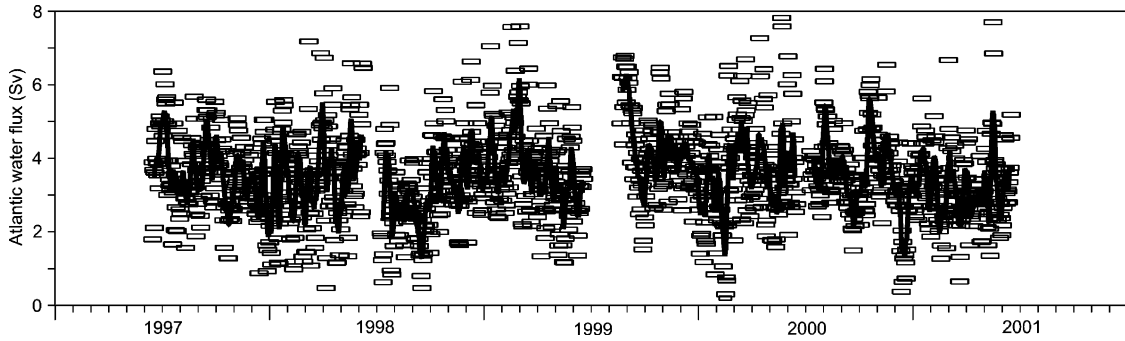


Fig. 24. Volume flux of Atlantic water through section N from June 1997 to June 2001. Rectangles indicate daily values. Continuous lines indicate 7-day running average values.

Table 5

Results of fitting various parameters to a sinusoidal seasonal model. Numbers in brackets for amplitude indicate percentage magnitude of amplitude relative to average value. Max-day is the day number in the year when the model predicts maximum to occur. Total volume flux is through that part of section N, which is from 62°25' N to 63°35' N and from the surface down to 600 m

Parameter	Average	Amplitude	Max-day
East vel. at 195 m at NB (cm s^{-1})	20.4	5.4 (26%)	47
Total volume flux (Sv)	5.01	0.88 (18%)	90
Atlantic water flux (Sv)	3.55	0.08 (2%)	242
Heat flux (TW)	125	15 (12%)	245
Salt flux ($10^6 \text{ kg}\cdot\text{s}^{-1}$)	128	3 (2%)	241

to be chosen and, in the following, we use the values in the top line of Table 4 with seasonal variation for MNAW source values, as discussed. With this choice, Atlantic water flux can be estimated for each of the 1348 days with sufficient ADCP coverage in the combined summer 1997 to summer 2001 period (Fig. 24). The daily estimates, as well as weekly averaged values, show variability on several time scales.

Seasonal variation of various parameters was studied by fitting time series of eastward velocity at a key point of the section, total volume flux, Atlantic water flux, heat flux, and salt flux to a sinusoidal seasonal model in a least-squares manner (Table 5). The total volume flux showed a consistent seasonal variation with an amplitude slightly less than 20% of the average flux and with a maximum in March–April, but the Atlantic water flux does not have a pronounced seasonal variation (Fig. 25). The reason for this is that

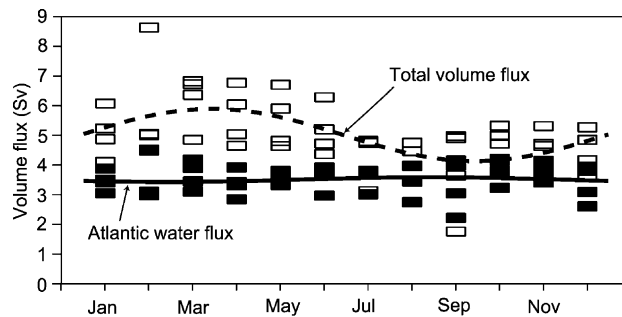


Fig. 25. Seasonal variation of the total volume flux (open rectangles) and Atlantic water flux (filled rectangles) through section N. Each rectangle indicates monthly average for 1 month with at least 15 days of observations. Curves show seasonal variation determined by model fit (Table 5) of total volume flux (dashed curve) and Atlantic water flux (continuous curve).

both the velocity field (total volume flux) and the areal extent of Atlantic water on the section (Fig. 7) vary seasonally, but with almost opposite phases. The heat flux carried by the Atlantic water has its maximum in late summer, as could be expected, but the salt flux carried by the Atlantic water does not have an appreciable seasonal amplitude.

In the preliminary report by Hansen et al. (2000), it was concluded that “if there is a consistent seasonal variation in the inflow of Atlantic water between Iceland and the Faroes, then it is probably relatively small, with an amplitude on the order of 0.5–1 Sv with a minimum in July–August”. The results from the present study (Table 5) are not in conflict with this, but they narrow the range of a possible seasonal variation considerably. The negligible seasonal amplitude of the Atlantic water flux is somewhat dependent on the method used. If we had assumed constant temperature and salinity fields, we would have found a significant seasonal amplitude (0.64 Sv), in phase with the volume flux. This is, however, in conflict with the observed seasonal variation of these fields (Fig. 7). The results in Table 5 are also based on the assumed seasonal amplitudes for the source characteristics of MNAW (0.58 °C and 0.02), but we tried to multiply these amplitudes by a factor of three, which only increased the seasonal amplitude of the Atlantic water flux to 0.25 Sv in a sinusoidal model fit. Thus, a seasonal amplitude for the Iceland–Faroe Atlantic water flux below 10% of the average value would seem to be a robust result.

In their latest estimate, Turrell, Hansen, Hughes, and Østerhus (2003) find the Faroe–Shetland Channel net inflow to have a small seasonal amplitude (0.2 Sv), with maximum in autumn. The inflow west of Iceland is much weaker (slightly less than 1 Sv) (Jónsson & Briem, 2003) than the other two branches in terms of average fluxes, but Stefánsson (1962) reported an appreciable seasonal variation of this branch with maximum in summer.

These results may be compared to the measurements by Orvik, Skagseth, and Mork (2001) who found that the Atlantic water flux through the Svinøy section, farther east in the Norwegian Sea, had a pronounced seasonal variation. The Atlantic water flows through the Svinøy section as a broad current with two branches that are fed both by the Iceland–Faroe inflow and the inflow through the Faroe–Shetland Channel. For the eastern branch, the seasonal variation found by Orvik et al. (2001) is compatible with our results and those of Turrell et al. (2003), if we assume that a larger fraction of the Iceland–Faroe inflow is steered into the eastern Svinøy section branch in winter. Such a variation has been observed in the Faroe–Shetland Channel by Turrell et al. (2003). This explanation implies that the western Svinøy section branch should be weaker in winter, in contrast to the findings by Orvik et al. (2001). Their results for the western branch were, however, inferred from hydrography and include therefore only the baroclinic part of the flow.

Interannual variation was studied by averaging Atlantic water flux and other parameters over the same period for each of the four deployments. The result (Table 6) shows some interannual variation, especially between the 1999–2000 and the 2000–2001 deployment periods. However, the Atlantic water flux only varies by about 16% between these two periods. With only 4 years of observations, any conclusions as to long-term trends in fluxes would be premature.

Table 6

Interannual variation. Average values of various parameters, averaged over the same period (22 August–8 June) for the four deployment periods. Total volume flux is through that part of section N, which is from 62°25' N to 63°35' N and from the surface down to 600 m

Parameter	1997–1998	1998–1999	1999–2000	2000–2001
East vel. at 195 m at NB (cm s ⁻¹)	21.0	23.8	23.7	15.8
Total volume flux (Sv)	5.18	5.22	5.55	4.53
Atlantic water flux (Sv)	3.50	3.53	3.86	3.30
Heat flux (TW)	121	121	135	115
Salt flux (10 ⁶ kg·s ⁻¹)	126	128	140	119

The variability on shorter time scales can be illustrated by a power spectrum of the Atlantic water flux (Fig. 26), which indicates that there is little variance on time scales of a few days. Fifty-three percent of the power in Fig. 26 was found at periods of 10 days or more. There seems to be an indication of a peak in the spectrum for periods around a week, but the reality and possible cause of this feature remain an object for future work. It should also be stressed that much of the variability on short time scales may be fictitious and derive from limited coverage of the section.

A notable feature of the short-term flux variability is demonstrated by Fig. 24. At a first glance, the daily flux values in this figure might give the impression of large variability. Note, however, that none of the 1348 daily flux estimates were negative, implying westward flow towards the Atlantic. This is in contrast to the velocity records from individual sites. The current velocity at specific locations may well show occasional reversal, even when averaged over a week (Fig. 11). When integrated over the section to produce flux values, these reversals are, however, canceled out. The values in Fig. 24 are, of course, not an exact representation of the actual Atlantic water flux for each day. Instrumental inaccuracies, limited coverage, and the approximations, which we have made, introduce errors in the flux estimate. These effects would, however, be expected to increase, rather than decrease, variability in the flux estimates. Thus, the actual Atlantic water flux should be less variable and even less likely to reverse, than indicated in Fig. 24. Even on daily time scales, the Iceland–Faroe Atlantic inflow is, thus, a highly stable flow.

6. Conclusions and outlook

The results obtained in this work confirm that the Iceland–Faroe branch of the Atlantic inflow is an important component in the budget of the Arctic Mediterranean. With an average flux of 3.5 ± 0.5 Sv, it carries slightly more Atlantic water than the branch that flows through the Faroe–Shetland Channel (3.2 Sv), according to the latest estimate (Turrell et al., 2003), and several times more than the Atlantic water flux of the branch west of Iceland (around 0.8 Sv according to Jónsson & Briem, 2003, and S. Jónsson, personal communication, 2003). With these estimates, the Iceland–Faroe branch carries 47% of the total Atlantic inflow to the Arctic Mediterranean and 42% of the total oceanic inflow, when the Pacific water flow through the Bering Strait is included (Roach et al., 1995).

To determine the importance of the Iceland–Faroe inflow branch in the heat and salt (freshwater) budgets of the Arctic Mediterranean, all of the exchange branches and their connections have to be considered. This is beyond the scope of this paper but, if we maintain the approximation that all of the outflows are

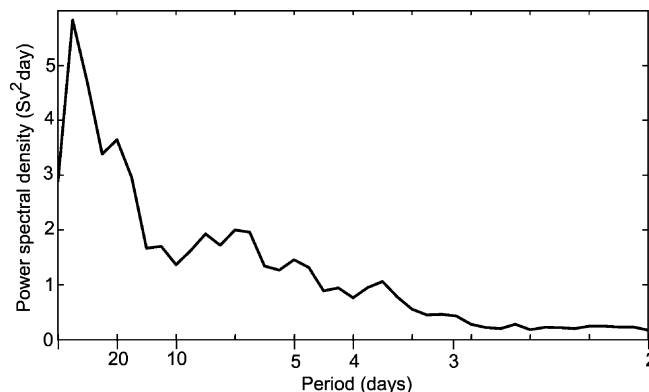


Fig. 26. Power spectrum of the Atlantic water flux for the period from summer 1997 to summer 2001, as an average of four spectra, each from one deployment.

close to zero in temperature, then the heat transport of the Iceland–Faroe inflow will be 124 ± 15 TW. This is of the same magnitude as the heat flux carried by the Faroe–Shetland inflow (123 TW), according to Turrell et al. (2003). The average salt flux carried by the Iceland–Faroe inflow was estimated to $(128 \pm 15) \times 10^6$ kg·s⁻¹, which is slightly above the salt flux through the Faroe–Shetland Channel (115×10^6 kg·s⁻¹), according to Turrell et al. (2003).

The Iceland–Faroe Atlantic inflow branch to the Nordic Seas, thus plays an important role in maintaining the volume, heat, and salt balances of the Arctic Mediterranean, and it is appropriate to consider how this role may be affected by anthropogenically induced climate change. Hansen and Østerhus (2000) have argued that the Atlantic inflow to the Nordic Seas is mainly driven by thermohaline forcing. Several (Rahmstorf, 1999), although not all (Latif, 2001), climate models predict a reduced thermohaline circulation as a consequence of anthropogenic carbon dioxide emission and Hansen, Turrell, and Østerhus (2001) have found observational evidence for reduced Iceland–Scotland overflow during the last half of the 20th century. If this decrease has not been compensated by increases in other overflow branches, the total inflow must have been decreased as well. Since the Iceland–Faroe branch seems to be the dominant inflow branch, a decrease in the volume flux of this inflow seems probable.

The observations, reported here, are of too short duration to allow any conclusions as to trends. Altimeter records indicate that the sea-surface slope from Iceland to the Faroes was slightly decreasing in the period 1993–2000 (D. Quadfasel, personal communication, 2003) and this might indicate a concurrent reduction in Iceland–Faroe Atlantic inflow, but more direct evidence is clearly needed. A continued monitoring of the inflow with moored equipment therefore has a high priority and the observational system must have an accuracy that can allow detection of relatively small changes. The system described in this work seems to have this capability and continued operation is planned. With support from the 5th Framework Programme of Europe, continuation has been secured until summer 2005. With successful operation, this will extend the time series to a length of 8 years, which may be sufficient to identify trends, if they are pronounced and persistent.

Acknowledgements

The observations reported in this work have received funding from the “Environmental Research Programme of the Nordic Council of Ministers (NMR) 1993–1998”, from the Danish and Norwegian Research Councils (Nordic WOCE project), from EU-MAST4 (VEINS project), and from the Fifth Framework Programme of the European Commission (MAIA project). This is publication no. A37 of the Bjerknes Centre for Climate Research.

Appendix A. Error sources

A number of approximations went into the flux calculations presented. We have tested the sensitivity of the results to these by neglecting or changing the approximations and noting the effect on the calculated Atlantic water flux. Neglecting the vertical extrapolation of ADCP data (Sections 3.3 and 3.4) and assuming instead constant velocities above the uppermost good measurement gave a flux reduction of 1.5%. Current velocities were also extrapolated horizontally (Section 4.1). Neglecting the shelf velocity (instead of using 6 cm s⁻¹, as assumed) would reduce the flux by 5%. In the other end of the section, neglecting the flow through the area under station N08 was found to reduce the average Atlantic water flux by 4%.

Horizontal interpolation was used to determine velocities for each box in the flux calculation. This was done by assuming linear variation and fixed ADCP positions (Section 4.1). Varying the interpolation scheme to reflect realistic positional variation (Table 1) or non-linear interpolation gave only small flux changes,

less than 2%. As previously discussed (Section 4.2), using Eqs. (4) instead of the ADCP measurements at NE and NF gave negligible changes in average flux for the 2000–2001 period and only small extra variance on shorter time scales (Fig. 19). As long as the general horizontal structure of the current (Fig. 17) remains constant, the use of these equations for the 1997–2000 period should therefore introduce only small errors. The ADCP depth is calculated from echosounding of bottom depth, corrected for sound speed variation and from mooring design. We tested the effect of errors in ADCP depth by changing the depth of the ADCP at the most critical site NB by ± 20 m. The change in Atlantic water flux was about 2%.

We have tested the sensitivity of flux estimates to Eq. (7) and its salinity equivalent by assuming the temperature and salinity fields to be constant, equal to their average. The seasonal variation was, as previously noted, strongly affected, as were short-term variations, but the effect on the average Atlantic water flux was only about 2%.

In addition to the errors associated with approximations, two processes may contribute to the fluxes. Using geostrophy to extrapolate to the surface layer (Section 3.4) implies neglect of Ekman transport. From tabulated wind stress values (Lindau, 2001), the average eastward Ekman transport through the Atlantic part of section N can be estimated to approximately 0.03 Sv. This is only about 1% of the average Atlantic water flux and has a seasonal amplitude of similar magnitude.

A second process involves the loss of Atlantic water between the Iceland–Faroe Ridge and the instrumented part of section N. The fluxes in Table 4 and elsewhere have been calculated out to and including the area centered around standard station N08 (Fig. 2). This includes by far the largest part of the Atlantic water that has recently crossed the Ridge, but some of it may have been mixed out into more northerly parts of the section. Like the Ekman transport, this process would tend to increase the Atlantic water flux and the heat and salt fluxes. This water is difficult to distinguish from the Norwegian North Atlantic Water (Fig. 6), which has already recirculated in the Norwegian Basin, and it is therefore difficult to quantify. On the average, we do not think the flux of this water is likely to exceed the average flux through the area centered around station N08 (4%).

Summarizing, we find total uncertainties for the average Atlantic water flux estimate to be less than 10%, when the uncertainty in Atlantic water source characteristics is not included. For fluctuations on shorter time scales, uncertainty estimates are more difficult to perform and we will not attempt that.

References

- Broecker, W. S., Peteet, D. M., & Rind, O. (1985). Does the ocean–atmosphere system have more than one stable mode of operation? *Nature*, 315, 21–26.
- Foreman, M. (1978). *Manual for tidal currents analysis and prediction*. Pacific Marine Science Report, 78–6.
- Gordon, L. (1996). Acoustic Doppler current profiler. Principles of operation. In *A practical primer* (2nd ed.) (p. 55). RD Instruments.
- Hansen, B. (1985). The circulation of the northern part of the Northeast Atlantic. *Rit Fiskideildar*, 9, 110–126.
- Hansen, B., & Larsen, K. M. H. (1999). *Traditional current meter observations in Faroese offshore waters 1977–1994. Data Report*. Technical Report, The Faroese Fisheries Laboratory, 99–01, 193 p.
- Hansen, B., Larsen, K. M. H., & Kristiansen, R. (1999). *ADCP deployments in Faroese waters 1997–1999*. Technical Report, The Faroese Fisheries Laboratory, 99–07.
- Hansen, B., Larsen, K. M. H., Østerhus, S., Turrell, B., & Jónsson, S. (1999). The Atlantic water inflow to the Nordic Seas. *The International WOCE Newsletter*, 35, 33–35.
- Hansen, B., Østerhus, S., Kristiansen, R., & Larsen, K. M. H. (1999). The Iceland–Faroe inflow of Atlantic water to the Nordic Seas. *ICES CM 1999/L:21*, 14 p.
- Hansen, B., Jónsson, S., Turrell, W. R., & Østerhus, S. (2000). Seasonal variations in the Atlantic water inflow to the Nordic Seas. *ICES CM 2000/L:03*, 15 p.
- Hansen, B., & Østerhus, S. (2000). North Atlantic–Nordic Seas exchanges. *Progress in Oceanography*, 45, 109–208.
- Hansen, B., Turrell, W. R., & Østerhus, S. (2001). Decreasing overflow from the Nordic seas into the Atlantic Ocean through the Faroe Bank channel since 1950. *Nature*, 411, 927–930.
- Hátún, H., Hansen, B., & Haugan, P. M. Using an “inverse dynamic method” to determine temperature and salinity fields from ADCP measurements. *Journal of Atmospheric and Oceanic Technology*, in press.

- Helland-Hansen, B., & Nansen, F. (1909). The Norwegian Sea, its physical oceanography. Based on the Norwegian researches 1900–1904. *Report on Norwegian Fishery and Marine-Investigations, Bergen*, 2 (2).
- Hermann, F. (1967). The *T–S* diagram analysis of the water masses over the Iceland–Faroe Ridge and in the Faroe Bank Channel (overflow '60). *Rapports et Procès-Verbaux des Réunions du Conseil International pour l'Exploration de la Mer*, 157, 139–149.
- Jónsson, S., & Briem, J. (2003). Flow of Atlantic water west of Iceland and onto the north Icelandic shelf. *ICES Marine Science Symposia*, 219, 326–328.
- Larsen, K. M. H., Hansen, B., Kristiansen, R., & Østerhus, S. (1999). *Shallow-water ADCP calibrations 1998–99*. Technical Report, The Faroese Fisheries Laboratory, 99–04.
- Larsen, K. M. H., Hansen, B., Kristiansen, R., & Østerhus, S. (2000). *Internal tides in the waters surrounding the Faroe Plateau*. In ICES Annual Science Conference CM 2000/L:09. (p. 13).
- Larsen, K. M. H., Hansen, B., & Kristiansen, R. (2000). *Nordic WOCE ADCP deployments 1999–2000*. Technical Report, The Faroese Fisheries Laboratory, 00–01.
- Larsen, K. M. H., Hansen, B., & Kristiansen, R. (2001). *ADCP deployments in Faroese waters 2000–2001*. Technical Report, The Faroese Fisheries Laboratory, 01–02.
- Latif, M. (2001). Tropical Pacific/Atlantic Ocean interactions at multi-decadal scales. *Geophysical Research Letters*, 28(3), 539–542.
- Lindau, R. (2001). In *Climate Atlas of the Atlantic Ocean* (p. 514). Berlin: Springer-Verlag.
- McCartney, M. S., & Talley, L. D. (1984). Warm-to-cold water conversion in the Northern North Atlantic Ocean. *Journal of Physical Oceanography*, 14, 922–935.
- Orvik, K. A., Skagseth, Ø., & Mork, M. (2001). Atlantic inflow to the Nordic Seas: current structure and volume fluxes from moored current meters, VM-ADCP and SeaSoar-CTD observations, 1995–1999. *Deep-Sea Research I*, 48, 937–957.
- Orvik, K. A., & Niiler, P. (2002). Major pathways of Atlantic water in the northern North Atlantic and Nordic Seas toward Arctic. *Geophysical Research Letters*, 29(19), 1896 (doi: 10.1029/2002GRL015002).
- Rahmstorf, S. (1999). Shifting seas in the greenhouse? *Nature*, 399, 523–524.
- Read, J. F., & Pollard, R. T. (1992). Water masses in the region of the Iceland–Faeroes Front. *Journal of Physical Oceanography*, 22, 1365–1378.
- Roach, A. T., Aagaard, K., Pease, C. H., Salo, S. A., Weingartner, T., Pavlov, V., & Kulakov, M. (1995). Direct measurements of transport and water properties through the Bering Strait. *Journal of Geophysical Research*, 100(C9), 18443–18457.
- Seager, R., Battisti, D. S., Yin, J., Gordon, N., Naik, N., Clement, A. C., & Cane, M. A. (2002). Is the Gulf Stream responsible for Europe's mild winters? *Quarterly Journal of the Royal Meteorological Society*, 128, 1–24.
- Simonsen, K., & Haugan, P. M. (1996). Heat budgets of the Arctic Mediterranean and sea surface heat flux parameterizations for the Nordic Seas. *Journal of Geophysical Research*, 101(C3), 6553–6576.
- Stefánsson, U. (1962). North Icelandic Waters. *Rit Fiskideildar*, 3, 269.
- Turrell, W. R., Hansen, B., Hughes, S., & Østerhus, S. (2003). Hydrographic variability during the decade of the 1990s in the Northeast Atlantic and southern Norwegian Sea. *ICES Marine Science Symposia*, 219, 111–120.
- Valdimarsson, H., & Malmberg, S. Aa. (1999). Near-surface circulation in Icelandic waters derived from satellite tracked drifters. *Rit Fiskideildar*, 16, 23–39.
- Worthington, L. V. (1970). The Norwegian Sea as a Mediterranean basin. *Deep-Sea Research*, 17, 77–84.
- Østerhus, S., & Hansen, B. (1995). *The Nordic WOCE trawl-resistant ADCP system*. In Proceedings of the IEEE Fifth Working Conference on Current Measurement, Feb. 7–9, 1995.
- Østerhus, S., Turrell, W. R., Hansen, B., Lundberg, P., & Buch, E. (2001). Observed transport estimates between the North Atlantic and the Arctic Mediterranean in the Iceland–Scotland region. *Polar Research*, 20(1), 169–175.

PAPER III



PERGAMON

Available online at www.sciencedirect.com

SCIENCE @ DIRECT®

Continental Shelf Research 23 (2003) 859–868

CONTINENTAL SHELF
RESEARCH

www.elsevier.com/locate/csr

Monitoring the Faroe Current using altimetry and coastal sea-level data

Hjálmar Hátún^{a,*}, Thomas A. McClimans^b

^a *Faroese Fisheries Laboratory, Nóatún 1, FO-110 Tórshavn, Faroe Islands*

^b *SINTEF Fisheries and Aquaculture, N-7465 Trondheim, Norway*

Received 8 February 2002; accepted 17 March 2003

Abstract

The possibility of using a coastal sea-level measurement program to compute flows in the Faroe Current (FC), north of the Faroe Islands, is studied using 3 years of Acoustic Doppler Current Profiler data together with water-level data at Tórshavn in the Faroes, and altimetry data from a region to the north of the islands. A significant correlation is found between the sea-level rise across the FC and both the flow of Atlantic water and the total flow. Based on this correlation, linear algorithms are suggested between the surface slope and the flows. A seasonality is found in open-ocean sea-level from altimetry, steric heights from hydrography and the *coastal* sea-level, all having a minimum in early March when the observed inflows are at a maximum.

© 2003 Elsevier Science Ltd. All rights reserved.

Keywords: Faroe Current; Slope current; Geostrophy; Water level; Altimetry; Correlation analyses

1. Introduction

The inflow of warm and saline Atlantic water over the Greenland–Scotland Ridge continues as the Norwegian Atlantic Current (NAC) along the Norwegian continental slope towards the Arctic regions. The Faroe Current (FC) flows eastward to the north of the Faroe Islands (Fig. 1) and this current accounts for approximately half of the total inflow of Atlantic water towards the Arctic (Hansen et al., 1999b). These water masses are of great importance to the regional climate and, as a

part of the *thermohaline circulation*, also to the global climate. A knowledge of the variability and possible changes in this inflow, is therefore needed to develop regional climate-models that are able to predict possible climate changes. Time-series of in situ current measurements are too short to establish any trend in the inflow and since these measurements are expensive to make, an alternative way to monitor the volume fluxes in these water masses would be valuable.

Employing the simplification of geostrophy, McClimans et al. (1999) found a good correlation between *5-day averages* of sea-level data at the Norwegian coast and current velocities along the Norwegian continental slope. Based on these results they suggested using coastal sea-level data to monitor the inflow of Atlantic water.

*Corresponding author. Tel.: +298-315092; fax: +298-318264.

E-mail addresses: hjalmarh@frs.fo (H. Hátún), thomas.mcclimans@sintef.no (T.A. McClimans).

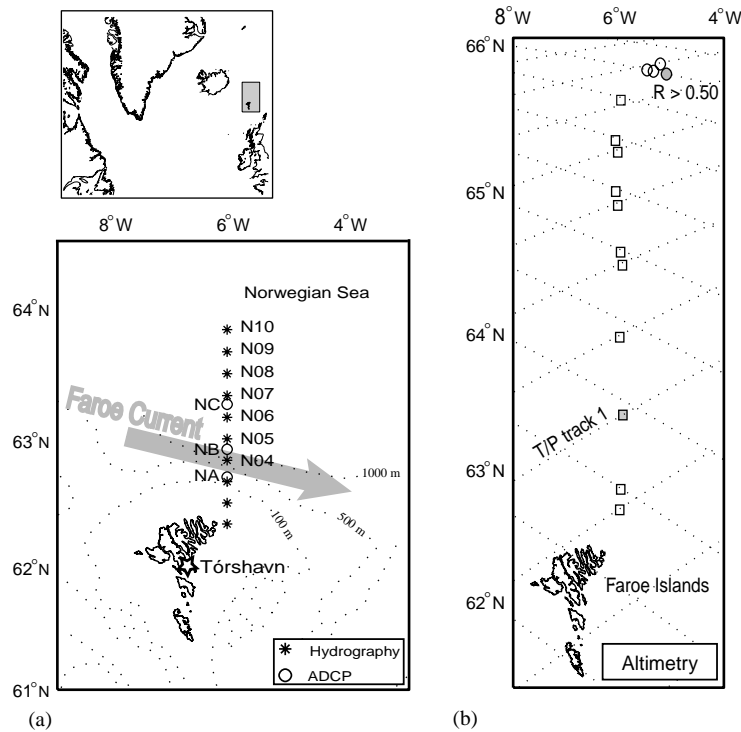


Fig. 1. (a) Location of the Faroe Islands and the capital, Tórshavn, where the coastal sea-level is measured. The CTD stations N04–N10 to the north are shown together with the ADCP instruments NA, NB and NC. The FC, which flows eastwards to the north of the islands, is also drawn. (b) Altimetry positions. The dots show all altimetry tracks, the squares show the measurement positions closest to the standard section, the filled square is the measurement point closest to the hydrography station N07. The area with the highest correlations ($R > 0.50$) between sea-level gradient and transports is illustrated with the circles, and the filled circle is the point with the very highest correlation ($R > 0.56$).

Alternatively, a set of bottom pressure sensors could monitor a flux between the sensors if the flow were predominantly barotropic. In this paper, we adopt these ideas and explore their applicability to the FC which is a mixed barotropic–baroclinic flow.

We consider a hydrostatic ocean of density $\rho(x, y, z, t)$ with a pressure field

$$p(x, y, z, t) = \int_z^{\zeta(x,y,t)} g\rho(x, y, z', t) dz' \quad (1)$$

and divide it into barotropic and baroclinic parts:

$$p(x, y, z, t) = \rho_0 g(\zeta(x, y, t) - z) - \int_z^{\zeta(x,y,t)} g'(x, y, z', t) dz'. \quad (2)$$

Here, z is the vertical coordinate, positive upwards, ρ_0 is a reference density, g is the

acceleration of gravity, $g' = g(\rho_0 - \rho)/\rho_0$, and $\zeta(x, y, t)$ is the unknown surface elevation. For a Boussinesq, quasi-stationary, linear, inviscid ocean, the equation of horizontal motion reduces to the geostrophic balance

$$\mathbf{u} \times \mathbf{k}f = \nabla_h p = g \nabla_h \zeta(x, y) - \nabla_h \int_z^{\zeta(x,y)} g'(x, y, z') dz', \quad (3)$$

where \mathbf{u} is the horizontal velocity, \mathbf{k} is the unit vertical vector, positive upwards, and f is the Coriolis parameter. The vertical derivative of Eq. (3) is the thermal wind equation that applies to the baroclinic mode

$$\partial \mathbf{u} / \partial z = \mathbf{k} \times \nabla_h g' / f. \quad (4)$$

By quasi-stationary, we mean that wave accelerations are negligible. To this end, we consider

5-day smoothing to eliminate tides and synoptic meteorological forcings. This filter favors monthly to seasonal variability, but includes some random variability due to mesoscale processes. This, and all other physical processes that are excluded in the geostrophic balance are considered as random noise. Frictional forces are negligible in a thin benthic (Ekman) layer, but are of concern at the surface due to wind forcing. Synoptic wind forcing is filtered out, but seasonal wind curl may contribute to “noise” since it is not taken into account in the physics.

A possible correlation between *coastal* water-level and current velocities must rest on the geostrophic balance of the pressure force resulting from the mass distribution and the sea-level elevation as derived in Eq. (3). The coastal sea-level variations at Tórshavn, adjusted for local air pressure, are given by

$$\zeta_T = \zeta_{FC} + \zeta_{OCEAN}, \tag{5}$$

where ζ_{OCEAN} is the water level to the north of the FC and ζ_{FC} is the geostrophic rise across the current. The good correlation in Norwegian waters (McClimans et al., 1999) was found by assuming a constant ζ_{OCEAN} . This assumption was based on the earlier map of Jacobs et al. (1992). Newer satellite altimetry (Pathfinder team, 2001) has revealed a significant seasonal variability. We therefore use the altimetry data to represent the

outer oceanic sea-level. The geostrophic rise, ζ_{FC} , includes both the barotropic component that is expected to dominate closer to the slope, and the baroclinic component that is expected to dominate farther offshore (see Fig. 3).

2. Overview of the data

In the present analysis we consider low-frequency processes for which the geostrophic balance applies. The motivation is that our database of hydrography is seasonal and the satellite altimetry has a 10-day resolution. Only the coastal water-level data has a high resolution in time and an accuracy better than 1 cm. In comparison, the satellite altimetry has an accuracy on the order of 2–3 cm. Details of the data are presented in this section.

2.1. Coastal water-level, air pressure and altimetry

Water-level and air pressure data measured at Tórshavn, throughout the nineties (Fig. 2) were obtained from the Danish Meteorological Institute (DMI). The water-level data are sampled each hour, and a daily average is found by averaging over approximately two semidiurnal lunar tidal periods (25 h). This gives essentially the same

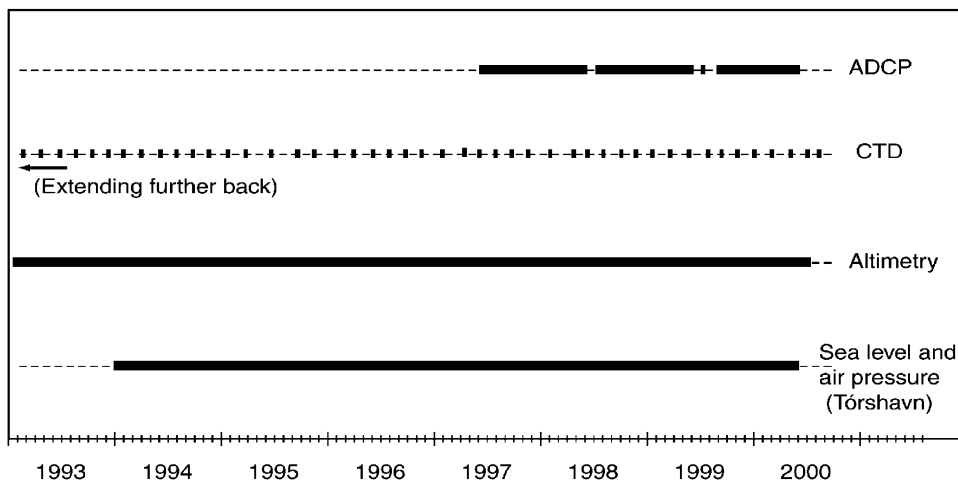


Fig. 2. Overview of data (thick horizontal bars). The dotted CTD-bar indicates that these data are only available from four to six cruises a year.

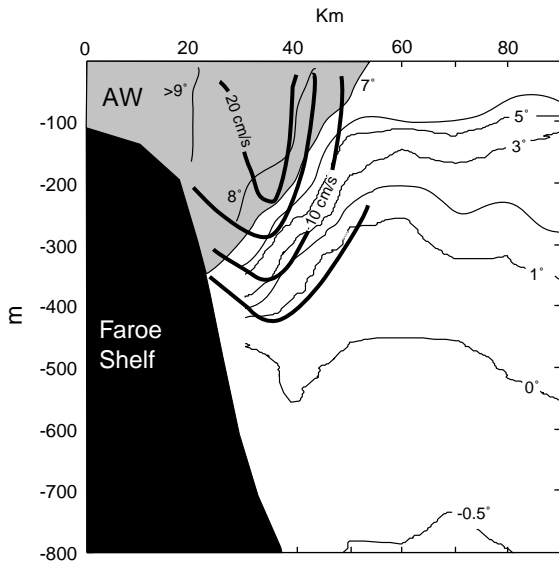


Fig. 3. A vertical section through the FC, looking west through the section in Fig. 1a. The averaged isovels are shown with the thick lines and the thin lines show the temperature field on 7 November 1999. The gray area indicates undiluted Atlantic water (AW, warmer than 7°C) on this particular day.

result as subtracting the tides predicted from the 12 largest constituents from the observed water levels (Noralf Slotsvik, pers. comm.). Water-level data from 3 January to 4 February 1998 and from 8 April to 29 June 1998 were missing in the time-series. These periods were patched with data from other sites in the Faroes, made available by the Faroese Office of Public Works (Heinesen, 2001). When low-pass filtered, these additional water-level time-series correlated well with the data from Tórshavn, $R = 0.97–0.99$. For two random variables x and y the correlation coefficient, R is defined as

$$R = \frac{1}{N-1} \sum_{i=1}^N \frac{(x_i - \bar{x})(y - \bar{y})}{s_x s_y}, \quad (6)$$

where N is the length of the time-series and s_x and s_y are the standard deviations for the two data records (Emery and Thomson, 1997).

The pressure data are sampled every 3 h (0, 3, 6, ..., 21 GMT), but some days these samplings are more irregular. All data for each day are averaged. One millibar increase in air pressure will in the static limit depress the sea-level about 1 cm, and in

order to account for this atmospheric contribution, an adjusted water-level time-series is produced by adding the air pressure time-series to the measured water-level series, the so-called inverse barometer effect,

$$\zeta_T = \zeta_{\text{measured}} + (p_{\text{atm}} - \overline{p_{\text{atm}}}), \quad (7)$$

where the overbar means averaged pressure. This eliminates most of the contribution from the meteorological variability.

Satellite altimetry data are also used (Pathfinder team, 2001). These data measured by the TOPEX/POSEIDON (T/P) and ERS-1 satellites are corrected for tides and the inverse barometer effect and sea-level anomalies are calculated relative to a mean which again is calculated over the past 3 years of data (refer to Pathfinder team, 2001 for details). The rms-error in the T/P-data is about 2 cm while it is somewhat higher for the ERS-1 data. The points where the T/P tracks cross the standard section are used together with a point further north situated at 65°46'N, 5°05'W, as shown in Fig. 1b. Each track has an exact repeat period of almost 10 days (9.92 days), giving us instantaneous data values with this sampling period. Data from the track labeled 'track 1' will be used later.

2.2. Acoustic Doppler Current Profiler and hydrographic data

As a part of the Nordic World Ocean Circulation Experiment (WOCE) and Variability of Exchanges In the Nordic seas (VEINS) projects, RDI Broadband Acoustic Doppler Current Profilers (ADCPs) were deployed in 1994 (Fig. 1a), and these have been measuring the current to date, with some gaps. Here, data from three mooring sites NA, NB and NC (see Fig. 1a), measured from June 1997 to June 2000, are used. The data from the ADCP instruments give current speed and directions in equidistant bins (depth intervals which are 10 m at NA and 25 m at NB and NC) through most of the water column above the instrument. The sampling interval was 20 min. All data have been preprocessed by the Faroese Fisheries Laboratory (FFL) (Larsen et al., 1999) and (Hansen et al., 1999a) and only daily averaged

velocities are used, from which the tidal signal has been removed (Hansen et al., submitted for publication). The ADCP data do not extend all the way to the surface and the uppermost bins can be rather gappy, due to a weak reflection of the sound pulse. If the data are too sparse, the entire day is error coded.

Hydrographic data from CTD (Conductivity, Temperature and Depth) stations N04–N10, spaced along the standard section north of the Faroes (Fig. 1a) are used to compute the buoyancy field. These data are acquired from 55 hydrographic cruises with R/V *Magnus Heinason*, along these standard stations (see Fig. 2).

A total eastward transport Q_{Tot} , perpendicular to the standard section is calculated for periods when at least three ADCPs (NA, NB and NC) have been measuring at the same time. Average temperature and salinity fields are calculated using many sections of hydrographic data, and the specific transport of Atlantic water, Q_{Atl} , ($T > 7^\circ\text{C}$, $S > 35.15$) is based on this TS -field in combination with current data for the periods shown in Fig. 2 (Hansen et al., 1999b). The accuracy of the Atlantic transport data is discussed in (Hansen et al., submitted for publication) and is roughly on the order of 0.5 Sv. The accuracy of the total transport data is somewhat less. The total volume flux in the FC contains some Arctic melt water in the East Icelandic Current that contributes to the buoyancy of the FC. It is unknown how much additional Atlantic water enters the Norwegian Sea through entrainment to these flows. From the hydrography, it appears to be less than 1 Sv. In addition, there is an unmeasured contribution of barotropic surface rise that reaches to the deeper layers out to the outer reference point, beyond the current meter section.

3. Results

The relation between the inflow transports, Q_{Tot} and Q_{Atl} , and the sea-level rise ζ_{FC} , is at first assumed to be linear, and these transports are used in place of ζ_{FC} in order to check the validity of Eq. (5).

3.1. The time-series

The basic time-series for the data to be analyzed in this paper are shown in Fig. 4. Here we present more than 6 years of surface rise across the FC and a 3-year long series of Atlantic water transport computed from in situ measurements.

3.2. Correlations

The instantaneously measured (and corrected) altimetry data are assumed to represent the local sea-level on the measurement day. Time-series of the sea-level gradient across the FC, ζ_{FC} , are obtained by subtracting the altimetry data from the adjusted coastal sea-level at Tórshavn, averaged over the days when the altimetric measurements are made. This ζ_{FC} -field, calculated from the altimetry field to the north of the Faroes, is compared to the inflow transports Q_{Tot} and Q_{Atl} . The highest correlations ($R > 0.5$) were found using the altimetry data from the region indicated with the circles in Fig. 1b. Scatter diagrams between ζ_{FC} and the transports, using the altimetry point giving the very highest correlations, are shown in Fig. 5. The full lines are “best fit” lines from a normal linear regression while the dashed lines show the so-called *neutral* regression lines (Emery and Thomson, 1997, Section 3.13). The latter lines can be a good choice when it is not

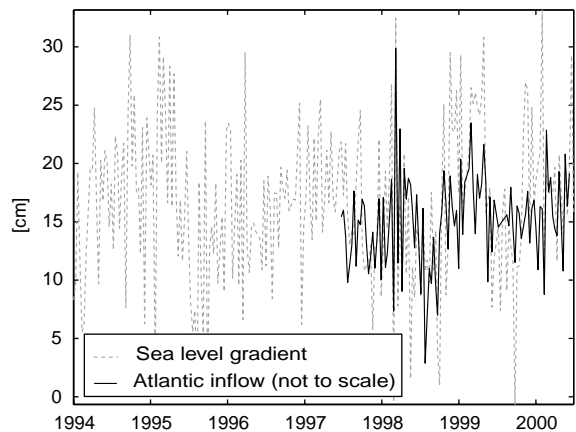


Fig. 4. Comparison of the more than 6-year long sea-level rise time-series ζ_{FC} and the 3-year long Atlantic water transport time-series Q_{Atl} .

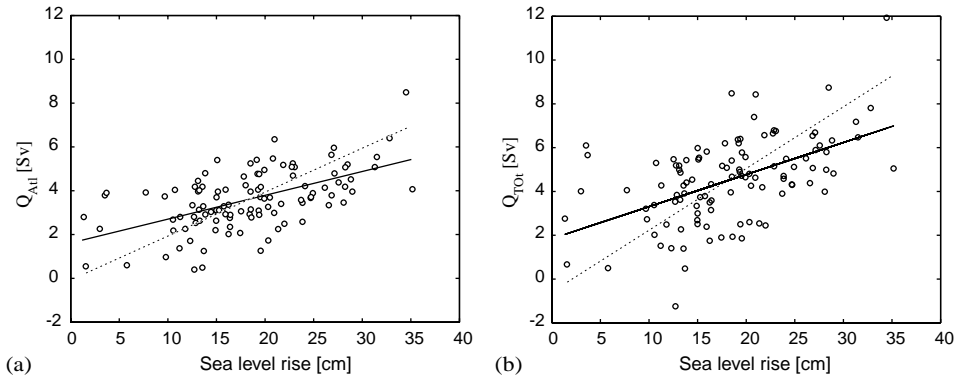


Fig. 5. Correlation between the sea-level rise across the FC and the daily inflow transports: (a) Atlantic inflow and (b) total inflow. Linear regression lines are fitted to the data (full lines) and the so-called *neutral* regression lines are also shown (dashed lines).

Table 1

Results from an ordinary linear regression between the transports Q_{Atl} and Q_{Tot} and the sea-level rise ζ_{FC} (see text for explanation)

	Correlation	Regression slope (Sv/cm)	Average (Sv)	σ_{rms} (cm)	Error (%)
Atlantic Q	0.56	0.11	3.6	5.8	19
Total Q	0.52	0.15	4.5	6.0	19

obvious which of the variables, Q or ζ_{FC} , is the dependent variable and which is the independent.

The results from the ordinary regressions are shown in Table 1. The σ_{rms} are the standard deviations of ζ_{FC} from the ordinary linear regressions, and by multiplying these with the slopes $dQ/d\zeta_{FC}$ the corresponding errors in the transports are found. These errors are given as a percentage of the average flows in the table. In reality, the relation between the transports and the surface rise is non-linear, depending on the thickness of the baroclinic transport. The data do not show a clear deviation from linearity to reveal such a distinction. The thermal wind (baroclinic velocity field) is treated in more detail by Hátún and Hansen (submitted for publication).

3.3. Coherency

A coherency analysis is also made between the inflows and the sea-level rise ζ_{FC} . The *coherency squared* between two time-series $x_1(t)$ and $x_2(t)$ is

given as

$$\gamma_{12}^2(\omega) = \frac{|G_{12}(\omega)|^2}{G_{11}(\omega)G_{22}(\omega)}, \quad (8)$$

where ω is the frequency, G_{11} , G_{22} are auto-spectra and G_{12} is the cross-spectrum between the time-series. This coherence-squared function gives the correlation between the time-series as a function of frequency ω . This analysis is made for the 3 years 1997–1998, 1998–1999 and 1999–2000, individually (340 days each year) and the three resulting coherence-squared functions are then averaged. Fig. 6 shows the result when using the Atlantic transport Q_{Atl} , and significant coherencies are found for the variations with periods $T_1 \approx 21$ days and $T_2 \approx 360$ days. The spectra also allow the calculation of the phase lag as a function of ω , but these phase lags were negligible here, indicating that the variations in the inflow and in the gradient are in phase. The high coherency at 360 days is clearly the seasonal signal in all the data, but it is not clear why the coherency at 21 days should be larger than the semi-annual signal. Since the Nyquist period is about 20 days, the coherency

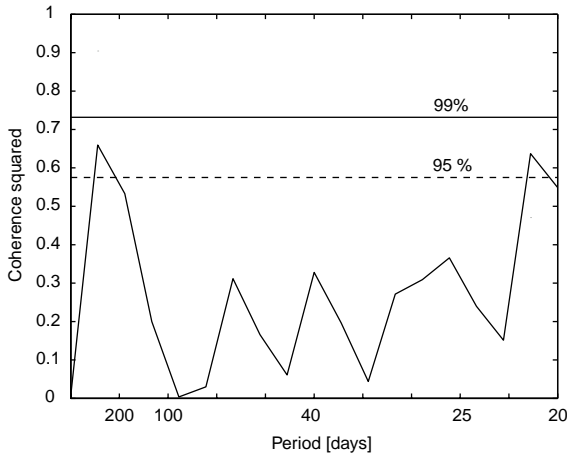


Fig. 6. Coherence-squared plot from an analysis between the transport of Atlantic water Q_{Atl} and the sea-level rise ζ_{FC} . The 99% and 95% significance levels are indicated.

may be high for a wider frequency range, but this cannot be found.

3.4. Altimetry and steric height

The steric anomaly which stems mainly from the buoyancy of the Atlantic water is given by

$$\zeta_{STERIC} = \frac{1}{\rho_{ref}} \int_{ref}^0 (\rho_{ref} - \rho(z)) dz, \quad (9)$$

where $\rho(z)$ is the varying density up through the water column and ρ_{ref} is the water density at a reference depth of 800 m, well below the Atlantic water in the FC. This reference density varied very little during the measurement period (Hansen and Østerhus, 2000). The steric height has been calculated using the hydrographic data at N07 (63°20'N, 6°05'W) and this is compared to altimetry data from a measurement point along T/P track 1, about 5 km away from the hydrographic station (Fig. 7). Altimetry data were interpolated into daily values using a cubic-spline interpolation and then sub-sampled at the 26 CTD-times. Comparing the sub-sampled altimetry and the steric height gave a correlation coefficient of $R = 0.75$. It is evident that altimetry data reflect the steric height.

Ignoring the barotropic mode that produces currents in the deeper, homogeneous layer, the

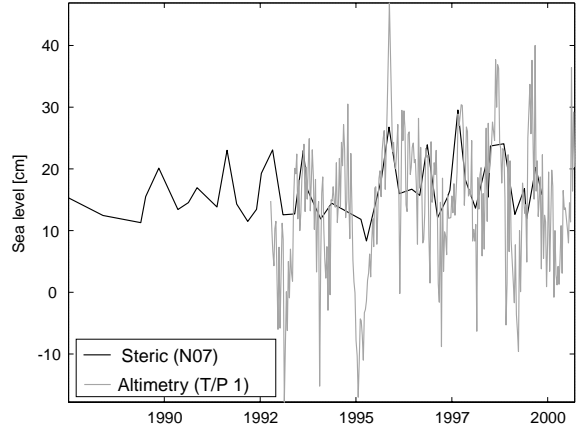


Fig. 7. Comparison of the steric height at station N07 and the altimetry from a point on track 1, which lies near the hydrographic station (see Fig. 1).

baroclinic transport is clearly related to the geostrophic balance between the Coriolis term and the slope of ζ_{STERIC} . Since ζ_{STERIC} is proportional to the thickness of the buoyant layer and the geostrophic velocity is proportional to the horizontal gradient of ζ , the integral across the flow is proportional to the square of the steric rise. This is the baroclinic transport.

3.5. Low-frequency (seasonal) variations

Both types of data in Fig. 7 show a clear seasonal variation and the same is found in the adjusted coastal water-level at Tórshavn. A less clear seasonality is found in the inflow transports.

To examine this further, a sinusoidal seasonal model of the form

$$a + b \sin \left(\frac{2\pi t}{365 \text{ days}} - c \right) \quad (10)$$

is fitted (using the utility “Curve Fix”) to the coastal water-level, the transports, the steric heights at hydrographic stations N05–N10 (only these are in water that is deeper than the 800 m reference depth) and the altimetry data from the points where the tracks cross the standard section, as shown with the squares in Fig. 1b. In Eq. (10), t is in days, the coefficient a is an offset, b is an amplitude and c is the annual phase relative to the

Table 2
Fitting of the sinusoidal seasonal model $a + b \sin(2\pi t/365 - c)$ to data

	a	b	Pos. (latitude)
Total flux (Q_{Tot})	4.5 Sv	0.8 Sv	—
Atlantic flux (Q_{Atl})	3.6 Sv	0.5 Sv	—
T/P track 59	—	6.9 cm	65° 19'N
T/P track 21	—	8.4 cm	64° 58'N
T/P track 7	—	7.1 cm	64° 53'N
T/P track 110	—	7.6 cm	64° 34'N
T/P track 45	—	8.0 cm	64° 27'N
T/P track 72	—	7.5 cm	64° 05'N
N10, T/P track 83	14.1 cm, —	2.0 cm, 7.9 cm	63° 50'N
N09	13.6 cm	2.2 cm	63° 40'N
N08, T/P track 34	15.4 cm, —	4.3 cm, 8.0 cm	63° 30'N
N07, T/P track 1	16.6 cm, —	4.8 cm, 8.2 cm	63° 20'N
N06	19.4 cm	4.5 cm	63° 10'N
N05	22.9 cm	4.6 cm	63° 00'N
T/P track 123	—	5.4 cm	62° 49'N
T/P track 32	—	5.2 cm	62° 39'N
WL at Tórshavn (ζ_T)	4.5 cm	5.9 cm	62° 00'N

Note: The rows are ordered with the southernmost measurements lowest and the northernmost highest in the table. The latitudes are shown but the longitudes are ignored since they all lie close to 6°W. Altimetry data and steric heights are put into the same rows if they are situated less than 5 km apart.

start of the time-series. The model fit, gave $0.55 < R < 0.75$, for all data. The results are shown in Table 2. The coastal water-level, the altimetry and the steric heights all show a minimum in March when the transports have their maximum.

The average was subtracted from the altimetry data prior to the analysis because the absolute values of these data are not very accurate, and the constant a is thus not meaningful here. For the steric heights, this constant increased from about 14 cm at N10, which is at the northern flank of the FC, to about 23 cm at N05 situated close to the current core (Table 2). This gives an average increase in steric height of roughly 9 cm across the current, which is the average baroclinic contribution to the total sea-level rise.

The seasonal amplitudes in steric height, b , decrease from 4.6 cm at N05 to 2 cm at N10 and we can deduce that steric height variations are probably low in the central Norwegian Sea. The amplitudes in the altimetry data, on the other hand, do not vary as much with latitude: between 7 and 8.5 cm.

4. Discussion

The scatter diagrams in Fig. 5 indicate a linear relation between the inflows and the sea-level rise, and this supports Eq. (3) with Eq. (5). From the results in Table 1, we now suggest the linear algorithms

$$Q_{Atl} = (11 \pm 2)\zeta_{FC}, \quad (11a)$$

$$Q_{Tot} = (15 \pm 3)\zeta_{FC}, \quad (11b)$$

where the Q 's are in Sv ($Sv = 10^6 \text{ m}^3/\text{s}$) and ζ_{FC} is in meters.

Comparing this to the findings of McClimans et al. (1999), we see that the coefficients found here are about half of those found in Norway. This means that a transport Q in the FC will correspond to a sea-level rise twice as large as a sea-level rise in Norwegian waters, induced by the same transport. This implies an equivalent barotropic current thickness that is half that of the NAC. The neutral regressions, shown in Fig. 5, give similar slopes to those found in Norway, implying a current thickness over 400 m, but,

although this seems plausible, the use of such a regression is not recommended when there are errors in both variables (Emery and Thomson, 1997).

The Atlantic transport showed a larger correlation to the sea-level rise than did the total transport, as seen in Table 1, and the coherency at the shorter period $T_2 \approx 21$ days (see Fig. 6) was also more significant between these two former time-series. The Atlantic water masses rest against the Faroe shelf, close to the current core, where the barotropic component is more dominant than in the more off-shore waters. The Atlantic inflow will therefore be the more barotropic of the two inflows. The barotropic component is proportional to ζ_{FC} while the baroclinic component is proportional to ζ_{FC}^2 , and variations will also be more rapid in the barotropic transport. This supports the better correlation between Q_{Atl} and ζ_{FC} , especially for the shorter time scales. Since the buoyancy of the FC is primarily derived from the Atlantic water, we expect a reasonable correlation also for the more sluggish baroclinic transport.

Some of the seasonal variation in the altimetry data closer to land captures the seasonality in the steric height, but, as seen in Table 2, this is probably not so in the region farther north where the largest correlations are found. The chosen altimetry area lies north of the Iceland-Faroe Front and to the east of the Jan Mayen Front (Hansen and Østerhus, 2000), and is therefore not disturbed by the dynamics in the FC or in the East Icelandic Current. We assume that the variability in the satellite altimetry closer to the FC reflects mesoscale eddies in the outer part of the inflow. An interesting observation is that the altimetry points giving the very highest correlations ($R > 0.50$) were all situated above a seamount rising about 600–700 m above the surrounding bathymetry. This bump could induce a Taylor column, protecting the region from spurious signals. The seasonality in the altimetry data here is probably caused by the annual sea-level variability in the entire Arctic Basin.

The seasonal variation in the coastal water-level, with a minimum in March when the inflow transport seems to be at a maximum, was a surprise at first (Hátún, 2000). However, when

subtracting the altimetry north of $63^\circ 15'N$, which has an even larger seasonal variation than that found at Tórshavn, from the data at Tórshavn, the apparent seasonality in sea-level gradient and in the transports are in phase, as is expected from geostrophy. Fig. 4 indicates, however, that the apparent seasonal variations during the years 1997–2000, when sufficient ADCP data exist, are not present in 1994 and 1996. A 2 year cycle seems to be more evident if anything, so if the relation between the sea-level gradient and the inflow found here, applies, we can deduce that the seasonal variation in the inflow is not a persistent feature, and varies with the NAO.

The analysis includes 108 data points so the correlations are statistically significant ($p < 0.001$), assuring us that the geostrophic balance in the FC can be monitored with sea-level measurements. It is not possible to use only altimetry data to calculate the sea-level rise. The altimetry data are adjusted with a global tidal model which is too inaccurate on shallow shelf water, so a combination of offshore altimetry and coastal water-level seems to be the necessary combination to estimate the rise. A recording bottom pressure sensor in the outer domain can be a viable alternative.

We have repeated the correlation analysis after removing the seasonal variability in both Q and ζ_{FC} . This reduced R from 0.56 and 0.52. With such low correlations it seems hardly reasonable to fit a line for predictive purposes.

The standard deviation of ζ_{FC} from the linear regression was nearly 6 cm whereof 2–3 cm can be assigned to the inaccuracy in the altimetry data. Some of the remaining error may be due to mesoscale eddy activity in the Iceland-Faroe Front, a coastal current which circulates the Faroe Plateau, possible local wind effects, some steric effect because of different densities in off-shelf and on-shelf waters, and the fact that the water-level signal at Tórshavn also can be affected by waters to the south, east and west of the islands. In addition to this, the baroclinic component in the FC that accounts for a large part of the total transport, is proportional to ζ_{FC}^2 .

A better understanding of these effects is necessary if a reliable algorithm linking sea-level gradients to the transports is to be established. Such an algorithm

would be a good supplement to the more expensive in situ current measurements, and it also would allow us to look back at the early nineties when no comprehensive current data are available.

5. Conclusions

The inflow of Atlantic water in the Faroe Current, Q_{Atl} , calculated from ADCP data and hydrographic data, has been compared to the sea-level rise, ζ_{FC} , across this current. The sea-level rise is found as the difference between the coastal water-level at Tórshavn and the oceanic sea-level measured by altimetry to the north of the Faroes. A reasonable correlation ($R = 0.56$, $p < 0.001$) between Q_{Atl} and ζ_{FC} is found when altimetry data from the region $65^{\circ}50'N$ and $5^{\circ}00'W$ are used. Linear algorithms, $Q_{Atl} \approx (11 \pm 2)\zeta_{FC}$ and ($Q_{Tot} \approx (15 \pm 3)\zeta_{FC}$) between, Q in Sv and ζ_{FC} in meters are suggested. It is close to a similar algorithm derived for the NAC. There is a seasonal variation in the steric heights, the coastal water-level and the altimetry data which all have a minimum in March and there is a seasonal variation in the water mass transports with a maximum in March. The sea-level rise across the Faroe Current shows a seasonal variation during the period 1997–2000, when ADCP data exist, but this seasonality is not evident in 1994 and 1996. During this period, however, there was an abnormally low seasonal variability in ζ_{OCEAN} . This leads us to think that the apparent seasonality in the inflow of Atlantic water is not a persistent phenomenon over decades.

Acknowledgements

This work was completed with support from the Nordic Arctic Research Program (Project No. 5-089) and the EU Fifth Framework Program

project MAIA (Contract No. EVK2-CT1999-00008). We thank Bogi Hansen and other colleagues in MAIA for helpful discussions. We also thank D. Hainbücher and an anonymous referee for suggestions that led to many improvements in our presentation.

References

- Emery, W.J., Thomson, R.E., 1997. Data Analysis Methods in Physical Oceanography. Pergamon Press, New York, 634pp.
- Hansen, B., Østerhus, S., 2000. North Atlantic–Nordic Sea exchanges. Progress in Oceanography 45, 109–208.
- Hansen, B., Larsen, K.M.H., Kristiansen, R., 1999a. ADCP deployments in Faroese waters 1997–1999. Faroese Fisheries Laboratory, Technical Report No.: 99–07, 57pp.
- Hansen, B., Østerhus, S., Kristiansen, R., Larsen, K.M.H., 1999b. The Iceland–Faroe inflow of Atlantic water to the Nordic seas. ICES CM 1999/L: 21, 14pp.
- Hansen, B., Østerhus, S., Hátún, H., Kristiansen, R., Larsen, K.M.H. The Iceland–Faroe inflow of Atlantic water to the Nordic seas. Progress in Oceanography, submitted for publication.
- Hátún, H., 2000. On the accuracy of computing slope current transports from current meter arrays. Diploma Thesis, Department of Physics, Norwegian University of Science and Technology, Trondheim Norway, 97pp.
- Hátún, H., Hansen, B. Using an “inverse dynamic method” to determine temperature and salinity fields from ADCP measurements. Journal of Atmospheric and Oceanic Technology, submitted for publication.
- Heinesen, S., 2001. Coastal Water Level Data. Landsverkfrø, dingurin, Tórshavn.
- Jacobs, G.A., Born, G.H., Parke, M.E., Allen, P.C., 1992. The global structure of the annual and semiannual sea surface height variability from geosat altimeter data. Journal of Geophysical Research 97, 17813–17828.
- Larsen, K.M.H., Hansen, B., Kristiansen, R., 1999. Nordic WOCE ADCP deployments 1994–1997. The Faroese Fisheries Laboratory, Technical Report.: 99–05, 53pp.
- McClimans, T.A., Johannesen, B.O., Jenserud, T., 1999. Monitoring a shelf edge current using bottom pressure or coastal sea-level data. Continental Shelf Research 19, 1265–1283.
- Pathfinder team, 2001. Altimetry data. WWW page, <http://neptune.gsfc.nasa.gov/ocean.html>.

Blank

PAPER IV

Variability in the Iceland-Faroe Front and in the Faroe Current due to incident Topographic Rossby waves

Hjálmar Hátún

Faroese Fisheries Laboratory, Tórshavn, Faroe Islands

Energetic signals with periods between three and seven days are repeatedly reported in the Nordic Seas. The transport variation in the Faroe Current, flowing eastward north of the Faroe Islands, has a spectral peak around five days, and these fluctuations co-vary with the along-isobath current velocities well below the inflowing Atlantic water. The signal is observed as a distinct, weak zonal oscillation throughout the water column north of the Faroe Current, which propagates southward with about 0.2 m/s. The oscillations satisfy the dispersion relation of a barotropic Topographic Rossby wave with a wavelength of 80 km, and they intensify as the wave propagates onto the relatively steep Faroe Shelf. The waves are most active during the period January-April and they are nearly absent from August to December. A simple two-layer model has been invoked to describe how these waves excite the Iceland-Faroe Front and cause oscillations in the Atlantic transport in the Faroe Current. The origin of the fluctuations is not known. It is, however, hypothesized that they are either generated along the Jan Mayen Ridge due to meandering of the Jan Mayen Front or in the Jan Mayen Channel, where through-flows exhibit oscillations with similar short periods and with a seasonal variation similar to that of the waves. These waves seem to influence the bifurcation of the Faroe Current at the north-eastern corner of the Faroe Plateau.

1. INTRODUCTION

Meridional oceanic transports of heat and salt towards Arctic regions are of key importance for regional and global climate. The relatively mild climate in Northern Europe and in the countries adjacent to the eastern Nordic Seas shore is partly ascribed to the pole-ward Atlantic inflow over the Greenland-Scotland Ridge [Seager et al., 2002]. After having released large amounts of heat to the region [Simonsen and Haugan, 1996], these Atlantic water masses sink due to their cooling and their relatively high salinity and the denser and deeper equatorward flowing overflows are formed. These overflows constitute much of the North Atlantic Deep Water (NADW), which is one of the key variables to Earth's response to climate change [Dickson and Brown, 1994].

The importance of this inflow for the marine ecology in the Arctic Mediterranean has been known for more than a century [Helland-Hansen and Nansen, 1909]. The local climate and the important fisheries, and thereby the living conditions on the Faroe Islands, is vitally dependent on the Atlantic water surrounding the islands. The Iceland-Faroe Front, situated just north of the Faroes (Fig. 1a), forms a boundary between the Atlantic- and the cold Arctic water masses, and small displacements in this front could therefore have critical consequence for this society.

The narrowness of the Atlantic inflow around the Faroes makes this an ideal region for monitoring of these important inflows. The Nordic WOCE (World Ocean Circulation Experiment) project, commencing in 1994, made it possible to deploy rows of semi-permanent acoustic Doppler current

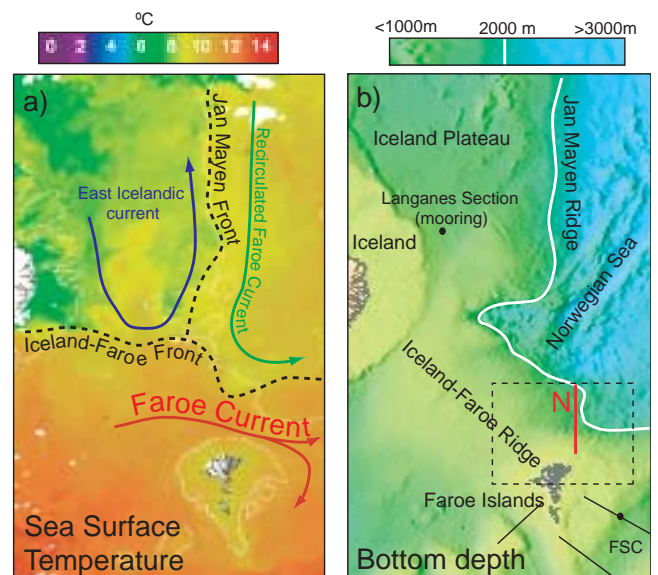


Figure 1 Regional geography: a) AVHRR Sea Surface Temperature (SST) composite observed during the period 19-25 August 2001. The approximate position of the main fronts and the main currents are illustrated; b) Topography obtained from the ETOPO 1 (1-minute resolution) database (<http://www.mapconnection.com/etopo.html>). The dashed rectangle indicates the discussed Faroe Shelf region and the meridional red line represents the standard section N (Fig. 2). Current measurements, other than those along the main section are shown as black dots and the black lines branching out from the Faroes are other standard sections.

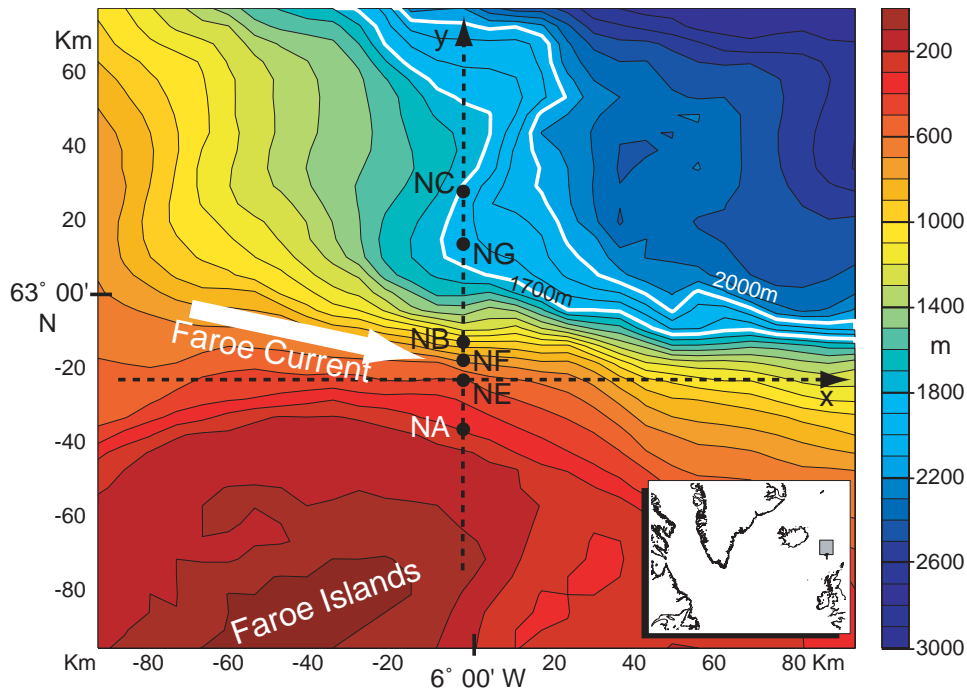


Figure 2 The measurement section with surrounding bathymetry. ADCP moorings are shown as circles and the coordinate frame, with the y-axis oriented along the section, is illustrated. The 1700 m and 2000 m isobaths are highlighted.

profilers (ADCPs) along the already existing standard hydrographic sections radiating out from the Faroes (Fig. 1b), and reliable time series of transports (volume, heat and salt) across Iceland-Scotland Ridge are now available [Hansen et al., 2003; Turrell et al., 2003]. The inflow branch between Iceland and the Faroes continues eastward, as the relatively narrow Faroe Current, sandwiched between the Iceland-Faroe Front and the Faroe Shelf (Fig. 1a). The standard measurement section N crosses the inflow in this area (Fig. 1b).

The Iceland-Faroe Ridge is a 4-500 m deep plateau extending from the Iceland Shelf to the Faroe Shelf, generally deepening towards the Faroes (Fig. 1b). The Iceland Plateau descends gradually into the abyss of the Norwegian Sea at the Jan Mayen Ridge. This north-south slope is relatively even to the north, but is disrupted by a gorge further south, where it joins the northern slope of the Iceland-Faroe Ridge east of Iceland. The isobaths near standard section N, but north of the 63°N meridian, are generally oriented north-south (Fig. 2) illustrating the rather weak east-west bottom gradient in this region. But at about 63°N, the isobaths congregate and become zonally aligned illustrating the steeper northern side of the Faroe Shelf. The Jan Mayen Front, which has been associated with the 34.8 isohaline [Read and Pollard, 1992], is linked to the Jan Mayen Ridge. To the south it typically intersects the more zonal Iceland-Faroe Front, which has been associated with the 35.0 isohaline [Hansen and Meincke, 1979], (Fig. 1a).

Short time-scale variability has often been neglected when discussing inter-ocean exchanges. This is mainly caused by a lack of observations and a lack of knowledge of the processes. It is thus often assumed, or hoped, that such variability will average out when looking at monthly and annual averages. With the increased monitoring of the oceans during the last decade(s), such small- and mesoscale processes and their impact on the large-scale circulations are presently getting an increased interest [Kantha and Clayson, 2000].

The large variability in the Iceland-Faroe Front was first addressed by Hansen and Meincke [1979]. They found eddies and meanders with horizontal scales of the order 50 km and considerable energy was found in the range from 3 to 24 days. Direct current observations showed transient current fluctuation in the period range of 3 to 5 days [Meincke and Kvinge, 1978] and based on a 1-year current record at near-bottom depth close to the front northwest of the Faroes, Willebrand and Meincke [1980] found a winter-doubling of horizontal kinetic energy for the 3- to 10-day period. These fluctuations will have implications for: 1) the intermittent overflows over the Iceland-Faroe Ridge [Hansen and Meincke, 1979], 2) heat and salt fluxes across the front directly into the Norwegian Sea [Willebrand and Meincke, 1980], [Hallock, 1985] and 3) the hydrography and marine ecosystem on the Faroe Plateau [Hansen and Meincke, 1984], [Gaard and Hansen, 2000]. Baroclinic instability in the front was found to be the generation mechanism for these oscillations, dwarfing the atmospheric influence by an order of magnitude [Willebrand and Meincke, 1980]. Oscillations with a similar period (2-3 days) were also observed along the Norwegian Shelf and the driving mechanism was assigned to baroclinic instability [Mysak and Schott, 1977], [Schott and Bock, 1980]. Periods in the range 3 to 7 days have since then been reported in the Norwegian Sea, where atmospheric forcing is found to be the driving agent [Skagseth and Orvik, 2002]. Another explanation for the characteristic variability in the mentioned period range has been basin scale modes with Kelvin-like disturbances circulating cyclonically around the GIN (Greenland-Iceland-Norwegian) Seas [Tom Hopkins, private correspondence]. This has, however, never been proven. Despite the large effort given to understand the variability in the Iceland-Faroe Front [Hansen and Østerhus, 2000], explanations on the generating mechanisms at play are still lacking.

The ADCP data set comprises the first both spatially and temporally comprehensive *in situ* observations from the re-

gion. The Atlantic transport in the Faroe Current, calculated from this data material [Hansen et al. 2003] showed variations at one week's time-scales. By analyzing current and hydrography data together, it was found that the near bottom expression of the Iceland-Faroe Front along section N had clear variations with periods on the order of a month, but a secondary spectral peak was also found for periods around 5-7 days [Hátún et al., 2003].

Most attention is normally given to the upper 500 m when studying the Atlantic inflow in the Nordic Seas, and the deeper layers are often overlooked. With only hydrographic data at hand, a level of no motion under the Atlantic layer has often been assumed in order to calculate fluxes. This paper will challenge this view, and supported by deep long-term current measurements at section N, it will be deduced that the abyss is not so peaceful after all. The previously suggested baroclinic instability is certainly present in the Iceland-Faroe Front, but southward propagating Topographic Rossby waves guided by the Jan Mayen Ridge and the Iceland-Faroe Ridge might well be the process that initiates the instabilities, and thereby determines the winter maximum observed.

Many authors have reported the dominance of bottom-trapped Topographic Rossby waves for sub-inertial periods [Rhines, 1970], [Csanady, 1988], [Shaw and Csanady, 1988], [Pickart, 1995]. Propagation of such waves onto a continental slope has likewise been observed and modeled by many [Thomson, 1971], [Kroll and Niiler, 1976], [Petrie and Smith, 1977], [Ou and Beardsley, 1980] [Louis and Smith, 1982], [Shaw and Csanady, 1988], [Aikman et al., 1988] and [Pickart, 1995].

A Topographic-Rossby mode resonance with a period of 1.8 days has been reported on the southwestern side of the Iceland-Faroe Ridge [Miller et al., 1996]. Apart from this, no literature on deep quasi-geostrophic motions exists for the Iceland-Faroe Ridge area, to my knowledge.

Section 2 starts by giving a short presentation of the data material, and the identification of a clear signal with a 4-6 days period is shown in Section 3. These oscillations are recognized as southward propagating Topographic-Rossby waves in Section 4 and two simple analytical models are employed in Section 5 in order to describe the propagation of the waves onto the Faroe Shelf. These models are also validated against data in section 5 and a summary and discussion follow in Section 6. Some supplementary information is given in an appendix.

2. DATA MATERIAL

The basic data material discussed in this paper is obtained along standard section N (Figs. 1- 3) extending northwards from the Faroe Shelf. The dataset includes Acoustic Doppler Current Profilers (ADCPs), a recording current meter (RCM, Aanderaa) moored near the sea bed, (Fig. 3a) and regular CTD-transects (Conductivity, Temperature and Depth). The periods of operation are shown in Fig. 3b. Information on the observations and data treatment may be found in Hansen et al., [2003]. The ADCP data are given as current magnitude and direction in evenly spaced depth intervals (bins), and the bins at each mooring have been interpolated to the same horizontal levels, having a bin height of 10m. Observations, sampled every 20 minute, are averaged to hourly values.

Current data from an ADCP on the Faroe Shelf in the Faroe-Shetland Channel (FSC) [Larsen et al., 2000] will be mentioned in brief (see Fig. 1b). Likewise will data from deep RCMs at the Langanes section [personal correspondence with Steingímur Jónsson], the Svinøy section [Orvik et al., 2001] and the Lofoten Basin [personal correspondence with Kjell Arne Mork] be mentioned briefly. Some results from a RCM moored in the Jan Mayen Channel [personal correspondence with Svein Østerhus] will be used.

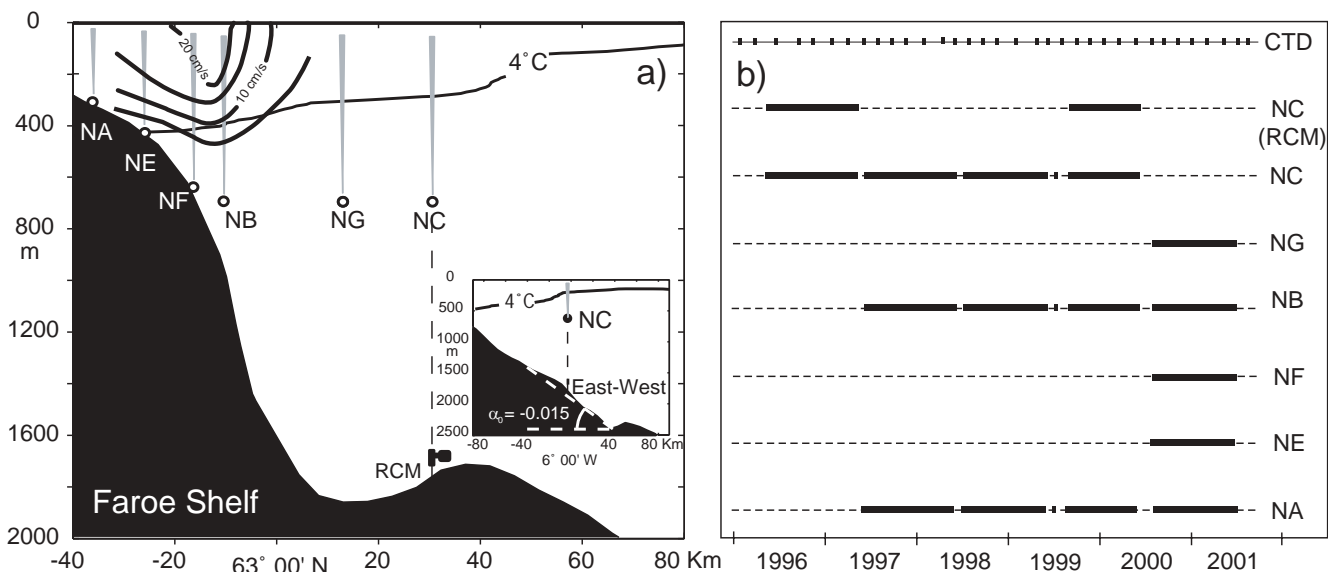


Figure 3 Basic data-material. a) A view from east to west of the measurement section. The Faroe Shelf is shown to the left, the ADCP instruments are illustrated with the circles, and the gray cones represent their acoustic beams. The bold lines illustrate the averaged profile of the jet-like Faroe Current, and the 4 °C isotherm measured on the 4-5 May 1999 is shown. The inset shows an east-west profile approx. 22 km north of mooring NC. The 4 °C isotherm measured on the 9th of May 1999 is shown, and the large-scale zonal bottom gradient, α_0 , is displayed. b) The periods when the instruments were in operation are illustrated as black rectangles, and the timing of CTD transects is shown with the black dots.

3. EVIDENCE OF OSCILLATIONS WITH A 4-6 DAYS PERIOD

3.1 Pattern of Variability and Periods

Regular and energetic fluctuations can be observed under the interface that segregates the Atlantic water masses in the wedge shaped Faroe Current from the Arctic water masses underneath. The residual eastward current velocities in this lower layer (> 500 m) are relatively small compared to the average velocity profile in the Faroe Current (Fig. 3a).

A nearly yearlong current time series from mooring NB at 600 m depth is shown in Fig. 4a. Wavelet analysis is applied to study the frequency content in this series as a function of time, and the so-called scalogram in Fig. 4b is obtained with this method. The scalogram shows the relative energy content in the signal as a function of time-scale (frequency, y-axis) and time (x-axis), and regions encircled with black lines are areas where the power spectrum is significantly higher than the spectrum for a red-noise lag-1 autoregressive process [Torrence and Compo, 1998]. The software used for the analysis in this paper is adopted from the URL: <http://paos.colorado.edu/research/wavelets/>, and the continuous *Morlet mother wavelet* is employed. Averaging the scalogram in time gives the *global wavelet spectrum* in Fig. 4c and three distinct spectral peaks, T5- ~ 4 -5 days, T5+ ~ 5 -6 days and T15 ~ 14 -16 days, respectively, emerge.

A 100-day period with regular oscillations in this lower layer is indicated with the dashed rectangle in Fig. 4a. In order to elucidate the distribution of variability related to these oscillations in the entire Faroe Current area, an EOF analysis (Empirical Orthogonal Function) [Preisendorfer, 1988] is applied to the *u*-component (eastward) of the full ADCP current field (Fig. 3), during the mentioned 100-day period. The leading

mode of variation (Fig. 5a) resembles the *Transport mode* discussed by Hátún et al. [2003] which accounted for more than 90% of the total transport variability in the Faroe Current. The appurtenant principal component (Fig. 5b), describing the temporal development of this mode, shows clear short-period oscillations which are in phase with the current oscillations below the interface (the Iceland-Faroe Front).

From wavelet spectra (Fig. 6) it is found that the T5 spectral peaks are evident in: a) the current (*u*-component) at all sub-interface observations (shown for NB and NC), b) the transport mode principal component, c) the upper layer current (*u*-component) near the shelf and d) in the bottom temperature measured at instrument NE (see Fig. 3) which describes the vertical movement of the pycnocline (interface) (Appendix B). The 2000-2001 data set with five ADCP instruments moored concurrently (Fig. 3) is the most extensive, and the wavelet spectra in Figure 6 have thus been calculated based on time series from this data set. The winter-spring period (21 December 2000 to 6 June 2001), which is the period when regular oscillations are most prominent (see section 3.2), has been used in the analysis. The instrument farthest north (mooring NC) was only deployed up to summer 2000. The same winter period as above, but for the year 1999-2000, has thus been used when analysis data from this particular mooring site. The oscillations are intermittent (see Fig. 4b), and T5-signals in the upper layer will be overwhelmed by other variability when frequency analysing long time-series. So energetic periods have to be selected when analysing the upper layer currents. The spectrum in Figure 6c is based on the 42-days period 25 April to 6 June.

The lower-layer *v*-components have much weaker T5 spectral peaks than the *u*-components (not shown), implying that the T5 oscillations are more zonal than meridional in the Faroe Current region. The T15 spectral peak when present, is usually more energetic than the T5 modes, but attention is given

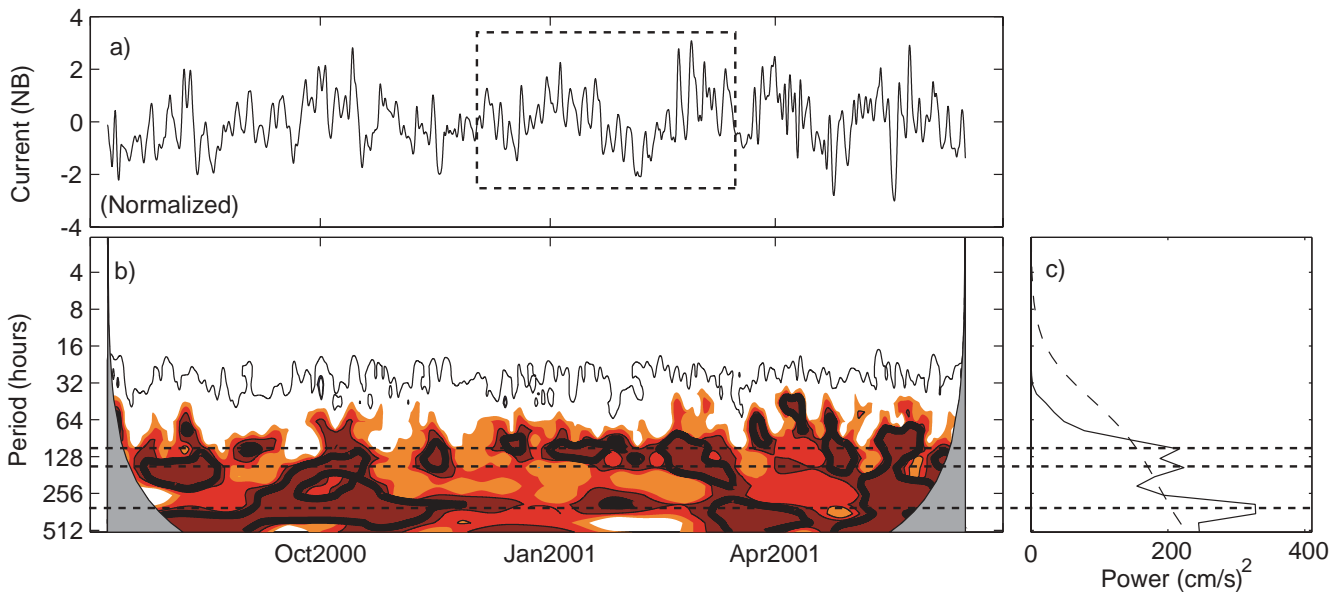


Figure 4 (a) The zonal current velocity at ADCP mooring NB (600m) during the year 2000-2001. For clarity, the series is de-tided prior to the analysis. (b) The local wavelet power spectrum (scalogram) of the normalized NB series. Regions with significant energy are shown with black lines and the cone of influence is shown as gray areas. The cone of influence (COI) is the region of the wavelet spectrum in which edge effects, caused by finite-length series, become important. (c) Global (time-averaged) wavelet spectrum. The dashed line shows a 95% confidence level based on a red noise background spectrum [Torrence and Compo, 1998], and the three significant period bands are indicated with horizontal dashed lines.

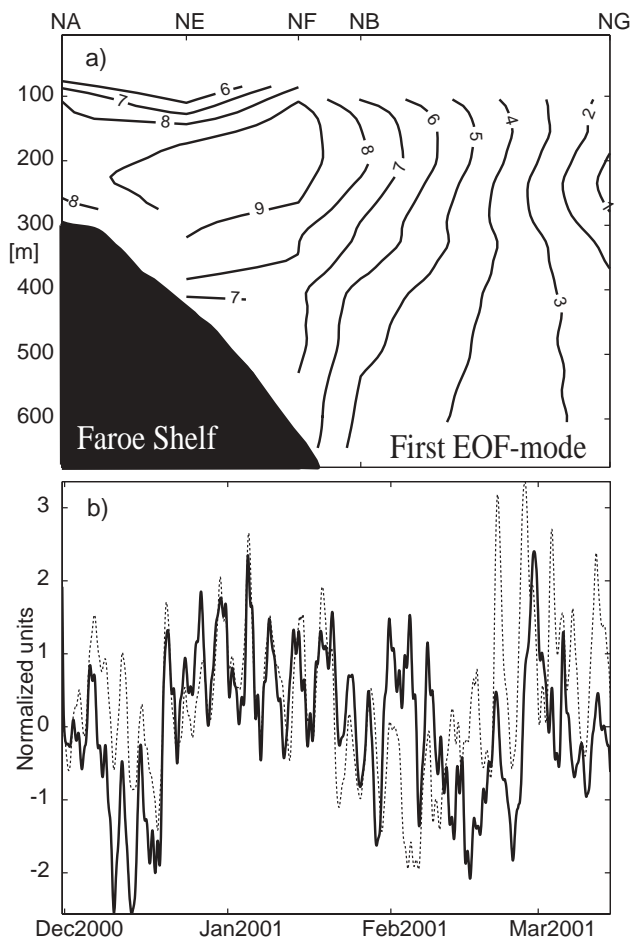


Figure 5 EOF-analysis of the 2000-2001 current field (NA, NF, NE, NB and NG). a) The first spatial mode explaining 35% of the total current variance. The units are not physical. b) The associated principal component (solid) and the zonal current velocity at ADCP mooring NB, at 600 m depth (dashed). The units are normalized and the 100-day period, illustrated with the dashed rectangle in Figure 4, is used.

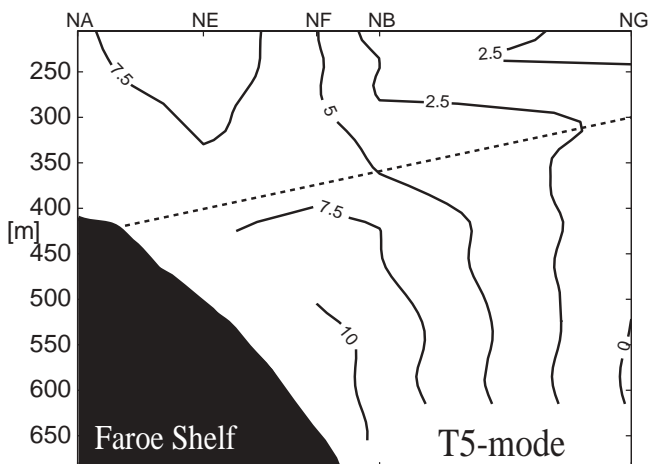


Figure 7 The first mode (explaining 70% of the total current variance) from an EOF analysis of the u -component. A 15-day period when the T5 signal was particularly evident is used. The dashed line marks the typical position of the main pycnocline (Appendix A). Units are not physical.

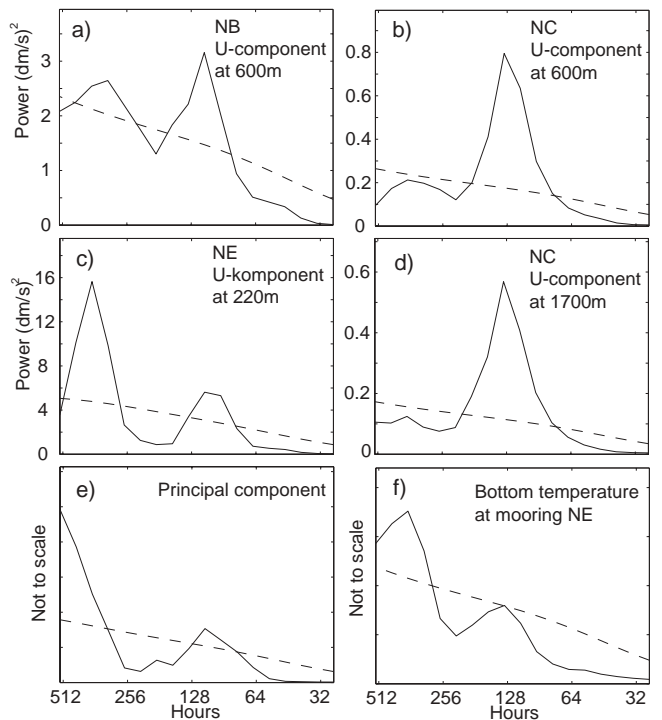


Figure 6 Six key wavelet spectra. The analysed periods are given in the text.

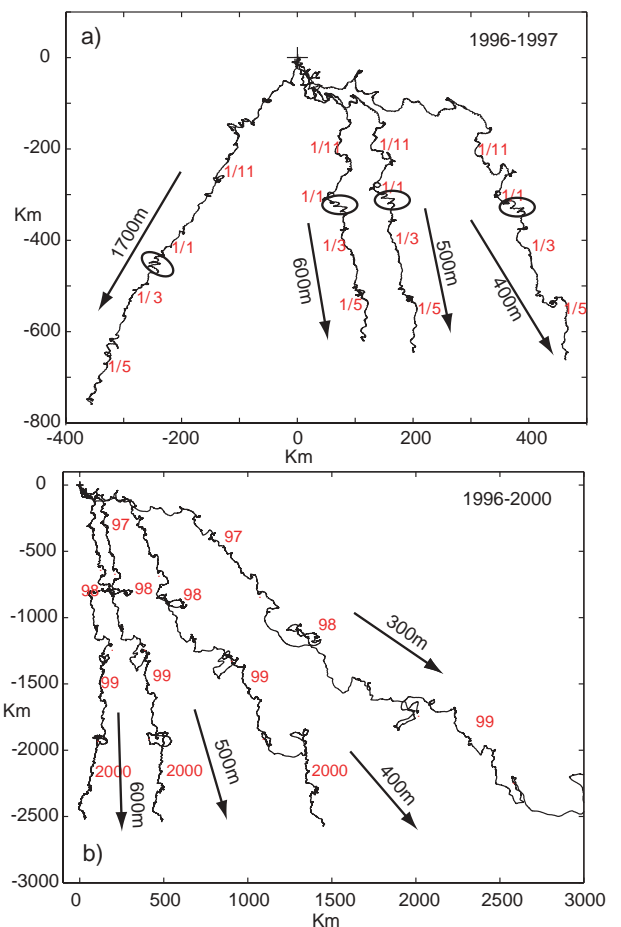


Figure 8 Progressive vector diagrams from: a) one-year long (1996-1997) current records measured at different depths at mooring NC. The deepest series (1700 m) is measured with the RCM, and the others are measured with the ADCP profiler. Dates are shown in red, and the flow directions are indicated with the arrows. b) Four-year long (1996-2000) current records as measured by ADCPs.

to the T5 modes in this paper.

From the spectrum of the principal component (Fig. 6e) it is clear that the EOF-mode represents both the T5-mode and variations on longer time-scales. In order to better isolate the T5 mode, an EOF-analysis is applied to a 15-day period with particularly energetic currents in the T5 period band. The first mode from this short-period EOF-analysis, is a dipole pattern (Fig. 7). This mode has much energy near the shelf, but under the pycnocline (mooring NF) and in the upper layer over the shelf break (mooring NE). The energy is fairly constant through the water-column in the lower layer, but is increasing towards the shelf (vertical isolines). A marked transition is seen at the pycnocline (dashed line). This pattern (the *T5-mode* hereafter) did not change substantially when using other short and energetic sub-periods. Therefore the pattern most likely represents a consistent physical mode.

3.2 Lower Layer Currents at NC

The very clear T5 signal at mooring NC (Figs. 6b and 6d), and the available current data at the bottom (RCM, Fig 3) recorded concurrently to the ADCP data through the upper 600 m, makes this mooring site the best suited for studying the T5 oscillations.

The progressive vector diagrams (PVDs) in Fig. 8 show that the residual bottom current flows towards the southwest following bottom topography (Figs. 2 and 8a), and that the flow veers towards the east going up through the water column (Fig. 8b). The straight PVDs indicate fairly persistent flows on average, and the horizontally aligned dates in Fig. 8 show that the southward flow in the lower layer is barotropic with some bottom intensification at 1700 m depth. The T5 oscillations, seen as ripples i.e. within the ellipses in Fig. 8a, seem to be throughout the water column as well.

High coherencies are found between currents in the lower layer (not shown), but these coherencies are lost when crossing the pycnocline. Whether this lack of coherency is due to a stronger variability in the upper layer overshadowing the T5 signal, or whether the T5-signal really is more energetic in the lower layer, is unclear. The T5-mode in Fig. 7 seems to sup-

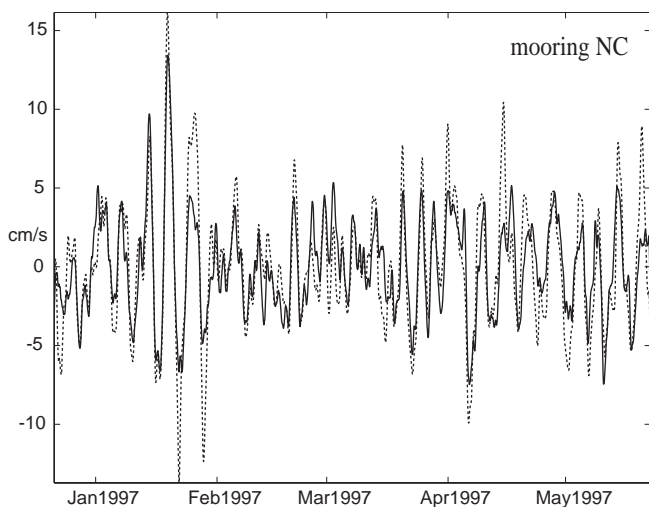


Figure 9 Zonal (cross-isobath) current velocities at 600 m (solid) and at 1700 m (dashed). The period from December 1996 to May 1997 is shown. Note that the bottom oscillations are stronger

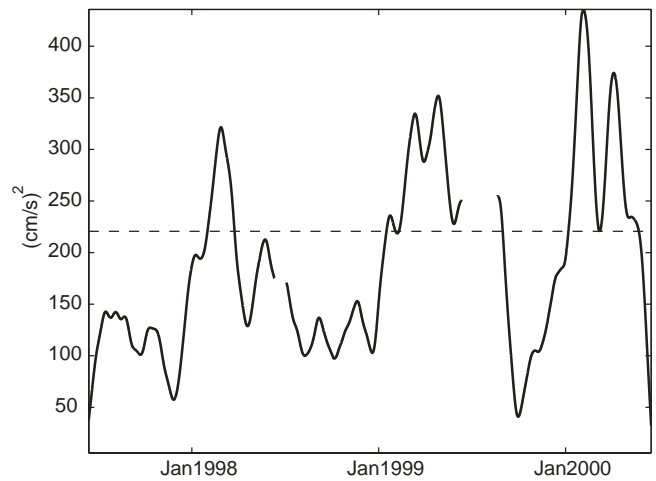


Figure 10 Scale averaged wavelet power over a three years period of the zonal fluctuations at NB (600 m) [Torrence and Compo, 1998]. The period-band 107-151 hours is used and monthly running averages are shown for clarity. The 95% significance level is shown as a horizontal line.

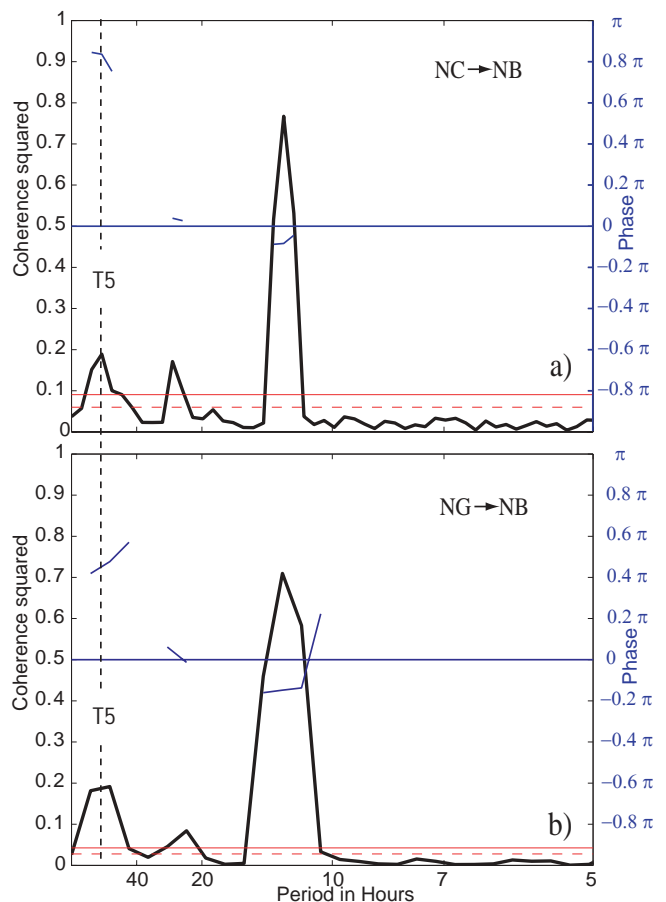


Figure 11 The coherence (black line) and the phase (blue lines) between the zonal current velocities at 600 m depths measured at: a) ADCP moorings NC and NB and b) ADCP moorings NG and NB. At the T5 period, the NC series leads the NB series by about 0.85π radians ≈ 55 hours and the NG series leads the NB series by about 0.4π radians ≈ 30 hours. The horizontal red lines represent the 99% significance level (solid) and the 95% significance level (dashed), respectively [Emery and Thomson, 1997].

port the latter.

T5 oscillations are slightly stronger near the bottom (Fig. 9) indicating that the T5-mode is somewhat bottom trapped [Pedlosky, 1986], [Rhines, 1970].

Three consecutive years of current data from mooring NC (600 m) show that the T5 oscillations are most vigorous during the spring months January -May, and most quiescent during the fall months August-November (Fig. 10). This seasonality is seen in all parameters which contain the T5 signal.

4. A TOPOGRAPHIC ROSSBY (T-R) WAVE

4.1 The T5-signal Propagation

The ADCP instruments at moorings NB and NC (Fig. 3) were concurrently operational during the three-year period from summer 1997 to summer 2000 with around one-month-long gaps in the summer, due to instrument service. Mooring NC was moved closer to land in summer 2000 and renamed NG (Fig. 3). The deepest bins (600 m) from these deployments are used to study the propagation of the T5 signal in the lower layer.

The coherence, using all three years of concurrent zonal current measurements at moorings NC and NB, is presented in Fig. 11a. The coherencies at semidiurnal, diurnal and at the T5-period, 12.42 h, 23.93 h, and 128 h, respectively, are clearly significant. No phase lag is seen at tidal periods, but the phase lag between moorings NB and NC at the T5 period is about 0.85π with NC leading NB. This means that the T5 signal observed at NC will reach NB about 55 hours, later. If T5 is a progressive wave traveling along topography from NC to NB, then the wavelength will roughly equal twice the distance between the moorings. This gives a wavelength of ~ 80 km and a southward phase velocity of about 0.20 cm/s.

The yearlong records from moorings NB and NG are analysed in the same way (Fig. 11b), giving significant coherencies at roughly the same periods as above. The coherent peaks are somewhat less sharp in Figure 11b compared to Figure 11a, since the series are shorter. The phase lag between moorings NB and NG at the T5-period is now roughly 0.45π , giving a southward phase velocity of about 0.22 cm/s.

4.2 The (T-R) Wave Dispersion Relation

The results above indicate that the T5 phenomenon is a T-R wave with the wavelength $\lambda \approx 80$ km, traveling from the north towards the Faroe Shelf with the phase velocity $c_0 \approx 0.2$ m/s. The meridional wavenumber is thus $l = -7.85 \cdot 10^{-5} \text{ m}^{-1}$ and the frequency is $\omega = 1.36 \cdot 10^{-5} \text{ s}^{-1}$.

The u and v current components are plotted as scatter plots in Fig. 12. Current fluctuations near the relatively steep and uniform Faroe Shelf (moorings NF and NB) are quite rectilinear, and a regression analysis results in the presented degree of linearity (the correlation coefficient, r) and the orientation of the major axis (ϕ). The scatter plots at moorings NC and NG, however, do not visually indicate any clear direction of oscillation. The oscillations of interest are of intermittent nature, and the regression angles will vary somewhat as found when using different shorter periods in the analysis. All peri-

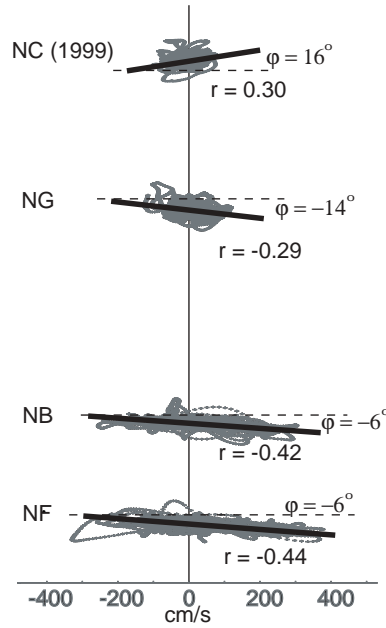


Figure 12 Scatter plots for the current at 600 m depths along the measurement section. The 170 days periods presented in Fig. 6 are used, and angles and coefficients of regression for each mooring are found. (Note that the NC series is not concurrent with the others)

ods during the yearlong series at NG showed angles near the displayed value, but some sub-periods of the four-year-long series at NC could give angles with even an opposite sign. Collecting all active sub-periods at NC (using a wavelet technique) resulted, nonetheless, in an angle similar to the displayed value.

Despite this uncertainty it appears that the waves are turning from positive regression angles at NC to negative regression angles at NG in order to follow the topography. The rectilinear and nearly zonal oscillations imply that the zonal wavenumber, m , is small. ($m \ll |l|$).

From the above, the dispersion relation of a T-R wave [Cushman-Roisin, 1994], and using the bottom depth of $H_0 = 1770$ m (at mooring NC), we can calculate the zonal bottom gradient:

$$\alpha_0 \equiv -\frac{\omega f}{g} \frac{1 + R^2 l^2}{l} = -0.015$$

where g is the acceleration of gravity and R is the deformation radius. This is very close to the actual bottom gradient north of the 63° N meridian as shown in the inset in Figure 3a. With the criteria $l^2 < f_0^2 / c_0^2$ fulfilled, the group velocity, and thereby the wave energy, will propagate towards the Faroe Shelf.

Rossby waves exist due to changes in the ambient potential vorticity pv [Pedlosky, 2003], and the topographic contribution to the ambient pv dominates the planetary contribution by about two orders of magnitude in the study area. The T-R waves will therefore tend to oscillate normally to the isobaths, but it is unclear how this alignment is when the radius of the bottom curvature is smaller than the wavelength, as is the case around moorings NC and NG (see Fig. 2).

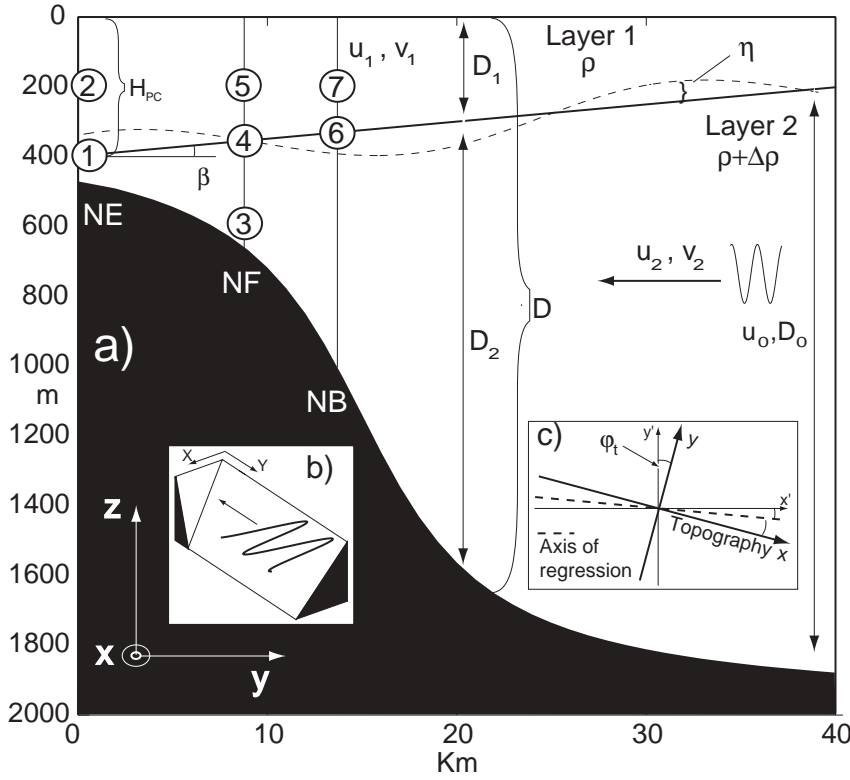


Figure 13 A two-layer model. a) Layer 1 (upper layer) and Layer 2 (lower layer) are divided by the permanent pycnocline $D_1 = H_{PC} - \beta y$ where H_{PC} is the depth at the origin (NE), and β is the slope. The depth from surface to bottom is labelled D and the undisturbed depth of the lower layer is $D_2 = D - D_1$. The time-dependent deflection of the interface from the averaged pycnocline is labelled η and the time-dependent layer depths are $h_1, h_2 = D_1 - \eta, D_2 + \eta$, for the upper and the lower layer, respectively. Current velocities are $u_{1,2}, v_{1,2}$, and the densities are ρ and $\rho + \Delta\rho$ for the two layers, respectively. The initial zonal lower-layer current velocity at the northern (deep) boundary is u_0 and the lower layer thickness at this point is D_0 . Numbered circles point out positions between which phase relations will be discussed. b) Sketch of the southward propagating waves meeting a steeper zonal topography. c) The coordinate frame used in the model is aligned with the topography, which makes an angle ϕ_t with frame (x', y') shown in Fig. 2. The axis of regression near the shelf (Fig. 12) is drawn in.

5. MODELLING THE ONTO-SHELF WAVE PROPAGATION

5.1 Simplifying Assumptions

The southward propagating topographic wave will follow the relatively gentle north-south topography, until it meets the much steeper nearly zonal Faroe Shelf as sketched in Fig. 13b (See also Fig. 2).

The model x -axis is aligned with the Faroe Shelf topography, and the y -axis is directed away from the shelf making the angle $\phi_t \approx 16^\circ$ with the meridional measurement section (Fig. 13c). The origin lies at mooring NE and the northern boundary is close to NG, giving a total stretch of 40 km. All parameters are displayed in Fig. 13a. The following simplifying assumptions are made:

1) Values (wavelength, phase velocity etc.) obtained along the measurement section, are used unaltered in the model coordinate frame.

2) The bottom topography and the permanent pycnocline depend only on y .

3) The wave stream function, from which current velocities (u, v) , and interface movements (η) can be derived, is of the form:

$$\varphi(x, y, t) = \varphi^0(y) e^{i(lx + my - \omega t)}$$

4) Friction is ignored

5) Reflected waves are ignored

Topographic waves in a stratified ocean will appear barotropic whenever the wavelength substantially exceeds the Rossby internal deformation radius. Increasing influence by stratification will enhance a bottom trapped mode [Pedlosky, 1986]. The T5 wavelength, $O(80 \text{ km})$, is much longer than the

internal Rossby radius, $O(20 \text{ km})$, but the observations indicate some degree of bottom trapping (see i.e. Figs. 7 and 9). The waves meet an upper layer of increasing depth as they progress due to the permanent pycnocline, and it is unclear whether these will propagate: a) unaffected by the stratification or b) whether they will be confined to the lower layer. Both extreme cases are studied using a simplistic model approach. The reality will naturally be somewhere between these extremes.

5.2 One-Layer Model (Barotropic)

The propagation of barotropic T-R waves onto a shelf has been discussed by Thomson [1971], Kroll and Niiler [1976], Louis and Smith [1982], Shaw and Csanady [1988], Aikman et al. [1988] and Pickart [1995].

The kinetic and the potential energy (“spin energy”) each is propagated onto the shelf with the group velocity, which again is proportional to the so-called slope parameter $S = D^{-1} \cdot \partial D / \partial y$, [Kroll and Niiler, 1976]. The bottom profile is nearly exponential close to the shelf and the slope parameter is thus fairly constant. Assuming that the group velocity is constant and the flux of kinetic energy is conserved, the zonal depth independent current amplitude is given as:

$$u^0(y) = u_0 \cdot \sqrt{\frac{D_0}{D}}, \quad (1)$$

where D_0, u_0 are the depth and the velocity, respectively, at the northern boundary (Fig. 13). D is the total layer depth. The potential energy has been neglected.

The linear relationship between the current components near the shelf (Figs. 12 and 13c) allows us to write:

$$v^0(y) = \gamma \cdot u^0(y), \quad (2)$$

where γ is a real constant. The flow across isobaths will induce vertical velocities at the bottom given by

$$w(z=D) = -v \frac{\partial D}{\partial y}. \quad (3)$$

For barotropic motion the continuity equation is

$$\frac{\partial u}{\partial x} + \frac{\partial v}{\partial y} + \frac{\partial w}{\partial z} = 0 \quad (4)$$

where the two first terms are independent of z , resulting in a vertical velocity which varies linearly with depth. The vertical motions on the ocean surface are very small compared to the interface motions, and these can thus be neglected. This gives a vertical motion at the undisturbed pycnocline of

$$w_{PC} = \frac{D_1}{D} \cdot w(z=D) = -v \cdot S \cdot D_1. \quad (5)$$

The vertical velocity induces motion on the pycnocline (η) given by

$$\eta = -i \cdot \frac{\gamma \cdot S \cdot D_1}{\omega} u. \quad (6)$$

Motion on the pycnocline generates baroclinicity and a barotropic mode in a stratified ocean with topography is strictly not possible [Pedlosky, 1986], but is here be used as a first approximation.

5.3 Two-Layer Model (Baroclinic)

In the Cape Hatteras region, observed deep topographic waves are decoupled from the local surface meanders of the current [Johns and Watts, 1988; Pickart and Watts, 1990], and such waves are thus likely forced elsewhere, but propagate onto a slope in the lower layer [Pickart, 1995].

Assuming that the southward propagating waves intensify as if they were confined to the lower layer, the zonal velocity in this layer will be given as (1) with D replaced with D_2 , (where again the potential energy has been neglected). The meridional velocity is likewise given by (2) with the depth-independent u^0 replaced with the u -component in the lower layer (u_2). With the assumptions of a small interface deflection compared to the layer thickness, a gentle interface deflection slope compared to the slope of the bottom and the averaged interface combined ($\eta \ll D_2$, $\partial\eta/\partial y \ll \partial D_2/\partial y$), and the fact that the bottom and pycnocline slopes in the x -direction are small compared to those in the y -direction, we can linearize the continuity equation for the lower layer. Using the linearized continuity equation together with equations (1) and (2), an expression for the interface undulation is obtained:

$$\eta_0(y) = \frac{u_2^0}{\omega} (D_2(\gamma \cdot m + l) - i \frac{1}{2} (\frac{\partial D}{\partial y} + \beta)\gamma), \quad (7)$$

where β is the slope of the undisturbed interface.

The momentum equations for both layers combined, linked by the pressure terms are:

$$x : \quad \frac{du_1}{dt} - fv_1 = \frac{du_2}{dt} - fv_2 - g' \frac{\partial h_1}{\partial x}, \quad (8a)$$

$$y : \quad \frac{dv_1}{dt} + fu_1 = \frac{dv_2}{dt} + fu_2 - g' \frac{\partial h_1}{\partial y}, \quad (8b)$$

where $g' = g \Delta\rho/\rho$ is the reduced gravity, h_1 is the time-de-

pendent upper layer thickness, and u_1, v_1 are the upper layer velocities (Fig. 13a). Guessing a solution on the form,

$$u_1 = u_1^0(y) \cdot e^{i(lx+my-\omega t)} + u_{FC},$$

we obtain:

$$u_1^0 \equiv u_2^0 + \frac{g'}{f} \left[i\eta_0 m + \frac{\partial \eta_0}{\partial y} \right] \quad (9a) \quad \text{and} \quad u_{FC} = \frac{g'}{f} \beta, \quad (9b)$$

where a small term related to the frequency has been disregarded.

The constant term is the *thermal wind* balance between the baroclinic current component in the Faroe Current, u_{FC} , and the permanent pycnocline. The term $u_1^0(y)$ is complex and contains the amplitude of the upper-layer oscillations and the phase between these and the deeper waves.

5.4 Validation of the Model

The process explained by the model has been validated against the ADCP dataset during the winter-spring period presented in Section 3.1, which is the period when T5-activity is expected (see Fig. 10).

5.4.1 Model parameters

The model parameters are determined from the bathymetry and observations (appendix A), and these are summarized in Table 1.

5.4.2 Amplitudes

The east-west current velocities associated with the waves in the lower layer intensify when approaching the slope and the interface (Figs. 7 and 12). The observed zonal current amplitudes in the lower layer, u_2 , are found as the standard current velocity deviation during the validation period, and these observed amplitudes are compared to the simulated current amplitudes in Fig. 14. The two-layer model (full curve)

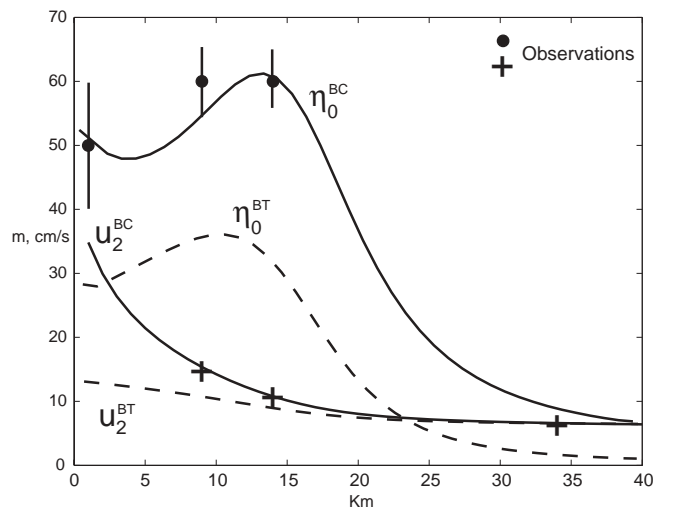


Figure 14 Modeled amplitudes of the current in the lower layer, u_2 , and of the pycnocline movement, η_0 . Observations are shown with dots (η_0) and pluses (u_2), and the vertical lines represent confidence intervals for the observed η_0 . The abbreviation BT refers to values from the barotropic one-layer model version (broken lines), and BC refers to the baroclinic two-layer model (full lines).

Table 1. Model parameters

Symbol	l	m	ω	β	γ	ρ_0	$\Delta\rho$	H_{pc}	U_0	a
Unit	m^{-1}	m^{-1}	s^{-1}	-	-	$kg\ m^{-3}$	$kg\ m^{-3}$	m	$m\ s^{-1}$	m^{-1}
Value	$1 \cdot 10^{-5}$	$-7.9 \cdot 10^{-5}$	$1.5 \cdot 10^{-5}$	0.006	0.18	1027.75	0.33	400	0.07	0.13

shows a realistic current intensification, while the one-layer model (dashed curve) generates too small velocities.

The incoming waves induce large vertical movements on the permanent pycno-/thermocline. Direct observations of these interface deflections with a time-resolution high enough to resolve the five-day motions are not available. Temperature and current time series from the ADCP instruments are thus used as proxy-series for the interface deflections at positions (1), (4) and (6) (see Fig. 13 and Appendix B). The amplitudes of these deflections (η) based on the proxy-series are compared to the modeled amplitudes in Fig. 14. The two-layer model again produces realistic values, while the one-layer, barotropic model gives too small values. This indicates that the intruding waves are better modeled using a two-layer model than a one-layer model approach.

The modeled current velocity amplitudes in the upper layer are in qualitative accordance to the observed current related to the waves.

5.4.3 Signal propagation

The wave-induced interface deflections and wave-related current signals in the upper layer are expected to move shore wards as the T5-wave propagates onto the shelf. The interface movements reveal a significant spectral peak in the T5 frequency band (Fig. 6f). The time it takes an interface wave-crest to propagate from position (6) to (4) and onto the shelf at (1) is found using lagged correlation analysis and coherency analysis. These observed time-lags are compared to the model-derived (the two-layer model) time-lags in Table 2, showing very good agreements. The interface series at (1) is highly coherent with the lower-layer current velocity at position (3) (Fig. 15), and the modeled phase difference between these parameters (8 hours) is in perfect accordance to the observations (Table 2).

Significant lagged correlations and coherencies at the T5 frequencies are also found between the zonal current compo-

Table 2. Time-lags between interface motions and upper layer zonal currents in different locations, and between the interface motion at position (1) and the lower layer current at position (3) (see Fig. 13a).

	$\eta^{(6)}-\eta^{(4)}$	$\eta^{(4)}-\eta^{(1)}$	$\eta^{(1)}-u^{(3)}$	$u^{(7)}-u^{(5)}$	$u^{(5)}-u^{(2)}$
Model	5 h	4 h	8 h	3 h	14 h
Data	8 h	4 h	8 h	8 h	15 h

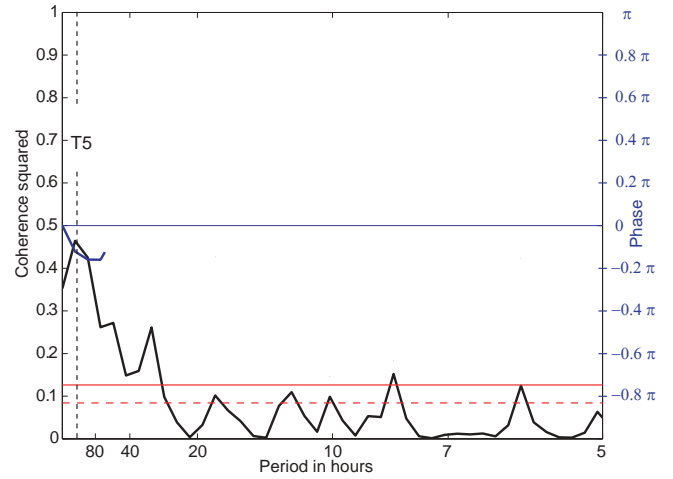


Figure 15 The coherence (black line) and the phase (blue lines) between the zonal current velocity measured at (3) (see Fig. 13) and the temperature measured at NE (1). The series have been de-tided prior to the analysis and significant coherence is found at the T5 period. The NE temperature series leads the NF current series by about 0.15π radians \cong 8 hours.

nents at positions (7), (5) and (2) (upper layer), despite the much stronger ‘noise’ related to other processes in this layer. The modeled time-lags from position (7) to (2) (Table 2) are also in qualitative agreement with the data.

6. SUMMARY AND DISCUSSION

6.1 Wave Propagation Onto a Slope

6.1.1 The Faroe Slope

Striking east-west current oscillations with a four to six days period are observed in the deep Arctic water masses beneath the Atlantic water masses north of the Faroe Islands. These oscillations are coherent throughout the lower layer, and deep current measurements (1700 m) reveal a bottom intensification. A four-year long current series shows a clear seasonality with most energetic oscillations from January to April, and an absence of fluctuations from August to December. Analyzing current records from ADCP instruments arranged in a line along standard section N north of the Faroe Shelf shows that the signal propagates southwards as a topographic Rossby wave with a wavelength of 80 km and a phase speed of 0.20 m/s. With the dispersion relation for such waves and the observed wave parameters, the east-west bottom gradient required to guide the waves can be calculated. The calculated bottom gradient agrees well with the actual bottom gradient in the region.

When the southward propagating waves meet the relatively

steep east-west topography of the Faroe Shelf and the stratification of the wedge shaped Faroe Current, the layer wherein they are confined becomes shallower, and this leads to an increased kinetic energy density as revealed by the along-section current observations at 600 m depths. A small decrease in wave period from 5-6 days to 4-5 days is also observed. The leading mode of variability (the T5-mode) associated with these waves indicates that the energy increase is confined to the lower layer in the offshore region, but that the transfer between the layers amplifies when approaching the shelf. A simple two-layer model assuming kinetic energy conservation in the lower layer explains the observed southwards increasing current amplitudes, while a one-layer model generates too small velocities.

The cross-isobath wave motion induces vertical motion, and in the two-layer system this induces waves on the interface. Interface deflections caused by the waves of more than 100 m are observed, and these are largest where the bottom is steepest. The two-layer model generates realistic interface excursions, while the one-layer model gives a too quiescent interface.

Propagation of such interface deflections towards the shelf are also observed, and the phase velocities are calculated using lagged correlation analysis and coherency analysis. The models predict realistic phase velocities. Observed and simulated phase relations between the interface deflections and the underlying wave oscillations are also in good agreement.

The wave-related signals in and under the interface are relatively clear and even very clear at great depths (1700 m), but in the Atlantic layer these are less obvious because of the many other processes present. It is therefore difficult to estimate how much of the wave energy actually is transferred into the upper layer. The leading mode from an EOF-analysis of the variance in the Faroe Current (during a 100-day period in spring 2001 and not to be confused with the T5-mode) is clearly associated to motions with a five-days period, as revealed by the principal component. The leading mode pattern resembles the *Transport mode* which Hátún et al. [2003] found to be tightly linked to the total transport in the Faroe Current. Observed eastward current pulses commence near the Faroe Current core (mooring NB, see Fig. 3) and propagate towards the shore (mooring NE) as they intensify. This signal is significant in lagged-correlation and coherence analysis, and the onto-shelf propagation velocity of these pulses are in gross agreement with the two-layer model prediction. This all indicates that the wave energy is transferred into the upper layer near the shelf.

6.1.2 From the literature

The propagation of Topographic Rossby waves onto a continental slope has previously been studied in the Mid-Atlantic Bight [Thomson, 1971], [Kroll and Niiler, 1976], [Louis and Smith, 1982], [Aikman et al., 1988] and [Pickart, 1995]. An increase in the kinetic energy density as the waves propagate onto the slope has been modeled [Veronis, 1966], [Kroll and Niiler, 1976] and observed [Aikman et al., 1988]. A shift to shorter periods has also been reported [Aikman et al., 1988].

The (de)-coupling of quasi-geostrophic motions between two homogeneous layers has been analytically studied by Rhines [1970], and deep topographic waves decoupled from the local surface meanders and eddies have been observed by Johns and Watts [1988] and Pickart and Watts [1990].

The analytical model by Kroll and Niiler [1976] predicts much wave reflection, some refraction along isobaths and some transmission onto the shelf. The reflections are not seen in observations [Louis and Smith, 1982; Thomson, 1971], and most reports from observations suggest a refraction of the wave energy along the isobaths [Aikman et al., 1988]. More current meter data along the isobaths are, however, needed to firmly verify this conjecture [Shaw and Csanady, 1988]. The current meters along section N are arranged in a line, and the issue of refraction is therefore not addressed here. The data are not analyzed for reflections either, and reflections are ignored in the applied analytical model.

The literature is also rather inconclusive about whether or not the wave energy is transferred onto the shelf. Some works report an 'insulation' of the incoming wave energy from the shelf [Louis et al., 1982], [Shaw and Csanady, 1988]. One hypothesis presented in Kelly and Chapman [1988] is that stratification may allow the divergence of vertical motion, breaking the vorticity constraint, and allowing fluid columns to cross isobaths more easily.

6.2 The Origin of the Waves

This issue has not been solved, but some hypothesis will be presented.

The generation mechanisms for planetary waves which have received most attention in the literature, arise from meteorological forces acting on the sea surface [LeBlond and Mysak, 1978]. Following the approach of Willebrand and Meincke [1980], and by using atmospheric fields from the NCAR/NCEP hindcast data-set, we conclude that the local atmosphere is not the direct driving agent for the observed T5-waves.

Based on 15 moorings on the American continental rise Hogg [1981] could calculate ray paths and concluded that the deep waves were generated underneath the Gulf Stream. In a model study, Csanady [1988] found that meander formation transfers energy to the lower layer, and that a burst of motion in the upper layer lasting for 1-10 days could be followed by a few cycles of oscillations in the lower layer. The forcing was found to be layer-to-layer pressure torques and not shear stress as often has been assumed [LeBlond and Mysak, 1978]. They find that bursts of meanders, associated with large-scale transitions in the Gulf Stream, force the waves, but it remains unclear what triggers the bursts and what determines the period [Pickart, 1995].

Wind fields from the NCAR/NCEP hindcast data-set in the Nordic Seas region are energetic at the five-days period during winter, but the intensification of the winds occurs about a month prior to the typical onset of the waves (not shown). The low-pressure systems passing through the region will induce meandering on the Jan Mayen Front and on the Iceland-Faroe Front, and this could generate deep waves in the lower layers according to the above. This lower layer wave energy would be canalised south along the ridge system, Jan Mayen Ridge - Iceland-Faroe Ridge, and accumulate at the Faroe Shelf. The southward propagation of waves takes time and such a process could thus explain the delay time of a month between the atmospheric energy and the wave energy at the Faroe Shelf.

Near-bottom current data from the Jan Mayen Channel, situated at the northern end of the Jan Mayen Ridge, have been analysed. These data show relatively vigorous rapid oscillations.

tions with significant energies at the five-day period, and the fluctuations commence in December and cease in March. The current pulses are likely strong enough, $O(20 \text{ cm/s})$, for setting up cross-isobath motions that can initiate a Topographic Rossby wave traveling southwards along the Jan Mayen Ridge (Fig. 1b). The propagation from the Jan Mayen Channel to the Faroe Shelf will take slightly more than a month, assuming the phase speed of 0.20 m/s , and the timing is therefore in reasonable agreement with the seasonality presented in Fig. 10. More data is needed to verify this speculation.

A Kelvin-wave-like phenomenon, propagating counter clockwise along the margin of the closed Nordic Seas basins would show a fast signal propagation, $O(2 \text{ m/s})$, and should thus be coherent and detectable over large distances. Comparing deep current measurements from the Langesnes section (Fig. 1b), the Faroe Current, the Svinøy section at the Norwegian Shelf and from the Lofoten Basin does not support this idea.

The presence of Island-trapped waves around the Faroe Plateau, see e.g. Brink [1999], with a five-days period has been tested using current observations from all sections branching out from the Faroes (Fig. 1). Such waves are not found.

6.3 Impact of the Waves

1) The vertical motion of the pycnocline (front) adjacent to the shelf might enhance mixing of deep water-masses and thus nutrients onto the Faroe Plateau [Hansen and Meincke, 1984]. Very little is known about the exchanges of water between the Faroe Plateau and the surrounding oceans, but this exchange is highly important for the primary production and the marine biology around the islands [Gaard and Nattestad, 2002].

2) A CTD transect along standard section N takes about a day to complete. The waves induce vigorous vertical movements on the interface, $O(100 \text{ m})$, with a period of five days. This means that the interface position at the completion of a CTD transect can be different from when initiating the transect. Aliasing could thus be a problem in the CTD data during the spring period with active waves.

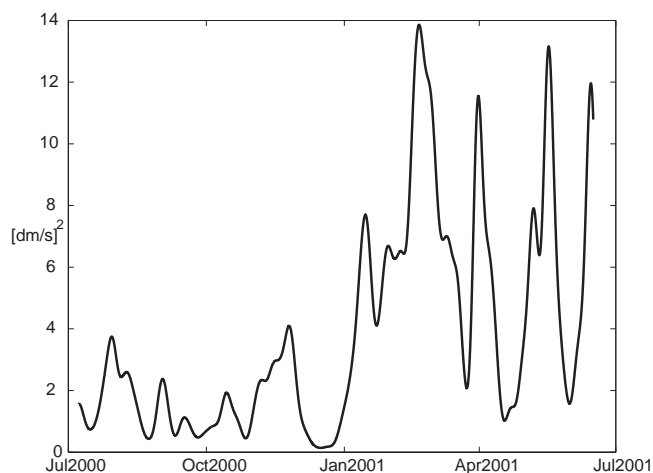


Figure 16 Scale averaged wavelet power of the meridional current fluctuations in the upper layer at (7) (see Fig. 13). The period-band from 80 hours to 192 hours is used.

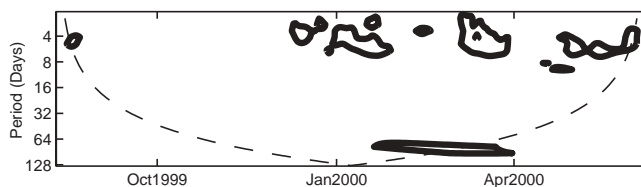


Figure 17 Cross-wavelet scalogram between the current near the core of the Faroe Current (NB at 200m) and current observations in the Faroe Current branch in the Faroe Shetland Channel (300m). Daily averages are used and the series lengths are 300 days. A cross-wavelet scalogram shows the correlation between two series as a function of period (time-scale) and time. Only regions, significant according to criteria presented in [Torrence and Compo, 1998], are displayed. The dashed line is the COI (see Fig. 4).

3) The presented model does not describe the v -component in the upper layer realistically, but it should be mentioned that the north-south motion in the Faroe Current also changes greatly in early January from a slow meandering to more rapid fluctuations (Fig. 16). A significant negative correlation is found between the upper-layer v -component at position (6) (Fig. 13) and the u -component at (2), implying that a strong eastward current pulse at (2) (compare to the dipole in Fig. 7) will induce a southward movement of the Faroe Current core. The mechanism linking these can be explained using a continuity argument.

During periods with active T5 waves the v -component can be very strong, $O(40 \text{ cm/s})$, in the region where the upper layer vanishes and the pycnocline outcrops as the Iceland-Faroe Front. As hypothesized by Hansen and Meincke [1979], the eddies in the front could be caused by barotropic-baroclinic instabilities. Following this, it is imaginable that the T5-waves could be an initiating mechanism for the baroclinic instabilities, which again produce eddies. This has an impact on the cross-front flux of heat and salt into the Norwegian Sea.

4) The Faroe Current is known to bifurcate at the northeastern corner of the Faroe Shelf where one branch is turning into the Faroe-Shetland Channel as shown in Fig. 1a. Little is known about the dynamics of this bifurcation [Meincke, 1978], [Hansen et al., 1998], but strong meridional displacements of the Faroe Current should be expected to play a role. Comparing current measurements from the Faroe Current measurement section and current observations from the Faroe Shetland Channel (see Fig. 1b) by using wavelet techniques, gives the cross-wavelet scalogram [Torrence and Compo, 1998] shown in Fig. 17. This rough and by no means conclusive analysis indicates a correlation at 3-10 days time-scales during the spring period. Furthermore, a correlation at longer time-scales has been found. The connection at shorter time-scales has been verified by a weak, marginally significant, coherence with the northern series leading by one-two days (not shown). The longer time-scale connection is verified by a correlation analysis, and is probably associated with a seasonal variation in both series. Knowledge on this bifurcation is important for understanding the Atlantic inflow towards the Arctic.

APPENDIX

A: Model Parameters

The adjustable zonal wave-number, l , determines the propagation direction of the waves, where $l = 0$, means wave propagation normal to, and onto the shelf.

The real bottom profile, met by the waves, varies as the wave propagation direction varies. An approximate bottom profile:

$H(y) = 2050 - H1(a) \cdot (0.5 - \pi^{-1} \arctan(a \cdot (y - 16)))$, is used, where a accounts for a possible varying bottom steepness, and $H1(a)$ keeps the bottom depth at the origin equal to the actual bottom depth at mooring NE.

The coefficient between the current components, γ , is determined from the difference between the topographic angle ϕ_i and the regression angles at moorings NF and NB (Figs. 11 and 12c).

The modeled pycnocline shoals linearly towards the north and the slope is determined from CTD and ADCP data. In reality this slope is steepest near the shelf and gentles northward, but the linear approximation is found to be reasonable. The stratification is strongest near the shelf ($N = 4.0-4.5 \cdot 10^{-5} \text{ s}^{-1}$) and somewhat weaker further offshore ($N = 2.8-3.5 \cdot 10^{-5} \text{ s}^{-1}$), with the lower values during the spring period (January to June). These values are large enough to justify the use of a two-layer model (N is the Brunt-Väisälä frequency). Averaging the density over and under the stratification maximum in 40 CTD transects sampled during the nineties, gives an estimate of the averaged density ρ_0 and the density difference between the layers, $\Delta\rho$. Only a few zonal CTD transects are available from the Faroe-Current region, but these indicate a gentle density variation with isopycnals shoaling towards the east (Fig. 3a, inset). This detail is neglected in the linearization of the continuity equation. The current amplitude of the incoming waves, u_0 , is determined by the current measurements (ADCP and Aanderaa) at mooring NC (Fig. 3).

All parameters are summarized in Table 1.

B: Proxy Series for the Pycnocline Deflection

The temperature at position (1) (see Fig. 13)

The position of the thermocline is clearest seen with temperature and salinity (CTD) data, but these data are highly under-sampled considering the T5-waves (3-5 sections each year). The ADCP instruments are equipped with a temperature sensor, giving a temperature record at the position of each instrument. Analyzing 40 CTD sections from 1990 to 2001 shows that the averaged depth to the permanent pycnocline 5 km north of NE is approximately 400 m. This means that the instrument at deployment NE (455 m depth) is situated near the foot of the permanent pycnocline. Being placed between cold and warmer water masses, this temperature record gives a good description of the thermocline/pycnocline movement near the shelf [Hátún et al., 2003]. The temperature at mooring NE is, however, only useful as a proxy for the T5 pycnocline-movements when the longer term average (> 10 days) of the pycnocline position lies near the instrument. Homogeneous water-masses surround the temperature sensor

when the interface is far above or below the instrument, and no signature of the T5 movements can be found.

Wavelet analysis of the temperature series finds periods with a clear T5 signature, which can last up to a month. Comparing the typical temperature excursions associated with the T5 fluctuations at mooring NE to the CTD data gives a vertical movement of the pycnocline on the order of $100 \text{ m} \pm 20 \text{ m}$ at position (1), (see Fig. 13a).

Current shear at positions (4) and (6)

Since no ADCP temperature record is available near the pycnocline at positions (4) and (6) (see Fig. 13a), the short time-scale pycnocline movement at these positions must be estimated from the current observations. The relatively strong stratification at the pycnocline is typically related to a steep vertical velocity gradient. The vertical current gradient (du/dz) of each observed profile is calculated, and the maximum value of this is used as a measure of the position of the pycnocline.

The standard deviation of the vertical pycnocline movement at both (4) and (6) during the year 2000-2001 is 66 m (132 m of vertical motion), and a similar value is found analyzing the CTD data monitored over a ten-year period. A coarse estimate of the vertical excursions associated with the T5 wave is 110-130 m.

REFERENCES

- Aikman, F., Ou, H. W., and Houghton, R. W. (1988), Current variability across the New England continental shelf-break and slope, *Continental Shelf Research*, 8, 625-651.
- Brink, K. H. (1999), Island-trapped waves, with application to observations off Bermuda, *Dynamics of Atmospheres and Oceans*, 29, 93-118.
- Csanady, G. T. (1988), Radiation of topographic waves from Gulf Stream meanders, *Continental Shelf Research*, 8, 673-686.
- Cushman-Roisin, B. (1994), *Introduction to Geophysical Fluid Dynamics*, 320 pp., Prentice-Hall, Inc., New Jersey.
- Dickson, R. R. and Brown, J. (1994), The production of North Atlantic Deep Water: Sources, rates, and pathways, *Journal of Geophysical Research*, 99, 12319-12341.
- Emery, W. J. and Thomson, R. E. (1997), *Data analysis methods in Physical Oceanography*, 634 pp., Pergamon, USA.
- Gaard, E. and Hansen, B. (2000), Variations in the advection of *Calanus finmarchicus* onto the Faroe Shelf, *ICES Journal of Marine Science*, 57, 1612-1618.
- Gaard, E. and Nattestad, K. (2002), Feeding, reproduction and seasonal development of *Calanus finmarchicus* in relation to water masses and phytoplankton in the southern Norwegian Sea, *ICES CM 1999/N:8*, 16 pp.
- Hallock, Z. C. (1985), Variability of frontal structure in the Southern Norwegian Sea, *Journal of Physical Oceanography*, 15, 1245-1254.
- Hansen, B. and Meincke, J. (1979), Eddies and meanders in the Iceland-Faroe Ridge area, *Deep Sea Research*, 26A, 1067-1082.
- Hansen, B. and Meincke, J. (1984), Long-term coastal sea surface temperature observations at the Faroe Islands, *Rapports et Procès-Verbaux des Réunions du Conseil International pour l'Exploration de la Mer*, 185, 162-169.
- Hansen, B. and Østerhus, S. (2000), North Atlantic-Nordic Seas Exchanges, *Progress in Oceanography*, 45, 109-208.
- Hansen, B., Østerhus, S., Hátún, H., Kristiansen, R., and Larsen, K.

- M. H. (2003), The Iceland-Faroe inflow of Atlantic water to the Nordic Seas, *Progress in Oceanography*, 54, 443-474.
- Hansen, B., Sælen, O. H., and Østerhus, S. (1998), The passage of Atlantic water east of the Faroes, *ICES Cooperative Research Report*, 225, 112-123.
- Hátún, H., Hansen, B., and Haugan, P. M. (2003), Using an “inverse dynamic method” to determine temperature and salinity fields from ADCP measurements, *Journal of Atmospheric and Oceanic Technology*, 21, 527-533.
- Helland-Hansen, B. and Nansen, F. (1909), The Norwegian Sea, *Fiskeridirektoratets Skrifter Serie Havundersøkelser*, 2, 1-390.
- Hogg, N. (1981), Topographic waves along 70° W on the continental rise, *Journal of Marine Research*, 39, 627-649.
- Johns, W. E. and Watts, D. R. (1988), Time scales and structure of topographic Rossby waves and meanders in the deep Gulf Stream, *Journal of Marine Research*, 44, 267-290.
- Kantha, L. H. and Clayson, C. A. (2000), *Small scale processes in geophysical fluid flows*, International Geophysic Series, 888 pp., Academic Press, San Diego, California.
- Kelly, K. A. and Chapman, D. C. (1988), The response of stratified shelf and slope waters to steady offshore forcing, *Journal of Physical Oceanography*, 18, 906-925.
- Kroll, J. and Niiler, P. P. (1976), The Transmission and Decay of Barotropic Topographic Rossby Waves Incident on a Continental Shelf, *Journal of Physical Oceanography*, 6, 432-450.
- Larsen, K. M. H., Hansen, B., and Kristiansen, R. (2000), Faroese GEM ADCP Deployments 1999-2000, Technical Report No.: 00-02, The Faroese Fisheries Laboratory, Tórshavn, Faroe Islands.
- LeBlond, P. H. and Mysak, L. A. (1978), *Waves in the Ocean*, Elsevier Oceanography Series 20, 602 pp., Elsevier, New York, USA.
- Louis, J. P., Petrie, B., and Smith, P. C. (1982), Observations of Topographic Rossby waves on the continental margin off Nova Scotia, *Journal of Physical Oceanography*, 12, 47-55.
- Louis, J. P. and Smith, P. C. (1982), The development of the barotropic radiation field of an eddy on a slope, *Journal of Physical Oceanography*, 12, 56-73.
- Meincke, J. (1978), On the distribution of low salinity intermediate waters around the Faroes, *Deutsche Hydrographische Zeitschrift*, 31, 50-63.
- Meincke, J. and Kvinge, T. (1978), On the atmospheric forcing of overflow events, *ICES CM 1978/C:9*, 12 pp.
- Miller, A. J., Lerasmusiaux, P. F. J., and Poulain, P. M. (1996), A topographic-Rossby mode resonance over the Iceland-Faroe Ridge, *Journal of Physical Oceanography*, 26, 2735-2747.
- Mysak, L. A. and Schott, F. A. (1977), Evidence for baroclinic instability of the Norwegian Current, *Journal of Geophysical Research*, 82, 2087-2095.
- Orvik, K. A., Skagseth, O., and Mork, M. (2001), Atlantic inflow to the Nordic Sea: Current structure and volume fluxes from moored current meters, VM-ADCP and Sea Soar-CTD observations, 1995-1999, *Deep Sea Research*, 48, 937-957.
- Ou, H. W. and Beardsley, R. C. (1980), On the propagation of free topographic Rossby waves near continental margins. Part 2: Numerical model, *Journal of Physical Oceanography*, 10, 1323-1339.
- Pedlosky, J. (1986), *Geophysical fluid dynamics*, 2nd ed., 710 pp., Springer-Verlag, New York, USA.
- Pedlosky, J. (2003), *Waves in the ocean and Atmosphere*, 260 pp., Springer, New York, USA.
- Petrie, B. and Smith, P. C. (1977), Low-frequency motions on the Scotian shelf and slope, *Atmosphere*, 15, 117-140.
- Pickart, R. S. (1995), Gulf Stream-Generated Topographic Rossby Waves, *Journal of Physical Oceanography*, 25, 574-586.
- Pickart, R. S. and Watts, D. R. (1990), Deep western boundary current variability at Cape Hatteras, *Journal of Marine Research*, 48, 765-791.
- Preisendorfer, R. (1988), *Principal Component Analysis in Meteorology and Oceanography*, Developments in Atmospheric Science, 425 pp., Elsevier Science Publishing Company Inc., Amsterdam, The Netherlands.
- Read, J. F. and Pollard, R. T. (1992), Water masses in the region of the Iceland-Faroes Front, *Journal of Physical Oceanography*, 22, 1365-1378.
- Rhines, P. (1970), Edge-, Bottom-, and Rossby Waves in a rotating stratified fluid, *Geophysical Fluid Dynamics*, 1, 273-302.
- Schott, F. A. and Bock, M. (1980), Determination of energy interaction terms and horizontal wavelengths for low-frequency fluctuations in the Norwegian Current, *Journal of Geophysical Research*, 85, 4007-4014.
- Seager, R., Battist, D. S., Yin, J., Gordon, N., Naik, N., Clementsen, A. C., and Cane, A. (2002), Is the Gulf Stream responsible for Europe’s mild winters?, *Q.J.R. Meteorological Society*, 128, 1-24.
- Shaw, P.-T. and Csanady, G. T. (1988), Topographic Waves over the Continental Slope, *Journal of Physical Oceanography*, 18, 813-822.
- Simonsen, K. and Haugan, P. M. (1996), Heat budgets of the Arctic Mediterranean and sea surface heat flux parametrizations for the Nordic Seas, *Journal of Geophysical Research*, 101, 6553-6576.
- Skagseth, O. and Orvik, K. A. (2002), Identifying fluctuations in the Norwegian Atlantic Slope Current by means of empirical orthogonal functions, *Continental Shelf Research*, 22, 547-563.
- Thomson, Rory O. R. Y (1971), Topographic Rossby waves at a site north of the Gulf Stream, *Deep Sea Research*, 18, 1-20.
- Torrence, C. and Compo, G. P. (1998), A practical guide to wavelet analysis, *Bulletin of the American Meteorological Society*, 79, 61-78.
- Turrell, W. R., Hansen, B., Hughes, S., and Østerhus, S. (2003), Hydrographic variability during the decade of the 1990s in the Northeast Atlantic and southern Norwegian Sea, *Marine Science Symposia*, 219, 111-120.
- Veronis, G. (1966), Rossby Waves with bottom topography, *Journal of Marine Research*, 24, 338-349.
- Willebrand, J. and Meincke, J. (1980), Statistical analysis of fluctuations in the Iceland-Scotland frontal zone, *Deep Sea Research*, 27A, 1047-1066.

Hjálmar Hátún: Faroese Fisheries Laboratory, Nóatún 1, FO-110, Faroe Islands. hjalmarh@frs.fo

Blank

PAPER V

Seasonal to Decadal Temperature Variations in the Faroe-Shetland Inflow Waters

Hjalmar Hátún¹, Anne Britt Sandø², Helge Drange^{2,3,4,5} & Mats Bentsen^{2,4}

A 53 years hind-cast simulation with a regional version of the Nansen Center version of the Miami Isopycnic Coordinate Ocean Model (MICOM) has been conducted to explore the nature of the observed seasonal to inter-annual variations in the temperature of the pole-ward flowing Atlantic Water (AW) crossing the Iceland-Scotland Ridge (ISR). It is found that the simulated long-term temperature variations closely resemble observations south of the ridge (Rockall Trough), north of the ridge (Svinøy section) and between (Faroe Shetland Channel, FSC). The simulated temperature on the Faroe Shelf is also compared to daily temperature observations from Mykines, revealing realistic long-term temperature variations, seasonal variations and a realistic seasonal modulation. The simulated time series in the FSC indicates that the phase and amplitude of the annual temperature cycle of the AW have varied by almost one month and 0.15 °C between the 1960s and 2001, illustrating the difficulty in unambiguously removing the seasonal cycle from the, sparsely sampled, time series. It is argued that the simulated time series can be used to complement the observed time series in periods with sparse sampling. Specifically, the observation-based cold anomaly in the late 1960s and the warming in the early 1980s should be treated with caution. Finally, the analysis indicates that it is not advisable to survey the hydrographic section less than four times a year if reliable decadal scale temperature variations are of interest.

1. INTRODUCTION

The southeastern part of the Nordic Seas is among the longest-time [Helland-Hansen and Nansen, 1909] and most frequently [Hansen and Østerhus, 2000] sampled regions of the World Ocean. It is also, together with the Barents Sea, a region of high biological production [Anderson et al., 2000; Sakshaug et al., 1994]. Mounting evidence shows that the biological production is closely related to the actual state of the marine climate in the region, particularly to the flow of warm, saline and nutrient-rich Atlantic water (AW) across the Greenland-Scotland Ridge (GSR), [Beaugrand and Reid, 2003]. Furthermore, the inflow of AW keeps the Barents Sea and the waters south of Svalbard ice free throughout the year, and is consequently of key importance for the local climate in western Scandinavia and north-western Russia. The salt transported into the Nordic Seas is of fundamental role for the formation of intermediate waters in the region, and it is a key component in the formation of abyss water that occasionally takes place in the Greenland Sea. The thermodynamic transformation of AW that takes place north of GSR is thus also linked to the Atlantic thermohaline circulation [Dickson and Brown, 1994].

The flux of AW entering the Nordic Seas between Iceland and the Faroes, and between the Faroes and Scotland, is about equally distributed and amounts to about 3.5 Sv (1 Sv = 10⁶ m³ s⁻¹) each [Hansen et al., 2003; Turrell et al., 2003]. A third

branch of AW enters the Nordic Seas through the Denmark Strait. The latter is rather weak with an inflow of less than 1 Sv [Kristmannsson, 2001]. The hydrography of the AW entering the Nordic Seas between the Faroes and Scotland has been routinely observed by the Faroese Fisheries Laboratory and the Marine Laboratory in Aberdeen throughout most of the 20th century. This is illustrated by an annual average of 3.6 hydrography cruises during the second half of the 20th century, yielding a truly unique source of information about the seasonal to decadal variability of the properties of the inflowing AW.

The Faroes-Scotland time series have been used in a series of studies, including tracing hydrographic anomalies propagating through the Nordic Seas [Belkin et al., 1998; Furevik, 2001]. Although frequently sampled, there are periods with only one or two observations per year. This, combined with a highly variable seasonal cycle in the Faroe-Shetland Channel (FSC) [Hansen et al., 1994], this can lead to difficulties in uniquely identifying the seasonal cycle and the inter-annual temperature anomalies in the series. The consequence of this can be that spurious temperature and salinity anomalies are deduced from the data material [Reverdin et al., 1994]. Here we present a hind-cast simulation with a regional version of the Miami Isopycnic Coordinate Ocean Model (MICOM) [Bleck et al., 1992] to 1) evaluate one aspect of the model performance, to 2) assess whether the observed time series can be complimented for the period 1948 to 2001, and to 3) provide guidance for the future sampling strategy of the Faroes-Scotland transect.

The paper starts with a description of the applied model system (Section 2). Then simulated and observed long-term

¹ Faroese Fisheries Laboratory, Tórshavn, Faroe Islands

² Nansen Environmental and Remote Sensing Center, Bergen, Norway

³ Geophysical Department, University of Bergen, Bergen, Norway

⁴ Bjercknes Centre for Climate Research, Bergen, Norway

⁵ Nansen-Zhu International Research Centre, Beijing, China

temperature variations from three standard hydrographical sections crossing current branches of the northward flowing AW are analysed. In Section 4, the daily temperature record from Mykines is analysed and used as background for a seasonality and aliasing analysis of the observed and simulated temperature time series from the FSC. In Section 5, some possible applications of a general circulation model (GCM) are illustrated followed by a discussion and conclusions in Section 6.

2. MODEL DESCRIPTION

The model system adopted in this study consists of the global Nansen Center version of MICOM [Bentsen et al., 2004; Furevik et al., 2002; Nilsen et al., 2003], and a regional version of the same model system covering the Atlantic Ocean between 30°N-78°N. The global version of the model used in this study has a horizontal resolution of about 40 km over most of the North Atlantic Ocean. The grid configuration of the regional model is identical to the global model but with doubled horizontal resolution, e.g. with about 20 km grid spacing in the region of the Iceland-Scotland Ridge (ISR).

The nesting approach applies a boundary relaxation scheme towards the outer (i.e., global) solution. This results in a so-called one way nesting where the boundary conditions of the regional model are relaxed towards the output from the global model. For the slowly varying baroclinic velocity, temperature, salinity and layer interface variables, this is a fully appropriate way to include the boundary conditions. For the barotropic variables, the relaxation approach requires careful tuning to avoid reflection of waves at the open boundaries. It is possible to compute the barotropic boundary conditions exactly while taking into consideration both the waves propagating into and out of the regional model, see ftp://micom.rsmas.miami.edu/bleck/open_bdy.tex for details. The regional model reads the global fields once a week and interpolates in time to specify the relaxation boundary conditions at each time step.

In the vertical, both model versions have 26 layers of which the uppermost mixed layer has temporal and spatial varying density, and the 25 layers below have constant density. Daily mean NCAR/NCEP re-analyses [Kalnay et al., 1996] fresh water, heat and momentum fluxes are used to force the system by applying the scheme of Bentsen and Drange [2000]: If the model sea surface state is equal to the NCAR/NCEP sea surface state, the turbulent fluxes of momentum and heat are taken from the re-analysis data. If the sea surface state differs between the ocean model and the re-analysis data, the fluxes will be modified, according to the Fairall et al. [1998] scheme.

In the regional model, the mixed layer temperature and salinity fields are linearly relaxed towards the monthly mean climatological values of Levitus et al., [1994] and Levitus and Boyer, [1994], respectively. The e-folding relaxation time scale is set to 30 days for a 50 m thick mixed layer, and is reduced linearly with the mixed layer exceeding 50 m.

The applied relaxation to climatology is rather weak, allowing for seasonal to inter-annual variations in the simulated mixed layer properties as is demonstrated below.

2.1 General Remarks on the Applied Model System

The applied horizontal grid resolution of about 20 km implies that the model is far from eddy-resolving in the region of interest, but sufficient to pick up the main topographic steering-effect on the currents, and similar to the distance between current meters and the standard hydrographic stations along the standard measurement sections in the region. The model grid will seldom coincide exactly with the actual positions of standard hydrographical stations, but this does not affect the results crucially, at least not when the mean value over a certain region is considered.

The simulated hydrography in the ISR-region is, on average, too fresh by about 0.1 psu [Furevik et al., 2002] and too cold by 0.44°C (see below). These deviations may, however, not influence the simulated seasonal to decadal-scale variability in salinity and temperature. Furthermore, simulated volume transports over the ISR, calculated as the net amount of water passing the openings from surface to bottom between 1948-2001, have been compared to transport values from the literature [Nilsen et al., 2003]. These are found to be reasonable although the branch north and northwest of the Faroes is too weak, possibly as a result of the non-eddy-resolving model resolution.

3. SIMULATED LONG-TERM HYDROGRAPHY IN THE FSC

High quality CTD-data are available from the Munken-Fair Isle section between the Faroes and Scotland (Fig. 1) since 1994. The salinity, horizontally integrated at 50 meters depths from the Shetland Shelf half way towards the Faroes, is compared to the simulated salinity treated in the same way (Fig. 2). The model explains the observed seasonality and the steep salinity increase during the 1990s. However, when the observed and simulated time series are considered for the Shetland Shelf region, the simulated salinity variability is much lower than the observed variability. This indicates that the simu-

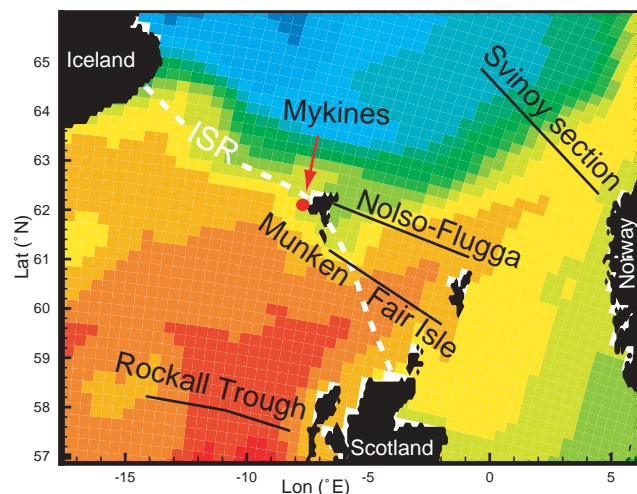


Figure 1. The temperatures T ($T < 3^\circ\text{C}$ for the bluish colors; $T > 9^\circ\text{C}$ for the pure red color) averaged over the mixed layer in the region of the ISR for the years 1996-2001. The standard hydrographical sections used in the analyses are indicated with the black lines and the coastal station at Mykines is shown with the red dot.

lated salinity is too diffusive or lacks details, but that integrated values are realistic. The simulated temperature, however, showed realistic variability both when considering a limited area on the Shetland Shelf and when looking at the integrated values. This observation is, among other processes, an indication of the weak atmosphere-ocean coupling for salinity (through evaporation minus precipitation and run-off) compared to temperature (through heat fluxes).

The observations from the Fair Isle-Munken section have been merged with observations from the Nolsoy-Flugga section further north in the FSC (Fig. 1) to produce a century long hydrography time-series [Turrell et al., 1993]. The averaged temperature field along the Fair Isle-Munken section is shown in the inset in Fig. 3b. The relatively warm pole-ward flowing Continental Shelf Current (CSC) is evident as the dark red colours on the Shetland Slope, and the equator-ward flowing cold overflow water is seen as the dark blue colours (extending from 500-600 m depth to the bottom).

The sub-region, shown with the white frame in the inset, covers the observations that are made inshore from the 300 m depth contour on the Shetland side of the channel. The hydrographic series provided by the Marine Laboratory in Aberdeen is calculated as a spatial average over this region and thus provides a good description of the hydrographical properties of the inflowing AW. A proper comparison of the observed and simulated salinity requires spatially integrated values from an area wider than the white frame, and since the observed salinity, in addition, is of less quality than temperature [Turrell et al., 1993], we focus on temperature in this study. When the simulated temperature is spatially averaged over the white frame area and compared to the observations, the temporal

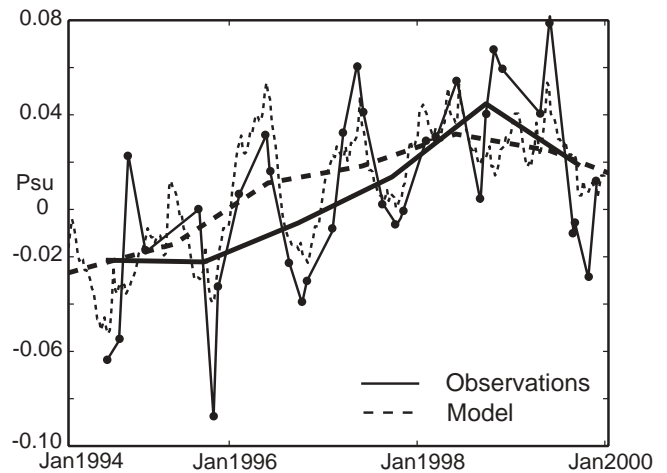


Figure 2. Horizontally averaged salinity deviations at 50 m depths along the Munken-Fair Isle section. The thicker lines show annual averages, and the individual measurements are indicated with the black dots.

average is 9.73°C and 9.29°C, respectively. The temperature anomalies shown in Fig. 3a are made by subtracting the average values from the actual time series.

In Fig. 3b, the observed data points in Fig. 3a have been binned into years and averaged, and the modelled data are picked out at the measurement times and averaged in the same manner. In addition, a three-year running average has been applied for clarity. The presented curves are raw comparisons between the observed and simulated temperature anomalies, and should therefore not be interpreted as the true temperature variation from 1948 to present.

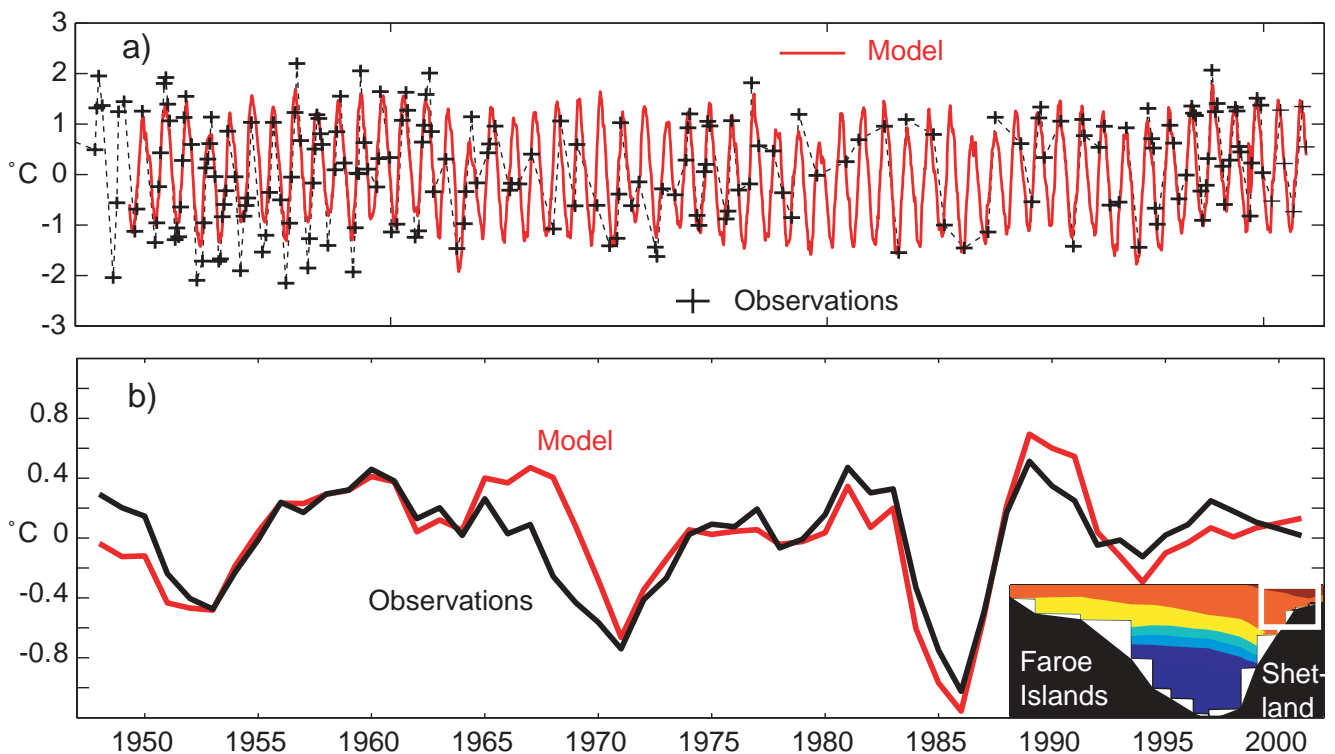


Figure 3. Temperature anomalies in the Faroe-Shetland Channel. Observed and simulated time series from the region shown within the white rectangle in the inset are presented (see text for details). a) The observations (plusses) and the weekly resolved simulated time series. b) Three year running averages (see text for averaging details).

The correlation between the 195 raw temperature observations and the corresponding simulated temperature is 0.93 (before low-passing), and the correlation between annual averages drops to 0.63. The very good raw data correlation is obviously much due to a correctly simulated annual cycle, but the annual averages are still significantly related. A comparison of annual averages is, however, not strictly meaningful since there is no straightforward way to remove the seasonal cycle before averaging as will be discussed in section 4.2. Nevertheless, this illustrates that the model is able to simulate the observed variability in the FSC. To further support this finding, the variability of the observed and simulated hydrographic conditions at the the Rockall Trough and the Svinøy section (see Fig. 1) has been conducted.

The Rockall Trough represents one pathway by which warm North Atlantic upper water reaches the Faroe-Shetland Channel. Temperature and salinity time series from a standard hydrographic section (the ‘Ellet section’, see Fig. 1) that crosses the northern Rockall Trough are available from ICES (www.ices.dk). Figure 4 shows the horizontally averaged, de-seasonalized anomalies over the uppermost 800 m [Holliday et al., 2000] and the simulated time series processed in the similar way. The temporal averages of the presented simulated and observed time series are 8.97 °C and 9.21 °C, respectively.

Furthermore, most of the AW inflow that passes through the discussed area in the FSC continues as the Shetland Current [Hansen and Østerhus, 2000] to the Svinøy section on the Norwegian Shelf (Fig. 1). Temperature measurements from high-quality CTD data along this section (supplied by the Institute of Marine Research, Bergen) have been spatially averaged over the region representing the AW inflow. Figure 5 shows the de-seasonalized observed and simulated time series. The temporal averages of the presented simulated and observed time series are both 7.4 °C.

In conclusion, the comparisons from the Rockall Trough and the Svinøy section show that the simulated long-term hydrographic conditions of the northward flowing AW are, indeed, realistic.

4. SEASONALITY AND ALIASING

4.1 Coastal Temperature at Mykines

Daily sea surface temperature (SST) measurements were made at Mykines (Fig. 1) during the period 1 January 1914 to 18 September 1969. The observation site is open to the Atlantic, the region has strong tidal currents (implying vigorous mixing), there are no river outlets close to the site, and the series represents Faroe Shelf condition within 0.2 °C [Hansen and Meincke, 1984].

The correlation between the raw Mykines series and the simulated temperature anomalies on the Faroe Shelf is 0.96 when monthly averages are compared and 0.75 when annual averages are considered. This shows that both the seasonal variations and interannual temperature variations on the Faroe Plateau are realistically simulated in an average sense. Observations and simulations are available concurrently from 1948 to 1969 and the number of samples each month during this period is shown as a stacked histogram in Figure 6b. Only the years 1949, 1950 and 1969 had entire months missing, and in

average there are 24 samples each month. With such a comprehensive data-coverage, annual averages are simply found by averaging every data point within each year, and by using the average seasonal cycle when isolated months are missing. By doing this, a fairly good correspondence is found between

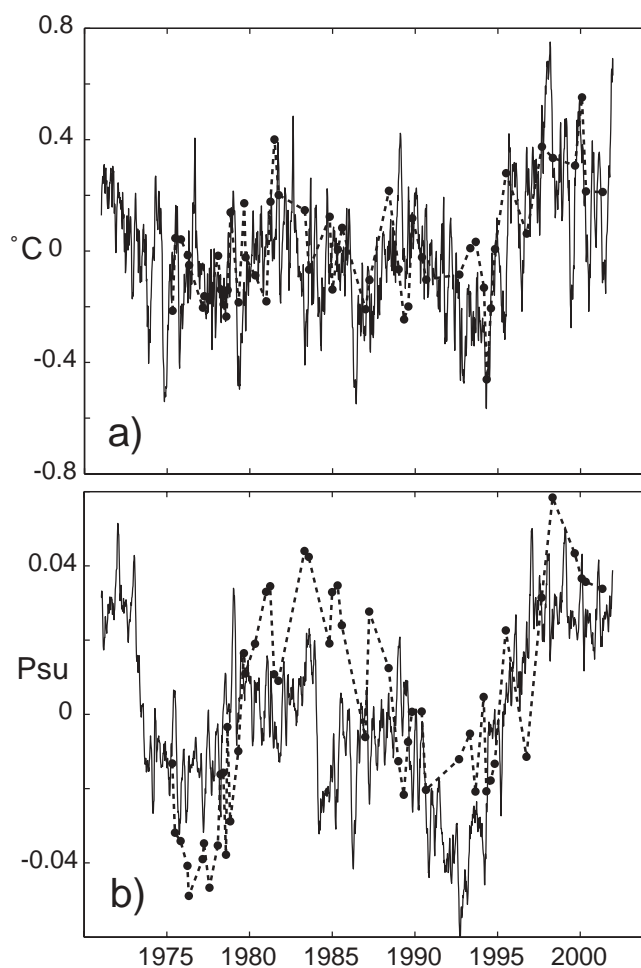


Figure 4. The hydrography along the full Rockall Trough line averaged from surface to 800 meters depth: a) de-seasonalized temperature anomalies (observations: dots, simulations: curve) and b) de-seasonalized salinity anomalies.

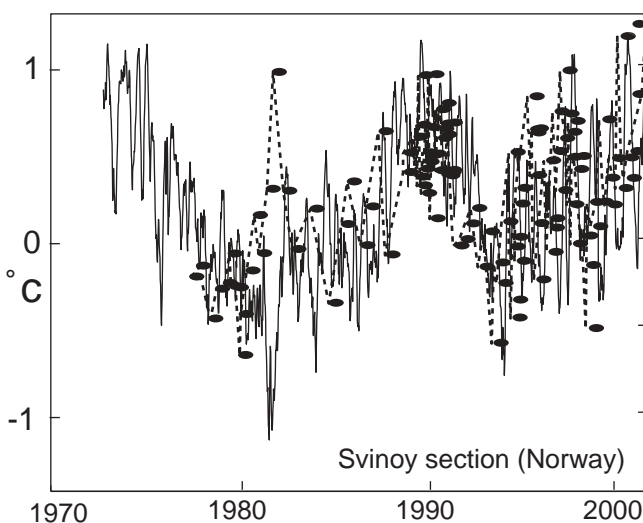


Figure 5. Temperature (de-seasonalized anomalies) from the Svinøy section averaged over an area embodying the northward flowing Atlantic water.

the two time series (Fig. 6a, inset). The temporal averages of the presented simulated and observed time series are 8.40 °C and 8.02 °C, respectively.

The temperature variations are clearly dominated by the seasonal cycle and aliasing would be a severe problem if only few samplings were available (see Section 4.2). In analysing time series with a few observations each year, as is the common case for oceanic records, one has to remove the seasonal signal before averaging in order to remove possible bias caused by the few observations. Since the long-term variation is often small compared to the seasonal signal, care must be applied to the seasonal filtering. The fact that the seasonal amplitude and the timing of the annual temperature maximum in the ISR area are very variable [Hansen et al., 1994], complicates filtering of the annual cycle further. Therefore, filtering the seasonal cycle using an averaged cycle could, for a year with an anomalous seasonal variation, bring in an error to the filtered series. Even though this error is relatively small compared to the seasonal amplitude itself, it can be severe considering the slowly changing long-term averages.

The Mykines series is suitable to evaluate the simulated seasonal cycle. The seasonal cycle is symmetric and well described by a simple trigonometric function of the form $A\cos(2\pi t/365.25-p)$, where A (°C) is amplitude, t (day-number) is time and p (rad) is phase. A combination of various trigonometric functions, allowing for non-symmetric seasonal cycles, did not fit the actual seasonality significantly better than the simple cosine.

Seasonal filtering is performed by fitting the cosine to a time-window of the series, and by subtracting the best-fit cosine from the year in the middle of the window. By letting the time-window slide through the full series (Fig. 6a, inset) one obtains the de-seasonalized (filtered) series in Fig. 6a (note difference in scales). The amplitude and the phase from this analy-

sis are found as time-dependent parameters. The narrower the window is, the better sudden changes in the seasonality are resolved, but a narrow window includes fewer values for the cosine-fitting and an error, caused by imperfect fitting, is brought in. It is found that a width of 8 yr minimizes the errors caused by imperfect fitting and by the varying seasonality.

Values of the seasonal amplitude and phase, obtained from both observations and the model, are displayed in Figs. 7a and 7b. The figure shows that the simulated seasonal amplitude is larger than in reality by about 0.2 °C, but that the changes in the two time series co-vary in time. The model obtains an increase in seasonality by nearly 0.2 °C from 1948 to 1969, while the observations show an increase of about 0.25 °C. The time for maximum temperature differs by less than two days between model and data, and both time series indicate that the maximum temperature is found 3-4 days earlier in the late 60s than in the late 40s. So, in addition to the long-term temperature variation and the average seasonal cycle, the model also predicts the seasonal modulation on the Faroe Plateau in a realistic way.

In the densely sampled Mykines series the ‘true’ annual averages and the ‘true’ seasonal cycle are known, and the need for a seasonal cycle with varying amplitude and phase can thus be tested. The temperature series is sub-sampled in different ways (monthly or more random) and the seasonal variations and the annual averages of these sub-sampled series are found using both a window-based, and full-series based de-seasonalizing method. By comparing the results to the ‘true’ values an error estimate can be obtained for each method. The window-based method is found to perform better than the method that assumes an average seasonal cycle.

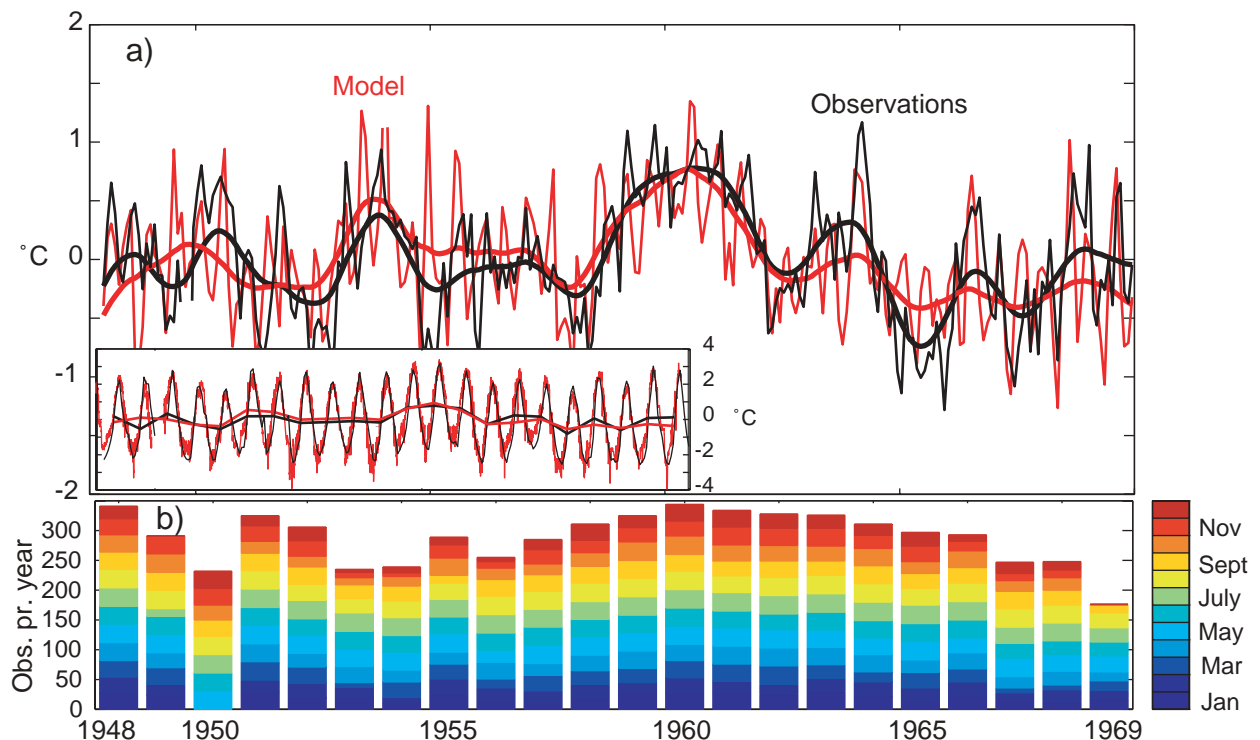


Figure 6. a) The coastal temperature (monthly averages and seasonal cycle removed) at Mykines (black) and the simulated temperature (seasonal cycle removed) on the Faroe Shelf (red). A 12-month running average is shown with the thicker lines. The inset shows the corresponding time series before de-seasonalizing. b) The sampling intensity during the period 1948-1969.

4.2 The Faroe-Shetland Channel

The observed FSC series in Fig. 3a has a character similar to the Mykines series with a dominating seasonal variation and a weaker decadal-scale variation. But, in contrast to the Mykines series, the sampling frequency is scattered throughout the measurement period (Fig. 8b), and aliasing will obviously be a severe problem.

No reliable information on a changing seasonality (amplitude and phase) can be obtained from available observations, but the temperature seasonality in the FSC is known to be very variable [Hansen et al., 1994]. This can even be seen by inspecting Fig. 3a, although the prominent decrease in the early 1960s could be due to a changed measurement strategy after 1960 [Turrell et al., 1993]. The error brought in by removing the observed seasonal cycle can therefore not be quantified with confidence and a model-data comparison of the true decadal-scale variations is thus not meaningful in itself. A model-data benchmarking is therefore limited to the point-wise comparison in Fig. 3.

Analyses shows that the modelled and observed seasonal cycles in the FSC are symmetrical and can be modelled with a simple cosine, just like was the case for the Mykines series. Fitting a cosine to the observed and simulated time series for the periods 1948 to 2001 gives the same amplitudes (1.32 °C), whereas phases differ by three days only and with maximum temperature in mid September. The seasonality is thus, in an average sense, simulated in a correct way.

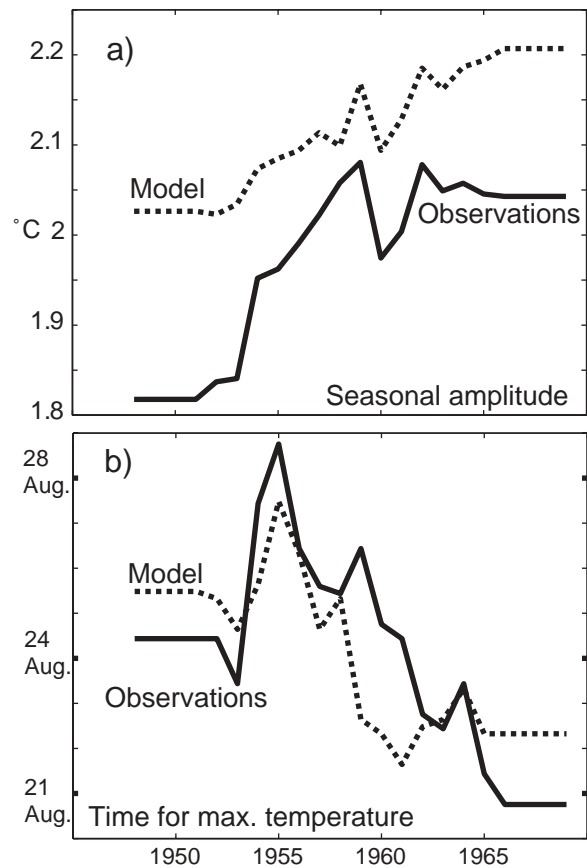


Figure 7. Change in the seasonal temperature variation on the Faroe Shelf: a) The observed (un-broken line) and simulated (broken line) strength in the seasonality, and b) the time, for each year, when the temperature maximum occurs.

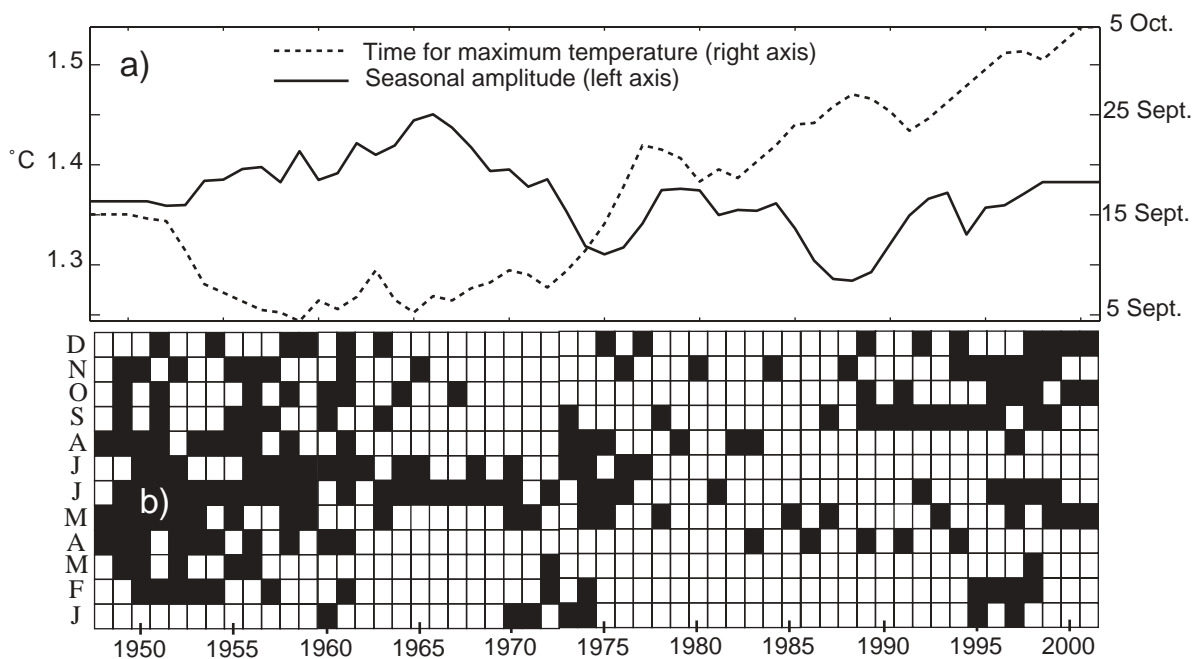


Figure 8. a) The simulated change in the seasonal temperature variation in the FSC. The un-broken curve (left y-axis) shows the amplitude of the seasonality and the broken curve (right y-axis) shows when, for each year, the temperature maximum occurs. b) Monthly overview over the employed measurement strategy in the FSC.

5.1 Model-Based De-seasonalizing Error in the FSC

The correlation coefficient between the time-series from Mykines and FSC is 0.75, and the seasonal amplitude, the phase and the long-term variations of the Mykines series are well described by the model. It is therefore reasonable to assume that the model should explain some of the seasonal modulation in the FSC as well. With this assumption, one can use the model to quantify the error brought in when removing the observed seasonality in the FSC series.

The window-based de-seasonalizing method to the complete model time series from the FSC gives the values of the seasonal amplitude and phase as shown in Figure 8a. The figure shows that the simulated temperature amplitude varies more than 0.15°C during the integration period, and that the maximum temperature is found nearly one month later in year 2001 than in the 1960s. Note the changes around 1965, and that the amplitudes and the phases are inversely correlated.

The main causes for making errors when filtering the annual cycle are linked to the observational frequency, the timing of the observations (Fig. 8b), or changes in the annual temperature cycle (Fig. 8a). The ‘true’ annually averaged series is then based on the full (weekly-averaged) simulated time series. A sub-sampled model time series with the employed measurement strategy in Fig. 8b is generated; the seasonal variation based on the sub-sampled series is found and subtracted (and thereby errors are deliberately brought in), and the annual averages are calculated. During this procedure, the full-length time series (1948 to 2001) is used in the cosine fitting. The difference between the ‘true’ annual averaged and the one obtained after sub-sampling gives an estimate on the error brought in (see grey band in Figure 10).

As a curiosity, the possibility to use the model as a guide for future monitoring is examined.

Sub-sampled model time series with one to six values each year are generated; the seasonal variation based on each sub-sampled series is found and subtracted, and the annual averages are calculated. This has been done for all combinations in each sub-sampled series, and the standard deviation from the ‘true’ annual average is calculated. The standard error found from the optimal way of placing the values throughout the year is provided in Fig. 9a. It follows that the gain in accuracy is particularly large for up to 4 values pr. year. The optimal measurement strategy when using four data-points each year, and based on 1948-2001 as the training period, is the third week in February, the first week in May, the second week in August and the first week in November (Fig. 9b), or about one month prior to the seasonal peaks and the zero-crossings of the annual temperature cycle. This is in accordance with the sampling rate of CTD data employed in the FSC and north of the Faroe Islands from the early nineties to present [Hansen et al., 2003; Turrell et al., 2003]. These monitoring programmes should thus be maintained and not reduced.

The standard de-seasonalizing error produced by the optimal measurement strategy of 4 cruises per year for the period 1948-2001 is about 0.04°C (Fig. 9a). For comparison, the standard error produced by the employed measurement strategy in the FSC over the same period is 0.17°C, or larger than would be obtained with only one optimally located observation each year (Fig. 9). The large discrepancy is mainly caused by periods with few, non-optimal timed measurements during periods with a suddenly changed seasonality. Note that in the late 60s only one to two measurements were made, mainly in June-July, and that this was a period when the seasonal amplitude decreased sharply (Fig. 8). The checkerboard in Fig. 9b shows

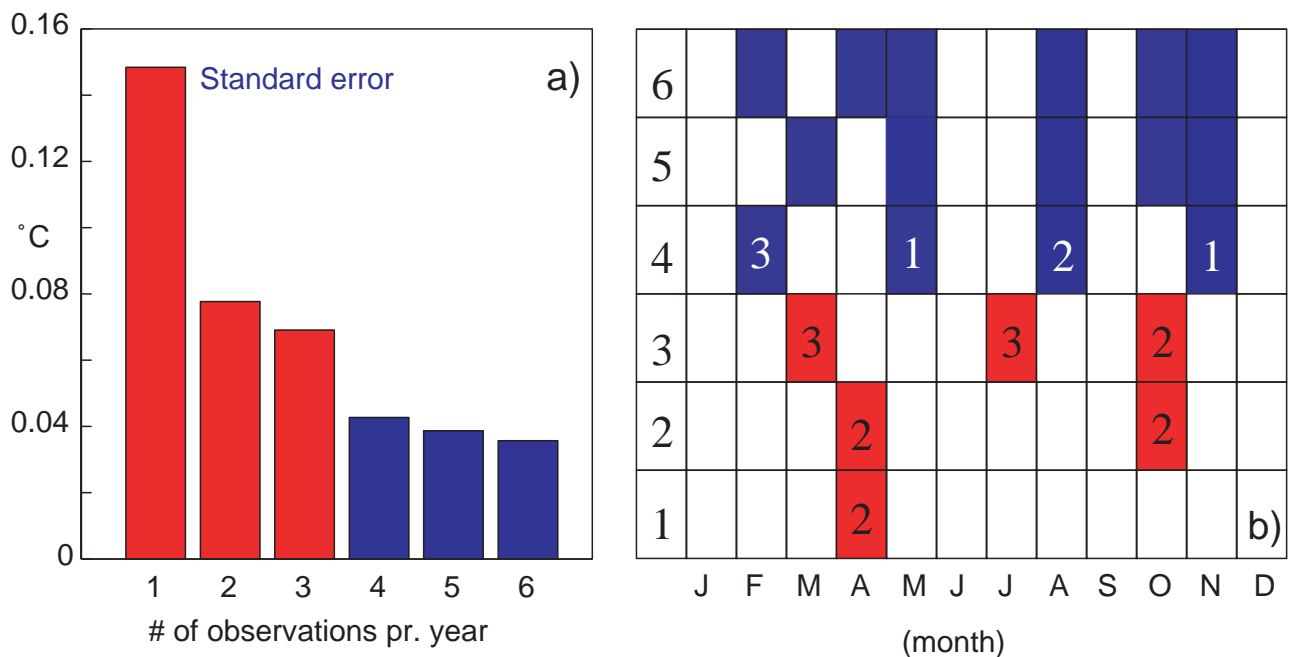


Figure 9. a) The error introduced by removing the seasonal variation as a function of available data points each year. Red bars show the error when less than four observations are taken each year. b) Optimal month (January to December) and week (indicated numbers) of observation, for 1 to 6 observations pr. year (left column). Months without numbers indicate the mid-month.

that it is not wise to monitor in June-July as this is near the zero-crossings of the annual temperature cycle.

5.3 Homogenisation of the Observed Temperature Time Series

If differences in the model-data comparison (Fig. 3) are small compared to the long-term variations and to the error brought in by filtering the seasonality, then the simulated time-series would have the potential to assist the observations during periods with sparse sampling. This is generally the case, except from the periods in the late 1960s and from 1989 to 1991 (Fig. 3b).

In Fig. 10, the full model time-series (weekly averaged values) is compared to the observed series, which has been de-seasonalized with a cosine fitted to the full-length series. Only anomalies are shown, with the averaging as in Fig. 3b. The error from the process of removing the annual cycle, as described above, is illustrated with the grey band.

The discussed uncertain period in the late 60s shows up as a period with a broad grey band and large deviation between simulations and observations. The 80s were surveyed once to twice a year and this is reflected in a model-data deviation and a rather broad error band. Only one cruise was made in 1990, but the previous and the subsequent year had a reasonable sampling (Fig. 8b) resulting in a narrow error-band, but still the model and the data disagree during this period. The observed series lies outside the error band throughout the 1990s, although good data are available for this period. The dashed line shows the result when analysing the high-quality CTD observations from 1994 to 2001 separately. This shows that a ‘contamination’ is introduced when analysing and making anomalies of the observed, full-length time-series as a whole, or that the high-quality CTD observations reduce the mismatch be-

tween the observed and simulated time series.

Sources for errors are many and unclear and the foundation for taking the analysis this far and for trusting the model more than observations are, admittedly, subjective. However, the presented analyses indicate the potential of using GCMs as interpolator for unevenly sampled ocean time series.

6. DISCUSSION AND CONCLUSIONS

The model compares well to the observed temperature variations on the Shetland side of the Faroe-Shetland Channel (FSC) at the irregular times when data are available (Fig. 3a,b). Support for the good model-data correspondence is found at the Rockall section (‘Ellet line’) and at the Svinøy section (Figs. 4 and 5). Furthermore, the applied model captures most of the seasonality, changes in the seasonality and the decadal temperature variations on the Faroe Shelf (Figs. 6 and 7).

Since the observed FSC time series is inhomogeneously sampled and with more energy on the seasonal cycle than on lower frequency variations, aliasing is a problem [Reverdin et al., 1994]. Reverdin et al. [1994] found that the use of available surface data can critically reduce the aliasing problem in the discussed FSC series. With support from the daily SST measurements from the Faroe Shelf and the fact that the model is able to simulate the observed surface temperatures on the Shetland Shelf practically perfectly (not shown), it should therefore be possible to further pursue the approach by Reverdin et al. [1994].

The variable seasonal cycle in the FSC [Hansen et al., 1994] enlarges the aliasing problem. Applying a time-window based de-seasonalizing procedure to the modelled series indicates that the seasonal modulation in amplitude and phase vary much throughout the integration period 1949–2001.

From telegraph cable measurements, Hansen et al. [1994]

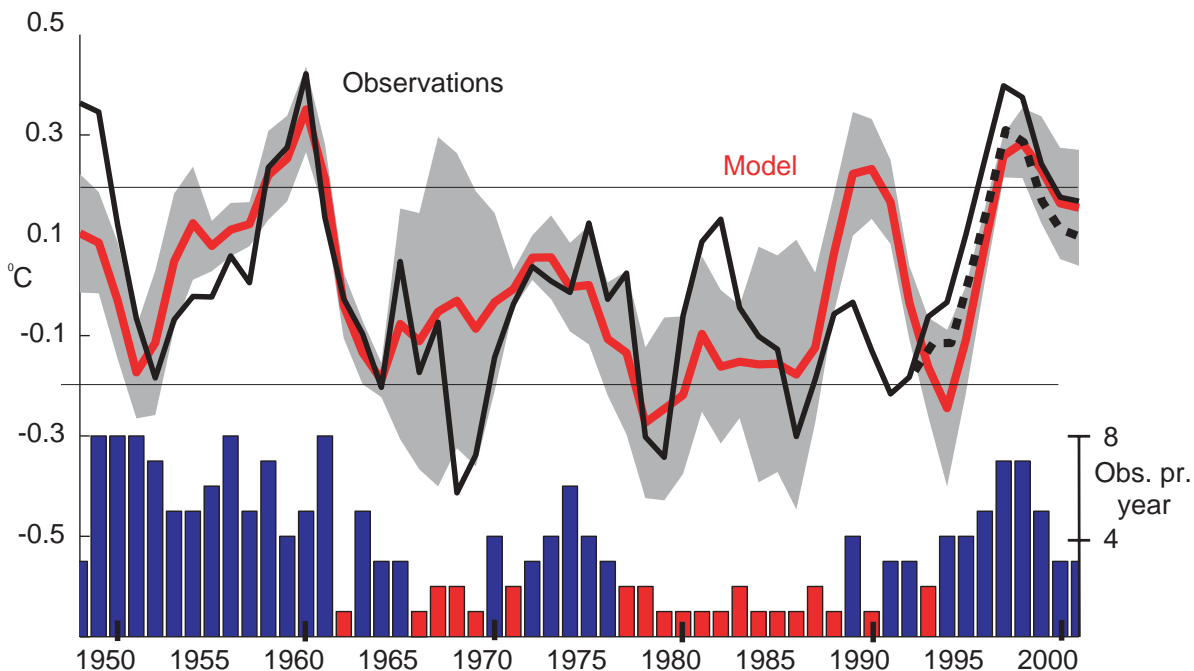


Figure 10. Observed temperature anomalies after removing the seasonal variation (three year running averages and de-trended), (black non-dotted line). The weekly resolved simulated time series is shown in red. The grey zone illustrates the error introduced by de-seasonalizing as found by comparing sub-sampled and the full, simulated time series. The number of measurements made each year is shown with the histogram, years with less than four observations are shown in red. The dashed line shows the observations when only the CTD observations from 1994 to 2001 are considered.

found that the seasonal temperature variation in the FSC almost turned off around 1910 and that this coincided with a temperature and salinity minima. They suggested that the changed balance between the Atlantic flow and the East Icelandic Current led to a disruption or reversion of the “normal” seasonal variation of the flow systems. The strongest model-predicted modulation of the temperature seasonality in the FSC (Fig. 8a) happened from 1965 to 1977, which coincides with the Great Salinity Anomaly (GSA) of the 1970s, [Dickson et al., 1988]. The explanation for the changes in seasonality during the 1970s GSA is likely the same as the explanation for the 1910s GSA [Hansen and Kristiansen, 1994]. This indicates that the simulated seasonal modulation is physical and not only a numerical artefact.

By assuming that the simulated time series is exact, an estimate of the de-seasonalizing errors introduced by using a subsampled temperature time series is possible. The analysis indicates that it is not advisable to survey the hydrographic section less than four times a year if reliable decadal scale temperature variations are of interest.

This last point is clearly seen when comparing de-seasonalized and averaged observations and the simulated low-frequency temperature variations (cfr. Figs. 3 and 10). The observed and the simulated time series follow each other closely, and the error band from the de-seasonalizing is narrow, in case of four or more samples per year. For periods with poor sampling (red bars in Fig. 10), the error-band widens and the two time series diverge. This result calls for caution in interpreting the seemingly cold anomaly in the late 1960s and the seemingly warm anomaly in the early 1980s in Fig. 10 as real anomalies.

The Mykines series shows no cold anomaly in the late 1960s, and thereby supports the simulated time series. However, a cold anomaly is prominent north of Iceland [Malmberg and Valdimarsson, 2003] and at 400 m depth at the Ocean Weather Station “Mike” (OWSM) [Østerhus and Gammelsrød, 1999] in the late 1960s, indicating that a cold anomaly might have been an isolated feature in the Nordic Seas. The warm anomaly in the early 1980s is evident in the observed Rockall series and in the observed Svinøy series (Figs. 4 and 5). The model represents the anomaly at the Rockall section, but not at the Svinøy section. This anomaly is therefore probably real, but the model is seemingly not able to pass it properly through the FSC. The reason for the model-data misfit during the years 1989-1991 is unclear. The observed Rockall series shows no warm anomaly during this period, but both model and observations show this anomaly very clearly at the Svinøy section.

It should be mentioned that a potential problem in using the observational temperature series as presented here is the mix of the Fair Isle-Munken and the Nolsoy-Flugga sections. Analyses of the simulated temperature series from the two sections support fusion of the two lines, although the short overlap between the two observed temperature series [Ellet and Turrell, 1992] makes the fusion statistically weak.

Finally, an ultimate description of the ocean dynamics and thermodynamics will be based on data assimilation systems where observations and simulated fields are merged in an optimal way. Unfortunately, the sparse temporal-spatial sampling of the ocean, in combination with the small length scales found in the region, makes such an approach difficult. It is therefore

encouraging that hind-cast simulations like the one presented here show realistic behaviour in several aspects, illustrating the potential of hind-cast simulations to expand observed time series, and to evaluate the highly observational-demanding and complex coupled atmosphere-sea ice-ocean climate models.

7. ACKNOWLEDGEMENT

The authors are grateful to Bogi Hansen, the Faroese Fisheries Laboratory, and Bill Turrell, the Marine Laboratory in Aberdeen, for providing the observed time series used in the work. The study has been supported by the Nordic Council of Ministers program Vestnordisk Océanklima, and the Research Council of Norway through RegClim and the Program of Supercomputing.

REFERENCES

- Anderson, L. G., Drange, H., Chierichi, M., Fransson, A., Johannessen, T., Skjelvan, I., and Rey, F. (2000), Seasonal and annual variability in the upper Greenland Sea based on measurements and a box model, *Tellus*, 52B, 1013-1020.
- Beaugrand, G. and Reid, P. C. (2003), Long-term changes in phytoplankton, zooplankton, and salmon linked to climate, *Glob. Change Biol.*, 9, 801-817.
- Belkin, I. M., Levitus, S., Antonov, J., and Malmberg, S. Aa. (1998), “Great Salinity Anomalies” in the North Atlantic, *Progress in Oceanography*, 41, 1-68.
- Bentsen, M. and Drange, H. (2000), Parameterizing surface fluxes in ocean models using the NCEP/NCAR reanalysis data. In: RegClim General Technical Report No. 4, pp 149– 158. Norwegian Institute for Air Research, Kjeller, Norway.
- Bentsen, M., Drange, H., Furevik, T., and Zhou, T. (2004), Simulated variability of the Atlantic meridional overturning circulation, *Clim. Dynam.*, *In Press*.
- Bleck, R., Rooth, C., Hu, C., and Smith, L. T. (1992), Salinity-driven thermohaline transients in a wind- and thermohaline-forced isopycnic coordinate model of the North Atlantic, *Journal of Physical Oceanography*, 22, 1486-1515.
- Dickson, R. R. and Brown, J. (1994), The production of North Atlantic Deep Water: Sources, rates, and pathways, *Journal of Geophysical Research*, 99, 12319-12341.
- Dickson, R. R., Meincke, J., Malmberg, S. Aa., and Lee, A. J. (1988), The “Great Salinity Anomaly” in the Northern North Atlantic 1968-1982, *Progress in Oceanography*, 20, 103-151.
- Ellet, D. J. and Turrell, W. R. (1992), Increased salinity levels in the NE Atlantic, *ICES CM 1992/C:20*, 12 pp.
- Fairall, C. W., E. F. Bradley, D. P. Rogers, J. B. Edson, and G. S. Young (1996) Bulk parameterization of air– sea fluxes for Tropical Ocean–Global Atmosphere Coupled-Ocean Atmosphere Response Experiment, *J. Geophys. Res.*, 101, 3747– 3764.
- Furevik, T. (2001), Annual and interannual variability of Atlantic water temperatures in the Norwegian and Barents Seas: 1980-1996, *Deep Sea Research*, 48, 383-404.
- Furevik, T., Bentsen, M., Drange, H., Johannessen, J. A., and Korabely, A. (2002), Temporal and spatial variability of the sea surface salinity in the Nordic Seas, *Journal of Geophysical Research*, 107(C12), 8009, doi:10.1029/2001JC001118.
- Hansen, B., Joensen, H. P., and Michelsen, V. E. (1994), Bottom temperature between Iceland and Shetland 1906-1962 measured in telegraph cables, *ICES CM 1994/S:5*, 14 pp.
- Hansen, B. and Kristiansen, R. (1994), Long-term changes in the

- Atlantic water flowing past the Faroe Islands, *ICES CM 1994/S:4*, 16 pp.
- Hansen, B. and Meincke, J. (1984), Long-term coastal sea surface temperature observations at the Faroe Islands, *Rapports et Procès-Verbaux des Réunions du Conseil International pour l'Exploration de la Mer*, 185, 162-169.
- Hansen, B. and Østerhus, S. (2000), North Atlantic-Nordic Seas Exchanges, *Progress in Oceanography*, 45, 109-208.
- Hansen, B., Østerhus, S., Hátún, H., Kristiansen, R., and Larsen, K. M. H. (2003), The Iceland-Faroe inflow of Atlantic water to the Nordic Seas, *Progress in Oceanography*, 54, 443-474.
- Helland-Hansen, B. and Nansen, F. (1909), The Norwegian Sea, *Fiskeridirektoratets Skrifter Serie Havundersøkelser*, 2, 1-390.
- Holliday, N. P., Pollard, R. T., Read, J. F., and Leach, H. (2000), Water mass properties and fluxes in the Rockall Trough, 1975-1998, *Deep Sea Research*, 47, 1303-1332.
- Kalnay, E., M. Kanamitsu, R. Kistler, W. Collins, D. Deaven, L. Gandin, M. Iredell, S. Saha, G. White, J. Woolen, Y. Zhu, M. Chelliah, W. Ebisuzaki, W. Higgins, J. Janowiak, K. C. Mo, C. Ropelewski, J. Wang, A. Leetma, R. Reynolds, R. Jenne, and D. Joseph (1996): The NCEP/NCAR 40-year reanalysis project. *Bullet. Amer. Meteorol. Soc.*, 77, 437-471.
- Kristmannsson, S. (2001), Flow of Atlantic Water into the Northern Icelandic Shelf area, 1985-1989, *ICES Cooperative Research Report*, 225, 124-135.
- Levitus, S. and Boyer, T. P. (1994), World Ocean Atlas 1994 Volume 4: Temperature. NOAA Atlas NESDIS 4.
- Levitus, S., Burgett, R., and Boyer, T. P. (1994), World Ocean Atlas 1994 Volume 3: Salinity. NOAA Atlas NESDIS 3.
- Malmberg, S. Aa. and Valdimarsson, H. (2003), Hydrographic conditions in Icelandic waters, 1990-1999, 219, 1-453.
- Nilsen, J. E., Gao, Y., Drange, H., Furevik, T., and Bentsen, M. (2003), Simulated North Atlantic-Nordic Seas water mass exchanges in an isopycnic coordinate OGCM, *Geophysical Research Letters*, 30(10), 1536, doi:10.1029/2002GL016597
- Østerhus, S. and Gammelsrød, T. (1999), The abyss of the Nordic Seas is warming, *Journal of Climate*, 12, 3297-3304.
- Reverdin, G., Cayan, D., Dooley, H. D., Ellet, D. J., Levitus, S., Penhoat, Y. D., and Dessier, A. (1994), Surface salinity of the North Atlantic: Can we reconstruct its fluctuations over the last one hundred years?, *Progress in Oceanography*, 33, 303-346.
- Sakshaug, E., Bjørge, B., Gulliksen, B., Loeng, H., and Mehlum, F. (1994), Structure, biomass distribution, and energetics of the pelagic ecosystem in the Barents Sea: A synopsis, *Polar Biol.*, 14, 405-411.
- Turrell, W. R., Devonshire, E., Payne, R., and Slessor, G. (1993), Analysis of the historic time-series obtained in the Faroe-Shetland Channel, *ICES CM 1993/C:29*, 21 pp.
- Turrell, W. R., Hansen, B., Hughes, S., and Østerhus, S. (2003), Hydrographic variability during the decade of the 1990s in the Northeast Atlantic and southern Norwegian Sea, *Marine Science Symposia*, 219, 111-120.

Annebritt Sandøe: Nansen Environmental and Remote Sensing Centre, Edv. Griegsv. 3A, 5059 Bergen, Norway.

annebrit@nersc.no

Helge Drange: 1) Nansen Environmental and Remote Sensing Centre, Edv. Griegsv. 3A, 5059 Bergen, Norway. 2) Geophysical Institute, University of Bergen, Allegaten 70, 5007 Bergen, Norway. 3) Bjerknes Centre for Climate Research, Allgaten 55, 5007 Bergen, Norway. 4) Nansen-Zhu International Research Centre, Beijing 100029, China. helge.drange@nersc.no

Hjálmar Hátún: Faroese Fisheries Laboratory, Nóatún 1, FO-110, Faroe Islands. hjalmarh@frs.fo

Mats Bentsen: 1) Nansen Environmental and Remote Sensing Centre, Edv. Griegsv. 3A, 5059 Bergen, Norway. 2) Bjerknes Centre for Climate Research, Allgaten 55, 5007 Bergen, Norway. mats.bentsen@nersc.no

